
Generation of Energetic Femtosecond Pulses at High Average Power

Reimund Martin Kaumanns



München 2020

Generation of Energetic Femtosecond Pulses at High Average Power

Reimund Martin Kaumanns

Dissertation
an der Fakultät für Physik
der Ludwig-Maximilians-Universität
München

vorgelegt von
Reimund Martin Kaumanns
aus München

München, den 20.01.2020

Erstgutachter: Prof. Dr. Ferenc Krausz
Zweitgutachter: Prof. Dr. Oleg Pronin
Tag der mündlichen Prüfung: 02.03.2020

Zusammenfassung

Die Entwicklung leistungsfähigerer Femtosekundenlaser mit höherer Pulsenergie und Durchschnittsleistung ermöglicht eine immer weitreichendere Anwendung von Lasersystemen. Die Erzeugung von leistungsstarken Attosekundenpulsen für empfindliche Messreihen und kompakte Röntgenquellen mit hoher Brillanz sind nur zwei denkbare Anwendungen von vielen.

Die erhofften Lasersysteme mit Durchschnittsleistungen im Kilowatt Bereich, hunderten von Millijoule Pulsenergie und Pulsdauern von wenigen Femtosekunden basieren auf einer signifikanten Weiterentwicklung bestehender Technologie, die zum Teil Gegenstand dieser Arbeit ist. Mittels eines regenerativen Dünnscheibenverstärkers konnte zum ersten mal die Verstärkung von Laserpulsen bis zu einer Energie von 200 mJ bei einer Wiederholrate von 5 kHz, einer Dauer von circa 1 ps und einer Durchschnittsleistung von 1 kW gezeigt werden. Die ausgezeichneten thermischen Eigenschaften des Dünnscheibenkonzepts in Verbindung mit einer tiefgreifenden Untersuchung der Verstärkereigenschaften und einer sorgfältigen Optimierung des Aufbaus ermöglichen einen hochstabilen Laser mit einem annähernd beugungslimitierten Ausgangsstrahl. Der Verstärker kann als ideale Pumpquelle für einen optischen parametrischen Verstärker (OPV) genutzt werden, der dann die Erzeugung von Pulsen mit einer Energie bis zu 20 mJ und einer Dauer von wenigen Femtosekunden bei einer Wiederholrate von mehreren Kilohertz ermöglichen könnte.

Ein alternativer Ansatz zur Erzeugung von Femtosekundenpulsen aufbauend auf dem vorgestellten Lasersystem wird ebenfalls untersucht. In einer der ersten Realisierungen einer nichtlinearen Verbreiterung in einer Multipasszelle konnten Pulse mit einer Energie von 18 mJ bei einer Wiederholrate von 5 kHz spektral verbreitert und deren Komprimierbarkeit auf eine Dauer von 41 fs demonstriert werden. Eine weitere Skalierung bis zu Pulsenergien von 40 mJ und 75 mJ wird gleichfalls gezeigt. Diese Energien sind (soweit bekannt) die höchsten, bei denen ein Puls mit einer Frequenz von mehreren Kilohertz verbreitert wurde. Der vorgestellte Ansatz weist einen beispiellosen Durchsatz von über 95 % und eine hervorragende Skalierbarkeit bezüglich der Durchschnittsleistung auf. Im Gegensatz zum OPV Ansatz wird die meiste Eingangsenergie in den erzeugten Femtosekundenpuls überführt, weshalb für eine gegebene Ausgangsenergie weniger komplexe Laserquellen notwendig sind.

Die Ergebnisse dieser Arbeit stellen einen bedeutsamen Schritt für die nächste Generation von Femtosekundenlasern dar. Eine simulierte Erweiterung des Systems erlaubt sogar eine höhere Pulsenergie von 100 mJ bei einer Pulsdauer von mehreren zehn Femtosekunden und einer Wiederholrate von 5 kHz.

Abstract

The development of more powerful and more energetic femtosecond laser systems builds the foundation for an even wider application of lasers. Powerful attosecond sources for sensitive experiments and compact high brilliance X-ray sources are only two examples of a vast field of possibilities that can be made accessible.

The envisioned lasers with kilowatt scale average powers, hundreds of millijoule of pulse energy and pulse durations down to the few-cycle regime require significant technological advances that are partially introduced in this thesis. The amplification of laser pulses to an energy of 200 mJ with a repetition rate of 5 kHz, a duration of about 1 ps and an average power of 1 kW is demonstrated for the first time using a thin-disk regenerative amplifier. The excellent thermal properties of the thin-disk scheme in combination with a thorough investigation of the amplifier properties and a careful optimization of the design provides a highly stable laser output with an excellent virtually diffraction limited beam quality. This amplifier can be used as nearly ideal pump source for an optical parametric amplification (OPA) chain, which is predicted to facilitate few-cycle pulses with energies up to 20 mJ and a multi-kilohertz repetition rate.

In a second part an alternative approach to obtain a femtosecond scale pulse duration from the presented amplifier is studied. In one of the first implementations of a multipass nonlinear broadening stage, pulses of about 18 mJ are spectrally broadened with a repetition rate of 5 kHz, and compressibility down to 41 fs is demonstrated. Further pulse energy scaling to 40 mJ and 75 mJ is shown. To the best of the authors knowledge these energies represent the highest energies at which a pulse was spectrally broadened in the multi-kilohertz regime. The proposed approach features unprecedented throughputs over 95 % and excellent average power scalability. In contrast to the OPA scheme most of the input pulse energy is transferred into the femtosecond scale pulse and hence less complex source lasers are necessary for a given output pulse energy.

The record-breaking results of this thesis constitute an important step for next generation femtosecond laser sources. A simulated extension of the system allows for the generation of a pulse energy of 100 mJ, a pulse duration of tens of femtosecond and a repetition rate of 5 kHz close to the envisioned parameters.

Contents

Zusammenfassung	v
Abstract	vii
Introduction	1
1 Beam Propagation and Amplification	5
1.1 Maxwell's Equations and the Gaussian Mode	5
1.1.1 The Paraxial Helmholtz Equation	6
1.1.2 Hermite-Gaussian Modes	7
1.2 Propagation via ABCD Matrices	9
1.3 Resonators and their Parametrization	10
1.3.1 Resonator Definition	11
1.3.2 The Gouy Phase of a Resonator	12
1.3.3 Periodicity of Resonators	13
1.3.4 Propagation of Arbitrary Modes	14
1.3.5 Off-Axis Propagation	15
1.3.6 Resonator Robustness	17
1.4 Beam Quality Factor M^2	21
1.5 Pulse Propagation and Dispersion	23
1.6 Amplification by Stimulated Emission	24
1.6.1 Multi-Level Systems	24
1.6.2 Absorption and Emission Cross Sections	26
1.6.3 Signal Amplification	28
1.6.4 Figures of Merit for Gain Media	31
2 Picosecond Multi-Kilohertz Kilowatt Thin-Disk Amplifier	35
2.1 Layout and Performance	36
2.1.1 System Design	36
2.1.2 System Performance	38
2.2 Chirped Pulse Amplification	40
2.3 Geometries and Materials	42
2.3.1 Gain Medium Geometries	42
2.3.2 Dopants	44
2.3.3 Host Materials	44
2.3.4 Pockels Cell	46
2.4 Optimal Working Point	49
2.5 Intracavity Power and Damage Threshold	55
2.6 Thermal Distortions	59
2.6.1 Temperature Calculation	59

2.6.2	Thermally Induced Wavefront Aberrations	61
2.6.3	Comparison to the Numeric Model	63
2.6.4	Impact of Air	64
2.7	Design Optimization	67
2.7.1	Resonator Design	67
2.7.2	Mechanical Design	71
2.8	Preamplifier	74
2.9	Optimization of the Frontend	76
2.10	Conclusion	80
3	Nonlinear Broadening of High Energy Pulses	83
3.1	Nonlinear Optical Effects	83
3.1.1	Nonlinear Wave Equation	83
3.1.2	Second Order Nonlinear Effects	85
3.1.3	Third Order Nonlinear Effects	86
3.2	Generation of Broadband High Energy Pulses	93
3.2.1	Optical Parametric Amplification	93
3.2.2	Nonlinear Broadening in Waveguides	94
3.3	Multipass Cell Design	96
3.4	Experimental Results	101
3.5	Limitations	106
3.5.1	Ionization	106
3.5.2	Wavebreaking	109
3.6	Energy Scaling	111
3.6.1	Astigmatic or Elliptic Beams	112
3.6.2	Thin Plate Multipass Cells	114
3.6.3	Pulse Stacking	116
3.6.4	Circular Polarization	117
3.6.5	Input Pulse Duration	118
3.6.6	Cell Length	119
3.6.7	Higher Order Modes	123
3.7	Conclusion	127
	Summary and Outlook	129
A	Preamplifier	133
A.1	Robustness of a Linear Resonator	133
A.1.1	Mechanical Robustness	133
A.1.2	Spot Size Robustness	134
A.1.3	Temporal Robustness	135
A.1.4	Conclusion	136
A.2	Design for a Millijoule Thin-Disk Resonator	137
B	Numeric Thin-Disk Amplification Model	139
B.1	Pump Phase	139
B.1.1	Excitation	139
B.1.2	Depletion	140

B.1.3 Upper Level Population	140
B.2 Emission Phase	141
B.2.1 Gain	141
B.2.2 Multipass	142
B.3 Equilibrium Population	143
B.4 Dynamics	143
C Nonlinear Phase Retrieval	145
D Data Archiving	147
Bibliography	149
List of Publications	161
Acknowledgements	163

List of Figures

1.1	Gaussian beam propagation	8
1.2	Gouy phase accumulation	12
1.3	Arbitrary mode propagation in a resonator	15
1.4	Off-axis propagation in a resonator	16
1.5	Linear and ring resonator	17
1.6	Ring resonator robustness	20
1.7	High order mode propagation	22
1.8	Level schemes for gain media	25
2.1	Schematic of the laser system	36
2.2	Amplifier layout	37
2.3	Amplifier output power	38
2.4	Beam quality of the amplified beam	39
2.5	Compression of the amplified beam	40
2.6	Chirped pulse amplification principle	41
2.7	Thin-disk schematic	43
2.8	Simulated output energy of the amplifier	51
2.9	Simulated disturbance robustness of the amplifier	52
2.10	Simulated buildup of the amplifier	53
2.11	Measured buildup of the amplifier	55
2.12	10 kHz output power of the amplifier	57
2.13	Simulated and measured disk temperature	61
2.14	Amplifier output power versus pump wavelength	62
2.15	Amplifier output power versus pump spot shape	63
2.16	Amplifier simulations results compared to experimental results	64
2.17	Amplifier behavior for humid and dry air	66
2.18	Caustic of the amplifier's resonator	68
2.19	Amplifier spot size variations	69
2.20	Beam profile stability of the amplifier	70
2.21	Housing and mount design of the amplifier	71
2.22	Impact of water cooling for the amplifier thermalization	72
2.23	Impact of water cooling for the amplifier output power	73
2.24	Preamplifier layout	74
2.25	Preamplifier resonator caustic	75
2.26	Preamplifier output power	76
2.27	Amplifier spectrum and pulse duration with fiber frontend	77
2.28	Compact grating stretcher design	78
2.29	Yb:CALGO preamplifier caustic and output spectrum	78
2.30	Amplifier spectrum and pulse duration with Yb:CALGO frontend	79

3.1	Instantaneous frequency of SPM	89
3.2	Working principle of a multipass cell	96
3.3	Layout of the multipass cell	97
3.4	Experimental realization of the multipass cell	101
3.5	Output spectrum of the 3 m long multipass cell	102
3.6	Compressed pulse of the 3 m long multipass cell	103
3.7	Beam quality of the 3 m long multipass cell	104
3.8	Homogeneity of the 3 m long multipass cell	105
3.9	Ionization pressure dependency	108
3.10	Dispersive behavior of the 3 m long multipass cell	110
3.11	Wave breaking in a multipass cell	111
3.12	Astigmatism compensation in a multipass cell	113
3.13	Spectral broadening in a thin plate multipass cell	115
3.14	Output spectrum of the 8 m long multipass cell	120
3.15	740 fs pulse in an 8 m long multipass cell	122
3.16	First order doughnut mode propagation in a multipass cell	126
A.1	ABCD scheme in a linear resonator	133

List of Tables

2.1	Properties of potential gain materials	45
2.2	Thin-disk amplifier simulation parameters	50

List of Acronyms

AR	anti-reflective
ASE	amplified spontaneous emission
BBO	β -barium borate
COF	capillary optical fiber
CPA	chirped pulse amplification
CW	continuous wave
DKDP	potassium dideuterium phosphate
FL	Fourier limit
FR	Faraday rotator
FWHM	full width half maximum
GDD	group delay dispersion
GVD	group velocity dispersion
HR	highly-reflective
IBS	ion beam sputtering
KDP	potassium dihydrogen phosphate
KLM	Kerr-lens mode locked
$\lambda/4$	quarter wave plate
$\lambda/2$	half wave plate
LNB	lithium niobate
LTA	lithium tantalate
Nd:YAG	neodymium yttrium aluminium garnet
OPA	optical parametric amplification
PC	Pockels cell
RoC	radius of curvature
RTP	rubidium titanyl phosphate
SH-FROG	second harmonic frequency-resolved optical gating
SPM	self phase modulation
TD	thin-disk
TFP	thin film polarizer
Ti:Sa	titanium sapphire

TOD	third order dispersion
YAG	yttrium aluminium garnet
Yb^{3+}	ytterbium
Yb:CALGO	ytterbium doped $CaGdAlO_4$
Yb:LuAG	ytterbium lutetium aluminium garnet
Yb:YAG	ytterbium yttrium aluminium garnet

Introduction

When the first laser was proposed in the year 1960 by Theodore Maiman [1], the impact of this invention was still difficult to estimate. In fact Theodore Maiman commented that “a laser is a solution seeking a problem”. Today the application of laser light in science and industry is standard practice and several scientific breakthroughs were only enabled by the usage of lasers [2].

Many lasers are designed for metrology applications. Continuous wave (CW) lasers are commonly used to measure e.g. surface structures, temperatures or precise distances. Pulsed lasers add the possibility to temporally resolve measurements with high accuracy. Even very fast events like electronic motions are captured by laser pulses with a duration on the attosecond scale [3] and these pulses can be regarded as the shortest events created by humankind. For example using pulsed lasers for molecular spectroscopy facilitates the measurement of the unique absorption spectrum of a molecule (the *molecular fingerprint*) and the time resolved response function of a molecule. This method is also known as *field-resolved spectroscopy* [4]. The conjoined usage of time-domain and spectral data enables amongst others the detection of the slightest trace of a certain molecule in a solution.

Lasers can also be used to modify material properties or create extreme conditions where materials show a special behavior. These applications typically depend on lasers with high average or peak powers and peak powers on the order of petawatt were demonstrated with pulsed lasers. When properly focused, these lasers generate extreme intensities up to $5.5 \times 10^{22} \text{ W/cm}^2$ [5], hence lasers do not only provide the shortest events created by humankind, but also the most intense. These intense lasers often work with very low repetition rates on the order of a few hertz or less in order to provide single events with an extremely high intensity. An exemplary field of application is the acceleration of electrons or even ions. While the former can be used to create X-rays for medical imaging [6], the latter can be utilized in particle therapies to treat tumors [7].

Using high intensity effects with high repetition rates for more sensitive measurements or faster results is however challenging and the necessary laser sources are subject of latest research. These lasers require a pulse duration on the femtosecond scale to obtain laser events that are highly localized in time. The technology for such lasers was coined *third generation femtosecond technology* [8] and leads to the development of a whole new class of lasers with terawatt scale peak intensities and average powers approaching the kilowatt scale. The possibilities that this new laser class provides are difficult to foresee, but it surely extends the applicability of lasers into new regimes.

The already mentioned laser based X-ray generation would be revolutionized by a third generation laser system. A compact X-ray source with a high brilliance would become feasible and enable the wide application of high resolution and low dose medical imaging. The most common principle that is used to create X-rays

(e.g. for medical imaging) has not changed since more than 120 years and is still based on X-ray tubes. The radiation emitted from X-ray tubes suffers from a low brilliance with a large angular divergence and bandwidth. This low brilliance yields (for example) a low spatial resolution in medical imaging applications with a large dose required for a sufficient contrast to noise ratio [6]. An all-laser based concept for a high brilliance X-ray source can tackle these issues. The concept is based on a high intensity pulse with a duration of a few tens of femtoseconds that accelerates electrons to relativistic velocities. The photons from a second pulse scatter from these relativistic electrons and are upshifted to the X-ray regime. A kilohertz repetition rate ensures a sufficient flux for practical medical imaging applications [6].

Another field of application for this new laser class are effects with very low efficiencies. As example the generation of energetic isolated attosecond pulses on the nanojoule to microjoule scale requires powerful few-cycle pulses with energies of tens of millijoule [9]. To obtain better statistical significance for attosecond metrology, a high repetition rate is favorable. Thus a few-cycle laser with a high peak power and a high repetition rate can enable sensitive measurements of nonlinear processes with attosecond scale time resolution.

The workhorse for highly intense laser systems are titanium sapphire (Ti:Sa) lasers [8, 10]. This gain material has a broad bandwidth that naturally supports pulse durations from few-cycle to a few tens of femtosecond. The large emission bandwidth of Ti:Sa and the separation of pump and emission wavelengths also cause a large energy loss during the transition of a pump photon to an emitted photon. This energy loss manifest as thermal load for the gain material and is one reason why Ti:Sa systems are typically limited to relatively low average powers below 100 W. In contrast lasers based on ytterbium can provide much higher average powers in the kilowatt regime but their pulse duration is comparatively long with durations on the order of picoseconds [10].

The challenge of this new laser class is hence that either broadband lasers like Ti:Sa need to be pushed towards higher average powers or technologies that enhance the pulse energy and pulse duration of existing high average power architectures need to be developed. However, the thermal issues of Ti:Sa (and similar) systems make their usage extremely challenging and promising results have not been demonstrated to this day. Consequentially the enhancement of existing high average power architectures is regarded as more promising.

This thesis investigates and applies technologies that pave the way towards a third generation femtosecond laser system. It focuses on the approach to develop a highly energetic ytterbium based laser source with high average power that is subsequently used to obtain a femtosecond scale pulse duration. With ytterbium based InnoSlab technology average powers of about 500 W, pulse energies of 54 mJ and a pulse duration of 1.5 ps were already demonstrated [11]. A pulse energy of 23 mJ with an average power of 674 W and a pulse duration of 235 fs was recently obtained with a coherent combination of ytterbium fiber lasers [12]. A thin-disk laser system with an even higher pulse energy and average power is developed in the scope of this thesis. The designed thin-disk laser system represents the most energetic multi-kilohertz single mode laser to date (to the best of the authors knowledge) with a pulse energy of up to 200 mJ, an average power of 1 kW and a pulse duration of

about 1 ps. The thin-disk geometry [13] has close to ideal properties regarding heat transport and enables an amplification scheme with low thermal distortions, high average powers and a high beam quality while still providing a large aperture as necessary for high pulse energies. The thin-disk technology is therefore considered to be a key technology for third generation femtosecond laser systems.

The developed thin-disk laser is an ideal pump source for an optical parametric amplification (OPA) scheme [8]. In an OPA scheme a powerful and highly energetic pump source is used to amplify a broadband signal to higher energies. With this technique few-cycle pulses with an energy of 53 mJ were already generated at a repetition rate of 1 kHz [14]. The pulse energy and average power of these systems is however limited by the low conversion efficiency from near infrared pump to near infrared signal on the order of 10 % and some thermal constraints. To date output average powers significantly beyond 100 W could not be demonstrated [15].

Therefore in a second step this thesis investigates an alternative approach for the generation of highly energetic femtosecond scale pulses with high average power. A nonlinear compression scheme in a gas-filled multipass cell is evaluated as the most promising approach. In one of the first experimental implementations of a multipass nonlinear broadening stage, about 18 mJ of pulse energy is spectrally broadened at a repetition rate of 5 kHz and the compressibility to a pulse duration of 41 fs is demonstrated. Further pulse energy scaling to 40 mJ and 75 mJ is shown. To the best of the authors knowledge these energies represent the highest energies spectrally broadened in the multi-kilohertz regime. Finally a technology to further increase this energy to values beyond 100 mJ is theoretically investigated. These unique parameter set of pulse duration, energy and repetition rate constitute an important step for next generation femtosecond laser sources.

The thesis is structured as follows:

- Chapter 1 introduces the theoretical basis for laser light propagation and amplification. Also a novel method to summarize resonator properties is proposed. The method parameterizes several resonator properties by a common variable and provides an intuitive understanding of resonator features. The method also helps to greatly simplify the derivation of an optimal resonator structure.
- Chapter 2 presents the high energy amplifier that was developed in the scope of this work. The design choices are evaluated and possible limitations identified. The behavior of the amplifier is thoroughly investigated supported by a numerical model and potential optimizations are reviewed.
- Chapter 3 compares different methods to obtain femtosecond scale pulses from the laser system presented in chapter 2. One of the first experimental implementations of a multipass nonlinear broadening stage is investigated and further scaling towards even higher energies is analyzed.

Chapter 1

Beam Propagation and Amplification

The following chapter gives a short introduction into the basic concepts of laser beam propagation, optical systems and laser amplification. These concepts are later used to implement a high energy amplifier and a subsequent nonlinear compression stage.

First of all the conditions for laser modes and a set of possible modes called *Hermite-Gaussian Modes* are derived. Afterwards a special type of optical system is explained in more detail: the resonator. A resonator is the key element of the amplifier and the compression stage developed within the scope of this thesis. It is shown that most resonator properties can be described by a phase accumulated during one transition through a resonator. A figure of merit for the quality of a laser mode is established and the properties of a pulsed laser are introduced. Finally the amplification of a (pulsed) laser in a pumped gain medium is discussed. Based on the phenomena absorption, stimulated emission and spontaneous emission, a formalism to describe laser amplification is introduced and some principal figures of merit for gain media are derived.

1.1 Maxwell's Equations and the Gaussian Mode

Maxwell's equations couple the two electro-magnetic fields, the electric field $\boldsymbol{\mathcal{E}}(\boldsymbol{r}, t)$ and the magnetic field $\boldsymbol{\mathcal{H}}(\boldsymbol{r}, t)$, in space \boldsymbol{r} and time t . This forms the basis for a description of electro-magnetic fields like light.

In a dielectric medium, Maxwell's equations are expressed by [16, p. 154]

$$\nabla \times \boldsymbol{\mathcal{H}} = \frac{\partial \boldsymbol{\mathcal{D}}}{\partial t} \quad (1.1)$$

$$\nabla \times \boldsymbol{\mathcal{E}} = -\frac{\partial \boldsymbol{\mathcal{B}}}{\partial t} \quad (1.2)$$

$$\nabla \cdot \boldsymbol{\mathcal{D}} = 0 \quad (1.3)$$

$$\nabla \cdot \boldsymbol{\mathcal{B}} = 0 \quad (1.4)$$

$$\boldsymbol{\mathcal{D}} = \epsilon_0 \boldsymbol{\mathcal{E}} + \boldsymbol{\mathcal{P}} \quad (1.5)$$

$$\boldsymbol{\mathcal{B}} = \mu_0 \boldsymbol{\mathcal{H}} + \mu_0 \boldsymbol{\mathcal{M}} \quad (1.6)$$

The electric flux density $\boldsymbol{\mathcal{D}}$ is related to the electric field $\boldsymbol{\mathcal{E}}$ with the vacuum permittivity ϵ_0 . The polarization density $\boldsymbol{\mathcal{P}}$ describes the material reaction to an

applied electric field. Likewise the magnetic flux density \mathbf{B} and the magnetic field \mathbf{H} are coupled by the vacuum permeability μ_0 with the magnetization density \mathbf{M} being the material contribution. On the basis of these equations, an expression for laser modes is derived and discussed in the following sections.

1.1.1 The Paraxial Helmholtz Equation

In a linear, nondispersive, homogenous and isotropic medium (e.g. air), the polarization density is linearly connected to the electric field [16, p. 156]

$$\mathbf{P} = \epsilon_0 \chi \mathbf{E} \quad (1.7)$$

leading to \mathbf{D} being coupled to the electric field using the electric permittivity ϵ and the electric susceptibility χ

$$\mathbf{D} = \epsilon \mathbf{E} \quad (1.8)$$

$$\epsilon = \epsilon_0(1 + \chi). \quad (1.9)$$

Similarly the magnetic field \mathbf{B} is defined using the material permeability μ

$$\mathbf{B} = \mu \mathbf{H} \quad (1.10)$$

yielding Maxwell's equations in a simplified form

$$\nabla \times \mathbf{H} = \epsilon \frac{\partial \mathbf{E}}{\partial t} \quad (1.11)$$

$$\nabla \times \mathbf{E} = -\mu \frac{\partial \mathbf{H}}{\partial t} \quad (1.12)$$

$$\nabla \cdot \mathbf{D} = 0 \quad (1.13)$$

$$\nabla \cdot \mathbf{B} = 0. \quad (1.14)$$

Applying the identity for a vector field \mathbf{F}

$$\nabla \times (\nabla \times \mathbf{F}) = \nabla(\nabla \cdot \mathbf{F}) - \nabla^2 \mathbf{F} \quad (1.15)$$

to the electric field \mathbf{E} and using the relationship $c = 1/\sqrt{\mu\epsilon}$ with c being the speed of light in the medium gives

$$\nabla^2 \mathbf{E} - \frac{1}{c^2} \frac{\partial^2 \mathbf{E}}{\partial t^2} = 0. \quad (1.16)$$

This equation is called wave equation and any solution for it is a valid electric field \mathbf{E} for the given conditions.

For a monochromatic wave with angular frequency ω

$$\mathbf{E} = \text{Re}\{\mathbf{E}(\mathbf{r}) \exp(i\omega t)\} \quad (1.17)$$

the wave equation is simplified to the Helmholtz equation

$$\nabla^2 \mathbf{E}(\mathbf{r}) + k^2 \mathbf{E}(\mathbf{r}) = 0. \quad (1.18)$$

Here the wavenumber k is

$$k = \frac{\omega}{c} = n \frac{\omega}{c_0}, \quad (1.19)$$

with $n = c_0/c$ being the refractive index of the medium and c_0 the speed of light in vacuum.

Equation 1.18 can be further simplified by using the slowly varying envelope approximation. In that case \mathbf{E} is defined using a carrier frequency along z that is identical to the wavenumber k and an envelope $\mathbf{A}(\mathbf{r})$ that slowly varies along z

$$\mathbf{E} = \mathbf{A}(\mathbf{r}) \exp(-ikz). \quad (1.20)$$

For a position independent $\mathbf{A}(\mathbf{r}) = \mathbf{A}_0$, this represents a plane wave oscillating with a periodicity (or wavelength) $\lambda = 2\pi/k$ along z [16, p. 44]. Using monochromatic plane waves for solving Maxwell's equations shows that the electric field \mathbf{E} and the magnetic field \mathbf{H} are transverse to the propagation direction z [16, p. 165], which is why they are called *transverse electromagnetic* or *TEM* waves. For monochromatic plane waves, the intensity I of the electric field is calculated via [16, p. 166]

$$I = \frac{|\mathbf{E}|^2}{2\eta}. \quad (1.21)$$

Here η is the impedance of the medium $\eta = \eta_0/n$ with $\eta_0 = \sqrt{\mu_0/\epsilon_0}$.

Plugging equation 1.20 into equation 1.18 yields

$$\frac{\partial^2 \mathbf{A}(\mathbf{r})}{\partial x^2} + \frac{\partial^2 \mathbf{A}(\mathbf{r})}{\partial y^2} + \frac{\partial^2 \mathbf{A}(\mathbf{r})}{\partial z^2} - 2ik \frac{\partial \mathbf{A}(\mathbf{r})}{\partial z} = 0. \quad (1.22)$$

The plane wave solution $\mathbf{A}(\mathbf{r}) = \mathbf{A}_0$ is the trivial solution to this equation. Note that choosing a different carrier frequency than the wavenumber k in equation 1.20 would yield a nonexistent field $\mathbf{A}_0 = 0$ as trivial solution for equation 1.18. The slowly varying envelope approximation now states that [16, p. 48]

$$\left| \frac{\partial^2 \mathbf{A}(\mathbf{r})}{\partial z^2} \right| \ll k \left| \frac{\partial \mathbf{A}(\mathbf{r})}{\partial z} \right|. \quad (1.23)$$

The paraxial Helmholtz equation for monochromatic light is therefore

$$\frac{\partial^2 \mathbf{A}(\mathbf{r})}{\partial x^2} + \frac{\partial^2 \mathbf{A}(\mathbf{r})}{\partial y^2} - 2ik \frac{\partial \mathbf{A}(\mathbf{r})}{\partial z} = 0. \quad (1.24)$$

1.1.2 Hermite-Gaussian Modes

The space spanned by all solutions for the paraxial Helmholtz equation 1.24 is given by a set of orthogonal modes $\mathbf{A}_{m,n}(\mathbf{r})$. Every linear combination of solutions $\mathbf{A}_{m,n}(\mathbf{r})$ is again a solution to the paraxial Helmholtz equation. One solution space is spanned by the orthogonal *Hermite-Gaussian Modes*. Using equation 1.20, the Hermite-Gaussian Modes are ($\mathbf{r} = (x, y, z)$) [16, p. 96]

$$\mathbf{E}_{m,n}(\mathbf{r}) = \mathbf{E}_{0,0}(\mathbf{r}) H_m \left[\frac{\sqrt{2}x}{w} \right] H_n \left[\frac{\sqrt{2}y}{w} \right] \exp[i(m+n)\zeta] \quad (1.25)$$

$$\mathbf{E}_{0,0}(\mathbf{r}) = \mathbf{E}_0 \frac{w_0}{w} \exp \left[-\frac{x^2 + y^2}{w^2} \right] \exp \left[-\frac{ik(x^2 + y^2)}{2R} - ikz + i\zeta \right] \quad (1.26)$$

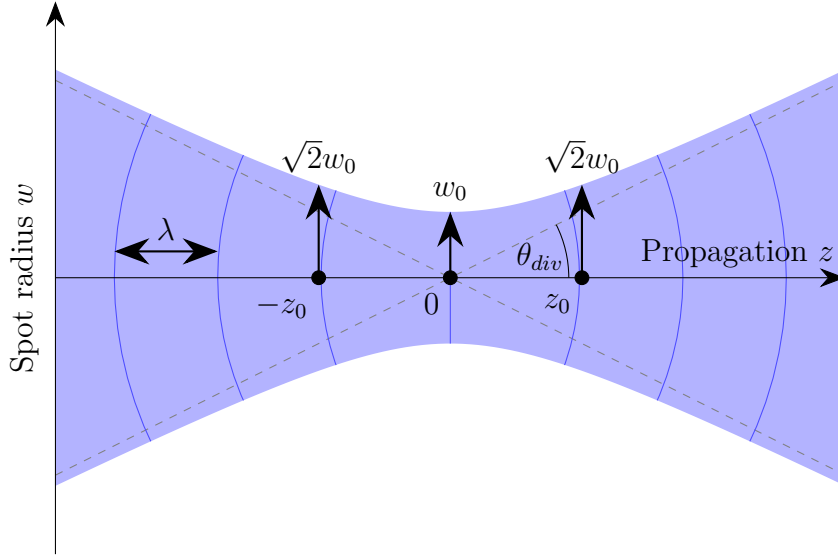


Figure 1.1: The spot radius $w(z)$ of an exemplary Gaussian Beam $\mathbf{E}_{0,0}(\mathbf{r})$ along the propagation direction z . The solid blue lines mark the wavefronts (i.e. the phase) of the Gaussian beam with the radius of curvature $R(z)$ and, for $|z| \gg z_0$, the separation λ . The Gouy phase $\zeta(z)$ is contributing to the wavefront position mainly within the range $(-z_0, z_0)$ effectively increasing the distance between the wavefronts around the focus. θ_{div} is the divergence angle of the emission cone.

with the distance z from the waist position (z increases as the beam propagates), the waist radius w_0 , the spot radius $w(z) = w_0 \sqrt{1 + (z/z_0)^2}$, the radius of curvature of the wavefront $R(z) = z[1 + (z_0/z)^2]$, the Gouy phase shift $\zeta(z) = \tan^{-1}(z/z_0)$ and the Rayleigh range $z_0 = \pi w_0^2/\lambda$. The Hermite polynomial H_m (and likewise H_n) is described by the recurrence relation

$$\begin{aligned} H_{m+1}(u) &= 2uH_m(u) - 2mH_{m-1}(u) \\ H_0(u) &= 1 \\ H_1(u) &= 2u. \end{aligned} \quad (1.27)$$

The 2D profile in the (x, y) plane of a Hermite-Gaussian mode is fully defined by a given wavenumber k , the position z and the Rayleigh range z_0 . For a system with a single wavelength, only the latter values change and hence a parameter q is defined as compact representation of the current beam parameters [16, p. 76]

$$\begin{aligned} q &= z + iz_0 \\ \frac{1}{q} &= \frac{1}{R(z)} - i \frac{\lambda}{\pi w(z)^2}. \end{aligned} \quad (1.28)$$

The zero order mode $\mathbf{E}_{0,0}(\mathbf{r})$ is of special importance in the following sections and an exemplary propagation is plotted in figure 1.1. Its intensity is given by [16, p. 77]

$$I_{0,0}(r, z) = I_0 \frac{w_0}{w(z)} \exp \left[-\frac{2r^2}{w(z)^2} \right] \quad (1.29)$$

with the radial position $r = \sqrt{x^2 + y^2}$ and the peak intensity I_0 . Since the intensity follows a Gaussian profile, the zero order mode is also called *Gaussian mode* or *Gaussian beam*. For a Gaussian beam, the spot radius $w(z)$ describes the radial distance at which the intensity has dropped by a factor $1/e^2$. At a distance from the waist equal to the Rayleigh range $z = z_0$, the spot has increased by a factor $\sqrt{2}$ compared to the waist w_0 . The Rayleigh range is therefore often used as a measure for the length of a focus, i.e. over which distance the spot size does not differ significantly from the waist size and the divergence is low. Long Rayleigh ranges that are typical for large spot sizes imply a long distance in which a beam can be assumed to be collimated. After a propagation far beyond the Rayleigh range, the emission approximates a cone with a divergence angle [16, p. 80]

$$\theta_{div} \approx \frac{w_0}{z_0}. \quad (1.30)$$

1.2 Propagation via ABCD Matrices

In linear systems, the input and output parameters are coupled by a matrix multiplication. This property can also be applied to linear optical systems. Approximating a laser beam as light ray with a position y_1 and an angle θ_1 with reference to the z -axis (i.e. the optical axis) and assuming linearity yields the relationship [16, p. 25]

$$\begin{bmatrix} y_2 \\ \theta_2 \end{bmatrix} = \begin{bmatrix} A & B \\ C & D \end{bmatrix} \begin{bmatrix} y_1 \\ \theta_1 \end{bmatrix}. \quad (1.31)$$

Here y_2 and θ_2 describe the output ray of the optical system. Negative angles θ correspond to rays that point downward from the optical axis in their direction of propagation. The matrix \mathbf{M} with the elements A, B, C and D fully describes the system properties. In case of systems consisting of spherical surfaces, free space propagation and material transmission or reflection, linearity can be assumed if all ray angles within the system fulfill the small angle approximation

$$\sin(\theta) \approx \theta. \quad (1.32)$$

A concatenation of linear optical systems $\mathbf{M}_1 \rightarrow \mathbf{M}_2 \rightarrow \mathbf{M}_3$ is calculated by simply multiplying their ABCD-matrices $\mathbf{M}_{123} = \mathbf{M}_3\mathbf{M}_2\mathbf{M}_1$. Thus a straight forward treatment of optical systems is possible. Basic building blocks for optical systems like the ABCD matrix for a lens or for a simple propagation can be found in literature [16, p. 26f]. The determinant of an ABCD matrix corresponds to the relation of the input and output refractive index n_1 and n_2 and is determined as $\text{Det}(\mathbf{M}) = n_1/n_2$ [16, p. 31]. In the following it is assumed that the first and last stage of the optical system are in the same environment and hence $n_1 = n_2$ or

$$\text{Det}(\mathbf{M}) = 1. \quad (1.33)$$

The ABCD formalism can also be used beyond ray optics. A Gaussian beam described by the incident and transmitted q-parameters q_{in} and q_{out} (equation 1.28)

is modified by an optical system ABCD according to [16, p. 92]

$$q_{out} = \frac{Aq_{in} + B}{Cq_{in} + D}. \quad (1.34)$$

This equation relates the incident radius of curvature R_{in} and spot radius w_{in} with an output radius of curvature R_{out} and spot radius w_{out} . Furthermore for the determinant holds $\text{Det}(\mathbf{M}) = 1$ and the total accumulated Gouy phase in the ABCD system is given by $\Delta\zeta$ (compare to equation 1.26). Using these relationships, the four unknowns A, B, C, D are coupled by four equations yielding the alternative description [17, 18]

$$A = \frac{w_{out}}{w_{in}} \cos(\Delta\zeta) - \frac{B}{R_{in}} \quad (1.35)$$

$$B = \frac{\pi w_{in} w_{out}}{\lambda} \sin(\Delta\zeta) \quad (1.36)$$

$$C = \frac{A}{R_{out}} - \frac{\frac{1}{R_{in}} \left(A + \frac{B}{R_{in}} \right) + \frac{B\lambda^2}{\pi^2 w_{in}^4}}{\left(A + \frac{B}{R_{in}} \right)^2 + \frac{B^2 \lambda^2}{\pi^2 w_{in}^4}} \quad (1.37)$$

$$D = \frac{1 + BC}{A}. \quad (1.38)$$

In conclusion the ABCD-Matrix of an arbitrary system can be deduced from the change of radius of curvature and spot radius as well as the accumulated Gouy phase $\Delta\zeta$. The matrix can be understood in first approximation as linear system that changes the position and angle of an incident ray.

1.3 Resonators and their Parametrization

This section introduces a special optical system called resonator with the classical ABCD formalism. Although the previously introduced ABCD formalism is commonly used to describe optical systems and deduce their properties, a description based on ABCD matrices is rather unintuitive and possible dependencies between the matrix entries are difficult to connect to the observed propagation in the system. It was found in the scope of this thesis that by rewriting the properties of an optical system using the alternative ABCD description from eqs. 1.35 to 1.38, the accumulated Gouy phase can give key insights into the propagation dynamics.

For the first time (to the best of the authors knowledge) a thorough investigation of resonator properties is performed, where each property is parameterized to yield a straightforward dependency to the accumulated Gouy phase. The accumulated Gouy phase is shown to be intuitively obtainable from the caustic of a resonator and to enable straightforward conclusions about the stability, minimum length, periodicity and robustness of a resonator as well as its off-axis and non-eigenmode propagation. This Gouy phase parametrization is later applied to obtain an ideal accumulated Gouy phase that optimizes the properties of a resonator. The parametrization also helps to intuitively understand the experimentally observed behavior of a resonator.

1.3.1 Resonator Definition

In a resonator, a beam is exactly reproduced after one cycle within an optical system. Ideally a beam can cycle in such a system for an infinite amount of time without changing its properties, making it especially useful for amplification systems, oscillators or other systems that benefit from a cycling laser beam. Using equation 1.34, the resonator definition is stated as

$$q_{eig} = \frac{Aq_{eig} + B}{Cq_{eig} + D}. \quad (1.39)$$

Here the q -parameter q_{eig} describes the *eigenmode* of the resonator that is reproduced after one transition. If for any arbitrary q , the equation

$$q = \frac{Aq + B}{Cq + D}. \quad (1.40)$$

holds, the system is *q-preserving* (and imaging). This is the case if $A = D = \pm 1$ and $B = C = 0$.

Solving 1.39 yields an expression for the eigenmode

$$q_{eig} = \underbrace{\frac{A - D}{2C}}_z + i \underbrace{\frac{\sqrt{4 - (A + D)^2}}{2|C|}}_{z_0}. \quad (1.41)$$

A condition for the q -parameter in equation 1.28 is that the Rayleigh length z_0 must be real and positive. This is true for the given system if

$$-1 < \frac{A + D}{2} < 1. \quad (1.42)$$

If this *resonator condition* is fulfilled, the optical system features an eigenmode and can be used as resonator structure. Such resonators are called *stable*.

For the eigenmode, we can assume that the output spot radius and radius of curvature equals the input. The eigenmode accumulates a certain amount of Gouy phase $\Delta\zeta_{eig}$, thus $w_{in} = w_{out}$, $R_{in} = R_{out}$ and $\Delta\zeta = \Delta\zeta_{eig}$ holds. Using equation 1.35 – 1.38 under these assumptions, the stability parameter S can be simplified to [18]

$$S = \frac{A + D}{2} = \cos(\Delta\zeta_{eig}). \quad (1.43)$$

Solving this equation for the Gouy phase accumulated by the eigenmode within one cycle yields

$$\Delta\zeta_{eig} = \text{sgn}(B) \cos^{-1}(S). \quad (1.44)$$

Here $\text{sgn}(B)$ solves the sign ambiguity induced by the cosine function [18]. The accumulated Gouy phase and the resonator stability are hence directly connected with the distinction that the accumulated Gouy phase also includes the sign information of the parameter B of the ABCD matrix. In the following, the accumulated Gouy phase is discussed in more detail and its usage as key parameter to define several resonator properties is motivated.

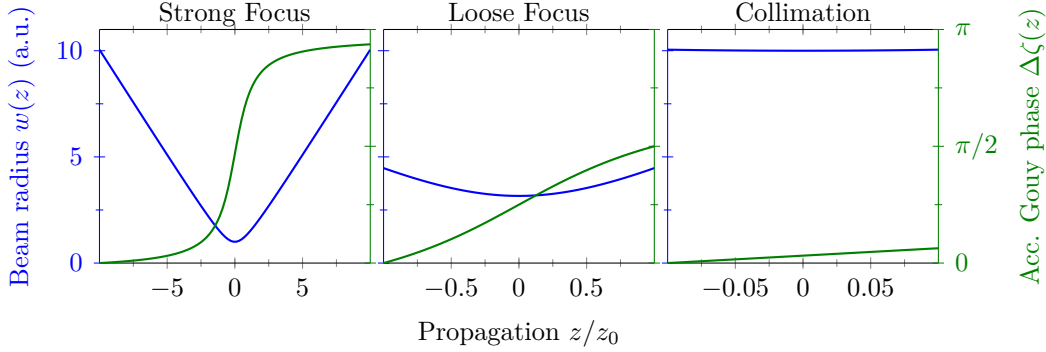


Figure 1.2: The caustic and the corresponding accumulated Gouy phase $\Delta\zeta$ for different focus configurations.

1.3.2 The Gouy Phase of a Resonator

The Gouy phase accumulated within a resonator roundtrip $\Delta\zeta_{eig}$ is an important design parameter and its value determines resonator properties like stability, periodicity and the propagation of non-eigenmodes. For a beam propagating from a position z_{min} to a position z , the accumulated Gouy phase is calculated by the equation [16, p. 77]

$$\Delta\zeta(z) = \zeta(z) - \zeta(z_{min}) = \tan^{-1} \frac{z}{z_0} - \tan^{-1} \frac{z_{min}}{z_0}. \quad (1.45)$$

A full focus within the resonator roughly adds a Gouy phase of π to the accumulated Gouy phase. This result is obtained by calculating the extreme case of equation 1.45, where $z_{min} \rightarrow -\infty$ and $z \rightarrow \infty$. A loose focus that corresponds to a transition through the Rayleigh range, i.e. $z_{min} \approx -z_0$ and $z \approx z_0$, adds a phase of around $\pi/2$. And finally the propagation of a large collimated beam with z and $|z_{min}| \ll z_0$ causes almost no change. These configurations are also exemplary depicted in figure 1.2. The Gouy phase of a resonator is then estimated by simply counting the loose and strong foci within one roundtrip and adding the corresponding accumulated Gouy phases. This method provides an intuitive way to determine the approximate Gouy parameter of a system.

To calculate the accumulated Gouy phase of a resonator more precisely, a new quantity is defined that gives the acquired Gouy phase per unit length. It is determined by a simple differentiation of equation 1.45

$$\frac{\partial\Delta\zeta(z)}{\partial z} = \frac{1}{z_0(1 + \frac{z^2}{z_0^2})} = \frac{\lambda}{\pi w(z)^2}. \quad (1.46)$$

To obtain an expression for the total accumulated Gouy phase in an arbitrary resonator, the contributions per unit length $\partial_z\Delta\zeta$ need to be summed over the propagation length L . This is mathematically done by an integral

$$\Delta\zeta_{Eig} = \int \frac{\partial\Delta\zeta(z)}{\partial z} dz = \frac{L}{L} \int \frac{\lambda}{\pi w(z)^2} dz = \frac{L\lambda}{\bar{A}_{spot}} \quad (1.47)$$

$$\bar{A}_{spot} = \frac{L}{\int \frac{dz}{\pi w(z)^2}} \quad \text{harmonic mean of spot area } \pi w^2. \quad (1.48)$$

The length of a resonator is then fully determined by the harmonic mean of its spot area and the acquired Gouy phase

$$L = \Delta\zeta_{Eig} \frac{\bar{A}_{spot}}{\lambda}. \quad (1.49)$$

The spot size in resonators is often constrained to be larger than a threshold value to avoid damages or ionization. In these cases a large accumulated Gouy phases $\Delta\zeta_{Eig}$ can often only be reached by enlarging the resonator length L . Long resonators can however reduce the mechanical stability as more optical components are involved in the design and longer propagation paths yield larger translations of a beam even for small angular errors. The reaction of a resonator to angular and translational errors is later discussed in more detail in section 1.3.6.

1.3.3 Periodicity of Resonators

To show that a resonator periodically creates a q-preserved iteration, the system's ABCD matrix is decomposed into its eigenvalues and eigenvectors. The eigenvalues $\lambda_{1,2}$ of an ABCD matrix are

$$\lambda_{1,2} = S \pm i\sqrt{1 - S^2}. \quad (1.50)$$

For stable resonators where $|S| < 1$, the eigenvalues become complex and are alternatively expressed by using equation 1.43

$$\lambda_1 = \exp(i\Delta\zeta_{eig}) \quad \lambda_2 = \exp(-i\Delta\zeta_{eig}). \quad (1.51)$$

The eigenvectors for the 2×2 matrix are given using equation 1.35, 1.36, 1.51 and 1.28

$$\mathbf{v}_1 = \sqrt{i\frac{\pi w^2}{2\lambda}} \begin{bmatrix} 1 \\ 1/q_{eig}^* \end{bmatrix} \quad \mathbf{v}_2 = \sqrt{i\frac{\pi w^2}{2\lambda}} \begin{bmatrix} 1 \\ 1/q_{eig} \end{bmatrix}. \quad (1.52)$$

One can decompose the ABCD matrix of a resonator into eigenvectors and eigenvalues using the eigenvalue decomposition

$$\mathbf{Q} = \sqrt{i\frac{\pi w^2}{2\lambda}} \begin{bmatrix} 1 & 1 \\ 1/q_{eig}^* & 1/q_{eig} \end{bmatrix} \quad (1.53)$$

$$\mathbf{Q}^{-1} = \sqrt{i\frac{\pi w^2}{2\lambda}} \begin{bmatrix} 1/q_{eig} & -1 \\ -1/q_{eig}^* & 1 \end{bmatrix} \quad (1.54)$$

$$\mathbf{\Lambda} = \begin{bmatrix} \exp(i\Delta\zeta_{eig}) & 0 \\ 0 & \exp(-i\Delta\zeta_{eig}) \end{bmatrix} \quad (1.55)$$

$$\mathbf{M} = \mathbf{Q}\mathbf{\Lambda}\mathbf{Q}^{-1}. \quad (1.56)$$

This way of writing the ABCD matrix \mathbf{M} greatly simplifies the derivation of several interesting properties of resonators. One obvious result is that the repeated transition

through a resonator \mathbf{M}^N , where N is the amount of passes through the resonator, is expressed by

$$\mathbf{M}^N = \mathbf{Q}\mathbf{\Lambda}^N\mathbf{Q}^{-1} = \mathbf{Q} \begin{bmatrix} \exp(iN\Delta\zeta_{eig}) & 0 \\ 0 & \exp(-iN\Delta\zeta_{eig}) \end{bmatrix} \mathbf{Q}^{-1}. \quad (1.57)$$

For $N\Delta\zeta_{eig} = k\pi$ where k is some integer number, the eigenvalues take the value $\lambda_{1,2}^N = \pm 1$ and the matrix multiplication becomes

$$\mathbf{M}^N = \pm \mathbf{Q}\mathbf{I}\mathbf{Q}^{-1} = \pm \mathbf{I} \quad \text{for } N = k\pi/\Delta\zeta_{eig}. \quad (1.58)$$

The unity matrix \mathbf{I} and its negative variant $-\mathbf{I}$ are q-preserving matrices. That means *any* mode that enters the resonator is exactly reproduced after $N = k\pi/\Delta\zeta_{eig}$ roundtrips. This is especially problematic for wavefront aberrations or similar distortions that are exactly reproduced and can therefore buildup over several iterations through the setup. Robust resonators favor rare occurrences of q-preserved or almost q-preserved iterations to avoid these buildups [19].

1.3.4 Propagation of Arbitrary Modes

In principle any mode q can propagate through a resonator. However the propagation of modes that are not eigenmodes is dynamic with changing parameters for every iteration until a q-preserved condition is reached again ($N\Delta\zeta_{eig} \approx k\pi$). For a deeper investigation of the propagation of arbitrary modes, it is first of all noted that the eigenvalue decomposition (equations 1.53 to 1.56) can be interpreted as three consecutive optical systems. By propagating an arbitrary mode q_{in} through these systems (equation 1.34), a general expression for the propagation through a resonator is found with an output mode q_{out} . The result is finally converted to a spot area by the relation $\pi w_{out}^2 = -(\text{Im } q_{out}^{-1})^{-1}\lambda$ (eq. 1.28). The squared output waist size for a single pass in a resonator then yields

$$w_{out}^2 = \overline{w_{out}^2} + \widehat{w_{out}^2} \cos(2\Delta\zeta_{eig}) + c_R \sin(2\Delta\zeta_{eig}). \quad (1.59)$$

$$c_R = \left(\frac{1}{R_{in}} - \frac{1}{R_{eig}} \right) \frac{\pi w_{eig}^2 w_{in}^2}{\lambda} \quad (1.60)$$

$$\overline{w_{out}^2} = \frac{w_{in}^4 + c_R^2 + w_{eig}^4}{2w_{in}^2} \quad (1.61)$$

$$\widehat{w_{out}^2} = \frac{w_{in}^4 - c_R^2 - w_{eig}^4}{2w_{in}^2} \quad (1.62)$$

An exemplary propagation is shown in figure 1.3.

The coefficient c_R models the impact of a wavefront mismatch between input mode q_{in} and eigenmode q_{eig} . If the wavefronts are mismatched (i.e. $R_{in} \neq R_{eig}$), this coefficient is different from zero and causes a sine contribution that manifests as phase shift of the spot area oscillation as visible in figure 1.3.

$\overline{w_{out}^2}$ represents the area of the propagating mode averaged over several passes. Note that this average spot area can be bigger than the actual eigenmode.

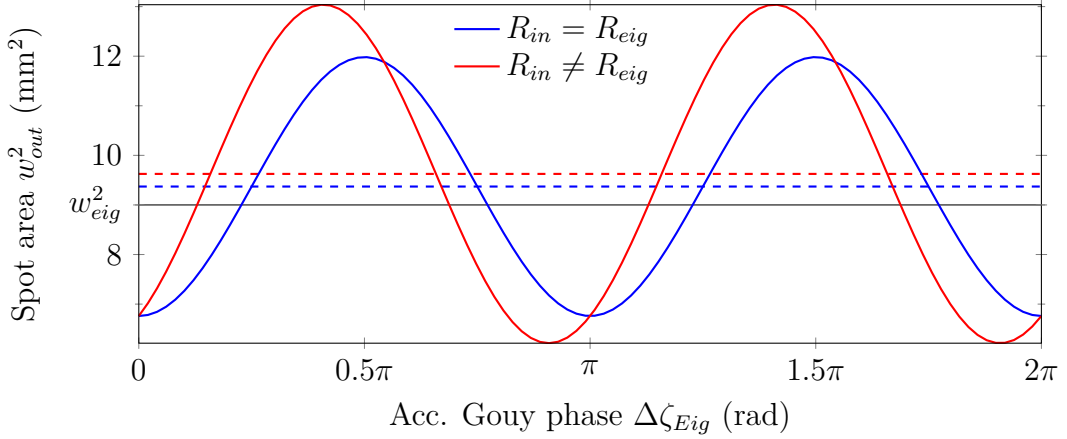


Figure 1.3: The exemplary propagation of arbitrary modes for different accumulated Gouy phases $\Delta\zeta_{eig}$. The calculation is based on a resonator with a collimated ($R_{eig}^{-1} = 0$) eigenmode with radius $w_{eig} = 3$ mm. The blue curve represents an input mode where the wavefront is mode matched but the input radius $w_{in} = 2.6$ mm is not. For the red curve a wavefront mismatch is added with $R_{in} = 100$ m. The dashed lines mark the corresponding average values w_{out}^2 .

Under the assumption of a wavefront matched input mode (i.e. $c_R = 0$), the amplitude of the oscillation is solely determined by the coefficient $\widehat{w_{out}^2}$. This also means that (assuming a wavefront matched input mode), the phase of the oscillation is always constant, does not depend on the input beam size and follows a cosine function.

The spot area after the second pass in a resonator is easily calculated by just doubling the accumulated Gouy phase $\Delta\zeta_{eig} \rightarrow 2\Delta\zeta_{eig}$ and reevaluating the equation above. Similarly the spot area is calculated for the third, fourth (and so on) pass. The spot area for modes that differ from the eigenmode hence changes with a sinusoidal pattern during several passes in a resonator.

The frequency of the oscillation depends on the actual resonator configuration given by the accumulated Gouy phase $\Delta\zeta_{eig}$ per pass. The higher the accumulated phase, the faster the underlying spot area oscillation over the passes.

With these equations the behavior of a non eigenmode in a resonator gives access to properties like the kind and degree of mode mismatch and the stability of a resonator. This is later used to mode match an input mode to an eigenmode and to experimentally determine the parameter $\Delta\zeta_{eig}$.

1.3.5 Off-Axis Propagation

So far a propagation on the optical axis was assumed. However resonators also show remarkable properties for beams that are coupled into a resonator with some offset from the optical axis. To analyze these properties, the 2D ray vector introduced in the beginning of section 1.2 is extended to a 3D representation

$$\begin{bmatrix} p_{in} \\ \theta_{in} \end{bmatrix} = \begin{bmatrix} y \\ \theta_y \end{bmatrix} + i \begin{bmatrix} x \\ \theta_x \end{bmatrix}. \quad (1.63)$$

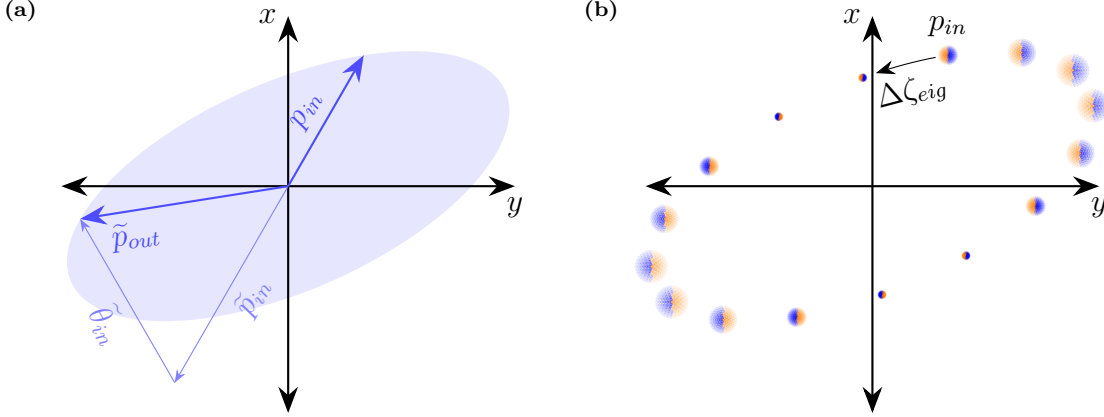


Figure 1.4: (a) The ellipse defined by the two conjugated half diameters p_{in} and \tilde{p}_{out} with $\tilde{p}_{in} = -\pi w_{Eig}^2 / (R_{Eig} \lambda) \times p_{in}$ and $\tilde{\theta}_{in} = \pi w_{Eig}^2 / \lambda \times \theta_{in}$, where p_{in} and θ_{in} are given in eq. 1.63. Note that \tilde{p}_{in} can flip direction depending on sign of the radius of curvature R_{Eig} and the sketch shows an ellipse for $R_{Eig} > 0$. All possible output positions p_{out} of a resonator follow the outer path of this ellipse. (b) An exemplary raytrace for the propagation of a collimated beam ($R \rightarrow \infty$) with a step size of $\Delta\zeta_{eig} = \pi/8$. The beam size does not follow eq. 1.59 owing to the ray approximation. Note that the beam is not geometrically rotated during propagation.

where the new imaginary part describes the position on the x-axis and the angle between x-axis and optical axis. With this notation arbitrary input positions and angles in the xyz space can be defined.

Plugging the input vector $\{p_{in}, \theta_{in}\}$ into a resonator $\mathbf{M} = \mathbf{Q}\mathbf{\Lambda}\mathbf{Q}^{-1}$ (equation 1.31 and 1.56) yields for the output position p_{out} ¹

$$\tilde{p}_{out} = \underbrace{-p_{in} \frac{\pi w_{Eig}^2}{R_{Eig} \lambda}}_{\tilde{p}_{in}} + \underbrace{\theta_{in} \frac{\pi w_{Eig}^2}{\lambda}}_{\tilde{\theta}_{in}} \quad (1.66)$$

$$p_{out} = p_{in} \cos \Delta\zeta_{eig} + \tilde{p}_{out} \sin \Delta\zeta_{eig} \quad (1.67)$$

This is in remarkable similarity to the parametric ellipse equation

$$\{x, y\} = u_x R_x \cos \gamma + u_y R_y \sin \gamma \quad (1.68)$$

with the x-axis and y-axis unit vectors $u_x = \{1, 0\}$ and $u_y = \{0, 1\}$, the radii R_x and R_y and the propagation parameter γ . In fact the vectors p_{in} and \tilde{p}_{out} create a skewed (non-orthogonal) coordinate system and the output position p_{out} is described by an ellipse within this coordinate system. A skewed ellipse stays an ellipse. The output position after propagation through an arbitrary resonator is therefore always part of an elliptic path defined by two vectors p_{in} and \tilde{p}_{out} as depicted in figure 1.4a.

¹ The output angle is similarly found

$$\tilde{\theta}_{out} = -p_{in} \left(\frac{\pi w_{Eig}^2}{R_{Eig}^2 \lambda} + \frac{\lambda}{\pi w_{Eig}^2} \right) + \theta_{in} \frac{\pi w_{Eig}^2}{R_{Eig} \lambda} \quad (1.64)$$

$$\theta_{out} = \theta_{in} \cos \Delta\zeta_{eig} + \tilde{\theta}_{out} \sin \Delta\zeta_{eig} \quad (1.65)$$

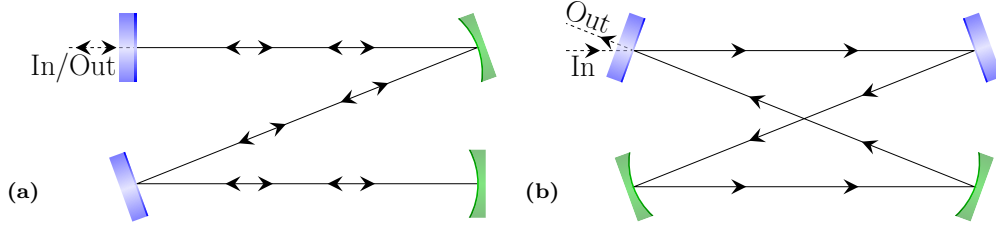


Figure 1.5: (a) The schematic setup of a linear resonator. The beam is coupled in and out coaxially and bounces two times over the central mirrors with each roundtrip. (b) The schematic setup of a ring resonator. The beam is coupled in and out with differing angles and the beam bounces only a single time over each mirror for each roundtrip. Blue elements mark plane mirrors while green elements mark concave mirrors in both pictures.

The accumulated Gouy phase $\Delta\zeta_{eig}$ determines the angular movement on the ellipse between the input position p_{in} and the output position p_{out} . Multiple roundtrips in a resonator cause the position to rotate angularly with a shift of $\Delta\zeta_{eig}$ per roundtrip (see figure 1.4b).

1.3.6 Resonator Robustness

In the previous sections, the propagation of a non-eigenmode beam within a resonator was analyzed in detail. The following section investigates the change of the eigenmode, if the resonator is distorted in some way. Two types of resonators exist and their stability behavior differs: the linear and the ring resonator. Their schematics are depicted in figure 1.5. In a ring resonator, the beam is guided once through any optical system involved in the resonator before it reaches its initial position again. Hence the propagation resembles a ring. In contrast, in linear resonators the beam propagates back and forth in a linear fashion.

The amplifier that is designed in the scope of this work is based on a ring resonator, which is why the robustness properties of this resonator type is discussed in more detail in the following. The discussion for a linear resonator can be found in the appendix A.1.

Mechanical Robustness

For the analysis of the mechanical robustness, it is assumed that the ring is distorted and the beam accumulates some translational shift s and some angular shift σ during one roundtrip. The resonator equation can then be written as [20]

$$\begin{bmatrix} x_{Eig} \\ \theta_{Eig} \end{bmatrix} = \begin{bmatrix} A & B \\ C & D \end{bmatrix} \begin{bmatrix} x_{Eig} \\ \theta_{Eig} \end{bmatrix} + \begin{bmatrix} s \\ \sigma \end{bmatrix}. \quad (1.69)$$

where $\{x_{Eig}, \theta_{Eig}\}$ defines the eigenmode position. Solving this equation for the eigenmode [20] and simplifying the result using eq. 1.35 to 1.38 yields

$$\begin{bmatrix} x_{Eig} \\ \theta_{Eig} \end{bmatrix} = \frac{1}{2} \cot \frac{\Delta\zeta_{eig}}{2} \begin{bmatrix} -\frac{\pi w_{Eig}^2}{R_{Eig}\lambda} & s + \frac{\pi w_{Eig}^2}{\lambda} \sigma \\ -\frac{\pi w_{Eig}^2}{R_{Eig}^2\lambda} - \frac{\lambda}{\pi w_{Eig}^2} & s + \frac{\pi w_{Eig}^2}{R_{Eig}\lambda} \sigma \end{bmatrix} + \frac{1}{2} \begin{bmatrix} s \\ \sigma \end{bmatrix}. \quad (1.70)$$

Minimizing the term $|\cot(\Delta\zeta_{eig}/2)|$ therefore also minimizes the sensitivity for any misalignment $\{s, \sigma\}$. I.e. the closer a resonator is designed to reach $\Delta\zeta_{eig} \approx \pi$, the more robust it is against misalignment.

Spot Size Robustness

However, there is a second source of distortion typically caused by changing focal lengths of resonator optics (e.g. thermal lenses). If the focal length of an optical element changes, this might have a severe impact on the eigenmode size. To find a design that is robust against such changes, a focal length distortion is modeled by an additional lens ABCD matrix \mathbf{M}_f with dioptric power $1/f$. For an undistorted system, the dioptric power is zero, i.e. $1/f = 0$. The distortion is introduced into the system \mathbf{M} by the multiplication $\mathbf{M}_{dist} = \mathbf{M}\mathbf{M}_f$. By solving the eigenmode equation for this distorted system \mathbf{M}_{dist} (eq. 1.39), the spot radius w_f at the place of distortion is determined [20] and simplified using eq. 1.35 to 1.38

$$\frac{1}{f_{eff}} = \frac{\pi w_{Eig}^2}{\lambda} \frac{1}{f} \quad (1.71)$$

$$w_f^4 = \frac{w_{Eig}^4}{1 + f_{eff}^{-1} \cot \Delta\zeta_{eig} - \frac{1}{4} f_{eff}^{-2}}. \quad (1.72)$$

Bigger eigenmode spot sizes increase the impact of the dioptric power change $1/f$. Also the maximum robustness against focal length distortions is reached where the derivative of the spot size reaches zero

$$\left. \frac{dw_f}{df_{eff}^{-1}} \right|_{f_{eff}^{-1}=0} = -\frac{w_{Eig}}{4} \cot \Delta\zeta_{eig} \stackrel{!}{=} 0. \quad (1.73)$$

In conclusion maximum robustness against focal length shifts is reached for

$$\Delta\zeta_{eig} = \Delta\zeta_{eig,robust} = \frac{\pi}{2} + k\pi \quad k \in \mathbb{Z}. \quad (1.74)$$

With this accumulated Gouy phase, the resonator fulfills the resonator condition (i.e. w_f does not approach infinity) if the distortion is within the range

$$-2 < f_{eff}^{-1} < 2. \quad (1.75)$$

The maximum spot size robustness and maximum mechanical robustness ($\Delta\zeta_{eig} \approx \pi$) are never reached simultaneously. In practice spot size robustness is considered to be more important as mechanically stable setups minimize the need for mechanical robustness. Thus typical Gouy phase values for ring resonators are near $\Delta\zeta_{eig,robust}$.

Shift of Eigenmode Position

By choosing $\Delta\zeta_{eig} \approx \Delta\zeta_{eig,robust}$, another ring resonator property comes into effect. The outcoupling of a resonator is often done at a position where the beam is collimated $R_{Eig} \rightarrow \infty$. This avoids the necessity of collimation optics and simplifies

the usage of the laser output. Under this condition and assuming $\Delta\zeta_{eig} \approx \Delta\zeta_{eig,robust}$, it can be shown that any distortion in the resonator causes mainly a translational shift of the eigenmode position. This property is derived by simplifying equation 1.70 using the given constraints

$$\begin{bmatrix} x_{Eig} \\ \theta_{Eig} \end{bmatrix} = \frac{1}{2} \begin{bmatrix} 1 & s + \pm z_0 & \sigma \\ \mp \frac{1}{z_0} & s + 1 & \sigma \end{bmatrix}. \quad (1.76)$$

Solving this for the distortion angle σ and output angle θ_{Eig} yields

$$\sigma = \frac{2x_{Eig} - s}{z_0} \quad (1.77)$$

$$\theta_{Eig} = \frac{x_{Eig} - s}{z_0} \quad (1.78)$$

The maximum position values for $|x_{Eig}|$ and $|s|$ are typically limited to some millimeters due to the size of the used optics. Assuming a maximum value on the order of the beam spot radius $w_{Eig} \approx |x_{Eig}|, |s|$ yields

$$|\theta_{Eig}| = \frac{|x_{Eig} - s|}{z_0} \leq 2 \frac{w_{Eig}}{z_0} = 2\theta_{div}, \quad (1.79)$$

where θ_{div} is the half angle divergence of a Gaussian beam (eq. 1.30, the waist radius equals the spot radius due to collimation $w_{0,Eig} = w_{Eig}$). For a collimated beam, this divergence is negligible and $|\theta_{Eig}| \approx 0$ holds in good approximation. Therefore even position shifts as large as w_{Eig} only cause minor angular movements in the resonator at positions where the eigenmode is collimated. In good approximation, the eigenmode mainly translates if the system is subject to distortion.

Temporal Robustness

In [21] a temporal instability mechanism is theorized caused by a delayed reaction of a gain element in the resonator. A time delay element in a system always implies a frequency dependency with possible resonances or run-away conditions. A robustness parameter G is used to determine the run-away condition. If its value is smaller than 1, no run-away is expected

$$G = V_{LB} \frac{x_{eig}(s=0, \sigma)}{\sigma} < 1. \quad (1.80)$$

Here V_{LB} describes the focal strength of an arbitrary nonlinear (thermal) lens with a positive value for a focusing lens. $x_{eig}(s=0, \sigma)$ is defined in equation 1.70. Assuming a typical positive nonlinear lens $V_{LB} > 0$ yields the simplified condition

$$\frac{\pi w_{Eig}^2}{2\lambda} \cot \frac{\Delta\zeta_{eig}}{2} < \frac{1}{V_{LB}}. \quad (1.81)$$

For a range $0 \leq \Delta\zeta_{eig} \leq 2\pi$, this true even for large nonlinear focal strengths (large values of V_{LB}) if $\Delta\zeta_{eig}$ approaches π and for $\Delta\zeta_{eig} \geq \pi$, this condition is always fulfilled. Thus a resonator with a large accumulated Gouy phase $\Delta\zeta_{eig}$ minimizes or even avoids possible temporal instabilities.

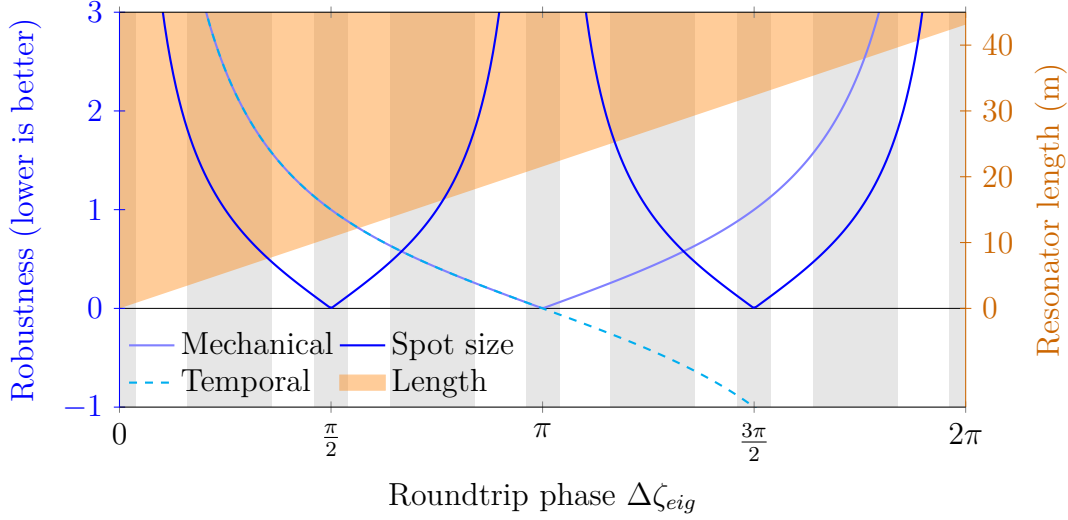


Figure 1.6: The robustness properties of a ring resonator. The lines refer to the robustness parameters from eq. 1.83 to 1.85, where lower values refer to more robust systems. The shaded areas in gray mark Gouy phases with an increased risk of unwanted distortion buildup taken from [22] and discussed in section 1.3.3. Finally the orange area defines possible resonator lengths. For the length calculation a beam diameter of $2w_{Eig} \geq 3$ mm was arbitrarily chosen (eq. 1.49).

Conclusion

In conclusion, three robustness parameters and the length dependency have been determined for ring resonators (smaller values are better):

$$\text{Length} \propto \Delta\zeta_{eig} \quad (\text{eq. 1.49}) \quad (1.82)$$

$$\text{Mechanical robustness} \propto \left| \cot \frac{\Delta\zeta_{eig}}{2} \right| \quad (\text{eq. 1.70}) \quad (1.83)$$

$$\text{Spot size robustness} \propto |\cot \Delta\zeta_{eig}| \quad (\text{eq. 1.73}) \quad (1.84)$$

$$\text{Temporal robustness} \propto \cot \frac{\Delta\zeta_{eig}}{2} \quad (\text{eq. 1.81}). \quad (1.85)$$

Figure 1.6 summarizes the findings from the previous sections. A single parameter, the accumulated Gouy phase $\Delta\zeta_{eig}$, defines the minimal resonator length, the robustness and possible distortion buildups.

A robust resonator is found for all Gouy phases where the robustness parameters from eq. 1.83 to 1.85 reach low values. Gouy phases of $\pi/2$ and $3\pi/2$ yield highly robust resonators against focal length distortions that change the spot size of the eigenmode. A Gouy phase around π maximizes the mechanical robustness and Gouy phases $\geq \pi$ render temporal instabilities impossible. A compromise between mechanical and spot size robustness is provided for Gouy phases slightly higher than $\pi/2$ or slightly lower than $3\pi/2$.

At the same time it is known from equation 1.49 that a large Gouy phase shift requires a long resonator. Figure 1.6 shows a range of possible resonator lengths as orange shaded region for an exemplary resonator that has a beam diameter of $2w_{Eig} \geq 3$ mm. It becomes obvious that for such a resonator, the robust area around a Gouy phase of $3\pi/2$ is only approachable with resonator lengths that are not feasible.

In fact long resonators are expected to show an increased sensitivity to mechanical distortions. Low angular errors σ are converted to large translational shifts s over the long propagation distance and even a mechanically stable design cannot compensate this (compare to equation 1.70). Additionally longer resonators typically rely on more optics that pose a potential source of distortion. This disadvantage of the region around a Gouy phase of $3\pi/2$ makes a ring resonator with a Gouy phase shift around $\pi/2$ more favorable.

It was also concluded in section 1.3.3 that certain Gouy phase shifts might cause an unwanted buildup of higher order components thereby degrading the beam quality. These phase shifts are investigated in more detail in [22]. Figure 1.6 highlights the phase shifts that can lead to an increased higher order buildup with a gray background and consequentially white areas mark phase shifts that are predicted to support high beam qualities. Gouy phase shifts slightly greater or smaller than $\pi/2$ are hence the preferred choice. Note that phase shifts greater than $\pi/2$ offer the advantage of a significantly higher mechanical robustness with the cost of a comparably low increase in resonator length.

In conclusion a phase shift of about $\Delta\zeta_{eig} \approx 0.55\pi$ guarantees good robustness with a rather short (and hence mechanically more stable) setup length. Choosing a radius of curvature R_{Eig} and a spot size w_{eig} then fully determines the ABCD matrix of the resonator.

1.4 Beam Quality Factor M^2

Features like waist size, spot size, eigenmode or divergence were so far treated assuming a Gaussian beam (eq. 1.26). In practice, a beam is often a mixture of a Gaussian beam and some higher order components (eq. 1.25). To quantify the similarity to a Gaussian beam, a figure of merit is introduced called M^2 [23]. It is defined using the beam parameter product $BPP = \Theta_{div}W_0$ as [16, p. 85]

$$M^2 = \frac{\pi}{\lambda} \Theta_{div} W_0. \quad (1.86)$$

Here W_0 is the measured (real) waist size W_0 and Θ_{div} is the measured half angle divergence. A value close to $M^2 \approx 1$ is considered to represent a Gaussian beam. An exemplary propagation of such a higher order mode beam is depicted in figure 1.7.

Measurement

The M^2 value is determined by tracking the 2σ radius of a beam during the propagation through a focus. To this end, the beam radius is defined as [24, p. 10]

$$W_{x,y} = \sqrt{2 \left(\sigma_x^2 + \sigma_y^2 \pm 2 \left| \sigma_{xy}^2 \right| \right)} \quad (1.87)$$

where σ_x^2 , σ_y^2 and σ_{xy}^2 are the second order moments of the power density distribution of the beam. While propagating through the focus, the beam size follows the equation [25, p. 28] [26, p. 188]

$$W(z)^2 = W_0^2 + \Theta_{div}^2 z^2. \quad (1.88)$$

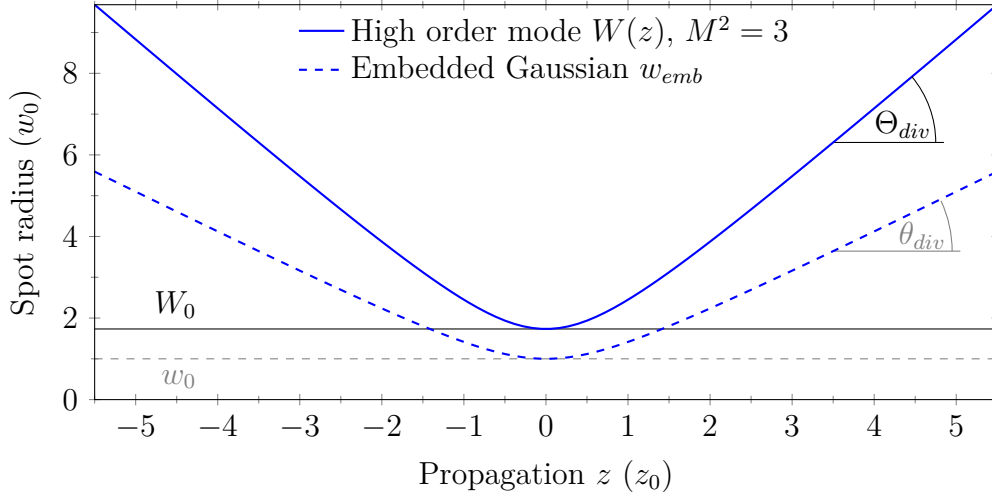


Figure 1.7: The exemplary propagation of a mode with an M^2 value of 3. The waist radius is W_0 and the divergence Θ_{div} . The corresponding embedded Gaussian mode is depicted with dashed lines and has a waist radius of w_0 , a divergence of θ_{div} and a Rayleigh length z_0 .

By fitting the measured waist radii $W_{x,y}(z)$ to this equation, W_0 and Θ_{div} are determined. Consequentially an M^2 value can be assigned to the measured beam. More details about the measurement of the M^2 value can be found in the corresponding ISO norm [24].

Embedded Gaussian

By noticing (based on equation 1.25), that every higher order mode follows the propagation of an embedded Gaussian beam $\mathbf{E}_{0,0}(\mathbf{r})$, the propagation of an arbitrary beam with $M^2 > 1$ can be calculated in good approximation. The embedded Gaussian spot size w_{emb} is simply found by a division of the measured spot radius W (eq. 1.87) by the measured beam quality $\sqrt{M^2}$ [26, p. 188]

$$w_{emb} = \frac{W}{\sqrt{M^2}}. \quad (1.89)$$

A propagation of such an embedded Gaussian beam and its corresponding higher order mode is plotted in figure 1.7. The q -parameter (eq. 1.28) defined for this embedded Gaussian beam yields a basis for further calculations. The calculated embedded spot size is converted back to a higher order spot size by simply multiplying with $\sqrt{M^2}$.

Mode Cleaning

As previously noted, a higher order beam is always bigger than its embedded Gaussian. A common method to remove the higher order components is therefore the introduction of some kind of aperture that introduces large losses for higher order components and low losses for the smaller Gaussian beam. The relationship between the M^2 after filtering, the aperture diameter D_{filt} and the Gaussian beam

size w_{emb} is approximately given by [27]

$$M^2 \approx \frac{D_{filt}^2}{4w_{emb}^2}. \quad (1.90)$$

This kind of mode cleaning with a hard aperture causes steep intensity edges at the border of the beam profile. These steep edges might in turn cause a coupling of energy from the fundamental (Gaussian) mode into higher order modes [19]. A more efficient way of mode cleaning is therefore the introduction of a soft aperture where the transmission (or gain) gradually increases towards the center while avoiding any abrupt changes.

1.5 Pulse Propagation and Dispersion

Lasers can operate in a continuous wave regime or as pulsed laser. Pulsed lasers emit a series of pulses where each pulse can be described by the wavefunction [16, p. 69]

$$\mathcal{E}(\mathbf{r}, t) = \mathbf{E}(\mathbf{r}, t) \exp(i\omega_0 t). \quad (1.91)$$

$\mathbf{E}(\mathbf{r}, t)$ is the slowly varying envelope and ω_0 the central optical frequency. If this envelope is time independent, the equation simplifies to the definition of a monochromatic wave (eq. 1.17). It is further assumed that the envelope is separable into a spatial and a time domain component (compare to eq. 1.20)

$$\mathbf{E}(\mathbf{r}, t) = \mathbf{E}(\mathbf{r})A(t), \quad (1.92)$$

where $A(t)$ describes the time domain component of the complex pulse envelope.

The Fourier transformation of the pulse defined in eq. 1.91 yields the amplitude spectrum $|\mathcal{A}(\omega - \omega_0)|$ of the pulse

$$\mathcal{E}(\mathbf{r}, t) \xrightarrow{\mathcal{F}} \mathbf{E}(\mathbf{r})\mathcal{A}(\omega - \omega_0). \quad (1.93)$$

Here $\mathcal{A}(\omega) = |\mathcal{A}(\omega)| \exp(i\varphi(\omega))$ is the Fourier transformation of the pulse envelope $A(t)$. A purely linear phase $\varphi(\omega) = -\omega\Delta t$ in the frequency domain corresponds to a simple shift of the pulse envelope along Δt in the time domain and can often be ignored in the spectral analysis. In contrast higher order phases define the envelope shape $A(t)$ in time domain.

If the pulse accumulates some higher order phase during the propagation through an optical system, the system is said to be dispersive. The parameter [16, p. 184]

$$GDD = \frac{\partial^2 \varphi(\omega)}{\partial \omega^2}, \quad (1.94)$$

is then called *group delay dispersion (GDD)*. A typical consequence of GDD is the temporal stretching of the pulse envelope $A(t)$. A dispersion coefficient is commonly defined as [16, p. 185f]

$$D_\lambda = -2\pi \frac{c_0}{\lambda_0^2} GDD \quad \lambda_0 = \frac{2\pi c_0}{\omega_0}. \quad (1.95)$$

The dispersion coefficient is a measure of the temporal pulse stretching per unit spectral width $\Delta\lambda$. An estimate for the elongation is [16, p. 353]

$$\Delta t_{FWHM} \approx |GDD| \times \Delta\omega_{FWHM} \quad (1.96)$$

$$\Delta t_{FWHM} \approx |D_\lambda| \times \Delta\lambda_{FWHM}, \quad (1.97)$$

where FWHM indicates a width measurement based on the full width half maximum. An initially short pulse $A(t)$ approximates the duration Δt_{FWHM} in case of strong dispersion. The same dispersion causes longer output pulses if the bandwidth $\Delta\lambda_{FWHM}$ (or $\Delta\omega_{FWHM}$) is increased. Therefore broadband systems are more sensitive to dispersion effects. Elongated pulses can also be compressed back to their initial duration. To this end the pulse propagates through a system with inverted group delay dispersion. This principle is often used in chirped pulse amplification systems where temporal broadening and compression is introduced on purpose to reduce the peak power in a system [28].

One of the properties of the Fourier transformation is that the product of the spectral bandwidth and the time duration defined over the root mean square has an uncertainty [26, p. 334]

$$\Delta t_{rms} \Delta\omega_{rms} \geq \frac{1}{2}. \quad (1.98)$$

The actual value of the time-bandwidth product depends on the shape of the pulse and the dispersion. A pulse with a purely linear spectral phase (i.e. $\varphi(\omega) \propto \omega$) is called *Fourier limited* or *transform limited* since the product of bandwidth and duration reaches the lower limit for its spectral shape [26, p. 334]. A large bandwidth of the amplitude spectrum hence enables very short transform limited pulses.

1.6 Amplification by Stimulated Emission

Stimulated emission and absorption form the basis of classical laser amplifier systems. This chapter discusses the basic mechanisms behind emission and absorption in gain materials and introduces a simplified effective two level formalism to enable the calculation of gain and absorption of these materials. A vast amount of gain materials exist and to provide a better way of comparison, some general figure of merits and properties of gain materials like stored energy, large signal gain, amplification bandwidth and dynamic stability are explained.

1.6.1 Multi-Level Systems

A gain medium can be interpreted as a multi-level system with different energy levels. Following this model each energy level is populated by a certain electron density. This means that for each energy level, a certain percentage of available electrons is excited to have the corresponding energy connected to this level. Electrons can be excited to a higher energy level by absorbing energy or they can decay to a lower energy level by emitting energy. In the scope of this work, electrons are excited by the absorption of a photon (also referred to as *pumping*). A decay of an electron to a lower level is connected to the emission of a photon (*radiative decay*) or for example

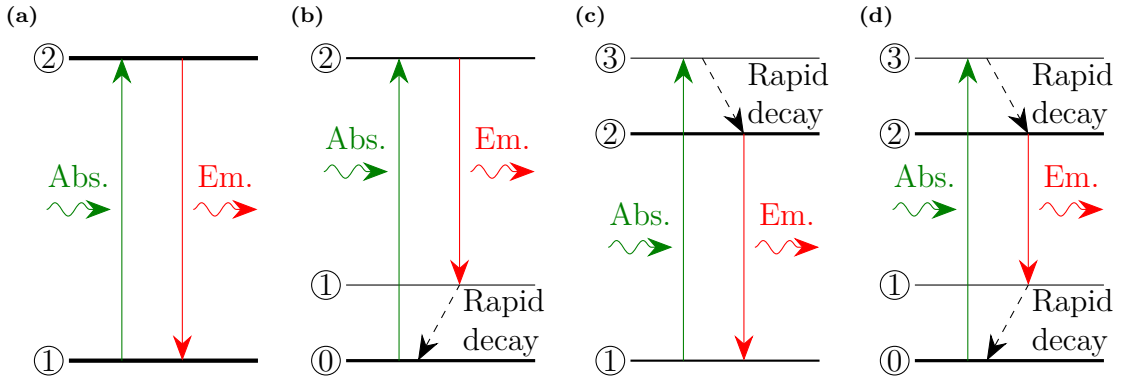


Figure 1.8: Shown are various level configurations for gain media. *Abs.* indicates an absorbed photon, *Em.* an emitted photon and dashed lines a transition with a short lifetime. Horizontal lines highlight the energy levels with a line thickness that correlates with a typical population density. Illustrated are a (a) two-level, (b) lower three-level, (c) upper three-level and a (d) four-level system.

by setting up a mechanical vibration in the lattice of a crystal that manifests as crystal heating (*nonradiative decay*). Nonradiative decay is typically very rapid but limited to small energy differences between the concerning levels. More details can be found in [2].

The most simple gain medium is a non degenerate two-level medium as schematically depicted in figure 1.8a. Here the upper energy level has the electron density N_2 , the lower energy level the density N_1 and the total electron density is $N = N_1 + N_2$. Neglecting any nonradiative transitions, the amount of electrons being excited from level 1 to level 2 is then given by [2, p. 25]

$$\frac{\partial N_2}{\partial t} = N_1 B_{12} \rho \quad (\text{absorption}), \quad (1.99)$$

where ρ is an energy density given by the number of photons per unit volume in the medium. The decay of an electron from level 2 to level 1 can be triggered by one of the photons in the medium. This process is called *stimulated emission* and is the key mechanism that enables laser amplification. The electron decay connected to stimulated emission is given by

$$\frac{\partial N_2}{\partial t} = -N_2 B_{21} \rho \quad (\text{stimulated emission}). \quad (1.100)$$

Finally some electrons spontaneously decay from level 2 to level 1 by *spontaneous emission*

$$\frac{\partial N_2}{\partial t} = -N_2 A_{21} \quad (\text{spontaneous emission}). \quad (1.101)$$

The coefficients A_{21} , B_{21} and B_{12} are called *Einstein coefficients* as they were originally introduced by Albert Einstein. They are a figure of merit how probable the transitions are. The sum of all three processes mentioned above yields the rate of emission and absorption and is also called *rate equation*. The electron density is

required to be constant in a steady state system and the rate equation is then

$$\frac{\partial N_2}{\partial t} = -N_2 B_{21} \rho - N_2 A_{21} + N_1 B_{12} \rho \stackrel{!}{=} 0. \quad (1.102)$$

In the non-degenerate case $B = B_{21} = B_{12}$ holds such that solving this equation for the density N_2 yields

$$N_2 = \frac{N}{2 + \frac{A_{21}}{B\rho}}. \quad (1.103)$$

Thus even for an infinitely high density of photons, the upper laser level population cannot exceed the value $N/2$ in a two-level gain medium. This means the upper level electron density is always smaller than the lower level density $N_2 < N_1$. Comparing this result to the rates for absorption (eq. 1.99) and stimulated emission (eq. 1.100) leads to the conclusion that the absorption is always stronger than the stimulated emission and no signal gain due to stimulated emission can be expected.

In order to use stimulated emission as tool for the amplification of a signal, more complex energy level structures are necessary. Prominent examples are three-level and four-level systems. The general idea is to provide a third or a fourth energy level that acts as temporary storage of electrons.

The storage can effectively reduce the density N_1 of electrons in the lower laser level such that $N_2 > N_1$ becomes valid (also known as *population inversion*) and a signal gain is possible. This variant is shown in figure 1.8b, where the level 0 acts as additional energy level. Alternatively the storage can provide electrons to the upper level N_2 to reach population inversion (illustrated in figure 1.8c, where a level 3 is used to this end). A four-level system can provide two storage levels and both mechanisms can be combined (figure 1.8d), such that a positive gain is reached with a low threshold energy density ρ .

A condition for these additional energy levels is that they are connected to fast decay times (i.e. much faster than the radiative decay) and an effectively immediate redistribution of electrons into the proper energy levels is possible. This condition typically implies that these additional energy levels are close to the lower level 1 or upper level 2 to enable nonradiative decay.

1.6.2 Absorption and Emission Cross Sections

The energy level structure of most real gain media is even more complex than the simplified multi-level systems introduced in the previous section. Often several lower and upper energy levels are present. Each of these levels can have different electron populations and can interact with each other making their treatment difficult. In a common approximation, each energy level is populated according to the thermal equilibrium energy distribution (i.e. the *Boltzmann distribution*) [29]. Given two energy level populations in thermal equilibrium N_0 and N_1 with corresponding energy levels E_0 and E_1 , their ratio is described by

$$\frac{N_1}{N_0} = \exp\left(-\frac{E_1 - E_0}{k_B T}\right). \quad (1.104)$$

This approximation solves the issue of multiple unknown populations in a system. It is further assumed that the energy levels involved in an amplification process can be approximated by two effective laser levels with populations N_1 and N_2 . If some electron populates one of these effective levels, it is immediately redistributed to the real energy levels hidden behind these effective levels following the Boltzmann distribution. By using this approximation, even complex multi-level systems can be treated in a simple two level scheme. As example in a four level scheme (figure 1.8d), the energy levels 0 and 1 would be summarized as level **1** and the levels 2 and 3 as level **2**.

These two effective levels are coupled by the absorption and the emission cross section $\sigma_a(\omega)$ and $\sigma_e(\omega)$. The cross sections correlate to the probability of an incident photon being absorbed or triggering a stimulated emission at a certain optical frequency $\omega = 2\pi c/\lambda$ and implicitly incorporate the complex energy level structure hidden behind the two level approximation. The effective cross sections are used instead of the Einstein coefficients B_{12} and B_{21} of the ideal two-level medium.

The emission and absorption cross sections are thermally coupled and for a system in thermal equilibrium one can derive the relation [29]

$$\frac{\sigma_e}{\sigma_a} \exp\left(\frac{\hbar\omega}{k_B T}\right) = \frac{N_1}{N_2} = \exp\left(\frac{E_z}{k_B T}\right). \quad (1.105)$$

The zero phonon energy E_z is virtually equal to the energy gap between the lowest sublevel of the lower laser level **1** and the lowest sublevel of the upper laser level **2**. In a four level system (figure 1.8d), this would be the energy gap between level 0 and level 2.

For a steady state system, the amount of absorbed and emitted photons per timeframe has to be the same. This leads to the rate equation for an effective two level system with the photon flux per frequency interval $\Phi(\omega)$ (unit $1/(\text{Hz s m}^2)$) and the rate of spontaneous emission per frequency interval $a(\omega)$ as replacement for the coefficient A_{21} [29]. Similar to equation 1.102, the rate equation for a steady state system is then given by

$$\underbrace{N_2 \sigma_e(\omega) \Phi(\omega) + N_2 a(\omega)}_{\text{emission rate}} = \underbrace{N_1 \sigma_a(\omega) \Phi(\omega)}_{\text{absorption rate}}. \quad (1.106)$$

Often the integrated version of this rate equation is useful for calculations [29]

$$N_2 \int \sigma_e(\omega) \Phi(\omega) \frac{d\omega}{2\pi} + \frac{N_2}{\tau} = N_1 \int \sigma_a(\omega) \Phi(\omega) \frac{d\omega}{2\pi} \quad (1.107)$$

$$\tau = \frac{2\pi}{\int a(\omega) d\omega}. \quad (1.108)$$

Here the spontaneous emission coefficient $a(\omega)$ reduced to a lifetime τ of the upper laser level. The lifetime τ is connected to the rate $N_2 \tau^{-1}$ that gives the amount of spontaneously emitted photons per timeframe. With this rate a pumped upper state N_2 would be depleted within a lifetime τ after stopping the pump.

In a simplified case only two optical frequencies are involved in the amplification process: the pump frequency ω_P and the lasing frequency ω_L . In this case the

integrals are simplified to

$$N_2 (\sigma_{eP}\Phi_P + \sigma_{eL}\Phi_L) + \frac{N_2}{\tau} = N_1 (\sigma_{aP}\Phi_P + \sigma_{aL}\Phi_L). \quad (1.109)$$

The photon flux for the lasing and pumping frequency is Φ_L and respective Φ_P . σ_{eP} and σ_{eL} are the emission cross sections and σ_{aP} and σ_{aL} the absorption cross sections for the pump and the lasing light. This equation forms the basis for the following analysis of laser amplification.

1.6.3 Signal Amplification

The rate equation 1.109 describes the relationship between stimulated emission, spontaneous emission and absorption. It also provides a way to derive expressions for the amplification (or equivalently attenuation) of a signal Φ_L (or Φ_P) that passes through a medium. The following sections introduce a gain and an attenuation coefficient for the signal gain in a pumped medium. This forms a basis for further calculations of amplification systems. Also possible disturbances for signal amplification are presented.

Small Signal Gain and Absorption

The small signal gain of an amplifier is the gain that a continuous or weak pulsed signal experiences during one transition through an amplifier. A signal is considered to be weak if its amplification does not alter the state of the amplifier significantly (i.e. the level populations N_1 and N_2 are not significantly changed). Constant population densities can be safely assumed for continuous wave signals as the gain medium is required to reach a steady state in that case and the populations are not changed over time.

The photon flux $\Phi_L(z)$ (where z describes a position in the gain medium along the signal's propagation direction) increases during the propagation due to stimulated emission of photons. $d\Phi_L(z)/dz$ describes the increase of photons per time frame and unit volume at the position z . This equals the depopulation of the upper level per time frame and unit volume that can be described using the lasing (stimulated) emission and absorption components of the rate equation 1.109. The emission rate is therefore given by the equation

$$\frac{d\Phi_L(z)}{dz} = N_2\sigma_{eL}\Phi_L(z) - N_1\sigma_{aL}\Phi_L(z). \quad (1.110)$$

N_1 and N_2 are assumed to be uniform (i.e. spatially independent) in the material. Solving the equation for $\Phi_L(z)$ yields

$$g = N_2\sigma_{eL} - N_1\sigma_{aL} \quad (1.111)$$

$$\Phi_L(z) = \Phi_L(0) \exp(gz). \quad (1.112)$$

The factor $\exp(gz)$ is the small signal gain experienced by a weak signal $\Phi_L(0)$ with the gain coefficient g . Obviously the signal is only amplified for $g > 0$ or

$N_1/N_2 < \sigma_{eL}/\sigma_{aL}$. This condition does not fulfill relation 1.105 and hence a gain requires a system outside thermal equilibrium.

Such a non-equilibrium system is achieved by pumping electrons from the lower level **1** to the upper level **2**. Similar to the increase of photon flux by stimulated emission, absorption decreases the photon flux and consequentially the upper laser level becomes more populated. Using the same reasoning as in derivation of the small signal gain, the absorption of pump light is described by the equation

$$\alpha = N_2\sigma_{eP} - N_1\sigma_{aP} \quad (1.113)$$

$$\Phi_P(z) = \Phi_P(0) \exp(\alpha z). \quad (1.114)$$

α is the absorption coefficient and is negative for the pump light.

With these equations a gain that is experienced by a weak or continuous signal or respectively the attenuation of pump light can be calculated in a straight forward fashion. In later sections this is used to determine some important figure of merits for gain materials. Also these equations form the basis for a numerical simulation of the gain behavior within an amplifier system.

Large Signal Gain

The derivation of the small signal gain assumes a quasi constant population density in the upper and lower laser level during the amplification process. However, in case of pulsed laser operation, an input signal can be strong enough to change the system properties during propagation. The energy per area of a pulse is called fluence $J(0)$ and is calculated from the photon flux $\Phi_L(0)$ of one pulse by the relation

$$J(0) = E_L \int \Phi_L(0) dt \quad (1.115)$$

with the lasing photon energy $E_L = \hbar\omega_L$. A pulse can be assumed to be amplified within the small signal gain approximation if the input pulse fluence is sufficiently small $J(0) \ll J_{Sat}$, where the saturation fluence J_{Sat} is [30]

$$J_{Sat} = \frac{E_L}{\sigma_{aL} + \sigma_{eL}}. \quad (1.116)$$

For higher pulse fluences, the leading part of the pulse depletes the gain medium to a degree that the trailing part is significantly influenced. This especially means that after one pass of the pulse, the stored energy in the medium is largely removed [31]. In this case the output fluence after amplification can be expressed by [30]

$$J(z) = J(0) \ln(G[\exp(J(0)/J_{Sat}) - 1] + 1) \quad (1.117)$$

$$G = \exp(gz). \quad (1.118)$$

This equation generalizes the gain for high pulse fluences.

For efficient energy extraction in single pass systems, operation close to this saturation energy is beneficial but sometimes hindered by the damage thresholds of the used crystals. However, for multipass systems where extraction can happen over multiple bounces, efficient extraction well below the saturation fluence is possible and commonly done.

Amplification Disturbances

Some properties of gain media limit the quality of the signal amplification. Examples for these effects are the reduction of amplification bandwidth for large signal gains, the unwanted amplification of spontaneously emitted light and a temporal instability called bifurcation that develops for high repetition rate lasers. These effects are discussed more detailed in the following to enable a deeper understanding of laser amplification especially in the regime of high gain factors and high repetition rates.

Gain Narrowing The gain coefficient $g(\omega)$ (eq. 1.111) of a laser material is in general frequency dependent. In the scope of the rate equation, this gain was approximated to have a value only at a certain wavelength ω_L , where ω_L is the frequency of maximal gain. In contrast, for the analysis of the output bandwidth, this dependency has to be taken into account.

The small signal gain follows an exponential function

$$G(\omega) = \exp(g(\omega)z) \quad (1.119)$$

and for a fixed gain coefficient, higher gains are reached by a longer propagation z . Due to the exponential relationship, even broadband gain coefficients $g(\omega)$ lead to narrow-band total gains $G(\omega)$ if z is chosen sufficiently large. This gradual decrease of amplification bandwidth with increasing gain is called *gain narrowing* and can be observed for pulsed and continuous laser amplification.

Assuming a Lorentzian profile of the gain coefficient $g(\omega)$, the full width half maximum bandwidth $\Delta\omega$ of the actual gain $G(\omega)$ is given by [2, p. 281]

$$\Delta\omega = \Delta\omega_g \sqrt{\frac{3}{10 \log_{10} G(\omega_L) - 3}}, \quad (1.120)$$

where $G(\omega_L)$ is the peak gain of the amplifier and $\Delta\omega_g$ the full width half maximum bandwidth of the gain coefficient.

The decrease of spectral bandwidth induced by large gains leads to longer Fourier limited output pulses and constitutes one of the fundamental limits of ultrashort high energy pulse amplification.

Amplified Spontaneous Emission Not only the signal is amplified in a pumped gain medium, but also the radiation that is spontaneously emitted with a lifetime τ (compare to equation 1.108). This phenomenon is called amplified spontaneous emission (ASE). The spontaneously emitted radiation propagates through the pumped medium and experiences a gain induced by stimulated emission. This in turn accelerates the depopulation of the upper laser level. Thus amplified spontaneous emission causes an effective decrease of the lifetime $\tau_{ASE} < \tau$. It is later shown that small lifetimes are especially problematic for high energy pulsed laser amplification. But also for low pulse energies or continuous wave lasers, ASE provides a typically unwanted amplification channel that lowers the quality of amplification.

The actual impact of ASE depends on many parameters like gain medium volume, surface properties, wavelength, pump intensity and emission direction. The

suppression of ASE is one of the key challenges in laser optimization as it creates an unwanted emission channel. In general the value of the effective lifetime τ_{ASE} needs to be determined by numerical simulations. However, for some special cases, analytic approximations to estimate the effective lifetime τ_{ASE} exist [32].

Bifurcation and Chaos The lifetime τ of a gain medium does not only describe the depletion of the upper laser level, it also causes a time dependence for the population of this level. In a simple picture the pump duration to fully populate the upper laser level to a density N_2 is approximately τ .

Now a pulsed laser amplification with a temporal pulse distance smaller than τ is considered that leads to a periodic depletion of this upper laser level. It is further assumed that a first pulse is amplified in the gain medium and depletes its upper laser level to a value lower than N_2 . Then due to the short temporal pulse distance, a second pulse arrives and depletes the gain medium before its old population density N_2 could be regained. Under this condition, operation points are possible where the second pulse is not amplified to the same level as the initial pulse. This effect is sometimes called *bifurcation* due to the visible splitting into a higher and a lower output energy while the gain is gradually increased [33].

This splitting can not only happen once but several times and in the worst case each single pulse is amplified with a different gain. In that case the system is *chaotic*.

Numerical calculations have shown that this effect is especially pronounced for weak input energies, many passes through the gain medium and repetition rates higher but close to the inverse lifetime τ^{-1} [34]. A deeper investigation of this dynamic behavior based on a numeric model can be found in appendix B.4.

1.6.4 Figures of Merit for Gain Media

A more general treatment of laser amplification yields different couplings between the aforementioned variables. The following sections explain the relationship of lifetime, gain, energy and bandwidth in more detail and introduces several important figures of merit used to describe amplification properties. The findings from this section are later used to compare different gain media regarding their suitability for the targeted amplification system.

Stored Energy

Assuming that a medium with length H is pumped with a photon flux Φ_P , this flux is completely and uniformly absorbed and no stimulated emission occurs, then the steady state population density N_2 of the excited laser level can be written as [32]

$$N_2 = \Phi_P \frac{\tau}{H} \quad (1.121)$$

with the excited laser level lifetime τ . This is due to the necessity that in a steady state every absorbed photon is compensated by a spontaneous emission of a photon, i.e. the absorption density Φ/H has to be equal to the spontaneous emission density N_2/τ . The stored energy E_{stored} in a medium with a pumped cross section of A , a

volume of $V = HA$, and a laser photon energy of $E_L = \hbar\omega_L = hc/\lambda_L$ is then [31, 32]

$$E_{stored} = E_L N_2 V = E_L \Phi_P A \tau = \frac{\lambda_P}{\lambda_L} P_{Abs} \tau. \quad (1.122)$$

Here the relationship between photon flux Φ_P and pump power $P_{Abs} \approx \Phi_P A E_P$ with pump photon energy $E_P = hc/\lambda_P$ was used.

A pulse that is amplified by a gain medium cannot gain more energy than the stored energy. Hence high energy laser systems obviously rely on gain media with long lifetimes τ making this property an important variable that needs to be maximized for optimized performance.

σ - τ Product

Equation 1.121 can also be used to rewrite eq. 1.112. Assuming low absorption at the emission wavelength $\sigma_{aL} \approx 0$ and \widetilde{H} being an effective amplification length, the small signal gain can be written as (using the relationship between N_2 and E_{stored} from eq. 1.122)

$$\Phi_L(\widetilde{H}) = \Phi_L(0) \exp(N_2 \sigma_{eL} \widetilde{H}) = \Phi_L(0) \exp\left(\frac{P_{Abs} \widetilde{H}}{E_P V} \tau \sigma_{eL}\right). \quad (1.123)$$

Under the assumption of complete pump light absorption, the gain is mainly governed by the material property $\tau \sigma_{eL}$ (sometimes called σ - τ product) that can also be expressed via the Füchtbauer-Ladenburg equation for narrow Lorentzian emission spectral bandwidths $\Delta\lambda_L$ [35]

$$\tau \sigma_{eL} \approx \frac{\lambda_L^4}{4\pi^2 n^2 c} \frac{1}{\Delta\lambda_L}. \quad (1.124)$$

There is no material dependence except for the refractive index n , the central emission wavelength λ_L and the bandwidth $\Delta\lambda_L$. Narrow bandwidth materials tend to have a larger σ - τ product and hence a higher gain than broadband gain materials. But the decrease of the bandwidth for higher gains will also lead to longer pulses with less sensitivity for dispersion (see section 1.5). The coupling between σ - τ product and amplification bandwidth hence requires that a compromise between gain and bandwidth needs to be found for each application.

Total Population Density and Doping Concentration

Another important property of gain media is their population density. The total population density N in a gain material is the sum of the lower and upper level population

$$N = N_1 + N_2 = c_{Dop} N_+ \quad (1.125)$$

The doping concentration c_{Dop} is the fraction of the material dependent cation density N_+ that contributes to the population density. Rewriting the absorbed pump power for an absorption length L

$$P_{Abs} = P_P(0) - P_P(L) \quad (1.126)$$

using $P_P(z) = \Phi_P(z)AE_P$, equation 1.114 and equation 1.122 yields (assuming a negligible emission cross section for the pump wavelength $\sigma_{eP} \approx 0$)

$$P_{Abs} = P_P(0) \left(1 - \exp \left[\left(\frac{E_{stored}}{E_L V} - N \right) \sigma_{aP} L \right] \right). \quad (1.127)$$

Efficient pump light absorption $P_{Abs} \approx P_P(0)$ calls for high values of the pump laser absorption cross section σ_{aP} and high population densities N . While a small value of σ_{aP} can be compensated by a multipass pump geometry as for example used in thin-disk lasers with a longer effective absorption length L , the population density N has to be high enough to enable sufficient values of the stored energy. More precise the population density has to fulfill

$$N \gg \frac{E_{stored}}{V E_L}. \quad (1.128)$$

Thus high doping concentrations are preferred for laser systems that rely on a large stored energy. Not all gain media support high doping concentrations and gain media that do are especially suitable for high energy applications.

Chapter 2

Picosecond Multi-Kilohertz Kilowatt Thin-Disk Amplifier

Pulsed laser emission is routinely generated since the introduction of the first lasers [1], for example by using pulsed pump sources or choppers. However, the generation of ultrashort pulses on the femtosecond to picosecond time scale required the introduction of mode-locking techniques [36]. For mode-locked lasers some element in the laser resonator creates high losses for continuous wave operation and lower losses for pulsed operation. This leads to the formation of a circulating pulse as steady state solution of the laser resonator.

The repetition rate of these lasers is the inverse round trip time of the resonator and for reasonable resonator lengths of some meters, this corresponds to tens or hundreds of megahertz. Additionally optical damage thresholds, ionization or strong nonlinearities limit the peak intensity of the steady state pulse. Therefore pulse energies obtained by ultrashort mode-locked lasers are restricted to the nanojoule to microjoule range [37]. Higher energies lead to challenging average and peak powers.

Significantly higher energies can be obtained by increasing the pulse duration to obtain lower peak intensities or by reducing the repetition rate and therefore the average power. A subsequent stage after the oscillator is then necessary to further amplify the modified laser pulses without the restrictions of the mode-locked laser.

Two amplifier types can be distinguished in the high energy regime: amplifier that focus on maximum energy per pulse with repetition rates of some hertz (or even less) and kilohertz amplifier that provide a compromise between high repetition rate and high pulse energy. In the following a thin-disk amplifier system is discussed that combines very high energies with high repetition rates. Over 1 kW of average power is obtained with a repetition rate of 5 kHz, pulse energies over 200 mJ and a pulse duration of about 1 ps. This amplifier system represents a six fold increase of output energy compared to a state of the art multi-kilohertz amplifier at the time of development [38].

After the presentation of the final layout and output parameters, the different components of the system are introduced in more detail and reasons for the constraints used in the construction of the system are given. First an overview of chirped pulse amplification as well as different gain materials and geometries is presented. This is followed by an explanation of the working principle of Pockels cells and the optimal configuration of the thin-disk amplifier. An analysis of the average power within the resonator is performed and the impact of thermally induced distortions is analyzed. The implementation of a preamplifier is motivated and its design is

briefly presented. Finally the impact of different frontends on the laser performance is compared.

2.1 Layout and Performance

This section introduces the general setup of the implemented system and shows some key results. The design is based on six stages: oscillator, pulse picker, stretcher, preamplifier, main-amplifier and compressor as schematically shown in figure 2.1. A successful compression of the amplified 1 kW, 200 mJ pulse and an almost diffraction limited beam quality is demonstrated.

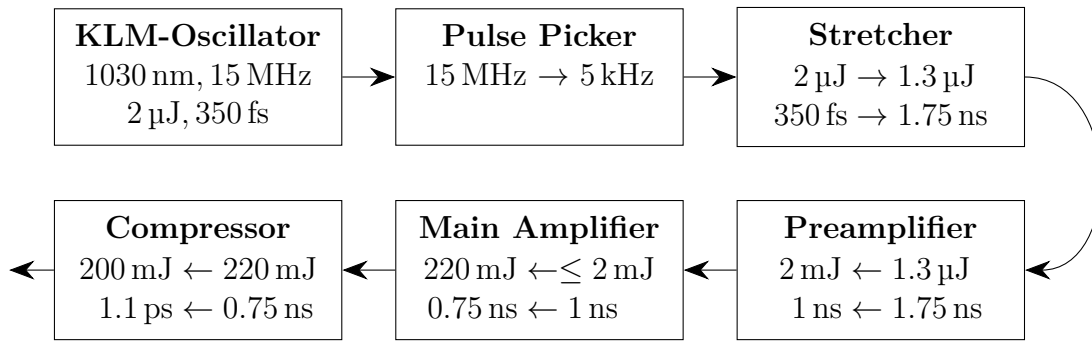


Figure 2.1: The schematic of the proposed system. A Kerr-lens mode locked (KLM) thin-disk oscillator provides a seed for a chirped pulse amplification system. Pulses are stretched to about 1.75 ns pulse duration, amplified to 220 mJ in two stages and recompressed to 1.1 ps with a pulse energy of 200 mJ and 5 kHz repetition rate.

2.1.1 System Design

The system is based on ytterbium yttrium aluminium garnet (Yb:YAG) as gain material and chirped pulse amplification (CPA) technology [28]. The results shown are obtained with a Kerr-lens mode locked (KLM) thin-disk oscillator [39] as frontend delivering pulses with an energy of 2 μ J and a full width half maximum (FWHM) pulse duration of \sim 350 fs. The bandwidth is about 3.5 nm centered around 1030 nm. A pulse picker (*Bergmann Messgeräte Entwicklung KG*) reduces the repetition rate of the frontend to 5 kHz or alternatively 10 kHz. To lower the peak intensities in the amplifier, the pulses are stretched to about 1.75 ns in a grating stretcher [40] with a dispersion of 500 ps/nm. A thin-disk based regenerative preamplifier increases the pulse energy to about 2 mJ. A fraction of this energy is sent into the main amplifier system that is described in more detail in this section. Typical input energies with good amplification results are about 0.1 mJ. After amplification in the main amplifier, the beam is compressed in a dielectric grating compressor [41]. The setup of the complete system is schematically shown in figure 2.1.

The propagation within the main amplification system is schematically depicted in figure 2.2. Two Yb:YAG thin-disks are embedded in a ring resonator structure and each bounce over the thin-disks results in a small gain of pulse energy by a factor on the order of 1.1. The reason why thin-disks are beneficial in these

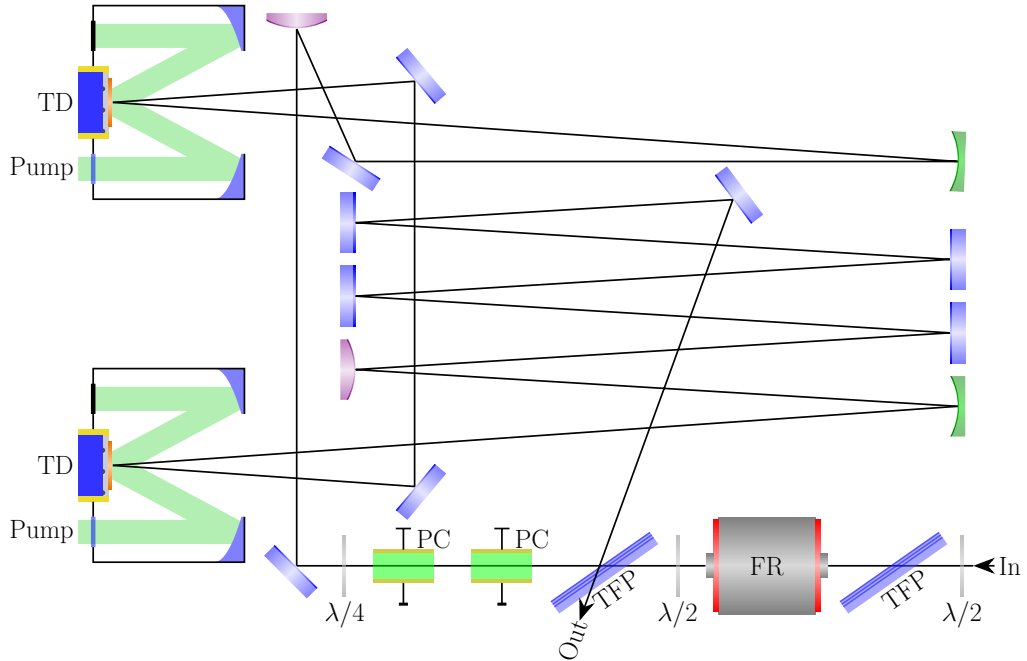


Figure 2.2: The schematic layout of the main amplifier. The input beam from the preamplifier (labeled *In*) is sent through an optical diode for protection against backreflection consisting of a thin film polarizer (TFP), a Faraday rotator (FR) and a half wave plate ($\lambda/2$). It is coupled into the ring-type resonator by an arrangement of a TFP, two BBO based Pockels cells (PCs) and a quarter wave plate ($\lambda/4$). Two Yb:YAG thin-disks (TDs) each pumped by a 969 nm diode laser with up to 3.5 kW of average power are used for amplification. The resonator is formed by two telescopes with convex (violet) and concave (green) mirrors. The output is labeled *Out*.

kind of amplifiers and a more detailed view on their working principle is found in section 2.3.1. Assuming a pulse is already present within the resonator shown in figure 2.2, it will propagate on a ring-shaped path around the thin-disks as long as it stays s-polarized thereby gaining more and more energy by subsequent passes through the gain medium. The exact caustic of the resonator is later derived and discussed in section 2.7.1. To trap a pulse in this ring-shaped path, two β -barium borate (BBO) crystals with a size between $12 \times 12 \times 15 \text{ mm}^3$ and $12 \times 12 \times 20 \text{ mm}^3$ are used as Pockels cell. The working principle of Pockels cells is explained in more detail in section 2.3.4, but in a simple picture they can be understood as voltage controlled waveplates. This means changing the applied voltage across a Pockels cell crystal changes its retardance. A bipolar high voltage switch (*Bergmann Messgeräte Entwicklung KG*) with a switching voltage of about $\pm 8 \text{ kV}$ is connected to both BBO crystals creating a total phase shift of $\pm \lambda/4$. In the negative case, the phase shift is canceled by the following $\lambda/4$ waveplate, in the positive case the phase shift adds up to a half wave plate turning the polarization from s to p or vice versa. If a p polarized pulse entering the ring should be trapped, the high voltage switch is set such that the polarization is turned from p to s. After the beam has passed the Pockels cells, the polarization of the voltage is inverted, the retardance cancelled and the polarization is kept during the next roundtrips, i.e. the pulse is trapped and gains more and more energy. Before outcoupling, the voltage is inverted a second time and the polarization is turned from s to p. The next bounce over

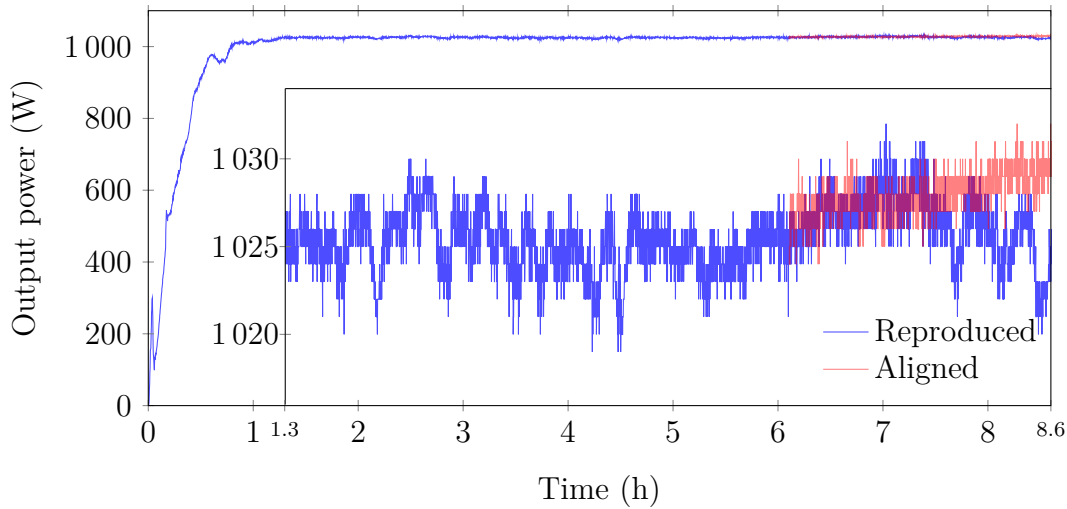


Figure 2.3: The output power of the proposed system. The system was aligned in a thermalized state and kept running. The last 2.5 hours before the system was switched off were logged and are displayed in red. After switching off, the system cooled down for about 15 hours before it was turned on again (blue). No further alignment was done during the measurements. The red and the blue curve are aligned to provide a comparison of the fully thermalized laser operation in the end of a day and the inset shows a zoom of the measurement after thermalization. The seed energy was 0.2 mJ and 38 roundtrips over two thin-disks each pumped with 1.7 kW were used.

the intracavity thin film polarizer (TFP) is then highly transmissive and the amplified pulse is coupled out. This amplification principle is called *regenerative amplification* and provides a compact and easily adjustable way to provide multiple passes over a gain medium. A well designed regenerative amplifier also exhibits a close to fundamental output mode due to the properties of the underlying resonator structure rendering these amplifiers ideal for thin-disk based amplification.

Two subtypes of regenerative amplifiers exist: the linear and the ring resonator based amplifier. An example of a linear regenerative amplifier is discussed in more detail in section 2.8, while the presented main amplifier uses a ring structure as shown in figure 2.2. Linear resonators provide a double pass per resonator roundtrip over the gain medium and the Pockels cell. The Pockels cell can be shorter, the gain per roundtrip can be higher and the system can be more compact compared to a similar ring laser approach due to the folding of the resonator. However, the necessity for a Faraday rotator in the output section limits the usage of linear resonators to average power regimes where the thermal lensing or induced birefringence of the Faraday rotator crystal (typically terbium gallium garnet) has only a minor impact [42]. A manufacturer's (*Electro-Optics Technology Inc.*) recommendation is to limit the average power to the order of 400 W. As the output power of the system substantially exceeds this limit, a ring resonator has been implemented.

2.1.2 System Performance

The main amplifier's output power of more than 1 kW for over more than 8 hours is shown in figure 2.3. To the best of the authors knowledge, this is the most energetic multi-kilohertz laser to date with a more than six fold increase of pulse energy

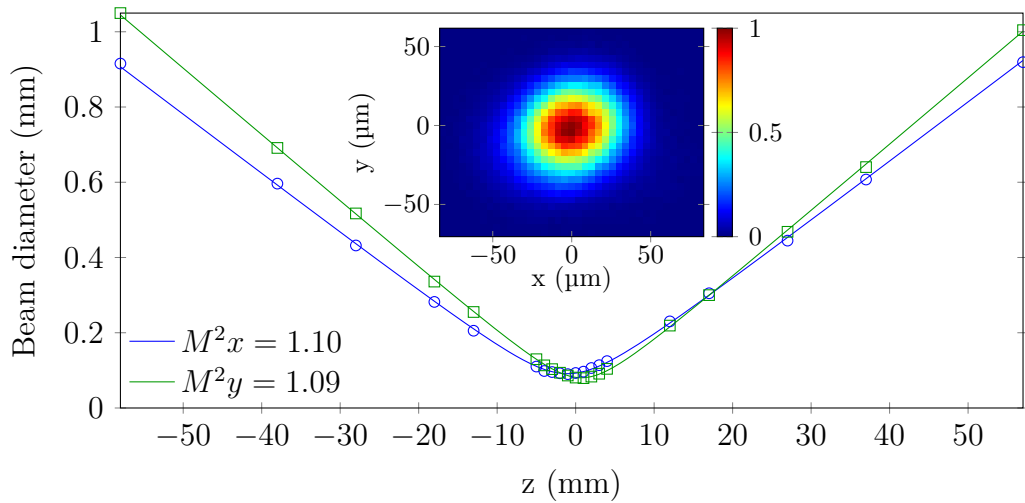


Figure 2.4: The measured M^2 (section 1.4) of the amplified beam measured at an output power of 1010 W after 36 roundtrips. The seed energy was set to 0.1 mJ and each disk was pumped with 1.7 kW. The inset shows the beam profile at the focus ($z = 0$).

compared to the state of the art at the time of its completion [38]. It provides a remarkable stability and reproducibility making it an ideal source for experiments that benefit from high energies but require a high repetition rate. A mean output power of 1025 W was reached with a standard deviation of 1.9 W (or 0.2%). The standard deviation of the pulse to pulse fluctuation over 150 samples was measured to be 0.5%. By changing the repetition rate from 5 kHz to 10 kHz, output powers of more than 1.4 kW were achieved for over 8 min before damages occurred. This marked to the best of the authors knowledge the highest average power extracted from a regenerative amplifier at the time of measurement. The damage processes involved are later discussed in more detail (see section 2.5).

The beam quality at 1 kW output power was evaluated using a commercial M^2 meter (*Ophir Spiricon Europe GmbH*) following the specification *ISO 11146* (see section 1.4). The output is almost diffraction limited with M^2 values of $M^2_x = 1.10$ and $M^2_y = 1.09$ on the x and y axis (see figure 2.4). The focus is essentially Gaussian with no visible higher order features. The M^2 values are remarkably constant over the output power range between 200 W and 1 kW and show no significant dependence on pump power or even repetition rate. Measurements with 10 kHz and 1 kW output power lead to the same M^2 values around 1.1.

The pulse duration was measured with an average power of 1100 W after the main amplifier (pump power per disk 1.8 kW, 38 roundtrips, 0.2 mJ seed) using a home-built second harmonic frequency-resolved optical gating (SH-FROG) device [43]. After the grating compressor, an average power of 1030 W was obtained. The measurement is shown in figure 2.5 and a virtually Fourier limited compression is reached with a flat spectral phase. The pulses have a FWHM duration of 1.08 ps and reach over 98% of the pulse intensity of a Fourier limited pulse. The output bandwidth is about 1.5 nm. The retrieved spectral shape agrees with the measured spectrum and a low G-error of 0.36% indicates a well retrieved pulse. Similar pulse durations were measured for a repetition rate of 10 kHz.

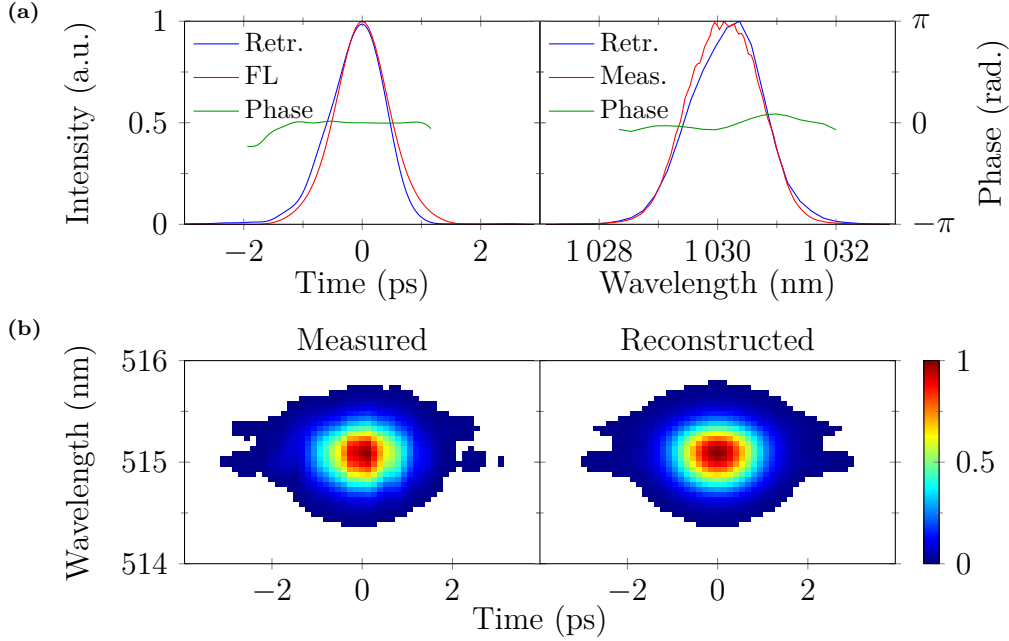


Figure 2.5: (a) The Fourier limit (FL) plotted together with the retrieved pulse shape and phase (left). The FWHM duration of the Fourier limit is 1.03 ps, the measured pulse is 1.08 ps long. On the right the measured and the retrieved spectrum and spectral phase are shown. The FWHM bandwidth is 1.5 nm. (b) The measured and retrieved SH-FROG signal. The G-error is 0.36%.

The parameter and design decisions made in order to reach the presented results are discussed in the following sections.

2.2 Chirped Pulse Amplification

To overcome the energy limitations of ultrashort laser sources, Strickland et al. [28] proposed the usage of *chirped pulse amplification (CPA)* systems. The peak intensity of a mode-locked laser supporting pulse durations of a few picoseconds or less is reduced by stretching the pulse duration to a multiple of the initial value. Typical stretching factors are 100 times to over 1000 times. To this end the pulse propagates through a highly dispersive setup, e.g. a long optical fiber or a grating stretcher [40]. The dispersion is typically given in units of ps/nm and approximately gives the FWHM duration of the stretched pulse per FWHM spectral bandwidth of the input pulse (eq. 1.95). For this setup a value of 500 ps/nm for a 3.5 nm broad oscillator spectrum would therefore yield an approximately 1.75 ns long output pulse (eq. 1.96). The more bandwidth is supported by the system, the less dispersion is necessary for sufficient stretching. The pulse is subsequently amplified and compressed back to its original duration (see figure 2.6). This method ensures relatively low peak powers during the whole amplification process thus avoiding limitations like nonlinear distortions or optical damages.

A successful implementation of CPA requires an exact matching of the stretching and compression stage, i.e. the spectral phase introduced during stretching has to match the negative of the phase introduced in the compressor. Current compression

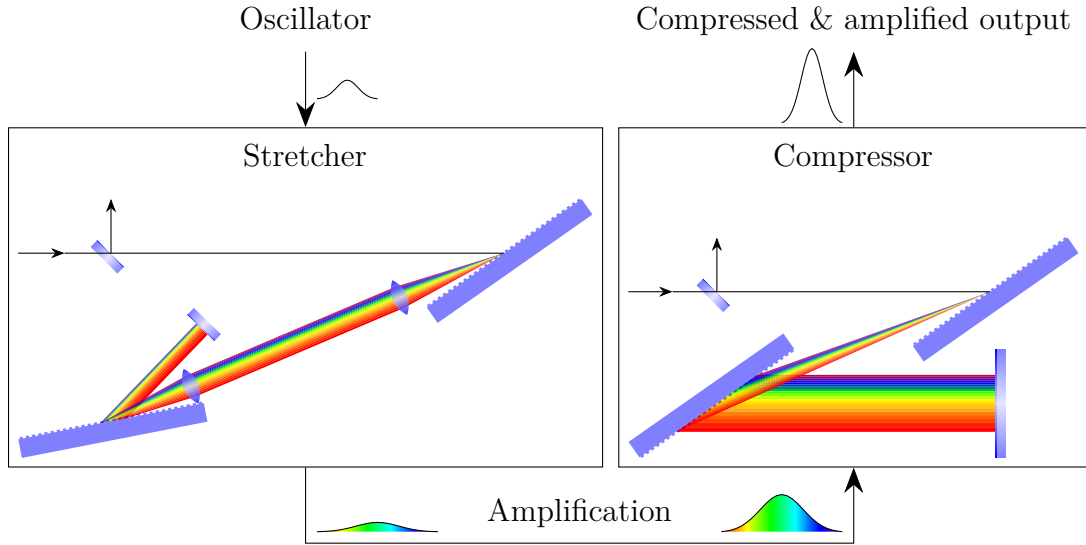


Figure 2.6: A schematic of the chirped pulse amplification principle. A weak pulse is stretched in time by a grating stretcher. The low intensity pulse can be amplified without risking damages or nonlinear degradation. A final compression stage removes the stretching and yields a high intensity, short output pulse.

techniques for high energy lasers mainly rely on dielectric gratings [41]. Grating compressors feature high group delay dispersion values beyond several hundreds of ps/nm allowing for high stretching factors, can be designed to have no transmissive elements that are typically a source of nonlinear distortions and are available in large dimensions supporting beam sizes of several tens of mm. These advantages make grating compressors ideal for usage in high energy environments. However, this implies that the stretcher phase has to match a grating compressor phase. A grating stretcher with opposite phase sign [40] provides virtually perfect matching, yet grating stretchers are costly and have dimensions comparable to their compressor counterpart despite the much lower energy present in the stretcher stage.

Alternatively compact fiber Bragg gratings tailored to match the phase of the grating compressor are used as stretcher stage [44]. Using fiber Bragg gratings requires precise manufacturing to keep the phase error between stretcher and compressor stage low and ensure proper compression. Thus this approach is limited in terms of maximal stretching factor and typically shows worse compression quality than a pure grating based CPA. Additionally fiber Bragg gratings only support nanojoule scale pulse energies assuming input pulse durations on the picosecond scale. Thus the first realization of the amplifier is based on a pure grating based CPA, but the possibility to use a fiber Bragg grating for a more compact frontend is later investigated in section 2.9.

The 350 fs long oscillator pulses are stretched to about 1.75 ns, therefore a stretching factor of ~ 5000 is used in this CPA setup. The stretcher is based on gold gratings with a line density of 1740 lines/mm, an input angle of 58.5° and a focal length of 2.2 m for both lenses. The optical distance between the gratings to reach a dispersion of 500 ps/nm is approximately 6 m. The setup supports a bandwidth of more than 7.5 nm before spectral components are clipped. The total efficiency is

65% and the total footprint of the setup is about $2.5 \times 1 \text{ m}^2$ (a later implementation has been optimized in size). The compressor is based on two dielectric gratings with a line density of 1740 lines/mm, an optical grating distance of about 2.8 m with a supported bandwidth of up to 6 nm and a total efficiency of roughly 94%. The footprint of the compressor is about $2 \times 1 \text{ m}^2$.

2.3 Geometries and Materials

The high average powers of the presented system cause a strong heating of the gain medium that leads to thermal aberrations like deformation of the gain material, thermal lensing or the change of spectral properties [45]. In the following, geometries and gain materials that reduce the heat load are discussed and evaluated regarding their suitability for high power and high energy lasers and the advantages of the thin-disk geometry for this setup are deduced. Also the Pockels effect is introduced and suitable crystals for high average powers and energies are compared.

2.3.1 Gain Medium Geometries

Heating effects can be counteracted by enhancing the cooling properties. Especially the geometry of the gain medium plays an important role for the thermal management. Apart from the classical rod geometry, thermal improvements could be reached by using fiber, slab and thin-disk geometries [46]. The main idea is to improve the ratio between the surface area of the gain material and the actual gain, i.e. the amplification coefficient and therefore the heat generation should be small compared to the surface area. This provides an efficient heat extraction by properly cooling the surface area of the gain medium.

Fiber Amplifier

Fiber amplifier consist of a fiber with doped core of up to a few hundred micrometer in diameter that is used for amplification. 3.5 kW of average power with a repetition rate of 80 MHz and a pulse duration of 430 fs are reached with a coherent combination of multiple of such fiber amplifiers [47]. For diffraction limited operation, fiber amplifiers are limited to small core diameters [46] and high energy pulses would yield high peak intensities and fluences causing nonlinear distortions and damages. For this reason single-fiber amplifiers are limited concerning their maximum energy although energies up to 23 mJ were reached by coherent combination of in total 96 pulses [12].

Slab Amplifier

For slab amplifier, the gain material has the shape of a rectangular plate with typical heights of a few millimeter [48]. Heatsinks are attached to the large-area upper and lower surfaces of the plate and provide efficient cooling. Larger mode sizes compared to fiber based approaches are possible in slab geometries [48, 49] and consequentially at multi-kilohertz repetition rate higher energies of up to 54 mJ with an average

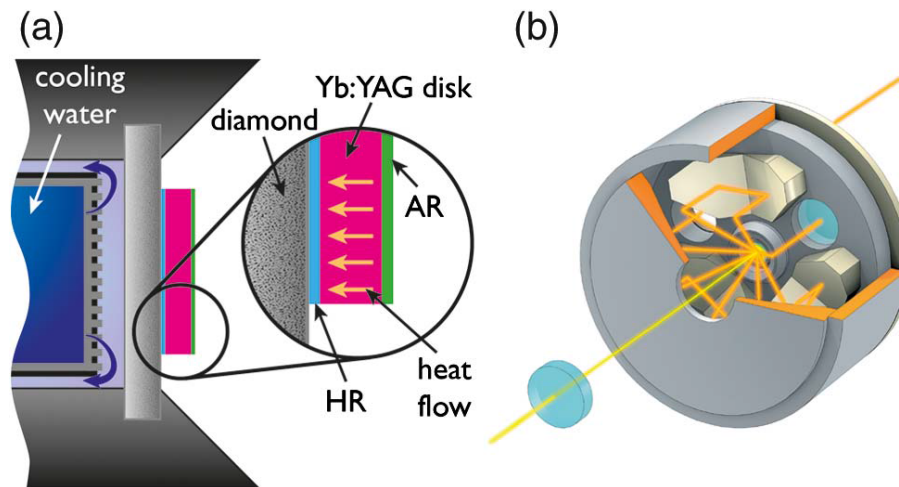


Figure 2.7: (a) The schematic of a thin-disk. A disk (often made of Yb:YAG) with a thickness of a few hundred micrometer is attached to a diamond heat sink. The disk's front has an anti-reflective (AR) coating while the back is highly-reflective (HR). The diamond heat sink is cooled by a water shower on the back. (b) The pump head of a thin-disk (courtesy of *TRUMPF Laser GmbH*). Pump light (orange) is reimaged onto the disk several times by a parabola and rooftop folding mirrors. A hole in the parabola enables the propagation of the amplified laser (yellow). Both images were taken from [8].

power of 500 W and a pulse duration of 1.5 ps are reached [11]. Slab lasers allow for compact lasers owing to their high single pass gain of 2–10 [49], but still show a coupling between mode size and heat extraction efficiency. Bigger mode areas eventually require higher crystals that limit the cooling efficiency of the heatsinks [48]. Thus energy scaling is limited for high average powers [50].

Thin-Disk Amplifier

This coupling between mode size and heat removal efficiency is solved in the thin-disk geometry. A schematic of a thin-disk is shown in figure 2.7. A thin disk with a thickness of a few hundred micrometer is attached to a cooled heat sink [13], for example to a water cooled diamond [8, 51]. A highly reflective layer (typically a dielectric coating) between the thin disk and the heat sink acts as mirror, while a small wedge of the disk prevents etalon effects. A pump laser is imaged multiple times onto the disk effectively increasing the absorption length of the pump light and simultaneously creating high pump intensities. By bouncing over the pumped area of the disk, a laser beam is slightly amplified by a factor on the order of 1.1 per pass. Although this amplification is less than for slab or fiber geometries, the now one dimensional longitudinal heat flow decouples the cooling properties from the mode size and due to the high pump intensities, the gain per length of material is comparably high reducing material induced distortions like thermal lensing or nonlinear aberrations. Implementing a thin disk in a resonator, regenerative amplifier or multipass arrangement compensates for the low gain per pass simply by bouncing over the disk multiple times [46]. Fabrication and handling of large-diameter disks is however challenging and disk diameters are typically below 20 mm. Apart from this, thin-disks are only limited by amplified spontaneous emission (ASE) [32]. In

contrast to slabs, the gain for spontaneous emission is higher than the gain for the actual laser beam since the gain across the disk is significantly higher than the gain through the disk. This makes thin-disks more vulnerable to ASE [49]. Yet this structure offers the advantage of large mode areas and hence high energies together with effective heat removal capabilities allowing for kilowatt scale average powers.

The amount of pump passes in the presented system is 24, which was state of the art for commercially available high power thin-disk pump systems at the time this amplifier was initiated [52]. The pump head used in this setup (*TRUMPF Laser GmbH + Co. KG*) is compatible with a disk diameter of 14 mm and can be used with either 940 nm or 969 nm pump laser diodes.

2.3.2 Dopants

Another possibility to minimize thermal issues is the usage a medium with relatively low heating. The dominant heat source is the energy loss between absorption and emission called *quantum defect* [46, 53]. For Yb:YAG this is the conversion of $\lambda_P = 940$ nm or $\lambda_P = 969$ nm pump light to $\lambda_L = 1030$ nm emission with the quantum defect (i.e. the best case fraction of pump power converted to heat) being $\eta_P = 1 - \lambda_P/\lambda_L$. In fact ytterbium (Yb^{3+}) doped materials exhibit especially favorable properties regarding the quantum defect among commonly used near infrared solid-state materials like erbium, neodymium, thulium, holmium, titan or chromium [46]. Not only are there Yb^{3+} pump/emission wavelength pairs with quantum defects below 10%, but mature diode pump lasers with multi-kilowatt average powers are commercially available for these pairs due to the availability of high power laser diodes in the spectral range from 790 nm to 1060 nm [54].

While the previously made statements to a lesser extent also hold for neodymium, Yb^{3+} doped media support about ten times shorter pulse durations on the order of 1 ps due to their broader gain bandwidth [46, 53, 55]. This broad gain bandwidth is not only important for the generation of ultrashort pulses, but it also simplifies the stretching of pulses to nanosecond scale in CPA systems. Another drawback of neodymium is the low typical doping concentration in common materials before quenching starts (around 1 at.% [56] in contrast to over 10 at. % for Yb^{3+} [53]).

2.3.3 Host Materials

The actual properties of a gain medium differ for varying combinations of dopant and host material. To highlight the advantages of yttrium aluminium garnet (YAG) as host material for a thin-disk laser, the amplification figures of merit discussed in section 1.6.4 are evaluated with a focus on the suitability for high output energies and powers.

Amplifying to high energies requires sufficient stored energy on the disk. This property scales linearly with the lifetime $E_{stored} \propto \tau$, resulting in long lifetimes being preferred for a high energy gain material. Besides that, a high value of stored energy implies the necessity of a high dopant concentration c_{Dop} . Since near infrared lasers around 1 μ m wavelength have advantageous properties for high average powers (see section 2.3.2), optimization of the small signal gain or equivalently the $\sigma\text{-}\tau$ product

	Unit	Material		
		Yb:YAG	Yb:LuAG	Nd:YAG
Bandwidth $\Delta\lambda_L$	nm	9	5.5	0.6
Emission λ_L	nm	1030	1030	946, 1064 , 1320
Pump λ_P	nm	940, 969	940, 969	808 , 880, 914, 938
Best Defect η_P	%	6	6	7
Typ. Doping c_{Dop}	at. %	10	10	< 2.5
Lifetime τ	ms	0.95	0.97	0.23
Emission σ_{eL}	10^{-20}cm^2	2.14	2.59	28
Absorption σ_{aP}	10^{-20}cm^2	0.82	0.82	6.7
Temp. Coeff. dn/dT	$10^{-6}/\text{K}$	7.8	8.3	7.9
Thermal Cond.	W/(m K)	6.1	7.4	14
Hardness	Mohs	8.5 [53]	8.4 [59]	8.5

Table 2.1: Principal properties of three potential high power laser materials. The bold wavelengths mark the emission and pump wavelength of the listed peak cross sections σ_{eL} and σ_{aP} . The values for Yb:YAG and Yb:LuAG are taken from [58] if not stated otherwise. The Nd:YAG values are summarized from [46], [55] and [60].

is limited. Best amplification properties are expected for low refractive index host materials that show a reasonably small spectral bandwidth $\Delta\lambda_L$.

Besides these dopant related properties, the host material also has to withstand a high temperature increase without drastic changes. This especially means that the host material should have a low temperature coefficient of the refractive index dn/dT and a high thermal conductivity.

A comparison of different host materials for Yb^{3+} done in [53] shows favorable properties for Yb:YAG. It has by far the highest $\sigma\text{-}\tau$ product together with among the highest lifetime τ and maximum dopant concentration c_{Dop} of all analyzed materials combined with a comparably high thermal conductivity and low dn/dT . Additionally the high hardness simplifies polishing thin thicknesses as needed for the thin-disk geometry. YAG is widely used as host material and the crystals can be grown with low complexity and high quality [46, 53, 57]. The high $\sigma\text{-}\tau$ product comes at the cost of a narrow but still reasonable emission bandwidth supporting a pulse duration around 1 ps [46, 53] (see eq. 1.124).

Another promising candidate is ytterbium lutetium aluminium garnet (Yb:LuAG) with a slightly larger $\sigma\text{-}\tau$ product ($2512 \times 10^{-20} \mu\text{s cm}^2$ for Yb:LuAG compared to $2033 \times 10^{-20} \mu\text{s cm}^2$ for Yb:YAG [58]), a 20% higher thermal conductivity as well as a hardness, dn/dT and maximum doping concentration very similar to Yb:YAG [45, 58]. However the gain bandwidth of Yb:LuAG (about 5.5 nm) is 40% less than for Yb:YAG (about about 9 nm) [45, 55, 58] yielding a significantly longer pulse duration.

Table 2.1 summarizes the investigated gain and dopant materials for the amplifier system from the previous sections with neodymium yttrium aluminium garnet (Nd:YAG) as exemplary neodymium based material. While the potential quantum defect of Nd:YAG can be low, its peak performance at the pump/lasing

wavelength combination 808 nm/1064 nm is only reached at the cost of a quantum defect as high as 24 %. The consequentially high heat load combined with the narrow emission bandwidth, the low doping concentration and the short lifetime contradicts the targeted system parameters. In contrast both Yb:LuAG and Yb:YAG show favorable properties. Due to the good availability of high quality crystals, its good compromise between pulse duration (i.e. bandwidth) and σ - τ product and good thermal properties, Yb:YAG is often distributed as standard disk material and also used for the presented system.

2.3.4 Pockels Cell

In conjunction with a polarizer and a waveplate, the purpose of the Pockels cell is to trap the pulse in the resonator by applying a voltage and to release the pulse once the voltage is switched off. It does so by using a crystal with a strong linear electro-optic coefficient that modifies the polarization of a propagating pulse once an electric field is applied. The Pockels cell forms the bottleneck of regenerative amplifier design and the maximum energy in any regenerative amplifier is ultimately limited by the damage threshold of the Pockels cell crystal and its coating. It adds at least two additional surfaces per roundtrip increasing the resonator losses and additionally it is often the longest transmittive element making it sensitive to thermal and nonlinear effects. Mechanical switches have been proposed as alternative [61] but a successful implementation is controversial due to the high mechanical stress for the components [62, p. 43]. The working principle of Pockels cells, a comparison of suitable crystals and their operation parameters are discussed in more detail in the following.

A simplified picture of the Pockels effect is the following [16, p. 836]: assuming that the refractive index of a crystal can be described as a function of an electric field $n(E)$, then it can be written as Taylor series

$$n(E) = n + a_1 E + \frac{1}{2} a_2 E^2 + \dots \quad (2.1)$$

Defining two new coefficients called electro-optic coefficients $\mathbf{r} = -2a_1/n^3$ and $\mathbf{s} = -a_2/n^3$, the series can be rewritten to

$$n(E) = n - \frac{1}{2} \mathbf{r} n^3 E - \frac{1}{2} \mathbf{s} n^3 E^2 + \dots \quad (2.2)$$

The second order term represents the *Kerr* effect, which will be explained in later sections, while the first order term represents the *Pockels* effect: a change of refractive index that linearly depends on an electric field. In case of centrosymmetric materials, the response of the material has to be same no matter what the direction (or mathematically the sign) of the electric field is. I.e. $n(E)$ has to be an even symmetric function. Since the existence of a first order term breaks this symmetry, the Pockels effect only occurs if the material is not centrosymmetric. In this case the Pockels coefficient \mathbf{r} has a value different from zero. The corresponding change of refractive index is then

$$\Delta n = -\frac{1}{2} \mathbf{r} n^3 E. \quad (2.3)$$

\mathbf{r} is in general a tensor that couples (in first approximation, [16, p. 852]) the refractive index of a crystal's principal axis to the electric field applied in x,y or z direction. This also means that applying an electric field e.g. along z direction can cause a shift of refractive index for one, two or all the principal axis, depending on the crystal structure and its Pockels coefficient tensor \mathbf{r} . Therefore the Pockels effect and its impact differs for every used crystal structure. A more detailed treatment for commonly used Pockels cell crystals can be found in [16, p. 849].

These commonly used crystals include BBO, rubidium titanyle phosphate (RTP), potassium dihydrogen phosphate (KDP), potassium dideuterium phosphate (DKDP), lithium niobate (LNB) and lithium tantalate (LTA)[63]. Unfortunately, not every crystal is suitable for high energy and high average power applications.

BBO can be seen as gold standard for high average power applications. It features a high damage threshold of about 10 J/cm^2 (10 Hz, 1064 nm, 10 ns [64]), is commercially available in sizes larger than $12 \times 12 \times 20 \text{ mm}^3$ and is only slightly hygroscopic.

RTP, LNB and LTA all have relatively low damage thresholds [63] and crystals with apertures of $>17 \times 17 \text{ mm}^2$ to compensate for this are not commercially available.

In contrast despite their low damage threshold, KDP and DKDP crystals can be grown with large apertures compensating for lower damage thresholds. However they show strong hygroscopic behavior and have to be used in a sealed environment. Coatings are more difficult to produce on hygroscopic substrates, are expected to have lowered damage thresholds [63] and are not suited for high average powers [62, p. 42]. Additionally KDP and DKDP need their voltage applied along the beam propagation axis due to their crystal symmetry. This requires ring electrodes with a degraded switching contrast or complex plasma electrodes [65]. Finally both KDP (0.04/cm@1064 nm) and DKDP (0.005/cm@1064 nm) show significantly stronger absorption coefficients than BBO ($<0.001/\text{cm}@1064 \text{ nm}$) [66] making them problematic in high average power systems.

In conclusion in order to reach high energies and high average powers, BBO is the most suitable Pockels cell crystal. For BBO applying an electric field $(E, 0, 0)$ in a right handed coordinate system (x, y, z) with the optical axis of BBO being coaxial to $(0, 0, 1)$ will yield the crystal principal axis $(0, 0, 1)$, $(1, 1, 0)$ and $(1, -1, 0)$ with the corresponding refractive indices $n_e(E)$, $n_{o1}(E)$ and $n_{o2}(E)$

$$n_e(E) \approx n_e(0) \quad (2.4)$$

$$n_{o1}(E) \approx n_o(0) - \frac{1}{2}r_{22}n_o(0)^3 E \quad (2.5)$$

$$n_{o2}(E) \approx n_o(0) + \frac{1}{2}r_{22}n_o(0)^3 E. \quad (2.6)$$

For a laser propagating along $(0, 0, 1)$ with linear polarization along $(1, 0, 0)$ this structure represents a perfectly aligned waveplate with a phase difference between the n_{o1} and n_{o2} axis of

$$\Delta\varphi(E) \approx \frac{2\pi L r_{22} n_o(0)^3 E}{\lambda}, \quad (2.7)$$

where λ is the free space wavelength, L the length of the crystal and $E = V/d$ the electric field generated by a voltage V applied across a crystal with height d .

Therefore a BBO crystal used in this configuration acts as switchable waveplate with tunable retardance.

For an exemplary quarter wave switch to be used in a $\lambda = 1030$ nm regenerative amplifier based on a $12 \times 12 \times 20$ mm³ BBO crystal with $r_{22} = 2.2$ pm/V and $n_o = 1.655$ [63] this yields a switching voltage of

$$V_{\lambda/4} \approx \frac{\lambda d}{4n_o^3 r_{22} L} \approx 15.5 \text{ kV}. \quad (2.8)$$

While this puts high demands on electronics, switching devices in the kilohertz range for these voltages are still commercially available. Nevertheless the electric fields of the switches are close to potential gas breakdowns and the length of the crystal as free design parameter has to be long enough to avoid them. Assuming a safe electric field of $V_{\lambda/4}/d < 2$ kV/mm [67] yields a minimum length of $L > 13$ mm for BBO based quarter wave switches in air.

The Pockels cells in the presented system are used with a bipolar switch. This means instead of switching between a retardance of 0 and $\lambda/4$, the implemented Pockels cells create a phase shift of $-\lambda/8$ or $\lambda/8$ per crystal. This halves the required peak voltage and minimizes the risk of electric breakdowns.

Due to their good availability, BBO crystals with apertures of 12×12 mm² and lengths of 15 – 20 mm are used in the amplifier. The warranted damage threshold is specified as $J_{LIDT} = 5$ J/cm² for an AR-coated crystal and $J_{LIDT} = 10$ J/cm² for the bulk (10 Hz, 1064 nm, 10 ns [64]). In cooperation with the manufacturer *CASTECH Inc.*, the coating's damage threshold was further optimized and the results were implemented in the presented system. As an example using the damage threshold scaling law of $J_{LIDT} \propto \tau^{1/2}$ [68] and a beam diameter of roughly 5 mm to avoid significant power loss due to clipping, the maximum pulse energy to stay within the warranted values on the AR-coated crystal is roughly 205 mJ for a duration of the stretched pulses of 1.75 ns. This is one of the main reasons why the pulse duration within the amplifier needs to be on the order of nanoseconds (compare to the system overview in figure 2.1).

The thermally induced stress on the surrounding crystal surface is in first approximation independent of the crystal aperture and just depends on the radial temperature difference between the center and surface [69] [70, p. 13]. Crystal fracture of coated BBO was observed for a radial temperature difference of 50 K equivalent to a thermal load of about 0.2 W in a 2 mm long crystal [71, 72]. Assuming an absorption coefficient of 1×10^{-3} /cm at 1030 nm [64, 66] yields maximum average powers of roughly 1 kW before 0.2 W is absorbed within 2 mm and crystal fracture is expected. More optimistic absorption coefficients around 1×10^{-4} /cm [72] still limit the intraresonator average power to values around 10 kW. These values can be even lower in the presence of small crystal or coating defects [72]. In fact average powers within the resonator on the order of 10 kW are realistic for the presented system and pose a fundamental potential risk for the used BBO crystals. The origin of these high average powers and their dependencies are discussed in section 2.5.

2.4 Optimal Working Point

Thin-disks based on Yb:YAG were evaluated to be the most suitable gain geometry to reach high average powers and high energy. The usage of thin-disks for laser amplification still offers some degrees of freedom and several parameters need to be determined accordingly to obtain maximized performance. To this end a numerical model was developed that extends the formalism from section 1.6 to a more general case with temperature dependent material properties and a dynamic change of population densities that is especially important for higher repetition rates (in this case $f_{rep} = 5$ kHz). The temperature model for thin-disks is later introduced in section 2.6.1 while the numeric model is explained in appendix. B. This numeric model enables the theoretical deduction of the optimal working parameters for the presented amplifier. It approximates the resonator as a multipass, thus no resonator effects are taken into account.

Thin disk systems benefit from high doping concentrations (see section 2.3.3), hence the doping concentration c_{Yb} for the following simulations is set to a value close to the maximum doping concentration of 12 at. % for Yb:YAG [53]. The disks are cooled with a water temperature of $T_0 = 28$ °C and a pumping wavelength of 969 nm is assumed in the following due to its lower thermal load (this is later evaluated in more detail, see section 2.6.1). The amount of pump passes is set to $M_p = 24$, which was state of the art for commercially available high power thin-disk pump systems at the time this amplifier was initiated [52]. The laser pump heads (*TRUMPF Laser GmbH + Co. KG*) are compatible with a disk diameter of $D = 14$ mm. To avoid parasitic modes induced by ASE, the pump spot radius w_{Pump} multiplied by 1.8 has to be smaller than the disk radius [73, p. 126], hence the pump spot radius w_{Pump} is set to $w_{Pump} = 3.5$ mm close to the maximum possible value. Maximizing the pump spot radius and intensity also maximizes the stored energy (eq. 1.122) as long as the ASE contribution remains small enough.

The pump intensity is limited to $I_{Pump} \leq 8$ kW/cm² due to an increased risk for optical damages [21]. In a thin-disk laser [74] with similar properties as the analyzed amplifier, a lowered output power for $I_{Pump} \geq 2$ kW/cm² due to thermally induced wavefront aberrations was observed (this is later discussed in more detail in section 2.6.2) that eventually leads to a collapse of output power at $I_{Pump} \approx 4$ kW/cm². Pump intensities beyond 4 kW/cm² are therefore believed to induce severe wavefront aberrations (especially when they are combined with thicker and therefore hotter disks) which is why pump intensities up to 4 kW/cm² are of particular interest in the following sections. However, the introduced numeric model does not cover additional losses induced by wavefront aberrations and the calculated results are based on a simple multipass scheme over thin-disks with a flat-top pump spot.

Using the relationship between M^2 , pump spot radius w_{Pump} and mode radius on the disk w_{Disk} from section 1.4

$$w_{Disk} \approx \frac{w_{Pump}}{\sqrt{M^2}} \quad (2.9)$$

with a nearly diffraction limited target M^2 of $M^2 \leq 1.2$ yields a mode radius of $w_{Disk} \approx 0.9w_{Pump}$. Bigger mode sizes lead to better beam qualities, but are only

Parameter	Variable	Value
Repetition Rate	f_{rep}	5 kHz
Doping	c_{Yb}	$\leq 12 \text{ at. } \%$
Water temp.	T_0	28 °C
Pump wavelength	λ_P	969 nm
Pump passes	M_p	24
Disk diameter	D	14 mm
Pump radius	w_{Pump}	3.5 mm
Mode radius	w_{Disk}	3.15 mm
Roundtrip transmission	\mathcal{T}_1	98 %
Max. pump intensity	I_{Pump}	4 – 8 kW/cm ²
Disk thickness	H	$\approx 150 - 200 \mu\text{m}$
Disk amount	i	2
Input energy	E_{In}	$\approx 0.1 - 1 \text{ mJ}$
Roundtrips	RT	$\approx 30 - 40$

Table 2.2: Listed are the input parameters used for the simulation (upper part) and the deduced parameters for an optimized amplifier performance (bottom part).

partially amplified due to the limited overlap with the pump spot and tend to be more alignment sensitive. This manifests as lower transmission per roundtrip within the scope of the numeric model. Typical values for the transmission per roundtrip are around $\mathcal{T}_1 = 98\%$.

The previous discussion already constrained several working parameters to fixed values. A summary of these values can be found in the upper part of table 2.2. The remaining free parameters are the disk thickness H , the amount of disks i , the input fluence J_{in} (or equivalently energy E_{In}) and the amount of roundtrips RT . They are determined in the following and the obtained results are listed in the lower part of table 2.2.

Disk Thickness and Amount

Ideally the maximum output energy resembles the stored energy on the disk minus some losses. This also implies that the maximum output energy is approximately independent of the seed energy E_{In} or alternatively the seed fluence $J_{In} = E_{In}/(\pi w_{Disk}^2)$ as long as the seed energy is much smaller than the output energy. This is in fact confirmed by the numeric model. The seed energy is therefore arbitrarily set to $E_{In} = 1 \text{ mJ}$ for the analysis of the disk thickness and later investigated in greater detail. A proper disk thickness and disk amount is identified by optimizing the output energy for a multipass system with a single disk ($i = 1$) and then adding enough disks to reach a pulse energy of 200 mJ. The resulting output energies for different disk thicknesses and pump intensities are shown in figure 2.8.

Surprisingly the system seems to be quite robust over the analyzed disk thicknesses between 100 μm and 300 μm for pump intensities up to 4 kW/cm². Yet the variation of output energies increases with increasing pump intensities. The optimal thickness

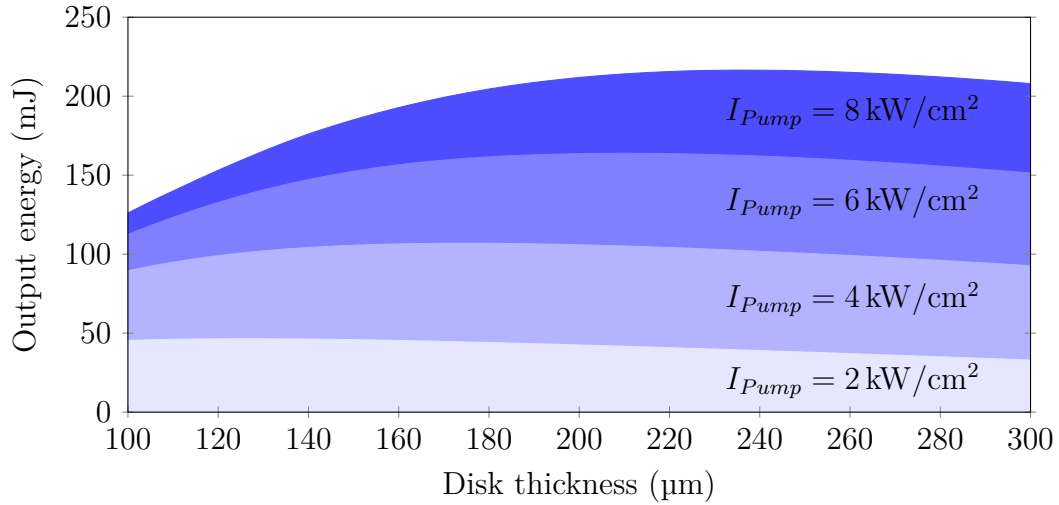


Figure 2.8: The calculated output energy of a single disk multipass with different pump intensities versus the disk thickness. The amount of passes has been optimized for each point to maximize the output energy.

for practical pump intensities around 4–6 kW/cm² can be found between 150 μm and 200 μm, whereupon thinner disks show favorable thermal properties. Future analysis is based on a thickness of $H = 170 \mu\text{m}$ in between the previously mentioned thicknesses.

The output energy of one disk is below the targeted value of about 200 mJ for practical pump intensities. Adding a second disk to the system and recalculating the system for $H = 170 \mu\text{m}$, $I_{Pump} = 4 \text{ kW/cm}^2$ and $E_{In} = 1 \text{ mJ}$ suggests an output energy of $E_{Out} = 263 \text{ mJ}$ that is considered sufficient for the design goal. The same system yields an output energy of $E_{Out} = 262 \text{ mJ}$ for $E_{In} = 1 \mu\text{J}$ confirming the approximated independence of maximum output energy from input energy.

Influence of Seed Energy

The seed energy E_{In} has no significant influence on the possible output energy of the amplifier. However, it has an influence on the laser dynamics. Too small (or rarely even too high) input energies can lead to system eigenvalues close or even bigger than one (see equation B.34) that are connected to unstable amplification properties [34] (see paragraph *Bifurcation and Chaos* in section 1.6.3).

Figure 2.9 shows the necessary roundtrips to reach the maximum output energy as well as the amount of pulses the system needs to stabilize to a new steady state after a disturbance (e.g. pump power fluctuations, seed pointing and so on) changed some system properties (calculated based on equation B.35).

A large number of roundtrips is necessary for small input energies to reach sufficient output energies, hence the pulse is affected more often by any imperfection in the laser (e.g. low quality optical surfaces or vibrations in the system). At the same time spontaneous emission that propagates along the multipass path can exhibit similar average powers as low energy seeds. Both compete during amplification and in conclusion a reduction of stability is expected for low energy seeds.

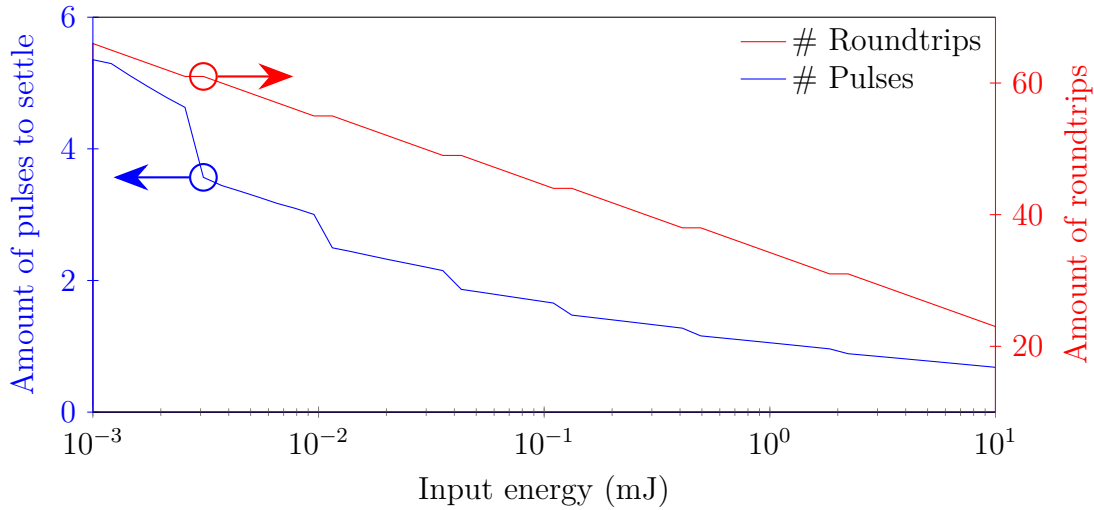


Figure 2.9: Depicted in blue is the amount of pulses necessary for the system to settle after a disturbance occurred at the point of maximum output energy (calculated by eq. B.35). Also plotted is the amount of roundtrips needed to reach the maximum output energy over different input energies (red). The targeted output energy is $E_{Out} \approx 260$ mJ. The pump intensity was set to $I_{Pump} = 4$ kW/cm² and a system with two disks is assumed.

On the other hand high input energies are amplified to high energies within a few roundtrips quickly depleting the disks. The filtering of unwanted input modes that dominantly happens within the first roundtrips (e.g. by a soft aperture consisting of the pump spot surrounded by the unpumped disk) becomes less effective and causes exceeding energy losses that cannot be regained by adding more roundtrips. In that case the output might exhibit multimode features, beamsize fluctuations or even pointing (depending on the frontend and alignment). Also higher input energies demand a frontend approaching the complexity of the discussed amplifier.

A robust system should provide a fast settlement after a disturbance without decreasing the roundtrip number too much. Input energies between 100 μ J and 1 mJ provide a good compromise between these two values and keep the demands on the frontend reasonable. The benefits of higher seed energies on the stability of regenerative amplifiers are also discussed in [75].

Energy Saturation Points

In a multipass system a pulse is amplified with every roundtrip depleting the gain medium until the roundtrip gain compensates the roundtrip losses. At this point the pulse keeps its energy before the losses cannot be compensated anymore and the pulse actually decreases in energy. This turnover point between energy gain and energy decrease is often called saturation.

In multi-kilohertz Yb:YAG systems, a second saturation point exists. To explain this phenomenon, an exemplary multipass system designed with a certain amount of roundtrips RT and a certain output energy E_{out} is assumed. If the design is changed to have more roundtrips, one would naturally expect a higher output energy (until the previously mentioned saturation point is reached where gain and roundtrip

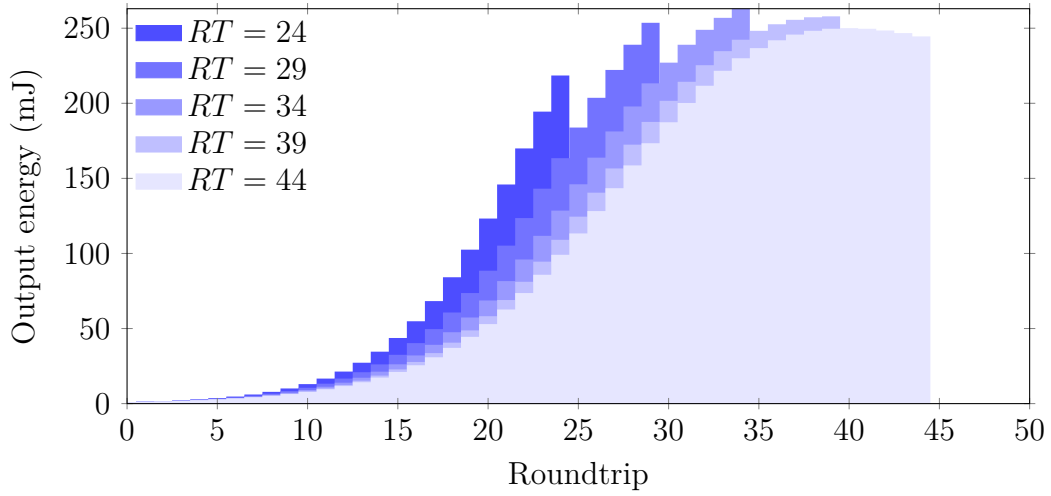


Figure 2.10: The buildup of the output pulse during amplification for different completed roundtrips RT . The pump intensity is $I_{Pump} = 4 \text{ kW/cm}^2$ and the input energy $E_{In} = 1 \text{ mJ}$. A saturation of output energy is observed for $RT = 34$ and a saturation of buildup for $RT = 39$.

losses compensate). A higher output energy also means that more electrons need to be excited to the upper level between two amplified pulses. This is counteracted by spontaneous emission and ASE. Thus at one point, the expected energy after an increase of roundtrips would require more electrons to be excited than possible within the duration between two pulses. At this point a design with more roundtrips RT would not lead to an increase in energy and the output energy saturates even before gain and roundtrip losses compensate each other.

It should be noted that the latter saturation is observed for the steady state output energy versus the designed roundtrip number RT , while the initially mentioned saturation is observed for the energy buildup. The buildup of pulse energy refers to the increase of pulse energy for an input pulse during its propagation in a multipass arrangement and is typically plotted as pulse energy after the first, second, third and so forth roundtrip until the pulse exits the multipass. Such a buildup of pulse energy is depicted for five exemplary multipass designs with total roundtrip numbers between $RT = 24$ and $RT = 44$ in figure 2.10.

If the beam is coupled out after $RT = 39$ completed roundtrips, the disks are left in a state where they can provide just enough gain to compensate the losses. This working point at buildup saturation offers the advantage of a very high pulse to pulse stability. If a single pulse with a slightly lower input energy enters the multipass at this working point, the disks are depleted slightly slower and the amplification behavior corresponds to a system with a normal input energy but less (e.g. 38) roundtrips. From figure 2.10 one can see that the output energy will not change a lot and hence the original pulse to pulse instability has been filtered out.

However after this pulse has passed, the disks are pumped starting from a higher upper level population $N_2(0)$, i.e. the working parameters of the amplifier have changed and the system needs to settle to a new steady state gain. If the input energy does not return to a normal value before the system has settled (typically within a few pulses, see figure 2.9), this new steady state gain will define the new

output energy. Again less input energy depletes the disks slower and the settled amplification behavior corresponds to a system with a normal input energy but less *completed* roundtrips RT . The optimal working point for such disturbances longer than a few pulses is closer to the steady state saturation at $RT = 34$. This distinction between fast and slow distortions yields two separate optimal working points.

According to figure 2.9, the system settles within about one pulse for $E_{In} = 1$ mJ. Including the pulse that caused the disturbance, two pulses are affected by the settlement process. Hence for a repetition rate $f_{rep} = 5$ kHz operation close to $RT = 39$ optimizes the noise behavior for frequencies above 2.5 kHz. The more common slower noise is filtered close to $RT = 34$, a working point that also features the advantage of higher output energies. For low repetition rate systems $f_{rep} < 1$ kHz that effectively settle immediately (see equation B.36) these two regimes join and the maximum output energy is reached at the point of buildup saturation. High repetition rates in contrast increase the distance between both regimes.

In a regenerative amplifier each single pass spatially overlaps with the previous one and no spatial separation of passes is observed. In such a case the total pulse energy seen by an optical element within a regenerative amplifier is calculated by adding the energies of all (virtual) pulses that are part of the buildup. The intracavity average power is the total pulse energy times the repetition rate and rises from 10.5 kW at $RT = 29$ to 14.7 kW at $RT = 34$ and finally to 19.3 kW at $RT = 39$ for comparable output energies. Thus to avoid thermal stress on resonator optics, the operating point $RT = 34$ (or even lower) is beneficial.

Comparison to Experiment

The theoretical predictions of the previous sections are also experimentally confirmed. While output powers of up to 1 kW were possible using a seed energy as low as 1 μ J, the output properties with this seed energy were sensitive to external distortions and the occurrence of bifurcation was more likely (as has already been shown in [75]). This sensitivity was drastically reduced by increasing the seed energy to values greater than 100 μ J. The avoidance of bifurcations and higher robustness are the key reasons for the implementation of a preamplification stage. As predicted, the presented amplifier system shows an increased sensitivity for noise in the 2.5 kHz domain and this noise has to be avoided in the input signal. An experimental evaluation of the saturation point with optimal pulse to pulse stability (close to $RT = 39$ in figure 2.10) has been prevented by the occurrence of damages that are most likely induced by the high intracavity average powers at this point.

A typical pulse build-up within the amplifier is shown in figure 2.11. For this measurement, a silicon photodiode was placed into stray light that exits the amplifier chamber. The shape closely resembles the expectations for the point of maximum output power as simulated in figure 2.10. Also the often used assumption of a quasi constant gain during the amplification is validated for a repetition rate of 10 kHz by the good overlap between the constant gain envelope and the measurement.

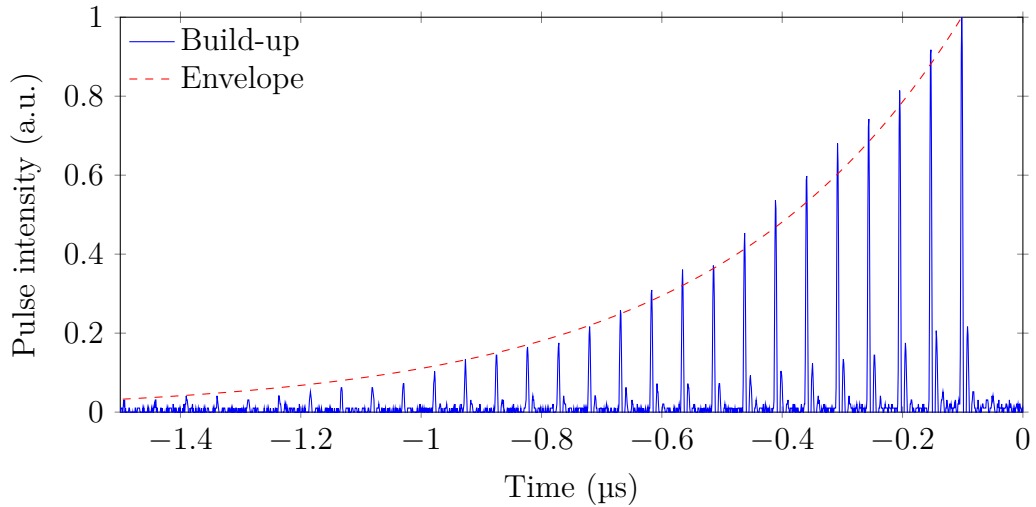


Figure 2.11: A typical build-up of the pulse energy within the amplifier measured by a silicon photodiode placed into stray light. The small post-pulses are caused by electronic ringing. The roundtrip time is 51.6 ns. 50 μ J are amplified to 1 kW at a repetition rate of 10 kHz over 45 roundtrips using a pump power of 1.54 kW per disk. The dashed line shows the expected output as envelope assuming a constant roundtrip gain of 1.13.

2.5 Intracavity Power and Damage Threshold

The numeric calculation of the optimal working point in the previous section estimated intracavity average powers on the order of tens of kilowatt. To understand the origin of these high average powers and to obtain insight into scaling laws and potential consequences, a deeper analysis is performed in the following. Also the scaling of mirror damages in regenerative amplifier configurations is analyzed and an intracavity scaling law is proposed.

The propagating pulse in a regenerative amplifier takes the same path every roundtrip. This significantly increases the thermal load for every component within the resonator and even small unblocked reflections can lead to significant heating of components. A good estimate for the effective power seen by intracavity components can be calculated by assuming a constant gain G for every roundtrip. For a ring resonator (the values for a linear resonator have to be doubled) a total amount of N (virtual) pulses with increasing energy have interacted with an arbitrary component, where N is the number of resonator roundtrips (compare to figure 2.11). The total energy E_{sum} seen by the optics is hence

$$E_{sum} = \sum_{n=1}^N E_{in} \cdot G^n. \quad (2.10)$$

Multiplying this by the repetition rate yields the average power

$$P_{sum} = \sum_{n=1}^N P_{in} \cdot G^n. \quad (2.11)$$

This forms a geometric series that can be simplified to

$$P_{sum} = P_{in} \cdot G \left(\frac{G^N - 1}{G - 1} \right). \quad (2.12)$$

By assuming a high gain, i.e. the output power P_{out} is much higher than the input power P_{in} or $P_{out}/P_{in} = G^N \gg 1$, this can be approximated by

$$P_{sum} \approx P_{out} \frac{1}{1 - 1/G}. \quad (2.13)$$

For thin-disk lasers, realistic roundtrip gains are on the order of $G \approx 1.1$. Therefore components within the resonator have to withstand pulse bursts that can reach an order of magnitude higher average powers than the actual output power. For a kilowatt scale amplifier, even typical AR coating reflectivities of 0.25% carry tens of watt of average power. If not properly dumped, these reflections cause uncontrolled heating and misalign the resonator. Thus proper cooling and careful dumping of reflections play a key role in the design of high power amplifiers. These high intraresonator powers also emphasize the need for low absorption transmissive optics like BBO crystals. In general transmissive optics with their reflective surfaces and slight absorptions should be avoided as far as possible. A high roundtrip gain can reduce the thermal load, but optimization of this parameter is very limited.

If the intraresonator power is the dominant reason for damages, scaling to higher average powers is severely hindered and a fundamental limit of regenerative amplifiers is found. To investigate this further, the repetition rate of the amplifier was doubled to 10 kHz (i.e. the fluences on the mirrors were halved at constant average power). The pump power was increased to 2 kW per disk while keeping the amount of roundtrips at 39 (compare to the settings of the 5 kHz operation in figure 2.3). An output power of over 1.4 kW was reached with a seed energy of 50 μ J and a spot size comparable to the 5 kHz operation presented in figure 2.3. To best of the author's knowledge, this was the highest average power extracted from a regenerative amplifier at the time of measurement. The measurement is shown in figure 2.12. Using equation 2.13 this roughly corresponds to an intraresonator power of 7.6 kW. A damage of the BBO crystal was observed after approximately 8 min of operation. The crystal has been regularly used with energies beyond 200 mJ, thus the applied pulse energy of 140 mJ is assumed to be lower than the damage threshold. This damage is therefore attributed to the increased thermal load on the crystal and stresses the importance of low intraresonator average powers. Damages due to high thermal loads are approximately independent of aperture size (see section 2.3.4) and our experiment supports the hypothesis that they form a fundamental limit of regenerative amplifier performance. Also average powers on the order of 10 kW were previously predicted to drastically increase the damage probability of BBO crystals [72].

In addition to the thermal stress of the components, the high fluence of the amplified laser pulses can cause damages of optical components. Beyond a pulse duration of a few tens of picoseconds, the damage process is dominated by heat deposition: the dielectric material of the coating melts or boils if confronted with a high fluence and the optic is damaged [68]. This process shows a $\tau^{1/2}$ dependence of the damage threshold fluence upon the pulse duration, which is why stretching the pulses to longer pulse durations helps to increase output energy. Coating defects can enhance the heat deposition and are assumed to have a significant influence on the damage threshold of optics [76].

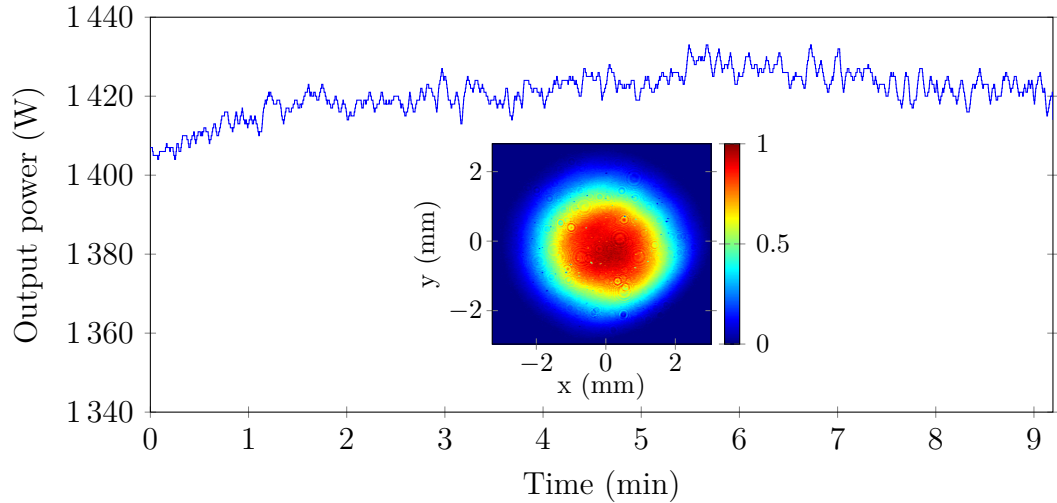


Figure 2.12: The measured maximum output power for a repetition rate of 10 kHz. The inset shows the corresponding beam profile with a $1/e^2$ spot size of 4.8 mm in x direction and 4.5 mm in y direction.

A measurement of the optical damage threshold for dielectric optics was performed. To this end pulses with a repetition rate of 1 kHz, a pulse duration of 1 ns and a central wavelength of 1030 nm were focused with an $1/e^2$ diameter of 330 μm onto a test optic. The fluence onto the test optic was changed by turning a half-wave plate in front of a polarizer and sending the reflected s-polarized light to the test setup. The fluence was slowly increased until a damage was observed, then the optic was shifted by a few millimeter to avoid an influence of the old damaged spot and a new test run was performed (the setup is discussed in more detail in [62, p. 52]). Two in-house ion beam sputtering (IBS) coated highly-reflective (HR) mirrors were tested using 14 measurement points on each mirror. The coating was a quarter wave stack coating based on Ta_2O_5 and SiO_2 . For both optics, damage thresholds between 24 J/cm^2 and 43 J/cm^2 were measured (ignoring outliers). A commercially available IBS HR coating (*Layertec GmbH*) was also tested with damage thresholds between 35 J/cm^2 and 75 J/cm^2 (16 sample points, 360 μm focus diameter) [77, p. 18]. The large spread of measured damage thresholds supports the assumption that these damages are strongly influenced by local coating defects. The performance of the commercially available coating is even close to bulk fused silica ($\sim 40 \text{ J}/\text{cm}^2$ [68]), suggesting that a high performance low-index coating material like HfO_2 is only of minor importance for long pulse durations in the nanosecond regime. Most importantly the optics need to be free of defects.

However damages within the resonator have been frequently observed for fluences of about 6 J/cm^2 well below the measured thresholds. To exclude possible thermal stress on the coatings, an infrared camera was used to measure the temperature difference across the mirror during operation. The detected temperature difference of 3 K (110 roundtrips, 1 μJ seed, 1.2 kW pump power per disk, 5 kHz repetition rate, 530 W output power) is considered to be negligible in terms of thermal stress. A different explanation for the drastic decrease of the observed damage threshold is the influence of burst operation.

In contrast to optics used outside of the resonator, mirrors and windows used within a regenerative resonator are not affected by just one pulse but by a burst of N pulses with exponentially increasing energy (see equation eq. 2.10). In a simplified case with N pulses of similar energy, the damage threshold fluence J_{LIDT} for the total pulse burst was found to increase proportional to $J_{LIDT} \propto \sqrt{N}$ (pulse duration 200 ps, wavelength 1030 nm, pulse separation 1.9 ns) [78]. Compared to the scaling law of the damage threshold and pulse duration $J_{LIDT} \propto \sqrt{\tau}$, a pulse burst of N pulses seems to be approximated by a single pulse with N times the length and N times the energy of one pulse from the burst. Transferring this simple picture to a pulse burst with exponentially increasing energy requires the definition of an effective burst length N_{eff} . Assuming a worst case effective length $N_{eff} \approx E_{sum}/E_{out} = (1 - 1/G)^{-1}$ (eq. 2.13), that corresponds to an effective burst consisting of N_{eff} pulses with constant amplitude E_{out} and total energy E_{sum} , yields for the damage threshold

$$J_{LIDT} \propto (1 - 1/G)^{-\frac{1}{2}}. \quad (2.14)$$

Again assuming a realistic roundtrip gain on the order of $g \approx 1.1$ yields a factor $\sqrt{11}$ increase of damage threshold. However, the total pulse burst within the resonator carries 11 times more energy than the output pulse (eq. 2.13). Therefore a pulse that is around $\sqrt{11} \approx 3.3$ times below damage threshold outside the resonator can already cause optical damages within the resonator. With this scaling, the empirically determined threshold of 6 J/cm^2 is in good agreement with the expected worst case damage threshold around 20 J/cm^2 outside the resonator. For a pulse energy of 200 mJ this threshold implies a minimum beam diameter of about 3 mm for the resonator design (the resonator caustic is later presented in figure 2.18).

2.6 Thermal Distortions

As already discussed the disk temperature has an impact on the amplification properties [45] and high temperatures due to high pump powers can lead to unexpected results. Additionally due to the usage of thin-disks as mirrors, not only thermal lenses but also thermal deformations are imprinted on the phase of the laser beam leading to distorted beam profiles in the far field. To minimize these effects, low disk temperatures are crucial and a deeper investigation of disk temperatures is necessary. Thus a simple theoretical model for the disk temperature is deduced and compared to experimental values. This is followed by experimental observations that are explained by temperature induced distortions. A numeric model for thin-disk amplification was developed (see appendix B) that incorporates the dynamic behavior of thin-disk amplifiers beyond the simplified steady state picture of chapter 1.6. The temperature model is combined with the numeric model and compared to the experimentally obtained results from the amplifier system. The results suggest that the wavefront aberrations pose the main loss channel. Not only the disks are subject to thermal lensing but also the atmosphere and this section concludes with an analysis about heated air within the resonator.

2.6.1 Temperature Calculation

The heat flow within a thin-disk is mainly one dimensional and the temperature can be simply modeled by solving Fourier's law of heat conduction

$$q(z) = -k \frac{dT(z)}{dz} \quad (2.15)$$

with the heat flux density q , the disk thermal conductivity k , the temperature T and z being the dimension perpendicular to the disc surface. The dominant heat source is the difference between absorbed pump power and emitted laser power due to the quantum defect λ_P/λ_L (compare to section 2.3.2) or other loss channels η_N like nonradiative decay [79, 80]. For a uniform absorption in the medium with the fraction of absorbed power converted to heat being $\eta = 1 - \eta_N \lambda_P/\lambda_L$, the absorbed intensity being I_{Abs} and the intensity converted to heat being I_{heat} , the heat flux density q is defined by

$$I_{heat} = \eta I_{Abs} \quad (2.16)$$

$$\frac{dq(z)}{dz} = \frac{I_{heat}}{H}. \quad (2.17)$$

I.e. the increase of heat flux per unit length corresponds to the absorbed intensity per unit length. Defining $z = H$ as the position of the free-space thin-disk surface and assuming a negligible heat flux on that surface (i.e. $q(H) = 0$) yields

$$q(z) = I_{heat}(z/H - 1). \quad (2.18)$$

With $T(0) = T_0$ being the temperature on the cooled thin-disk surface, eq. 2.15 can be solved

$$T(z) = T_0 + \frac{I_{heat}}{k} \left(z - \frac{z^2}{2H} \right). \quad (2.19)$$

In the following numeric calculations, the average temperature within the thin-disk is used as approximation to an effective uniform crystal temperature

$$T_{avg} = \frac{\int_0^H T(z) dz}{H} = T_0 + \frac{I_{heat} H}{3k}. \quad (2.20)$$

The maximum temperature that can be measured on the disk surface is

$$T_{max} = T(H) = T_0 + \frac{I_{heat} H}{2k}. \quad (2.21)$$

For diamond heatsinks, the temperature T_0 equals the temperature of the cooling water in good approximation. Assuming a complete absorption of pump power $I_{Abs} \approx I_{Pump}$, a thermal conductivity of $k \approx 6 \text{ W}/(\text{m K})$ [81] and using the power loss parameter η as fit parameter with typical values around $\eta \approx 0.1$ yields reasonably good results for the calculated disk temperature.

While these equations are sufficient for most applications, more precise results are obtained when the temperature and doping dependence of the thermal conductivity k and the absorbed pump light I_{Abs} are factored in. For Yb:YAG with a doping concentration c_{Yb} , the thermal conductivity is given by [81]

$$k(T, c_{Yb}) = (7.28 \text{ W}/(\text{m K}) - c_{Yb} 7.3 \text{ W}/(\text{m K})) \left(\frac{204 \text{ K}}{T - 96 \text{ K}} \right)^{0.48 - 0.46 c_{Yb}}. \quad (2.22)$$

At the same time, the absorbed pump intensity I_{Abs} and consequentially the intensity converted to heat I_{heat} is also sensitive to temperature changes [45] and is given by (compare to equation 1.126)

$$I_{Abs}(T) = I_{Pump} (1 - \exp[-L\alpha(T)]) \quad (2.23)$$

$$\alpha(T) = [\sigma_{eP}(T) + \sigma_{aP}(T)] N_2(\infty, T) - c_{Yb} \sigma_{aP}(T) N_+, \quad (2.24)$$

where $N_2(\infty, T)$ represents an approximation to the the excited level population density by using the steady state solution from the numeric model (see equation B.7). The temperature dependencies of the cross sections σ_{eP} and σ_{aP} are given in [45]. The intensity converted to heat I_{heat} is then calculated using eq. 2.16 and the average temperature T_{avg} within the crystal is determined by numerically solving the temperature dependent equation 2.20

$$T_{avg} = T_0 + \frac{\eta I_{Abs}(T_{avg}) H}{3k(T_{avg})}. \quad (2.25)$$

The maximum temperature is accordingly given by the reformulating eq. 2.20 and 2.21

$$T_{max} = \frac{3}{2}(T_{avg} - T_0) + T_0. \quad (2.26)$$

The validity of the temperature model was confirmed by a temperature measurement of an undepleted pumped disk. Different pump wavelengths and powers as well as different disk thicknesses were used and the disk surface temperature was tracked using an infrared camera (*FLIR Systems Inc.*). The results are shown in figure 2.13. Excellent agreement between theoretical prediction and the measured values is observed. This indicates the validity of the one dimensional heat flow model. Also the predicted cooler surface temperature for 969 nm pump light is confirmed.

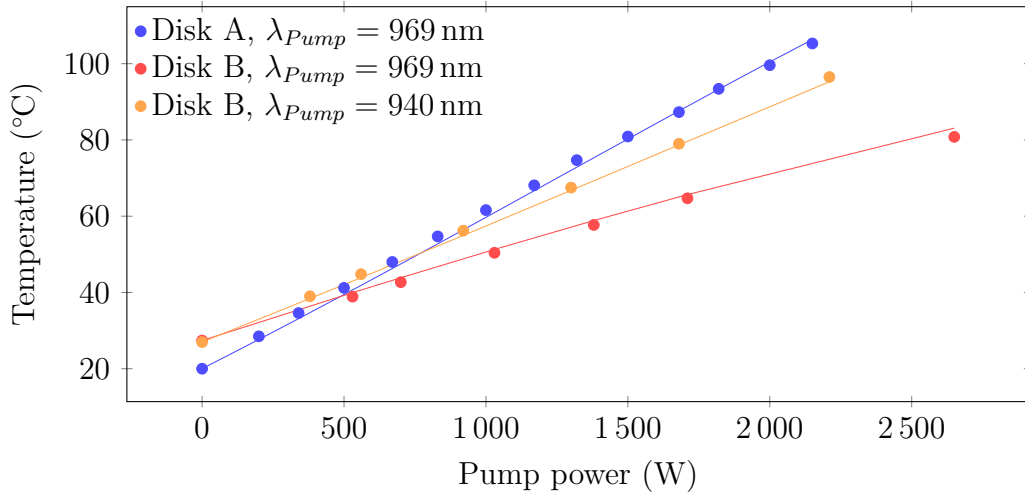


Figure 2.13: The measured and predicted (solid lines) disk temperature for different thicknesses and pump wavelengths. The efficiency drop due to nonradiative decays was assumed to be $\eta_N \approx 0.942$, which is in accordance to published values [79, 80]. *Disk A* is roughly 60% thicker than *Disk B*.

2.6.2 Thermally Induced Wavefront Aberrations

The temperatures of thin-disks can reach values beyond 100°C if operated with a room temperature coolant. This drastic temperature increase in the pumped area has two major consequences. First of all the disk can deform itself by thermal expansion in the pumped region or due to strain induced by the temperature difference between the cooled backside and the front [21]. Secondly the high temperature increase causes a shift of the refractive index following the parameter dn/dT that changes the optical path length through the disk. Both effects manifest as wavefront aberration of the laser beam and therefore coupling into higher order modes and finally increased losses if the mode is filtered e.g. by a resonator [74, 82].

This effect is one of the main reasons why cooler disk temperatures are highly desirable. Figure 2.13 clearly shows that a pumping scheme based on a wavelength of 969 nm leads to lower temperatures and is therefore expected to yield a better system performance. Unfortunately active wavelength stabilization is necessary in case of 969 nm based pumping due to the narrow absorption bandwidth of Yb:YAG in this region and corresponding pump lasers are more costly. To test the influence of the pump scheme on the amplifier output, a seed with an energy of $1\ \mu\text{J}$ was amplified over 111 roundtrips using a 940 nm and a 969 nm based pumping scheme with a pump spot diameter of 7 mm. The results are depicted in figure 2.14. As expected, higher output powers and slope efficiencies can be reached based on a 969 nm pumping scheme. A divergence from the linear behavior is seen for higher pump powers indicating the onset of nonlinear loss channels like aspherical wavefront aberrations.

The sensitivity of a laser system for spherical aberrations can be reduced by proper resonator design (section 1.3.6) or simply by (pre-)compensating the spherical wavefront shift with appropriate spherical optics [27]. For Yb:YAG thin-disks with

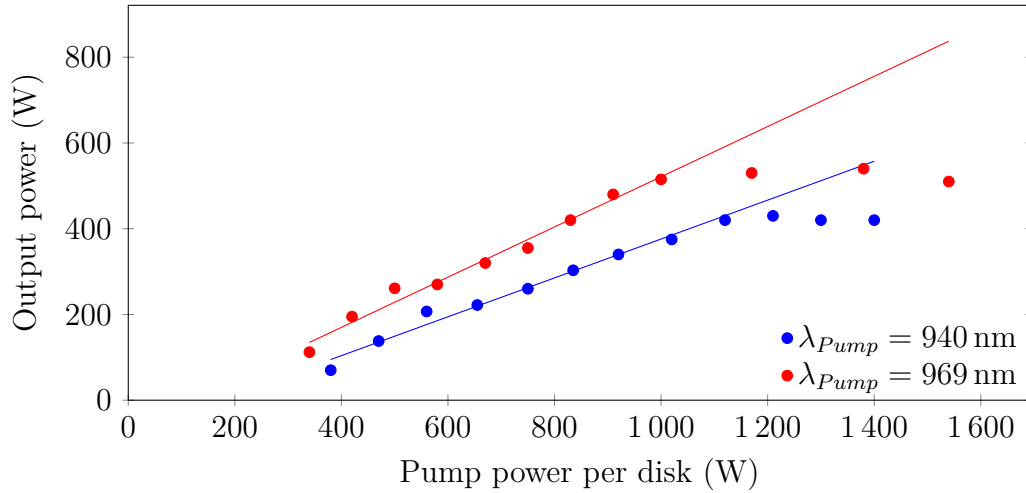


Figure 2.14: The output power of the system for 111 roundtrips and 1 μ J seed energy for a pump wavelength of 940 nm and 969 nm. A linear fit through the first 8 measurement points (solid lines) yield a slope efficiency of 30% (969 nm) and 23% (940 nm).

a diamond heatsink, these spherical aberrations are estimated to be smaller than

$$\frac{f^{-1}}{I_{pump}} \leq -8 \times 10^{-3} \text{ dpt}/(\text{kW}/\text{cm}^2) \quad (2.27)$$

for 969 nm pumping [27].

Compensation of aspherical aberrations is more complex and either requires tailored [82] or deformable [74] optics that reverse the aberration for each pass over the disk. These optics have to be placed into the beam path with an accuracy of a few hundred micrometer [82] and pose an added constraint for the laser alignment. This is especially challenging for high average power systems where the mode shifts during thermalization due to the movement of optomechanical components or atmospheric effects [83]. Since the shape of the wavefront aberration approximately follows the pump profile and steep edges represent a strong deviation from a spherical shape, the usage of a diffuse pump profile with smooth edges can also lower the aspherical contribution [82]. Due to its simplicity and robustness, this method is implemented in the presented amplifier system.

To this end the imaging system of the pump multipass (see figure 2.7) is misaligned to reach a diffuse pump profile on the disk. The original pump spot on the disk was a flat-top with 7 mm diameter. Then a collimation lens was misaligned by 6 mm to create a diffuse pump spot. The top-hat like pump profile of the original alignment and the diffuse more Gaussian-like pump profile of the misaligned setup are depicted as insets in figure 2.15.

Figure 2.15 also shows how severe the losses induced by the wavefront aberrations are. A 1 μ J seed was amplified over 60 roundtrips at 10 kHz repetition rate and the corresponding output power was tracked. A numerical simulation assuming 3.5% losses per roundtrip is shown for comparison. Both experimental curves show significantly lower output powers than expected by the simulation (appendix B). The decrease of output power is especially pronounced in case of a flat-top pump spot with

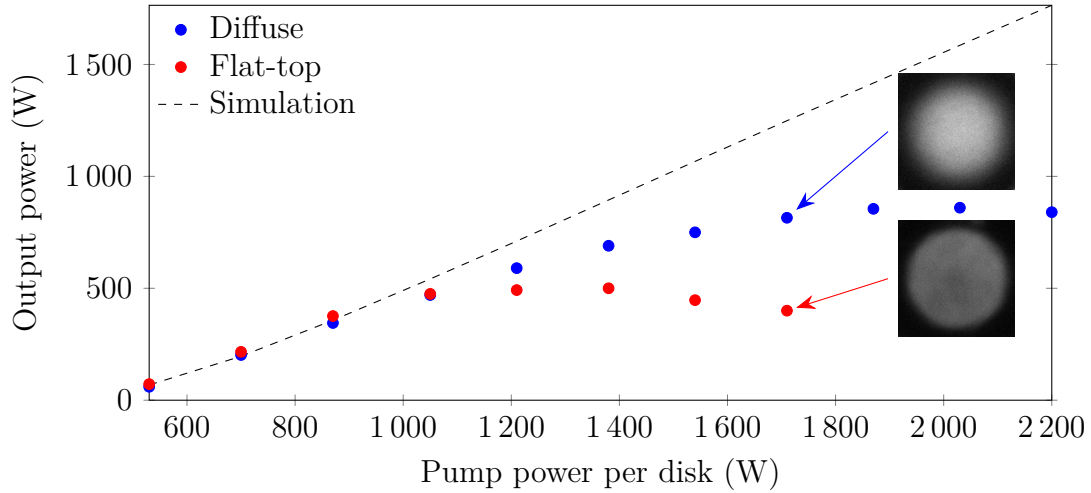


Figure 2.15: The output power of the system for 60 roundtrips and $1 \mu\text{J}$ seed energy for a flat-top and a diffuse more Gaussian-like pump spot. The expected output power according to numerical simulations (appendix B) is shown for comparison. The insets show the corresponding pump profiles.

step edges. Softer edges yield output powers closer to the numerical expectations. Very similar results are obtained in [74]. These differences are discussed in more detail in the following section.

2.6.3 Comparison to the Numeric Model

The measured and simulated data show a significant disagreement (see figure 2.15). However the disagreement is reduced in case of more Gaussian like pump spots.

In a consistency check for the numeric model, the experimental small signal gain for an input energy of $E_{In} \approx 5 \mu\text{J}$ and a pump spot diameter of 7 mm is compared to the simulated value. The small signal gain is the gain for one pass over one disk assuming that the signal is weak enough to neglect the depletion of the disk. This gain is not influenced by wavefront aberrations or resonator dynamics. Due to the higher upper level population density of this experiment, amplified spontaneous emission is expected to have a stronger impact compared to the amplification in a resonator. The results for the experiment and the simulation are shown in figure 2.16a. The simulated gain tends to be lower than the average experimental gain as expected by the worst case approximation for ASE in the numeric model (equation B.3). Nevertheless simulation and experiment are in good agreement.

This leads to the hypothesis that the observed disagreement in figure 2.15 is indeed solely caused by wavefront aberrations at high pump powers. To test this hypothesis, the numeric model is applied to a wavefront aberration compensated continuous wave laser published in [74]. The continuous wave laser is approximated by a high repetition rate laser with a period time much shorter than the material lifetime ($f_{rep} \approx 100 \text{ kHz}$) and a low power seed ($P_{In} \approx 1 \text{ W}$). The extracted power ideally equals the absorbed pump power compensated by heat generation in the disk, (amplified) spontaneous emission and roundtrip transmission \mathcal{T}_1 . If \mathcal{T}_1 is chosen correctly, the output power should be similar in the continuous and pulsed case. A

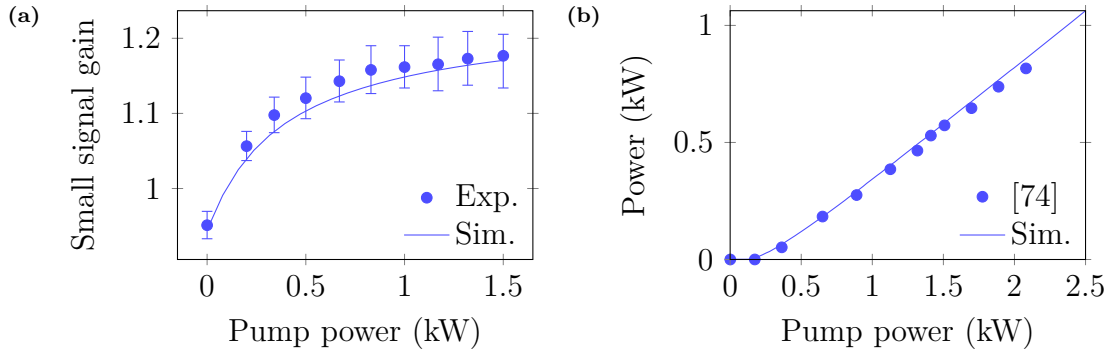


Figure 2.16: (a) The measured small signal gain of a thin disk compared to the small signal gain simulated by the numeric model. The error bars show the minimum and maximum gain based on a 2.5 min long observation. (b) The output curve of the continuous wave laser published in [74] compared to the result of the numeric model for a high repetition rate multipass amplifier.

common doping density of $c_{Yb} \leq 12$ at.% [58] and a transmission of $\mathcal{T}_1 \approx 98\%$ is assumed. The result is shown in figure 2.16b and shows excellent agreement. This indicates that the model replicates the gain dynamics within the amplifier correctly. The wavefront compensation is a key difference between the measurement shown in figure 2.15 and the measurement shown in figure 2.16b. Without the wavefront compensation, a severe drop of output power is observed in [74]. Thus the hypothesis that wavefront aberrations are the main source for the disagreement between the model and experiment is supported.

A consequence of this statement is that, under the assumption of an optimized amplifier working point (section 2.4), a further increase of output energies for the presented amplifier system almost exclusively relies on methods that reduce or compensate the wavefront aberrations. Methods for compensation were previously discussed and Gaussian-like pump spots were demonstrated to reduce aberrations (see section 2.6.2).

The heated disk medium obviously plays a major role as aberration source and further cooling optimizations or the usage of a gain medium with higher robustness against thermal loads can also lead to significant improvements in output power. A thorough comparison of gain media was previously performed (section 2.3.3) and finding a medium with a significant improvement compared to Yb:YAG is challenging. Also the disk was shown to have an almost perfectly linear heat flow (section 2.6.1) and the temperature is mainly determined by the thickness of the medium. Further cooling optimizations seem unlikely as the cooling properties of the currently used thin-disk concept are close to ideal.

Not only the disk can introduce aberrations but also the atmosphere within the amplifier can heat up and create a potential distortion source [84]. This is investigated in more detail in the next section.

2.6.4 Impact of Air

Apart from thermal lenses or temperature induced surface distortions of the disk, the atmosphere that is used within the amplifier has an influence on wavefront

aberrations. In the following some atmospheric effects are explained in more detail using the example of air as the amplifier's atmosphere. Most effects are induced by power absorption in air with the dominant absorber being water vapor for the region between 0.5 μm and 1.3 μm [85]. Although the absorption of air is relatively small ($\alpha = 0.139/\text{km}$ for 58 % r.H., [85]), it can cause significant heating considering the high average powers within the resonator. Another heat source is the active gain medium that is partially cooled by its surrounding air. Any effect caused by heating of air is therefore especially pronounced in the vicinity of the gain medium.

Heating yields air movements due to convection which might in return lead to laser instabilities and resonator misalignment with a typical upward shift of the eigenmode [83]. As long as these air movements are undisturbed and approximately laminar [84], they can be compensated by resonator realignment and their contribution to pointing is often overshadowed by other noise sources. This requires careful shielding from environmental influences like laboratory ventilation.

Another distortion by heated air results from thermal lensing. Air has a negative temperature coefficient of the refractive index $dn/dT \approx -1 \times 10^{-6}/\text{K}$ (632.8 nm, 1 bar, 0 % r.H. [86]). A Gaussian intensity profile consequentially yields an optical element with a intensity dependent reduced optical path towards the center of the beam. This corresponds to a concave lens with a linearly intensity dependent dioptric power [87]. This thermal concave lens with a Gaussian-like refractive index change does not represent a perfect parabolic lens and therefore induces mode distortions that are converted to losses by the amplifier's mode cleaning capability. The concave lens also has an impact on the eigenmode of the resonator. Numerical calculations have shown that the eigenmode becomes larger at every single position if an atmospheric concave thermal lens is present. Reliable quantitative statements require a more thorough simulation incorporating laser geometry, heat flux, exact absorption values and air movements beyond the scope of this thesis.

With water vapor being the dominant absorber of air, the humidity provides a degree of freedom that controls the heating properties of the amplifier mode. The refractive properties of air stay virtually constant over different humidities [86, 88] and thermal lens effects near the gain medium show no strong influence of water vapor [84]. Therefore any mode changes versus humidity can with high certainty be attributed to heating by laser absorption. A low humidity will yield smaller eigenmodes but less absorption and thermal lensing. Low humidities also have the potential to lower the damage threshold of optics [89]. High humidities are presumably enhancing the damage threshold of optics and lead to bigger eigenmodes, therefore putting the optics in total to a lower damage risk with the cost of increased mode aberrations.

The influence of absorption to the mode size was experimentally investigated. A silicon based beam profiler (*WinCAM* from *DataRay Inc.*) tracked the beam size in an optical distance of about 1.5 m after the amplifier output. Each disk was pumped with 1.2 kW and a seed energy of 200 μJ was amplified over a varying amount of roundtrips – one time with a low humidity environment with about 2% r.H. and a second time with typical lab humidity around 37% r.H.. The disk curvature can be assumed to stay approximately constant as the pump power is not changed. As expected a higher damage probability was observed in the dry atmosphere, which is

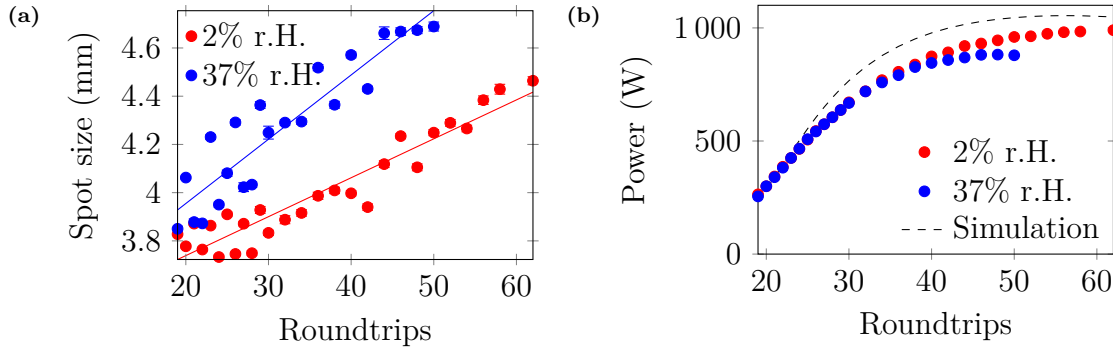


Figure 2.17: (a) The $1/e^2$ beam diameter versus the roundtrip number for different humidities together with linear fits (solid lines). (b) The output power versus the roundtrip number for different humidities. Additionally plotted is the simulated output for 2% roundtrip losses, a pump spot of 7 mm and a mode diameter of 6.3 mm on the disks.

why these experiments were done with a repetition rate of 10 kHz and lower fluences while providing the same average power. The results are shown in figure 2.17a. The beam size increases in both cases, which can be explained by some residual heating of the atmosphere, a thermal lens in the Pockels cell crystals or higher order lenses created by a partially depleted disk. However in case of the more humid air, the beam size increases 66% faster. As previously explained, this change is attributed to a thermal lens created by heated air. The spot size oscillations visible in figure 2.17a are later discussed in section 2.7.1 and originate from non-perfect mode-matching between the amplified mode and the eigenmode.

The presence of a nonlinear thermal lens indicates an additional source of wavefront aberration. Wavefront aberrations are known to cause significantly lower output powers (see section 2.6.2). Hence a dry air environment is expected to reach higher output powers. This is confirmed in figure 2.17b, which shows the output power over the roundtrips, yet the higher output power requires to operate the amplifier at a working point with increased damage probability.

Another source of wavefront aberrations – the heating of the disk – is enhanced by heated gas in front of the disk [84]. The thermal lens in front of the gain medium is mainly governed by the refractive index temperature coefficient dn/dT of the atmosphere used in the amplifier. Atmospheres with low temperature coefficients like helium or vacuum can reduce these thermal effects [84]. However in a helium atmosphere [67] or vacuum [90, p. 38], the voltage applied across the Pockels cell crystal is likely to cause breakdowns (see section 2.3.4). In that case the high voltage and consequentially the Pockels cell has to be put into a different atmosphere with optical windows within the resonator adding two transmissive optics and four more reflection surfaces.

During standard operation the presented amplifier is used in atmospheric air with a typical humidity around 40%. For the implemented resonator a lower probability of damages was observed for a high humidity at the cost of a slightly lowered output power. The atmospheric air environment also enables a simplified setup with less transmissive optics as well as easier maintenance and accessibility.

Electro-optical nonlinear effects in the atmosphere like the Kerr effect only have minor influence on the amplifier's performance as long as the pulses are sufficiently stretched (see section 2.2). They are therefore not further investigated in this context, but a more detailed analysis can be found in [62, p. 62].

2.7 Design Optimization

The previous sections presented some deeper insight into the behavior of thin-disk amplifiers. The knowledge about limiting properties, for example the high average power within the resonator or the sensitivity to wavefront distortions, enable an optimization of the design that renders the impact of these properties less significant. The high thermal load is connected a movement of the eigenmode due to moving mechanical components or the impact of air. The changing wavefront calls for a resonator that is robust against potential focal length shifts within the resonator. The following section introduces a resonator design that is optimized for largest robustness against focal length shifts while still providing a reasonably good mechanical robustness and large beam diameters for low damage probabilities. The mechanical robustness is further optimized by discussing mechanical designs and cooling possibilities that keep the potential misalignment due to thermal movements to a minimum.

2.7.1 Resonator Design

A well designed regenerative amplifier has an eigenmode at which it operates with maximum efficiency. Therefore the trapped pulse will converge towards this eigenmode after sufficient amplification. This provides high mode quality and beam stability.

The resonator for the high average power amplifier should have an eigenmode with large beam diameters (ideally above 3 mm) on all optics to avoid damages. Since the amplification is done in atmospheric air, a focus within the resonator needs to be avoided to prevent plasma formation. The Pockels cell has to be placed in a low divergence segment of the resonator with a beam diameter as large as possible but small enough to avoid clipping in the 12 mm aperture given by the crystal. Reasonable beam diameters for this case are 3 mm to 5 mm with a maximum beam divergence of less than 0.5° [91]. Two disks are necessary for sufficient energy extraction, a high roundtrip gain and low intracavity average power. To allow some breathing, misalignment, thermal lensing and eigenmode changes, the resonator is designed to have an eigenmode spot diameter on the disk of 5.5 mm, which is roughly 80% of the pump spot diameter. This spot diameter was empirically confirmed to yield good results by slightly changing resonator distances of the final resonator in order to increase or decrease the beam diameter and evaluating the results.

The disks are kept in short propagation distance to each other such that any angular shift of the beam on one of the disks does not introduce a severe misalignment on the second disk and a single angular correction by a motorized mirror in close

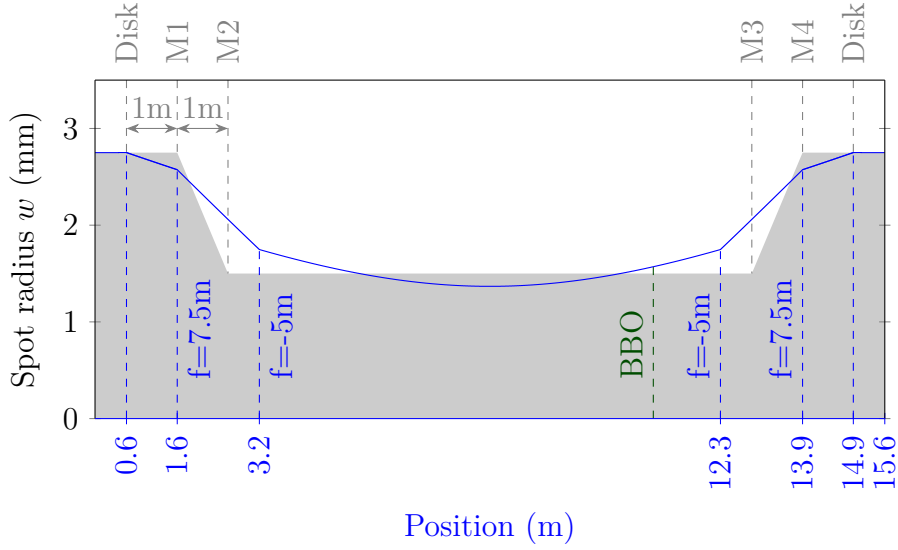


Figure 2.18: The resonator of the proposed amplifier at a disk curvature of 30 m. To accumulate the required Gouy phase in a short propagation length, the beam size must decrease as soon as possible. The distance between the curved optics is limited by physical constraints to values bigger than 1 m. A best case resonator (schematically drawn in gray) therefore decreases the beamsize as soon as possible after the approximately flat disk with the telescope mirrors M1 and M2 to reach the targeted minimum radius of 1.5 mm. The numerically optimized real resonator is shown in blue and approximates the shape of the best case resonator based on actual Gaussian propagation and available optics while providing a Gouy phase of $\Delta\zeta_{eig} \approx 0.55\pi$.

proximity can compensate distortions caused by both disks. The resonator is designed to be symmetric around a plane between both disks to guarantee equal spot sizes on both disks independent of any resonator distortions (e.g. caused by thermal lenses). The disk radius of curvature is approximately 20 m (concave). Due to thermal lensing, the effective radius of curvature tends to flatter values for higher pump powers. For a pump intensity of 4 kW/cm^2 , the disk's effective radius of curvature is assumed to be 30 m. To avoid a buildup of wavefront distortions and keep the resonator reasonably short and stable, the Gouy phase of the ring resonator is designed to approach $\Delta\zeta_{eig} \approx 0.55\pi$ with increasing pump power (compare to figure 1.6). Note that the resonator ABCD matrix is then fully determined by the fact that $R_{in}^{-1} = R_{out}^{-1} = 0$ (due to symmetry), $\Delta\zeta_{eig} \approx 0.55\pi$ and $w_{in} = w_{out} = 2.75 \text{ mm}$ (compare to eq. 1.35 - 1.38).

Figure 2.18 shows a best case resonator in gray according to the constraints. This best case is simply deduced by the requirement to accumulate a maximum amount of Gouy phase (i.e. to keep the beam diameter small where possible) while ensuring a certain beam diameter on the disks, a minimum diameter for the optics and a minimum distance between optics. This yields the most compact resonator for a given set of parameters and compactness is necessary for maximized robustness. With this technique a general resonator shape is determined consisting of two equal telescopes $M1/M2$ and $M3/M4$.

A resonator based on standard components is numerically calculated to match the deduced best case resonator. To this end a list with all permutations of standard

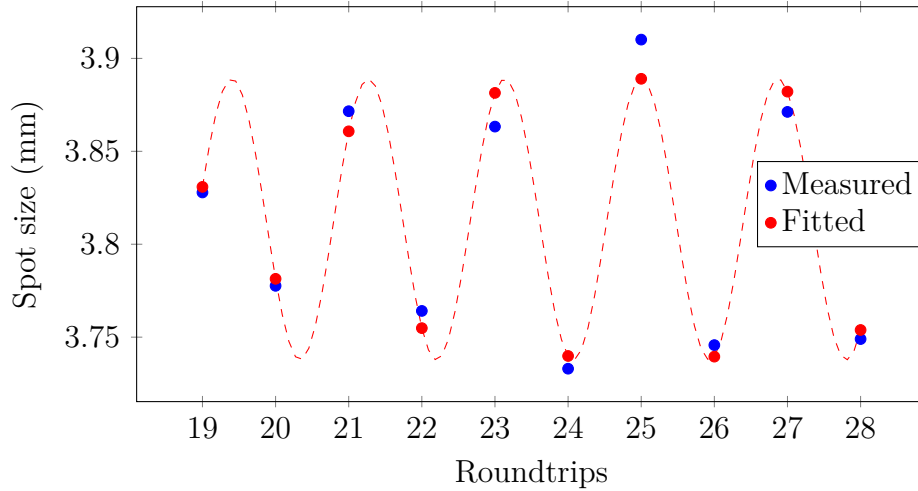


Figure 2.19: The measured output spot size (blue) of the resonator for a repetition rate of 10 kHz and a pump power of 1.2 kW per disk. Additionally a fit according to equation 1.59 with a fitted Gouy phase per roundtrip of $\Delta\zeta_{eig,RT} \approx 0.54\pi$ is shown (red). The output power increases from 264 W (19 roundtrips) to 574 W (28 roundtrips) during the measurement. A dashed sine is plotted as guidance.

concave and convex focal lengths is created that corresponds to a complete set of telescopes that can be build with standard optics. The distance between the two disks is minimized to a physically buildable value of 1.2 m and the telescope is placed as close to the disks as possible in a distance of 1 m. These constraints ensure that the segment with a large beam diameter stays as short as possible. The missing free parameters for a given telescope are then the distance between the telescope mirrors $M1 \rightarrow M2$, the propagation distance $M2 \rightarrow M3$ and the second telescope distance $M3 \rightarrow M4$. Only a single set of these three distances leads to the previously determined resonator ABCD matrix. Thus these distances are uniquely defined if a certain resonator ABCD matrix and telescope is given. By iterating over all standard telescopes, a telescope can be selected that provides the largest minimum beam diameter and feasible mirror distances > 1 m. This resonator is the optimized resonator with a caustic shown as blue curve in figure 2.18.

The Pockels cell crystal is placed in the slowly diverging part of the central propagation with a beam diameter of about 3.5 mm. While this value is critical for damage threshold considerations, small diameters at the crystal help to increase the system's robustness, simplify alignment and ensure reproducible output powers. Also the final spot sizes are expected to be slightly larger due to a thermal lens introduced by heated air as previously discussed in section 2.6.4. The length of the central propagation is experimentally optimized by shifting a mirror to yield maximum output power. This experimental adjustment is necessary due to some uncertainties in focal lengths and system distances.

In order to test the correct implementation of the calculated resonator, the evolution of the spot size with increasing roundtrips was measured. Each disk was pumped with 1.2 kW to simulate full operation without risking a damage of the undepleted disk and the humidity within the resonator was lowered to about 2% to avoid absorbance and thermal lensing in air. A silicon based beam profiler (*WinCAM*

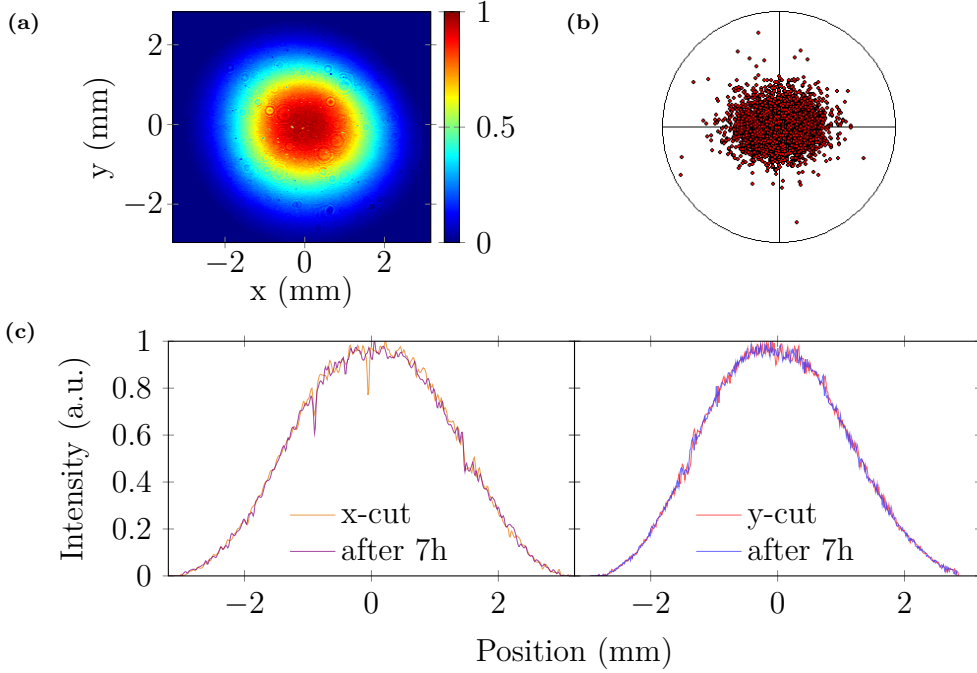


Figure 2.20: Different stability measurements done during the measurement shown in figure 2.3. (a) The beam profile measured about 1.5 m after the exit of the main amplifier resonator. The e^{-2} beam diameters were 4.2 mm for the minor and 4.7 mm for the major axis (mean is 4.5 mm). (b) The wandering of the beam profile. 8182 samples were taken over approximately 20 min. The circle radius is 150 μm , the measured standard deviation from the center was 30 μm . (c) The beam profile is cut through its center along the x and y axis and the values along the cuts are shown in two graphs. The original cuts show the profile after thermalization. Additionally shown are the profiles after 7 h of continuous operation.

from *DataRay Inc.*) measured the beam size about 1.5 m after the amplifier's output and the spot size was determined based on an effective diameter according to [92, p. 22] as approximation to the $1/e^2$ diameter. The measured spot size should ideally follow equation 1.59. With each roundtrip, the phase $\Delta\zeta_{eig}$ is increased by the accumulated Gouy phase of a single roundtrip. Hence fitting equation 1.59 to the measured spot sizes using $\Delta\zeta_{eig} = N\Delta\zeta_{eig,RT}$ (Roundtrip number N and roundtrip phase $\Delta\zeta_{eig,RT}$) yields a measurement of the design parameter $\Delta\zeta_{eig,RT} \approx 0.55\pi$. The result is shown in figure 2.19 and Gouy phase per roundtrip $\Delta\zeta_{eig,RT} \approx 0.54\pi$ very close to the design target was measured.

The output characteristics reached with this resonator show very favorable properties. A high spatial stability is observed and the resonator mode is virtually constant over a period of over 7 h. The beam profile and its wandering characteristics are depicted in figure 2.20. The position stability close to the amplifier was measured to be below 0.7% relative to the beam diameter. Both the beam profile and the wandering pattern show a circular profile, hence no axis is preferred over another. It was previously theoretically predicted that large beam resonators show low angular pointing (see paragraph *Shift of Eigenmode Position* in section 1.3.6). This is in congruence with the observation that the output beam shows no dramatic decrease of position stability even if propagated over more than 10 m.

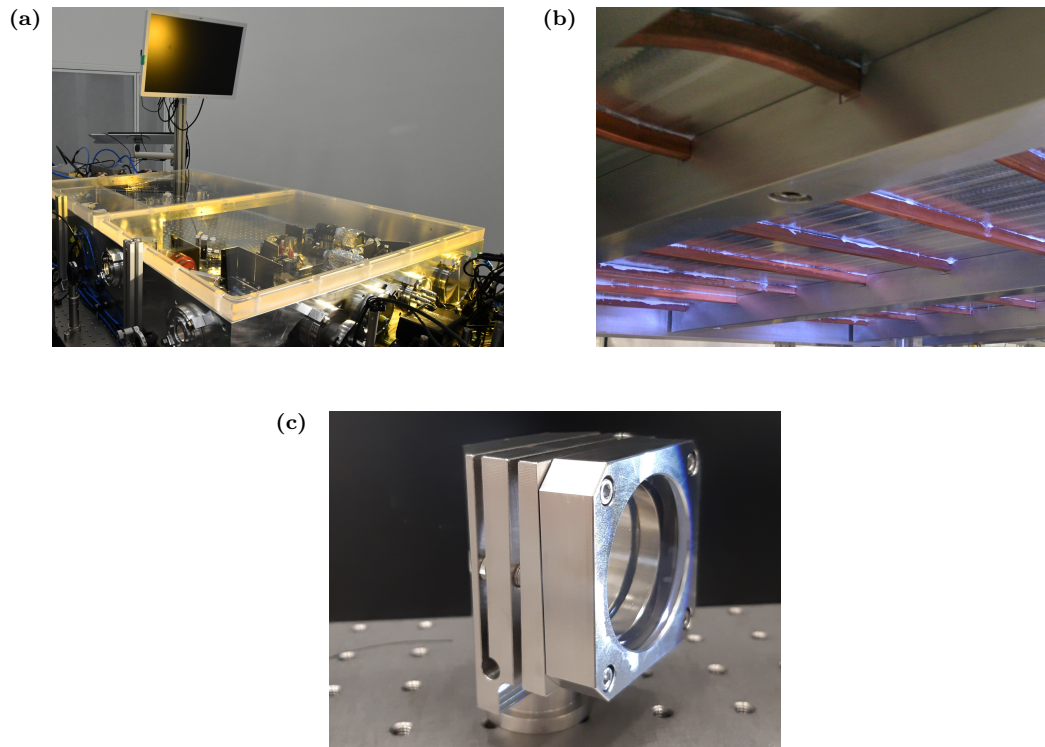


Figure 2.21: (a) Amplifier setup with a monolithic aluminum housing. (b) Water cooling pipe attached to the baseplate. (c) Exemplary flexure mirror mount.

Figure 2.20c shows the profile change over a period of 7 h. No significant changes are observed and the profile can be assumed to stay constant after thermalization of the amplifier is reached. This property is especially important for any following multipass setups that require excellent mode stability for reliable mode matching into the systems.

2.7.2 Mechanical Design

A stable resonator has been deduced in the previous section. While a robust reaction to distortions is important, these distortions can be prevented in the first place by using a stable mechanical design.

To this end the laser is built into a monolithic aluminum housing (depicted in figure 2.21a) that is kept close to room temperature by a water cooling pipe attached to the baseplate (figure 2.21b). The monolithic design ensures that movements induced by repeated heating and cooling cycles do not cause a different rest position and the alignment is highly reproducible from day to day. The same idea is implemented for the mirror mounts. Monolithic stainless steel flexure mounts are used where possible (design by *TRUMPF Scientific Lasers GmbH + Co. KG*, a similar mount is shown in figure 2.21c). The mirrors are mounted from their front surface using a spring loaded system to avoid bending moments.

A direct water cooling of these mirror mounts was tested but caused a movement of the flexures that followed the coolant temperature. To avoid the mode instabilities induced by this movement, no direct mount cooling is implemented and the mirror

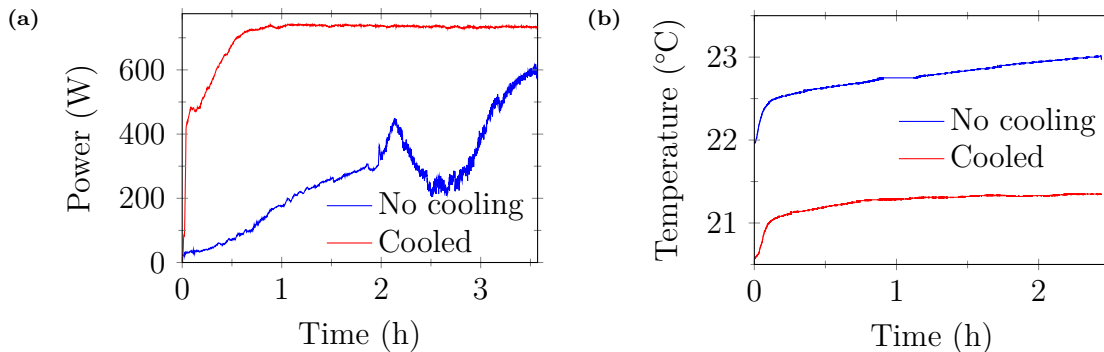


Figure 2.22: (a) The warmup curves of the amplifier for an output power of ~ 700 W with ($50 \mu\text{J}$ seed energy, 38 roundtrips) and without ($200 \mu\text{J}$ seed energy, 32 roundtrips) a water cooled housing. The pump power per disk was 1.2 kW and the repetition rate 10 kHz . No realignment was done during the warmup. (b) The housing temperature with and without water cooling during the warmup towards an output power of 700 W with a seed energy of $200 \mu\text{J}$ and 32 roundtrips. A short sensor failure is visible after about one hour in the uncooled reference.

mounts are kept at low temperatures by carefully shielding them from any stray light with water cooled anodized aluminum apertures. Water cooling is also applied to the mounts of the Pockels cell crystals. Water tubes made out of Perfluoralkoxyalkan (*Festo AG & Co. KG*) ensure that no water evaporates and increases the humidity within the chamber. Typically a coolant temperature of 20°C is used.

To test the effectiveness of the applied water cooling, two measurements where the amplifier has been aligned to an output power of roughly 700 W on the previous day are compared. The repetition rate is 10 kHz and the pump power per disk 1.2 kW . The uncooled reference used a seed energy of $50 \mu\text{J}$, and 38 roundtrips, the cooled reference was measured under slightly different conditions with a seed energy of $200 \mu\text{J}$ and 32 roundtrips. The amplifier was turned on and its warmup towards the final output power was measured. The comparison is shown in figure 2.22a. In case of the uncooled reference, the measurement was aborted after approximately 3.5 hours since no thermalization could be reached and only a manual realignment enabled an output power of 680 W. The active cooling of the housing led to significantly faster thermalization and the previous output power was reached within slightly more than one hour.

A comparable behavior is seen by tracking the temperature within the housing during a similar warmup to 700 W ($200 \mu\text{J}$ seed energy, 32 roundtrips 10 kHz repetition rate and 1.2 kW pump power per disk). A temperature sensor (*Sensirion AG SHT2x*) is placed into the housing with no direct contact to the aluminum and shielded from possible stray light. As can be seen in figure 2.22b, the temperature saturates at about 21.4°C after slightly more than one hour if the housing is actively cooled. If this cooling is removed, no saturation is visible even after 2.5 hours. This stresses the importance of active cooling to minimize the temperature increase and therefore possible misalignment due to thermal cycles. Also active cooling significantly improves the thermalization time.

Unfortunately active water cooling creates a coupling between the coolant temperature and the output power of the system. Due to the slow response of the

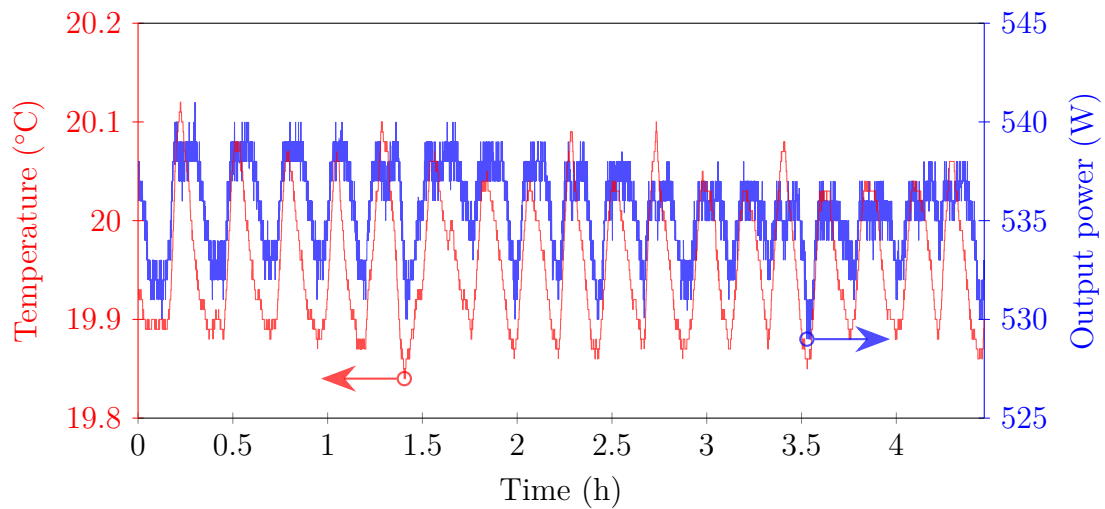


Figure 2.23: The output power of the amplifier in comparison to the the measured coolant temperature of the housing. 100 μJ were amplified to 500 W at a repetition rate of 5 kHz over 32 roundtrips using a pump power of 1.2 kW per disk.

housing, this coupling is less significant than in the case of directly cooled flexure mounts. To quantify this coupling, a 100 μJ seed was amplified to about 500 W at 5 kHz repetition rate within 32 roundtrips and a pump power per disk of 1.2 kW. After thermalization, a measurement of the output power and of the housing coolant temperature was started simultaneously. The cooling water temperature was measured by placing a high resolution temperature sensor (*Greisinger GMH 3750*) into the output of the used chiller. The measurement is depicted in figure 2.23 and shows a clear correlation between the output power and the coolant temperature. A peak to peak instability of almost 1% can be explained by the influence of the cooling water. The oscillation of the cooling water arises from the chiller constantly compensating the temperature drifts of the laboratory process water. Since the process water is used as coolant for the chiller, temperature drifts are directly imprinted on the performance of the chiller. The exact pattern of the temperature change is therefore subject to change from day to day depending on the performance of the process water. The temperature feedback control of the used chiller is limited in its resolution to $\pm 0.1^\circ\text{C}$, which is why the water temperature oscillates within these boundaries. A significantly higher output stability of the amplifier is expected if the stability of the cooling temperature can be improved. However a stability of $\pm 0.1^\circ\text{C}$ is currently state of the art for high power chillers with a cooling capacity beyond 1 kW and better stabilities are not commercially available.

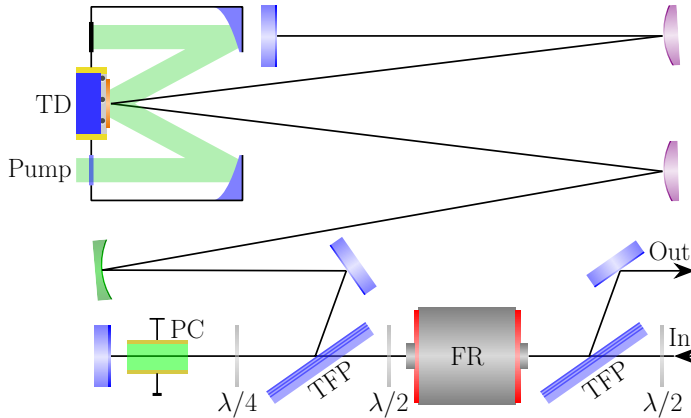


Figure 2.24: The schematic layout of the preamplifier. The input beam from the oscillator (labeled *In*) is sent through an optical diode for the separation of input and output consisting of a thin film polarizer (TFP), a Faraday rotator (FR) and a half wave plate ($\lambda/2$). It is coupled into the linear-type resonator by an arrangement of a TFP, a BBO based Pockels cell (PC) and a quarter wave plate ($\lambda/4$). A thin-disk (TD) pumped by a 940 nm diode laser with up to 140 W of average power (*Jenoptik JOLD-140*) is used for amplification. The resonator is formed by two convex (violet) and one concave (green) mirrors. The output is finally labeled *Out*.

2.8 Preamplifier

As has been discussed in section 2.4, the amplifier chain benefits from a preamplification stage that provides seed pulse energies in the millijoule range for the main amplifier. For this reason a small (footprint $0.75 \times 0.45 \text{ m}^2$) preamplifier was developed. It is an Yb:YAG thin-disk regenerative amplifier with a linear resonator as schematically depicted in figure 2.24. The usage of the thin-disk concept allowed the usage of available components and the straight forward adaption of optimization techniques.

Due its low target output power of less than 10 W, a linear resonator with an implicit double pass over the disk and through the Pockels cell could be implemented. The resonator was chosen to be longer than 4 m for a roundtrip time above 25 ns in order to provide enough time for the Pockels cell to switch. For the same reason the Pockels cell is placed close to one end mirror. The output of the resonator is virtually perfectly collimated by choosing a flat end mirror close to the outcoupling. A pump spot size of 3 mm is created by 36 passes of 940 nm pump light over the disk, which has a concave radius of curvature of 2 m. Based on these constraints, an optimized resonator is derived in appendix A and its caustic is shown in figure 2.25. The collimated output has a beam diameter of about 2.6 mm. This value was chosen to be close to the waist size of the main amplifier to provide an almost perfectly mode matched beam that is easily coupled into the main amplifier without the need for any telescopes or other mode matching optics.

The preamplifier amplifies a $1 \mu\text{J}$ seed to 2 mJ at 5 kHz repetition rate using 100 roundtrips with a pump power of 66 W. The average power stability is about 0.6 % and an exemplary output power trace is shown in figure 2.26a. The power trace was measured with an air-cooled thermopile sensor (*Ophir 50150A-BB-26*).

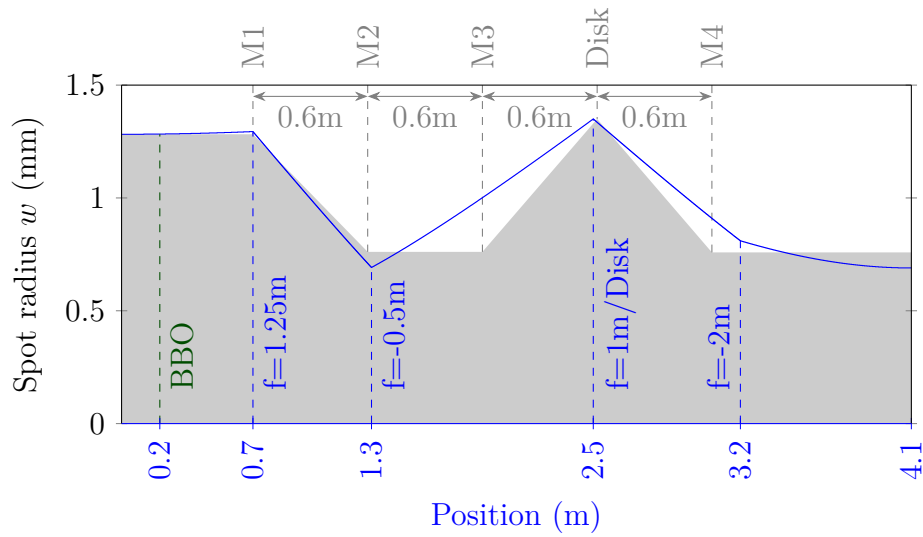


Figure 2.25: The resonator of the preamplifier at a disk curvature of 2 m. To accumulate the required Gouy phase in a short propagation length, the beam size must decrease as soon as possible. The distance between the optics is limited by physical constraints to values close to 0.6 m. A best case resonator (schematically drawn in gray) therefore decreases the beamsize after the incoupling using the mirrors M1 and M2, then increases the beam size to match the pump spot on the disk and finally quickly decreases the beam again. The numerically optimized real resonator is shown in blue and discussed in more detail in appendix A. It approximates the shape of the best case resonator based on actual Gaussian propagation and available optics while providing a roundtrip Gouy phase close to $\Delta\zeta_{eig} \approx \pi$.

In conclusion the implementation of a preamplification provides a seed beam for the main amplifier with similar size and wavefront as the main amplifier's eigenmode. Besides the beneficial mode matching, the output beam of the preamplifier provides low angular pointing and a well defined position and wavefront in close proximity to the amplifier stage due to the properties of its resonator. The higher input energy into the main amplifier increases the robustness and stability and prevents entering bifurcation regimes.

The implementation of a preamplification stage also decouples the main amplifier from the used oscillator. Instead of using a high power KLM oscillator in combination with a grating stretcher, the usage of a more compact fiber oscillator combined with a fiber Bragg grating stretcher is possible. The much lower pulse energy in the picjoule range expected from such a frontend can be compensated by the preamplifier to provide a constant input energy into the main amplifier. The sensitivity of the preamplifier to low seed energies was tested by attenuating the pulses from the KLM oscillator using absorptive filters and seeding the preamplifier with energies between 5 pJ and 500 pJ. Then the output power and bifurcation characteristics were analyzed. The result is depicted in figure 2.26b. The slope efficiencies slightly varied between 25% (5 pJ) and 28% (500 pJ). No bifurcation was observed during these measurements, hence the preamplifier can be used even with seed energies as low as 5 pJ and repetition rates of 10 kHz. This result motivated the implementation of a significantly more compact fiber based frontend that is investigated in more detail in the next section.

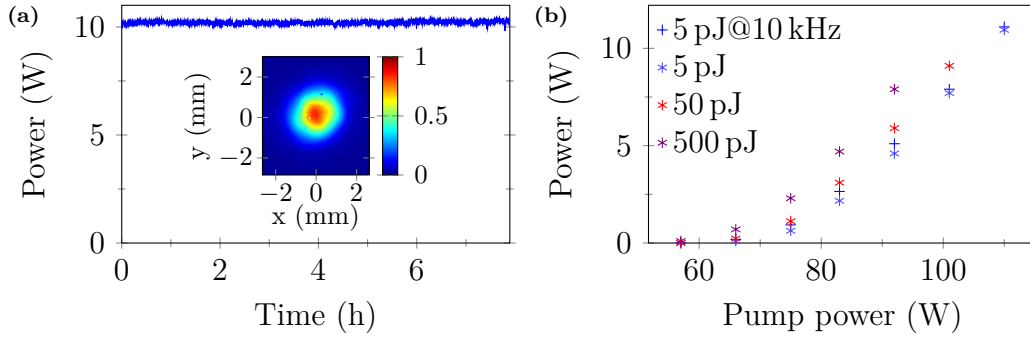


Figure 2.26: (a) The measured output power of the preamplifier for a repetition rate of 5 kHz, a seed energy of 1 μ J, a pump power of 66 W and 100 roundtrips. The measurement has a standard deviation of 0.6%. The inset shows the corresponding beam profile in a distance of about 2 m after outcoupling. (b) The output power of the preamplifier for low seed energies and a repetition rate of 5 kHz if not noted otherwise. 100 roundtrips were used during this measurement. No bifurcation was observed and the slope efficiencies vary only slightly between 25% and 28%.

2.9 Optimization of the Frontend

The previously used frontend consisting of a KLM thin-disk oscillator and grating stretcher has a footprint of $3.5 \times 1.5 \text{ m}^2$, which resembles about half of the total system size. To minimize the occupied table space, an alternative fiber based frontend with a significantly reduced footprint of just $0.87 \times 0.51 \text{ m}^2$ has been implemented. It consists of a commercial fiber oscillator with a pulse energy of 1 nJ and a bandwidth of about 40 nm centered around 1040 nm (*Menlo Systems Orange*). The output pulses are picked with nearly 100% efficiency in free-space to obtain a repetition rate of 5 kHz (or 10 kHz). Afterwards the beam is coupled into a fiber Bragg grating (*TeraXion Inc.*) and stretched with 500 ps/nm.

The fiber Bragg grating supports a bandwidth of 5 nm centered around 1030 nm and is matched to the phase of the used grating compressor. The total throughput of the fiber stretcher is about 5% yielding an input pulse energy into the preamplifier of about 50 pJ. To reach an output energy of 200 mJ, a total gain of 4×10^9 is needed compared to just 4×10^5 total gain for the previous frontend pulse energy of 1 μ J. This higher gain leads to a stronger gain narrowing effect (see section 1.6.3). According to equation 1.120, the new output bandwidth is expected to decrease by about 27% from 1.5 nm to 1.1 nm. This corresponds to an estimated longer output pulse duration of 1.47 ps instead of 1.08 ps.

These predictions are in good agreement with the measured bandwidth and pulse duration of the new frontend shown in figure 2.27. The pulses tend to be slightly shorter than predicted and a pulse duration of 1.4 ps (with a retrieval uncertainty of about ± 0.1 ps) is obtained for an output pulse energy of about 106 mJ. The seed energy into the main amplifier was 200 μ J and 32 roundtrips were used with a pump power of 1 kW per disk and a repetition rate of 5 kHz. For this measurement only a fraction of about 1 mJ was sent into the compressor to show compressibility. The compression quality is slightly worse than for a purely grating based CPA setup (see figure 2.5). This is attributed to the non perfect match between the fiber Bragg grating stretcher and the dielectric grating compressor. Still good compression to

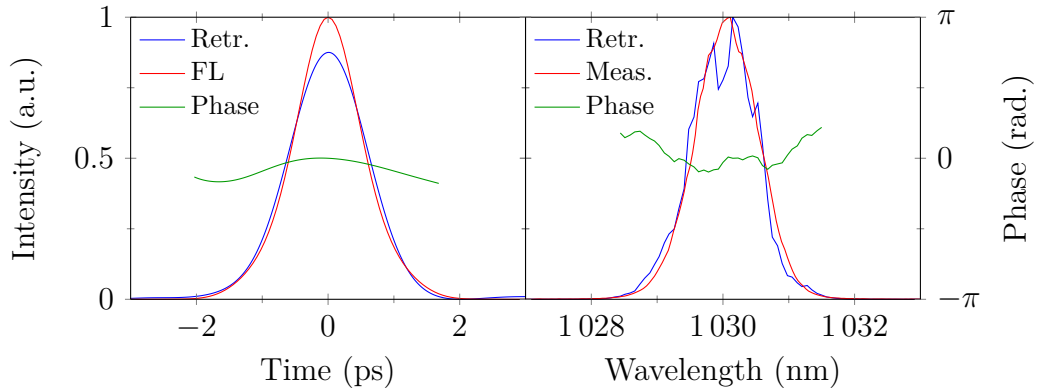


Figure 2.27: On the left the Fourier limit (FL) plotted together with the retrieved pulse shape and phase of main amplifier seeded with a fiber frontend. The FWHM duration of the Fourier limit is 1.18 ps, the measured pulse is 1.4 ps long. On the right the measured and the retrieved spectrum and spectral phase are shown. The measured FWHM bandwidth is 1.1 nm. The G-error of the used SH-FROG retrieval is 0.16%.

88% of the peak value of the transform limit was demonstrated with a Gaussian-like output pulse. The output bandwidth is about 1.1 nm.

The usage of a compact fiber based frontend relies on low oscillator energies in the nanojoule range to avoid nonlinearities or damages in the used fibers. Thus a significant increase of oscillator pulse energy is hardly possible. However to avoid strong gain narrowing, a gain medium with a broad amplification bandwidth can be implemented in the preamplification stage. With broadband preamplified pulse energies up to one millijoule, the total gain that is subject to the stronger gain narrowing of Yb:YAG reduces to values as low as 200.

Unfortunately broadband pulses exceed the capabilities of highly dispersive fiber Bragg stretchers. The maximum bandwidth that is currently commercially available for fiber stretchers with a dispersion of 500 ps/nm is about 5 nm. Only the central part of this bandwidth provides good matching with a grating compressor. The deviation from the compressor phase increases for more broadband pulses leading to incompressible pulses. Thus the usage of a broadband preamplifier relies on a grating based stretcher. For this reason a new compact grating stretcher design was realized based on an Öffner type stretcher [93] combined with a double pass. The footprint of the grating stretcher could be reduced from $2.5 \times 1 \text{ m}^2$ to $1.2 \times 0.6 \text{ m}^2$ while supporting bandwidths up to 10 nm with an efficiency of about 55% and a dispersion of 500 ps/nm. The implementation of the stretcher is also shown in figure 2.28. Spectral bandwidths broader than 10 nm lead to increased losses due to clipping at the edges of the stretcher optics.

This grating based compact stretcher is combined with a regenerative thin-disk amplifier that uses ytterbium doped CaGdAlO_4 (Yb:CALGO) as thin-disk material. Yb:CALGO provides an amplification bandwidth of 80 nm centered around 1030 nm [94]. Thus its emission bandwidth shows an almost perfect match with the emission bandwidth of Yb:YAG, which is $1030 \pm 4.5 \text{ nm}$. The material has been shown to be usable in thin-disk configuration [95], yet its roughly two times lower thermal conductivity and lifetime compared to Yb:YAG and its more than six times lower

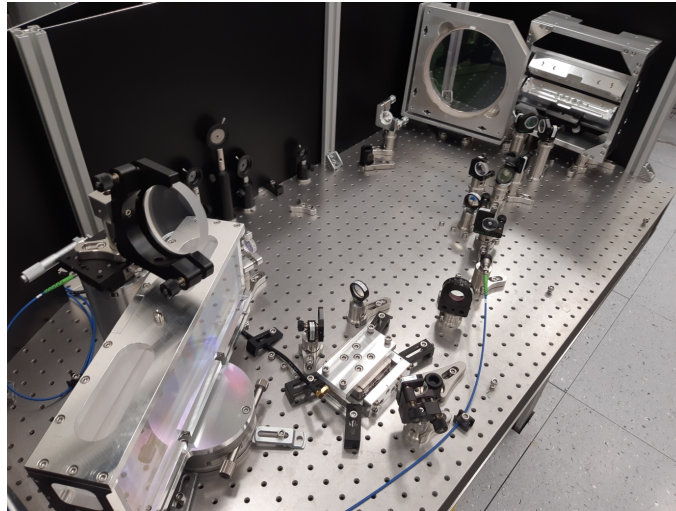


Figure 2.28: A compact double pass Öffner stretcher with a dispersion of 500 ps/nm and a footprint of $1.2 \times 0.6 \text{ m}^2$.

σ - τ product of $315 \mu\text{s cm}^2$ [53] constraints the material to use cases with lower energies and average powers. One example for such a use case is a preamplifier and consequentially the disadvantageous properties of Yb:CALGO are expected to be negligible. The caustic of the resonator is shown in figure 2.29a. A pump spot diameter of about 3 mm was used with a pump wavelength of 976 nm and a pump power up to 400 W (*DILAS Diodenlaser GmbH*). This system is seeded with a new fiber oscillator with an optimized mode-locking technique and a slightly higher pulse energy of 4 nJ at a central wavelength of 1030 and a bandwidth of 14 nm (*Menlo Systems YLMO*). Stretched pulses with an energy of about 1.5 nJ are then amplified to about 0.8 mJ within 350 roundtrips using a pump power of 170 W. The uncompressed broadband output spectrum is shown in figure 2.29b.

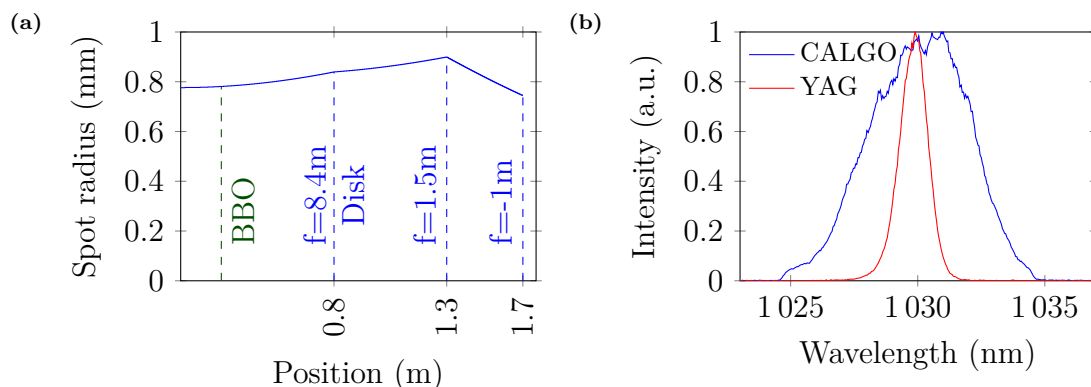


Figure 2.29: (a) The linear resonator of the used Yb:CALGO amplifier with a disk radius of curvature of 16.8 m. (b) The output spectrum of the Yb:CALGO amplifier (blue) for an output energy of 0.8 mJ (350 roundtrips, 170 W pump power, 5 kHz repetition rate) is shown in comparison with the output of the Yb:YAG amplifier (red) with an output energy of about 1.6 mJ (100 roundtrips, 88 W pump power, 5 kHz repetition rate). Both amplifiers used the same seed energy of about 1.5 nJ.

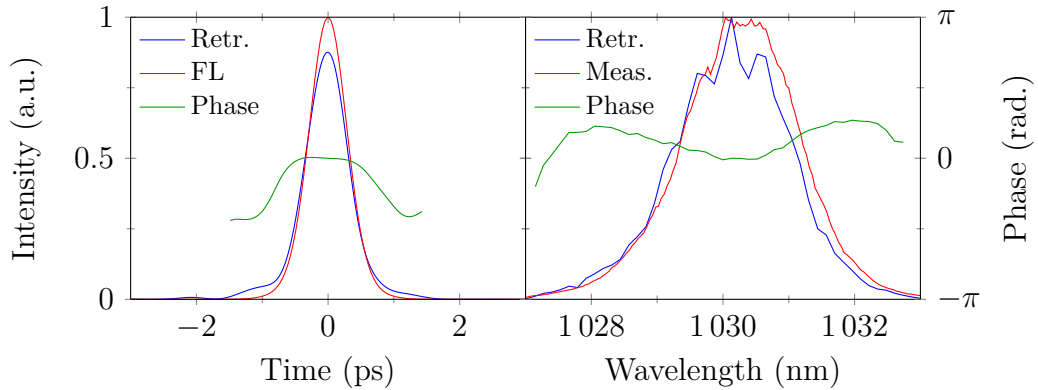


Figure 2.30: On the left the Fourier limit (FL) plotted together with the retrieved pulse shape and phase of the main amplifier seeded with a combination of a fiber oscillator and an Yb:CALGO amplifier. The FWHM duration of the Fourier limit is 0.68 ps, the measured pulse is 0.74 ps long. On the right the measured and the retrieved spectrum and spectral phase are shown. The measured FWHM bandwidth is 2 nm. The G-error of the used SH-FROG retrieval is 0.35%.

The main amplifier uses a fraction of 300 μJ from the Yb:CALGO system as input and amplifies it further to a pulse energy of about 100 mJ with a pump power of 1 kW per disk and 32 roundtrips at a repetition rate of 5 kHz. The total Yb:YAG gain is hence reduced to only 333 yielding an expected pulse duration of about 720 fs and bandwidth of about 2.25 nm (equation 1.120).

A fraction (ca. 1 mJ) of the amplified pulse was compressed and the measurement is shown in figure 2.30. The pulse duration and bandwidth are close to the analytic predictions. The gain narrowing was successfully compensated and a pulse duration of about 740 fs was reached. The current grating compressor limits the spectral bandwidth of the output pulses to about 5 nm before clipping at the compressor gratings is observed. Thus further optimization towards even shorter pulses is limited in the presented system. The broader bandwidth comes at the cost of an increased sensitivity to compressor misalignment and phase mismatch. This increased sensitivity to dispersion for broadband pulses has already been discussed in section 1.5. For this reason the compression does not show the same high quality as in the case of the microjoule seeded amplifier chain as depicted in figure 2.5. The reached peak intensity is 88% of the Fourier limit. Also a lower temporal stability of the pulse shape has been observed. Further optimization is however possible and the demonstrated successful combination of two gain materials to increase the emission bandwidth is a promising tool to further enhance the output properties of high gain laser systems.

2.10 Conclusion

In conclusion the performance and properties of the most-energetic multi-kilohertz single-mode amplifier to date have been shown. Almost diffraction limited pulses with energies up to 200 mJ and pulse durations of 1.08 ps at a repetition rate of 5 kHz are generated.

An overview of different gain materials, dopants and geometries has been given and the advantages of Yb:YAG thin-disks for high energy and high average power applications were introduced. A detailed numerical model was developed and applied to the amplifier system. It gives insight into robust operating points and allows the prediction of disk temperatures. Also the determination of the required disk amount and their thickness rely on this model. The usage of input energies close to one millijoule was motivated and their advantages numerically confirmed. A main advantage is that systems seeded with higher energies settle faster to a steady state after they are distorted, which increases the overall system robustness.

The sensitivity of optics used for high intracavity average powers has been evaluated. In an experiment with an output power of 1.4 kW, the highest average power extracted from a regenerative amplifier at the time of measurement was reached. A predicted higher damage probability for BBO crystals in high average power environments was confirmed. The results lead to the hypothesis that a fundamental limitation of regenerative amplifiers is reached when the intracavity power is close to 10 kW.

A significant reduction of output power compared to the numerically predicted output power has been observed for high pump powers. Several measurements lead to the conclusion that this reduction can be attributed to wavefront distortions mainly introduced by different thermal lenses. Possibilities to reduce these distortions were proposed and evaluated for their advantages and disadvantages. Especially the usage of diffuse pump spots helped to reduce these distortions without significant drawbacks.

The amplifier's resonator was numerically optimized based on a novel method of reducing several stability properties to a single design variable. A direct measurement of the resonator stability has been demonstrated using a new method based on the oscillating beam size of a propagating beam. The optimized resonator helped to reach excellent spatial and temporal stability characteristics. Stable operation over more than 7 h has been achieved.

The mechanical components were optimized for reproducibility and stability and in conclusion monolithic components were used where possible. This includes the usage of flexure mounts and a water cooled monolithic aluminum housing. The possibility to keep the system's temperature low by using a water cooled housing drastically improved thermalization times and stability, yet this comes at the cost of a coupling between amplifier performance and water temperature.

High seed energies can only be provided by a preamplifier. Hence a design for a compact and robust preamplification stage has been discussed. To this end the novel method of reducing several stability properties of a resonator to a single design variable in order to numerically calculate an optimized resonator shape has been

adapted for linear resonators. The introduced preamplification demonstrated stable output properties for input energies as low as 5 pJ.

This stable behavior was used to test a new highly compact frontend with less than a tenth of the footprint of the previously used frontend. The high compactness was reached by a fiber oscillator in combination with a fiber Bragg grating as stretcher. The resulting low energies on the order of 50 pJ were subsequently amplified to more than 100 mJ and a pulse duration of 1.4 ps with a Gaussian-like pulse shape was obtained. The longer pulses produced by this frontend are the result of stronger gain narrowing. The implementation of the broadband preamplifier gain material Yb:CALGO not only allowed to overcome the stronger gain narrowing but also to reach a pulse duration of only 740 fs for a main amplifier output energy of 100 mJ.

While the presented amplifier shows remarkable properties regarding stability, pulse energy and repetition rate, its pulses are still too long for experimental applications like electron acceleration or attosecond pulse generation. Further temporal compression is necessary and the next sections cover methods and experimental results to decrease the pulse duration of this system to several tens of femtoseconds with high pulse energies of several tens of millijoules.

Chapter 3

Nonlinear Broadening of High Energy Pulses

While the laser amplifier system discussed in chapter 2 provides an energetic pulse with a high repetition rate, its pulse duration in the picosecond regime is longer than the optimal duration for many applications. The following chapter discusses various approaches to enhance the pulse duration of the amplifier with a focus on maximizing the output energy of the pulse compression stage. To this end a short introduction into nonlinear optical effects is given. Then several possibilities to obtain high energy broadband pulses are compared. A broadband spectrum is connected to a very short Fourier limit and hence facilitates potentially short pulse durations. The usage of a multipass cell is identified as most promising approach for the nonlinear broadening of pulses in the multi-kilohertz regime and a record-breaking experimental realization is discussed in more detail. Finally further energy and bandwidth scaling of multipass cell based nonlinear broadening is evaluated.

3.1 Nonlinear Optical Effects

The previous sections covered the propagation and amplification of a nanosecond scale pulse. The long pulse duration often enabled the negligence of nonlinear effects and allowed for a simplified treatment of the involved dynamics. In contrast to this, shorter pulse durations on the femtosecond to picosecond scale require the inclusion of these effects. The following sections give an overview over important nonlinear effects that are later used to increase the bandwidth of the amplifier discussed in chapter 2. Their origin is derived starting from the nonlinear wave equation and especially the third order effects are discussed in greater detail.

3.1.1 Nonlinear Wave Equation

To derive the nonlinear Schrödinger equation for an isotropic homogeneous dielectric medium, equation 1.7 is altered to represent a nonlinear relationship between the polarization and the electric field [16, p. 876]

$$\mathcal{P} = \epsilon_0 \chi \mathcal{E} + \underbrace{\epsilon_0 \chi^{(2)} \mathcal{E}^2 + \epsilon_0 \chi^{(3)} \mathcal{E}^3 + \dots}_{\mathcal{P}_{NL}}. \quad (3.1)$$

Hence the electric flux density \mathcal{D} is defined as

$$\mathcal{D} = \epsilon \mathcal{E} + \mathcal{P}_{NL} \quad (3.2)$$

and Maxwell's equations are expressed by

$$\nabla \times \mathbf{H} = \epsilon \frac{\partial \mathbf{E}}{\partial t} + \frac{\partial \mathbf{P}_{NL}}{\partial t} \quad (3.3)$$

$$\nabla \times \mathbf{E} = -\mu \frac{\partial \mathbf{H}}{\partial t} \quad (3.4)$$

$$\nabla \cdot \mathbf{D} = 0 \quad (3.5)$$

$$\nabla \cdot \mathbf{B} = 0. \quad (3.6)$$

Applying the identity 1.15 to the electric field \mathbf{E} yields

$$-\frac{1}{c^2} \frac{\partial^2 \mathbf{E}}{\partial t^2} - \mu \frac{\partial^2 \mathbf{P}_{NL}}{\partial t^2} = \nabla (\nabla \cdot \mathbf{E}) - \nabla^2 \mathbf{E}. \quad (3.7)$$

In general the term $\nabla (\nabla \cdot \mathbf{E})$ is nonvanishing. Its contribution is however negligible especially if the slowly varying amplitude approximation is valid or in the case of transverse infinite plane waves [96, p. 71]. Assuming $\nabla (\nabla \cdot \mathbf{E}) = 0$, the nonlinear wave equation is given by

$$\nabla^2 \mathbf{E} - \frac{1}{c^2} \frac{\partial^2 \mathbf{E}}{\partial t^2} = \mu \frac{\partial^2 \mathbf{P}_{NL}}{\partial t^2}. \quad (3.8)$$

It is beneficial to rewrite this equation in the frequency domain

$$\nabla^2 \mathbf{E} + k^2 \mathbf{E} = -\omega^2 \mu \mathbf{P}_{NL}, \quad (3.9)$$

where \mathbf{E} and \mathbf{P}_{NL} are the Fourier transforms of \mathbf{E} and \mathbf{P}_{NL} and k is the wavenumber. This equation represents a Helmholtz equation with a source term $\omega^2 \mu \mathbf{P}_{NL}$. The source term acts as new light source for previously nonexistent frequency components and forms one of the basis of nonlinear optics. Solving the Helmholtz equation yields [16, p. 934]

$$\mathbf{E}_{NL} = \int_V \mu \omega^2 \mathbf{P}_{NL}(\mathbf{r}') \frac{e^{-ik|\mathbf{r}-\mathbf{r}'|}}{4\pi|\mathbf{r}-\mathbf{r}'|} d\mathbf{r}' \quad (3.10)$$

The emitted radiation from the source term can hence be interpreted as the addition of spherical waves associated with different source points [16, p. 878]. The total electric field consists of the solution for the source free wave equation \mathbf{E}_0 (see section 1.1.1) and the electric field radiated by the source

$$\mathbf{E} = \mathbf{E}_0 + \mathbf{E}_{NL}. \quad (3.11)$$

The source term is influenced by the field \mathbf{E} due to the nonlinear nature of \mathbf{P}_{NL} . At the same time it modifies this field by radiating new frequency components \mathbf{E}_{NL} and hence creates a feedback loop. The first Born approximation is applied in the following to solve this feedback. Assuming an incident field \mathbf{E}_0 , the nonlinear polarization is approximated by $\mathbf{P}_{NL}(\mathbf{E}) \approx \mathbf{P}_{NL}(\mathbf{E}_0)$. The radiation \mathbf{E}_{NL} emitted by this source is assumed to be small enough such that the modification of the field \mathbf{E} is negligible and no feedback has to be calculated [16, p. 878].

The nonlinear emission is mainly governed by the term $\mathbf{P}_{NL}(\mathbf{E}_0)$. The different orders of the nonlinear polarization (see equation 3.1) yield different generated frequency components and are discussed in the following in more detail.

3.1.2 Second Order Nonlinear Effects

Second order effects are caused by a nonlinear polarization that is sufficiently described by

$$\mathcal{P}_{NL} = \epsilon_0 \chi^{(2)} \mathcal{E}^2. \quad (3.12)$$

This equation implies that changing the direction (the sign) of \mathcal{E} does not change the direction of the nonlinear polarization, thus the direction of the output relative to the input changes with the orientation of the input. This is impossible in centrosymmetric materials. Second order nonlinear effects are therefore only observable in materials that are non-centrosymmetric.

In order to investigate the effects caused by the second order nonlinearity, an input field comprising of two components at optical frequencies ω_1 and ω_2 is defined. To reduce complexity, the following calculations are based on monochromatic plane waves

$$\mathcal{E}_0(t) = \text{Re}\{E(\omega_1) \exp(i\omega_1 t) + E(\omega_2) \exp(i\omega_2 t)\}. \quad (3.13)$$

This input field is used to calculate equation 3.12. This yields the following polarization components in frequency domain that are different from zero [16, p. 883].

$$P_{NL}(0) = \frac{\epsilon_0 \chi^{(2)}}{2} [|E(\omega_1)|^2 + |E(\omega_2)|^2] \quad (3.14)$$

$$P_{NL}(2\omega_1) = \frac{\epsilon_0 \chi^{(2)}}{2} E(\omega_1) E(\omega_1) \quad (3.15)$$

$$P_{NL}(2\omega_2) = \frac{\epsilon_0 \chi^{(2)}}{2} E(\omega_2) E(\omega_2) \quad (3.16)$$

$$P_{NL}(\omega_1 + \omega_2) = \epsilon_0 \chi^{(2)} E(\omega_1) E(\omega_2) \quad (3.17)$$

$$P_{NL}(\omega_1 - \omega_2) = \epsilon_0 \chi^{(2)} E(\omega_1) E^*(\omega_2) \quad (3.18)$$

The term $P_{NL}(0)$ is called *optical rectification* and describes a DC potential difference that can be measured across the dielectric material. Typical voltages are on the order of several hundred microvolts [16, p. 881]. The terms $P_{NL}(2\omega_1)$ and $P_{NL}(2\omega_2)$ are the *second harmonic generations (SHG)* of the fundamental frequencies ω_1 and ω_2 . Finally $P_{NL}(\omega_1 + \omega_2)$ is called *sum frequency generation (SFG)* and $P_{NL}(\omega_1 - \omega_2)$ *difference frequency generation (DFG)*.

A special case of a DFG process is the *optical parametric amplification (OPA)*. In this case a strong pump beam with a frequency ω_1 interacts with a signal beam ω_2 to create an auxiliary beam $\omega_3 = \omega_1 - \omega_2$ (sometimes called *idler*). In order to conserve energy, this process is equivalent to a photon with energy $\hbar\omega_1$ splitting up into a photon with energy $\hbar\omega_2$ and $\hbar\omega_3$ [16, p. 886]. The signal and the idler therefore undergo amplification while the pump beam is depleted.

Another special case is observed if a DC field with $\omega_2 = 0$ is applied as second electric field. In that case the SFG and DFG term are identical and are summed up as

$$P_{NL}(\omega_1) = 2\epsilon_0 \chi^{(2)} E(0) E(\omega_1). \quad (3.19)$$

This linear contribution to the polarization can be interpreted as a change of the permittivity ϵ (see section 1.1.1)

$$\epsilon_{DC} = \epsilon_0 \left(1 + \chi + \underbrace{\Delta\chi}_{2\chi^{(2)}E(0)} \right). \quad (3.20)$$

In a nonmagnetic ($\mu = \mu_0$) and undisturbed medium, the refractive index n is defined by the equation (see section 1.1.1)

$$n^2 = \frac{c_0^2}{c^2} = \frac{\epsilon}{\epsilon_0} = 1 + \chi. \quad (3.21)$$

The differentiation of $\chi = n^2 - 1$ yields

$$\frac{d\chi}{dn} = 2n \quad (3.22)$$

or alternatively [16, p. 882]

$$\Delta n = \frac{\Delta\chi}{2n} = \frac{\chi^{(2)}E(0)}{n}. \quad (3.23)$$

Hence the field $E(0)$ linearly changes the refractive index of the medium. This effect has been previously introduced as Pockels effect (see section 2.3.4) and can be interpreted as nonlinear effect of second order.

3.1.3 Third Order Nonlinear Effects

Third order effects are dominant in centrosymmetric materials due to the absence of second order effects. They are described by the nonlinear polarization

$$\mathcal{P}_{NL} = \epsilon_0 \chi^{(3)} \mathcal{E}^3. \quad (3.24)$$

In the following two consequences of third order effects are introduced: the optical Kerr effect and four wave mixing. The optical Kerr effect describes the behavior of a monochromatic wave in a third order medium and allows a simple explanation of an effect called *self phase modulation*. Four wave mixing treats third order effects in the frequency domain and gives insight into the coupling between several frequencies.

Optical Kerr Effect

The optical Kerr effect can be derived by assuming a monochromatic optical input field $\mathcal{E}(t) = \text{Re}\{E(\omega) \exp(i\omega t)\}$. The nonzero components of the nonlinear polarization density in the frequency domain are for this case (eq. 3.24) [16, p. 895]

$$P_{NL}(\omega) = \frac{3\epsilon_0 \chi^{(3)}}{4} |E(\omega)|^2 E(\omega) \quad (3.25)$$

$$P_{NL}(3\omega) = \frac{\epsilon_0 \chi^{(3)}}{4} E^3(\omega) \quad (3.26)$$

The term $P_{NL}(3\omega)$ represents the *third harmonic generation* and can be interpreted as a special case of four wave mixing that is introduced later. The term $P_{NL}(\omega)$ describes a nonlinear emission with the same frequency as the incident field and hence describes a modification of the input.

Similar to the derivation of the Pockels effect in section 3.1.2, the nonlinear polarization $P_{NL}(\omega)$ can be treated as change of susceptibility $\Delta\chi$

$$\Delta\chi = \frac{3\chi^{(3)}}{4} |E(\omega)|^2 = \frac{6\chi^{(3)}\eta}{4} I. \quad (3.27)$$

Here η is the impedance of the medium $\eta = \eta_0/n$ with $\eta_0 = \sqrt{\mu_0/\epsilon_0}$. It relates the intensity to the electric field via $I(\omega) = |E(\omega)|^2/(2\eta)$ (equation 1.21). Following equation 3.23, the change of susceptibility can be expressed as change of refractive index

$$\Delta n = \frac{\Delta\chi}{2n} = \underbrace{\frac{3\chi^{(3)}\eta}{4n}}_{n_2} I. \quad (3.28)$$

The change of refractive index is hence proportional to the intensity of the optical field with a proportionality constant n_2 . This constant is also called *nonlinear refractive index* or *optical Kerr coefficient* [16, p. 896].

Using $c_0 = 1/\sqrt{\mu_0\epsilon_0}$, the nonlinear refractive index n_2 and the third order nonlinear susceptibility $\chi^{(3)}$ are related by ¹

$$n_2 = \frac{3\chi^{(3)}}{4\epsilon_0 c_0 n^2}. \quad (3.29)$$

The dependency of the refractive index on the intensity of the incident field

$$n(I) = n_0 + \Delta n = n_0 + n_2 I, \quad (3.30)$$

where n_0 is the linear refractive index, forms the basis of the optical Kerr effect.

Self Phase Modulation

Assuming a plane wave pulsed laser with a slowly varying envelope (see equation 1.20 and 1.92)

$$E(t) = A(t) \exp(-ikz), \quad (3.31)$$

then the slowly changing intensity $I(t)$ of the wave at the time t and the refractive index n are [16, p. 987]

$$I(t) = \frac{|A(t)|^2}{2\eta} \quad (3.32)$$

$$n(t) = n_0 + n_2 I(t). \quad (3.33)$$

¹A alternative definition of the third order susceptibility yields the expression [16, p. 876]

$$n_2 = \frac{3\chi^{(3)}}{\epsilon_0^2 c_0 n^2}.$$

With $k = n\omega/c_0$, the slowly varying envelope can hence be expressed by the equation

$$E(t) = \underbrace{A(t) \exp\left(-i \frac{n_2 \omega}{c_0} I z\right)}_{A_{SPM}(t)} \exp(-ik_0 z). \quad (3.34)$$

where k_0 is the linear wavenumber $k_0 = n_0 \omega / c_0$. After a propagation $z = L$, the additional nonlinear phase [16, p. 896]

$$\Delta\phi_{max} = \frac{n_2 \omega}{c_0} L I_{max} \quad (3.35)$$

is accumulated at the point of maximum pulse intensity I_{max} . This phase is created by the laser field itself, which is why this process is called *self phase modulation (SPM)*. The accumulated nonlinear phase is sometimes also called *B-integral*.

A new self phase modulated pulse envelope is defined by

$$A_{SPM}(t) = A(t) \exp\left(-i \Delta\phi_{max} \frac{I(t)}{I_{max}}\right). \quad (3.36)$$

The SPM hence keeps the absolute value of the pulse envelope constant, but adds a time varying phase. The spectrum of this new envelope is calculated by a Fourier transform (eq. 1.93) of $A_{SPM}(t)$. This spectrum shows new frequency components due to the newly added time varying phase. A self phase modulated pulse is hence spectrally broadened.

To determine the temporal distribution of these newly created frequencies, an instantaneous frequency is defined [16, p. 939]

$$\omega_i(t) = \omega_0 + \frac{\partial\phi}{\partial t}, \quad (3.37)$$

where ϕ is the time domain phase of a propagating pulse envelope and ω_0 the frequency at the peak of the pulse (typically the central frequency). It gives an estimate for the frequency ω_i that is present at a certain temporal position t . For a Fourier limited pulse that experienced SPM, the instantaneous frequency is

$$\omega_i(t) - \omega_0 = \partial_t \phi = -\frac{\Delta\phi_{max}}{I_{max}} \partial_t I(t). \quad (3.38)$$

An exemplary instantaneous frequency distribution for a SPM broadened Gaussian pulse is shown in figure 3.1.

The bandwidth of a spectrally broadened pulse can be approximated by the difference between maximal and minimal instantaneous frequency [97, p. 90]

$$\Delta\omega \approx \max(\omega_i) - \min(\omega_i). \quad (3.39)$$

This difference is also highlighted for the exemplary pulse in figure 3.1.

In the scope of this thesis a broadening factor is defined as figure of merit that describes the factor between the the input pulse duration and the Fourier limited output pulse duration of a setup. Assuming a time-bandwidth product of

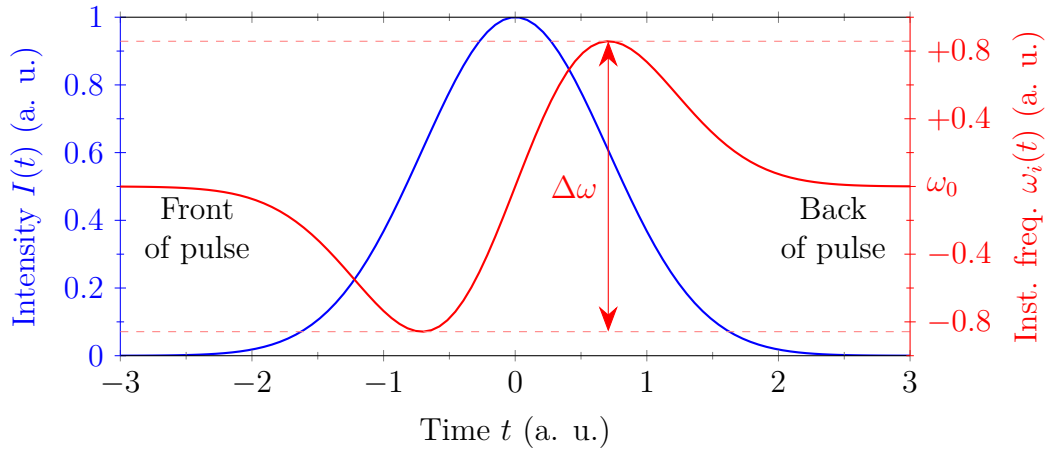


Figure 3.1: An exemplary pulse $I(t)$ with the corresponding SPM induced instantaneous frequency distribution $\omega_i(t)$ referenced to ω_0 . Also shown is the obtained spectral bandwidth $\Delta\omega$ of the SPM broadened pulse.

the broadened spectrum similar to a Gaussian spectrum and defining the FWHM Fourier limit of the broadened spectrum as τ_{FL} and the $1/e^2$ bandwidth as $\Delta\omega$ yields the relationship $\Delta\omega \tau_{FL} \approx 4\sqrt{\ln 4}$. With this assumption, the broadening factor

$$\frac{\tau_{FWHM}}{\tau_{FL}} \approx \tau_{FWHM} \frac{\Delta\omega}{4\sqrt{\ln 4}} = \frac{\Delta\phi_{max}}{\sqrt{e}} \quad (3.40)$$

is deduced for a Fourier limited Gaussian input pulse $I(t)$ with FWHM duration τ_{FWHM} . The broadening factor hence linearly increases with the nonlinear phase $\Delta\phi_{max}$.

So far it was implicitly assumed that the system is dispersion and absorption free, has an instantaneous response and that the nonlinear refractive index does not alter the pulse shape or beam profile. While an instantaneous response can be safely assumed for systems that are not Raman active [97, p. 41], the following sections describe the validity of these assumptions in the other cases and give a phenomenological description of the consequence in case these assumptions are not valid anymore. A more general treatment of self phase modulation that includes dispersive and absorptive systems is found in [96, p. 561].

Dispersive Systems A dispersive system stretches (or compresses) the pulse during its propagation while new frequencies are generated. This creates a change of pulse shape $I(t)$, which feeds back onto the nonlinear phase added to the pulse and hence changes the way new frequencies are generated. This violates the previously made assumption of negligible dispersion.

To estimate the accumulated nonlinear phase and the dispersion that still justifies a dispersionless treatment of the system, a length called *dispersion length* L_D is defined as [97, p. 58]

$$L_D = \frac{\tau_{FWHM}^2}{|GVD|4 \ln 2} \quad (3.41)$$

with the group velocity dispersion $GVD = \partial^2 k / \partial \omega^2$ and the full width half maximum pulse duration τ_{FWHM} . With these parameters and assuming a Fourier limited Gaussian like input pulse, an analytic approximation for the temporal broadening is given by [97, p. 102]

$$\frac{\tau_{out}}{\tau_{in}} = \sqrt{1 + \sqrt{2} \Delta\phi_{max} \frac{L}{L_D} + \left(1 + \frac{4}{3\sqrt{3}} \Delta\phi_{max}^2\right) \frac{L^2}{L_D^2}}. \quad (3.42)$$

Here τ_{in} and τ_{out} are the input and output pulse durations of the system and $\Delta\phi_{max}$ is the nonlinear phase accumulated over a distance L . Assuming a significant accumulation of nonlinear phase $4\Delta\phi_{max}^2 \gg 3\sqrt{3}$, a temporal broadening of the pulse less than 15% is expected for

$$\Delta\phi_{max} L < 0.2L_D. \quad (3.43)$$

As an example atmospheric argon has a GVD of $14.175 \text{ fs}^2/\text{m}$ [98]. The nonlinear length L_D for a pulse duration of 1 ps is therefore approximately 25 km. Thus as long as the product of accumulated nonlinear phase and system length is less than 5 km, dispersion is considered to be weak.

If there is positive dispersion that cannot be neglected, the pulse intensity decreases with increasing pulse duration and a saturation of the nonlinear mechanism sets in. With positive dispersion any newly created frequency components are pushed towards the shoulders of the pulse finally creating an almost rectangular pulse shape [97, p. 102]. The instantaneous frequency reaches very high values at the slopes of this pulse due to the rapid change of intensity (compare to eq. 3.38) which finally causes a breakup of the pulse. For weak dispersions $\tau_{FWHM}^2 \gtrsim 10GDD$ (or $L/L_D \lesssim 0.3$) and a Fourier limited Gaussian input pulse, wave breaking occurs approximately after an accumulated nonlinear phase that fulfills [99]

$$\Delta\phi_{max}^{(WB)} L \approx 1.12L_D. \quad (3.44)$$

Self Steepening The intensity dependent change of the refractive index does not only change the phase of the pulse, but also the propagation velocity of the pulse. At the point of maximum intensity, the higher nonlinear refractive index slows down the pulse while the low intensity shoulders stay unaffected. The peak is hence slowly shifted towards the trailing part of the pulse. This process causes the generation of a very steep trailing shoulder while flattening the leading shoulder. In frequency domain, this leads to an asymmetrically broadened spectrum with larger broadening on the blue side. This process is also called *self-steepening* [97, p. 116].

In a dispersion-free system with a Gaussian input pulse, the pulse reaches an infinitely steep trailing shoulder after acquiring a nonlinear phase of [97, p. 117]

$$\Delta\phi_{max}^{(SS)} = \omega_0 \tau_{FWHM} \frac{1}{6} \sqrt{\frac{e}{\ln 4}}. \quad (3.45)$$

Similar to the previously introduced dispersion induced wave breaking, the pulse experiences a significant distortion at this point and starts to break apart.

Using the propagation of a pulse with a FWHM duration of 1 ps centered at a wavelength of 1030 nm as example, a breakup of the pulse due to self-steepening is expected for an accumulated nonlinear phase of 427 rad. This corresponds to a phase that is hardly reached in practice and consequentially self-steepening is negligible for pulse durations in the picosecond regime. Significant self-steepening is typically observed for pulse durations on the order of 100 fs or shorter [97, p. 118].

Kerr Lensing So far the impact of the intensity dependent nonlinear refractive index on the pulse shape and frequency distribution has been discussed. It was noted that the Kerr effect introduces an intensity dependent phase shift with various consequences for the pulse spectrum and shape. Another important aspect is the change of the phase over the spatial beamprofile [16, p. 897]. At the high intensity central part of a beam, the Kerr effect is especially pronounced and a large phase shift is observed. In contrast, the low intensity outer areas of the beam experience almost no nonlinear phase shift. This variation ultimately causes a concave wavefront distortion that leads to a focusing beam. This nonlinear focusing is called *Kerr lens*.

A Kerr lens is however not an ideal lens. Assuming a Gaussian beam input, the distortions introduced by the non-ideal lens can be treated as coupling into higher order modes [100].

If a beam is focused by a Kerr lens, its area decreases and its intensity rises. This amplifies the nonlinearity and hence the Kerr effect and the lens becomes even stronger. However, also the beam's diffraction becomes stronger for smaller beam sizes. For low powers, the diffraction eventually overpowers the Kerr lensing and the beam starts to diverge again. For high powers, this is not the case and the focusing continues until it is stopped by ionization or damage. The threshold power between these two regimes is called *critical power* and is defined as [96, p. 329]

$$P_{cr} = \frac{\pi(0.61)^2\lambda^2}{8nn_2}. \quad (3.46)$$

If the peak power of a pulse is higher than this critical power, it will eventually collapse. Note that not the intensity of the pulse but only the power is relevant for this process.

Four Wave Mixing

Another possibility to investigate third-order nonlinearities is the analysis in the frequency domain with different interacting waves. The result of a third order nonlinearity can also be seen as the combination of three waves resulting in a fourth wave. Similar to section 3.1.2, the analysis is done by defining an input wave consisting of three waves [16, p. 900]

$$\mathcal{E}_0(t) = \sum_{l=1}^3 \text{Re}\{E(\omega_l) \exp(i\omega_l t)\}. \quad (3.47)$$

By plugging the input wave from equation 3.47 into the nonlinear polarization given in equation 3.24, two additional patterns for the polarization components in

the frequency domain are obtained besides the already introduced third harmonic generation and phase modulation effects [16, p. 895 & p. 900] [97, p. 398]

$$P_{NL}(\omega_1 + \omega_2 - \omega_3) = \frac{3\epsilon_0\chi^{(3)}}{2}E(\omega_1)E(\omega_2)E^*(\omega_3) \quad (3.48)$$

$$P_{NL}(\omega_1 + \omega_2 + \omega_3) = \frac{3\epsilon_0\chi^{(3)}}{2}E(\omega_1)E(\omega_2)E(\omega_3). \quad (3.49)$$

The latter term yields a new frequency $\omega_4 = \omega_1 + \omega_2 + \omega_3$ and can be thought of as extension of the third harmonic generation. However this process is typically rather inefficient [97, p. 399].

The term in equation 3.48 describes an effect that is often referred to if the term *four wave mixing* is used (although in general all third order effects can be described as four wave mixing process). The fourth frequency generated in this case is $\omega_4 = \omega_1 + \omega_2 - \omega_3$ or as *frequency matching condition*

$$\omega_1 + \omega_2 = \omega_3 + \omega_4. \quad (3.50)$$

Assuming that all involved waves are plane waves with the wave vector \mathbf{k}_l and position \mathbf{r}

$$E(\omega_l) \propto \exp(-i\mathbf{k}_l \cdot \mathbf{r}) \quad (3.51)$$

the nonlinear polarization as defined in equation 3.48 is

$$P_{NL}(\omega_4) \propto \exp(-i\mathbf{k}_4 \cdot \mathbf{r}) \propto \exp(-i[\mathbf{k}_1 + \mathbf{k}_2 - \mathbf{k}_3] \cdot \mathbf{r}) \quad (3.52)$$

or as *phase matching condition*

$$\mathbf{k}_1 + \mathbf{k}_2 = \mathbf{k}_3 + \mathbf{k}_4. \quad (3.53)$$

Efficient four wave mixing requires the frequency matching condition and the phase matching condition to be fulfilled. Note that four wave mixing is implicitly included in the previous discussion of self phase modulation (section 3.1.3) and the presented formalism just enables a different treatment in the frequency domain.

A special case that becomes more important in later sections is *three wave mixing* [16, p. 901]. In that case two driving frequencies are the same $\omega_0 = \omega_1 = \omega_2$ and hence the matching conditions simplify to

$$2\omega_0 = \omega_3 + \omega_4 \quad (3.54)$$

$$2\mathbf{k}_0 = \mathbf{k}_3 + \mathbf{k}_4. \quad (3.55)$$

The frequencies $\omega_3 = \omega_0 + \Delta\omega_0$ and $\omega_4 = \omega_0 - \Delta\omega_0$ are symmetrically located around the driving frequency ω_0 . In a dispersion free system with coaxial propagation, the phase matching and the frequency matching conditions are always fulfilled simultaneously. Hence an ongoing back and forth conversion from a center frequency to some sidebands and recombination from these sidebands back to the center frequency is expected in such a system.

Now a limited mirror bandwidth or another attenuation effect is introduced and the frequency ω_4 vanishes as the beam propagates. Its symmetric frequency ω_3 cannot recombine back to the center frequency and slowly builds up until it is powerful enough to cause significant interference effects in time domain. When this point is reached, the fast intensity oscillations of the pulse are imprinted on the phase by the SPM mechanism causing a vast amount of newly generated frequencies that are hardly compressible due to the complex phase structure. This mechanism is assumed to limit the expected maximal nonlinear phase that does not cause a pulse breakup in systems with bandwidth limitations even if dispersion and self-steepening can be neglected.

3.2 Generation of Broadband High Energy Pulses

Two principal possibilities exist to create broadband high energy and average power pulses [70]: the spectrum of a high energy source can be directly broadened using the nonlinear effects presented in section 3.1 or alternatively one could generate a low energy broadband seed and amplify it using high energy pulses as pump for an optical parametric amplification (OPA, see section 3.1.2) [8]. Both concepts are briefly introduced in the following.

3.2.1 Optical Parametric Amplification

OPA schemes have been implemented various times in the near infrared regime [14, 101–103] with a typical conversion efficiency from infrared pump power to output power of $\sim 10\%$. Therefore the implemented amplifier system (chapter 2) is expected to yield output energies on the order of 20 mJ if used in an OPA scheme.

The kilowatt scale average power of the amplifier system might however limit the output energy to lower values as it causes an increased heating of the nonlinear OPA crystals. High temperatures can cause strong thermal lenses and degrade the beam quality of the output. Also if the average pump power exceeds a threshold, thermal cracks or loss of phase matching is expected [70, p. 13] [71, 72]. This threshold was calculated to be on the order of 10 kW for BBO crystals [72].

Experimentally thermal cracks were observed for radial temperature differences across the BBO crystal on the order of 50 K [72] using a 515 nm pump with an average power of 100 W [71]. Recently a 515 nm pump with an average power up to 364 W was successfully applied in an OPA scheme with a radial temperature difference on the order of 20 K without thermal damages [103]. The difference of the observed heating in the two previously mentioned systems can be partially attributed to differing crystal qualities and improved cooling schemes [72].

Despite these successes, scaling OPA systems towards kilowatt scale average output power remains a challenging task [70, p. 14] due to their low efficiency and thermal sensitivity. The possibility to directly broaden high pulse energies and high average powers is therefore investigated the following sections in more detail.

3.2.2 Nonlinear Broadening in Waveguides

The direct spectral broadening of pulses relies on nonlinear processes that are by definition intensity dependent. As a consequence the outer areas in the spatial profile of a Gaussian beam experience less broadening than the high intensity center. The newly generated frequencies do not follow a Gaussian intensity profile anymore and have significant higher order contributions.

A proper broadening mechanism hence relies on some sort of mode cleaning mechanism that ensures a well defined mode. The spectrum can be assumed to be spatially homogeneous if every frequency component has the same mode, which is an important property of a nonlinearly broadened pulse. The most common way to provide such mode cleaning is the usage of optical fibers that favor only a single mode.

A closely related mechanism is nonlinear broadening in a filament, where self-focusing due to the Kerr effect and plasma-defocusing caused by an ionized medium counteract and form a waveguide [96, p. 330]. The complex dynamics in a filament cause a degradation of the spatial homogeneity and pulse quality [104, 105] and subsequent filtering can drop the throughput to values below 50 % [106, 107].

This degradation is not expected from fiber based systems. High-energy fibers typically belong to the hollow core fiber class that feature a gas-filled core to provide a high damage threshold and often rely on SPM as dominant nonlinear broadening mechanism. Especially the introduction of capillary optical fibers (COFs) [108] enabled output energies of up to 5 mJ in the near infrared and pulse durations in the few-cycle regime [109]. The intensity in capillary optical fibers is limited by the ionization threshold of the used gas. The nonlinear refractive index can be tuned by changing the gas pressure but is ultimately limited by the constraint that the peak power must be below critical power (eq. 3.46) to avoid a collapse of the beam. With these constraints the maximal possible accumulation of nonlinear phase is calculated to be [110]

$$\Delta\phi_{max} = \pi\lambda \frac{I_{ion}}{P_0} L. \quad (3.56)$$

Here L is the (attenuation compensated) fiber length, P_0 is the peak power and I_{ion} is the gas ionization intensity. Thus in a COF system with a given pulse power and nonlinear gas, a large value of accumulated nonlinear phase can only be realized with a long fiber that can quickly exceed the physical constraints of laboratory space. This is especially true if the input pulses are highly energetic and have a high peak power P_0 .

The guiding mechanism of COFs can be understood as a repeated reflection from the inner surface of the capillary [111]. The intensity of higher order (hybrid) modes EH_{nm} is suppressed by an attenuation coefficient [112, p. 1796]

$$\alpha_{nm} = \left(\frac{u_{nm}}{2\pi}\right)^2 \frac{\lambda^2 L}{a^3} \frac{\nu^2 + 1}{\sqrt{\nu^2 - 1}} \quad (3.57)$$

with the capillary inner radius a , the mode dependent coefficient u_{nm} (e.g. $u_{11} = 2.405$ or $u_{12} = 5.52$ [112, p. 1797] with the fundamental mode being EH_{11}), the fiber

length L and the parameter $\nu = n_{COF}/n_{core}$ as the ratio of capillary material to core material refractive index. The attenuation of higher order modes is stronger than for the fundamental. The propagation of the fundamental mode is hence favored in a COF, higher order modes are attenuated stronger and some mode cleaning can be observed. Still the fundamental is attenuated as well: for a standard fused silica COF (250 μm diameter and 1 m length [70, p. 16]), the fundamental mode is attenuated by more than 20% and the total transmissions through some COF systems have been measured to be between 60% and 70% [108, 109, 113].

Milosevic et al. [100] further investigated the mode cleaning mechanism in hollow waveguides and bulk media. It was found that besides the attenuation of higher order modes in COFs, a dephasing mechanism between fundamental and higher order modes prevents the buildup of strong higher order components under the condition of a sufficiently slow accumulation of nonlinear phase (i.e. peak powers well below the critical power). It was concluded that the same mechanism should also prevent the buildup of higher order components during a simple propagation through a single focus without the guiding properties (and losses) of a hollow core fiber. A multipass cell with multiple transitions through foci was suggested, where each focus contributes a nonlinear phase shift small enough not to distort the mode preserving mechanism. The total nonlinear phase shift builds up over the foci and enables significant broadening within a single mode.

In order to understand why the buildup of higher order modes is prevented using a simple transition through a focus, the distorted propagation is simplified as a coupling between modes. A beam with the majority of its energy in the fundamental mode (eq. 1.26) is assumed. The Kerr lensing during the propagation through the focus distorts this fundamental mode and consequentially some energy is coupled into the higher order modes. While the fundamental mode propagates through the focus, it accumulates a Gouy phase shift of $\zeta(z) = \tan^{-1}(z/z_0)$. The higher order mode however accumulates a phase shift of $\zeta_{m,n}(z) = (m+n+1)\zeta(z)$. Thus the higher order mode and the fundamental mode dephase during their propagation with a relative phase difference of $(m+n)\Delta\zeta(z)$ where $\Delta\zeta(z)$ is the accumulated Gouy phase at position z . For the sake of simplicity it is assumed that the peak power is well below critical power and the energy is mainly coupled into the $\mathbf{E}_{1,1}$ mode (eq. 1.25). Figure 3.2 shows how in this case a buildup of high order modes is prevented and a clean output mode is obtained. The guiding in a COF is approximated as repeated reflections from the capillary surface or similarly as continuous focusing and defocusing. Thus the same dephasing mechanism is present in a COF.

These theoretical predictions were later numerically [114] and experimentally [115, 116] confirmed. The usage of a simple gas filled multipass cell was shown to create a highly homogeneous broadening with throughputs over 90%. Independently it was shown that a similar process also prevents the buildup of higher order modes in multipass-cells where the pulse accumulates the nonlinear phase in thin solid plates instead of a gas [117]. However, highly energetic pulses in thin plates tend to accumulate the nonlinear phase too fast, which is why thin plate based cells are more suitable for lower energies.

Nonlinear broadening in a multipass cell does not only provide almost perfect transmission, but also decouples the accumulated nonlinear phase from the length of

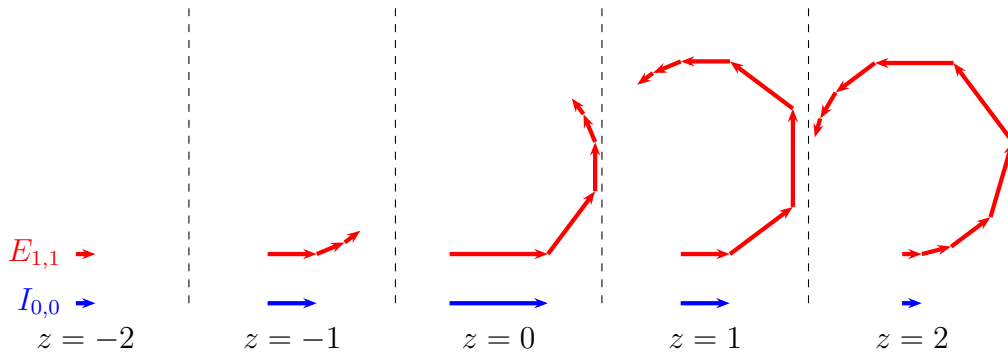


Figure 3.2: The simplified working principle of a multipass cell for peak powers $P_{max} \ll P_{cr}$. A fundamental mode $I_{0,0}$ and a higher order field $E_{1,1}$ propagate through a focus. The length of the arrow is proportional to the intensity ($I_{0,0}$) or amplitude ($E_{1,1}$) of the beam. The position z is normalized to the Rayleigh range. The Kerr lensing couples some amplitude approximately proportional to $I_{0,0}$ [100] into a higher order mode $E_{1,1}$ and the field $E_{1,1}$ builds up during propagation. Due to the difference in acquired Gouy phase, the higher order contribution $E_{1,1}$ dephases from the fundamental with an angle $2\Delta\zeta(z)$ shown as angle of the arrows. $\Delta\zeta(z)$ is the accumulated Gouy phase of the fundamental. The continuous coupling prevents a coherent buildup of the higher order mode. In a full focus propagation from $z = -\infty$ to $z = \infty$, the field $E_{1,1}$ almost returns to zero. I.e. the higher order buildup is cleaned away within one pass of the cell and the beam keeps its energy in the fundamental mode.

the system (compare to eq. 3.56). Accumulating more nonlinear phase is simply done by adding more passes in the cell. Consequentially potentially very large broadening factors are expected from these cells. The only limitations for the peak power of the pulse are the ionization intensity of the used gas and the damage threshold of the involved optics. The more relaxed constraints in comparison to the previously introduced guiding mechanisms make this approach the most suitable for high peak powers and pulse energies [114].

The next sections show the experimental realization of a multipass cell aimed at supporting high energies. After the setup and its results are introduced, a more detailed explanation of the working principle is given and the scaling limits are discussed. Finally some deeper analysis of the beam behavior is done and first results of energy scaling are shown.

3.3 Multipass Cell Design

This section introduces the multipass cell that is used in the following experiments and discusses the features of these cells. A vacuum chamber with a footprint of $4 \times 0.68 \text{ m}^2$ was constructed to house the multipass. The chamber can be filled with different gases up to atmospheric pressure. A simple two mirror resonator is placed into the cell, where each mirror has a size of $130 \times 300 \text{ mm}^2$ and the length of the resonator is $\sim 3 \text{ m}$. These mirrors are called *end mirrors* in the following and are labeled 2 and 3 in the schematic setup shown in figure 3.3. A custom ion-beam sputtered coating is used for most optics in the cell with a GDD value close to zero at 1030 nm and a maximum GDD of $|GDD| < 50 \text{ fs}^2$ throughout its reflection bandwidth. This avoids dispersive effects during the bounces over the mirrors. The

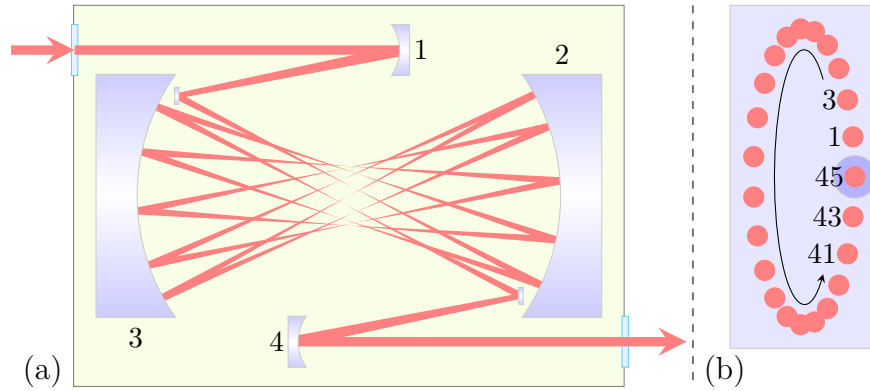


Figure 3.3: (a) Scheme of the multipass cell setup (top view). Mirrors 1 and 4 are concave 6 m RoC, and mirrors 2 and 3 are concave 1.5 m RoC. (b) Beam pattern on mirror 2. The spots are labeled according to the number of passes through the focus. After 45 passes, the beam is picked off by a plane outcoupling mirror.

mirrors provide a reflectivity of $> 99.9\%$ from 965 nm to 1100 nm to minimize losses. Thin fused silica windows with a thickness of 2 mm are used for incoupling to avoid unwanted nonlinearities outside the cell.

As known from section 1.3.5, an off-axis coupling into a resonator results in an elliptic multipass pattern through the resonator (compare to figure 1.4 and 3.3). For a two mirror resonator this principle is also known as *Herriott cell* [118]. The eigenmode of a Herriott cell resembles the shape of a focused Gaussian beam (see figure 1.1).

A Herriott cell configuration provides the maximum amount of focus transitions for a given amount of mirror bounces and the biggest beam diameter on a mirror for a given waist diameter and cell length among all multipass configurations. This makes such a multipass cell especially suited for high energy broadening with a large broadening factor.

In the following a more detailed analysis of the eigenmode properties is presented. This is followed by a description of the beam path and the mode matching process. Finally the amount of passes in a Herriott cell is analytically derived and an upper limit for the presented setup is deduced.

The Eigenmode

The waist size w_0 (or equivalently the Rayleigh length z_0) of the eigenmode is chosen such that intensity in the focus is lower than the ionization intensity I_{ion} of the gas used in the cell. At the same time the eigenmode on the end mirrors has to be large enough to avoid damages. To obtain sufficiently large beamsizes on the end mirrors, the resonator length has to be much larger than the Rayleigh length z_0 . This results in an accumulated Gouy phase from one mirror to another close to $\Delta\zeta_{eig} \approx \pi$. Thus the resonator has to be built near its stability edge and the radius of curvature (RoC) of the end mirrors was consequentially chosen to be $R = 1.5$ m (i.e. approximately half the resonator length).

The eigenmode radii on the end mirror w_{EM} and at the waist w_0 are then calculated by determining the eigenmode q_{eig} using equation 1.41 with the ABCD

matrix of the Herriott cell and propagating the mode q_{eig} to the waist or end mirror position. The radii are then given by ($\lambda = 1030$ nm)

$$w_0 = 572.59 \sqrt{\text{pm}} \sqrt{R} (s - s^2)^{1/4} \stackrel{s \rightarrow 1}{\approx} 572.59 \sqrt{\text{pm}} \sqrt{R} (1 - s)^{1/4} \quad (3.58)$$

$$w_{EM} = 572.59 \sqrt{\text{pm}} \sqrt{R} \left(\frac{s}{1-s} \right)^{1/4} \stackrel{s \rightarrow 1}{\approx} 572.59 \sqrt{\text{pm}} \sqrt{R} (1 - s)^{-1/4} \quad (3.59)$$

where s is the ratio between the actual end mirror distance (or resonator length) d and maximum stable length $2R$, i.e. $s = d/(2R)$.

Close to the stability edge $s \rightarrow 1$, the eigenmode size reacts sensitive to changes of the resonator length. Thus one of the cell mirrors is mounted on a translation stage to be able to tune out small differences between the eigenmode size and input beam size. The setup shown in figure 3.3 has a ratio of $s \approx 0.9953$, an eigenmode waist radius of about $w_0 \approx 0.18$ mm and eigenmode radius of $w_{EM} \approx 2.7$ mm.

The eigenmode for a given system is considered to be optimal if it enables a maximized input energy of E_{max} before gas breakdown or mirror damage is observed. This energy represents the highest energy a certain system configuration supports and is an important figure of merit. A simple way to deduce the value of E_{max} in a multipass cell close to the stability edge is proposed in the following.

If the energy E_{max} is reached with an optimal eigenmode featuring spot radii w_{EM} and w_0 , the peak fluence on the end mirror

$$2 \frac{E_{max}}{\pi w_{EM}^2} = 2 \frac{E_{LIDT}}{\pi \tilde{w}_{EM}^2} \quad (3.60)$$

is close to mirror damage threshold and the peak fluence in the focus

$$2 \frac{E_{max}}{\pi w_0^2} = 2 \frac{E_{BD}}{\pi \tilde{w}_0^2} \quad (3.61)$$

is close to gas breakdown. E_{LIDT} and E_{BD} are the damage and breakdown energies determined for an arbitrary (not optimal) eigenmode with spot radii \tilde{w}_{EM} and \tilde{w}_0 . It is noted from eq. 3.58 and 3.59 that the product of beam area and focus area for an arbitrary eigenmode is approximately constant

$$w_0^2 w_{EM}^2 \approx \tilde{w}_0^2 \tilde{w}_{EM}^2 \approx \text{const.} \quad (3.62)$$

Multiplying the previously stated fluences for gas breakdown and damage threshold and using equation 3.62 then yields the relationship

$$E_{max}^2 = E_{LIDT} E_{BD} \frac{w_0^2 w_{EM}^2}{\tilde{w}_0^2 \tilde{w}_{EM}^2} \approx E_{LIDT} E_{BD}. \quad (3.63)$$

This equation gives an estimate for the maximum energy throughput if only non optimized breakdown and damage energies E_{BD} and E_{LIDT} are given.

Each focus transition yields a certain accumulated nonlinear phase. Due to the spatial mixing of the beamprofile, not the peak nonlinear phase (eq. 3.35) but the average nonlinear phase is relevant. Also the length L in eq. 3.35 is exchanged by

an effective length that incorporates the changing beam size during propagation. The accumulated nonlinear phase per pass is then given by [114]

$$\Delta\phi_f = \frac{4\pi n_2}{\lambda^2} P_{max} \tan^{-1} \sqrt{\frac{s}{1-s}} = \frac{4\pi n_2}{\lambda^2} P_{max} \tan^{-1} \frac{d}{2z_0}. \quad (3.64)$$

Here P_{max} is the peak power of the incident pulse. For a focus transition with $d \gg 2z_0$ the equation simplifies to

$$\Delta\phi_f \approx \frac{2\pi^2 n_2}{\lambda^2} P_{max}. \quad (3.65)$$

An important conclusion is that for a tightly focused beam the accumulated nonlinear phase per pass does not change in first approximation even if some variation in the propagation path is present. This property ensures a stable broadening factor. The maximum possible nonlinear phase per pass is determined by setting $P_{max} = P_{cr}$ (eq. 3.46) and $n \approx 1$ for gaseous media yielding

$$\Delta\phi_{cr} \approx 2.88 \text{ rad}. \quad (3.66)$$

This value does not depend on the wavelength or the nonlinear refractive index.

Mode Matching

A plane mirror with a diameter of 25 mm is used in front of each end mirror to couple the beam into the cell and pick up the beam after propagation. Two concave mirrors (mirrors 1 and 4 in figure 3.3) with a RoC of 6 m are used to mode match the wavefront of the incoming collimated beam to the eigenmode wavefront or collimate the beam after the cell. A mirror telescope outside the chamber scales the beam diameter of the incoming beam to a value about twice the eigenmode diameter.

Successful mode matching is reached by comparing the size variations of the propagating beam with the variations expected from eq. 1.59. A wrong phase of the expected sinusoidal oscillation corresponds to a wrong wavefront or equivalently a wrong position of mirror 1 (compare to figure 1.3). Once the wavefront is matched, a visible amplitude of the oscillation means that the eigenmode size does not correspond to the input beam size and the resonator length needs to be changed by the translation stage below end mirror 3.

The beam describes almost a full ellipse on the end mirror before it is picked by the outcoupling mirror. For a full ellipse the output position of the beam exactly matches the input position. This ensures a good position (not angular) stability even for large setups or many bounces as the output position is then uniquely defined by the input position. Also according to section 1.3.5, a complete turn around the ellipse corresponds to a total accumulated Gouy phase that is a multiple of 2π . It is also known from section 1.3.3 that such a Gouy phase shift is equal to a q-preserving system. Hence the outcoupled beam closely resembles a q-preserved input beam. These properties are some of the reasons why the Herriott cell is known for its good mechanical and mode shape stability.

Number of Passes

The amount of bounces (or focus transitions) needed to return to the incoupling position is described by the passes N_f it takes to reach a total accumulated Gouy phase $N_f \times \Delta\zeta_{eig}$ that is a multiple of 2π (more details were discussed in section 1.3.5). The accumulated Gouy phase per pass $\Delta\zeta_{eig}$ of a Herriott cell can be calculated with its ABCD matrix and equation 1.44.

In the presented Herriott cell configuration with a single turn around the ellipse (i.e. a total Gouy phase of 2π), the amount of focus transitions is $N_f = 2\pi/\Delta\zeta_{eig} - 1$, where a reduction of -1 is due to the arrangement of the incoupling and outcoupling mirror. An approximation with good accuracy for $s \geq 0.95$ (less than 1% error) yields

$$N_f \approx \text{round} \left(\frac{\pi}{\sqrt{1-s}} - 1 \right). \quad (3.67)$$

Thus the amount of foci N_f is roughly proportional to the beam area on the end mirror πw_{EM}^2 for resonators near the stability edge. The value of N_f can be approximately doubled if the physical constraints of the setup allow two turns around the ellipse (i.e. a total Gouy phase of 4π). Analogous scaling rules apply for three or more turns. In the shown setup, the amount of bounces is $N_f \approx 45$ in a single turn.

The current setup requires a minimum spacing of approximately 30 mm between the bounces near the center region of the mirror to allow the positioning of the incoupling/outcoupling mirrors. The end mirror height with guaranteed specifications is about 80% of the total height or 240 mm. Geometrical considerations lead to the conclusion that the amount of bounces per mirror times the center spacing should roughly equal the circumference of a circle with a diameter equal to the major axis of the propagation ellipse. The amount of bounces per mirror $N_f/2$ is hence physically limited to about

$$\frac{N_f}{2} \lesssim \pi \frac{240 \text{ mm}}{30 \text{ mm}} \approx 25 \quad (3.68)$$

which corresponds to a maximum amount of about $N_f \approx 50$ bounces for the used optics.

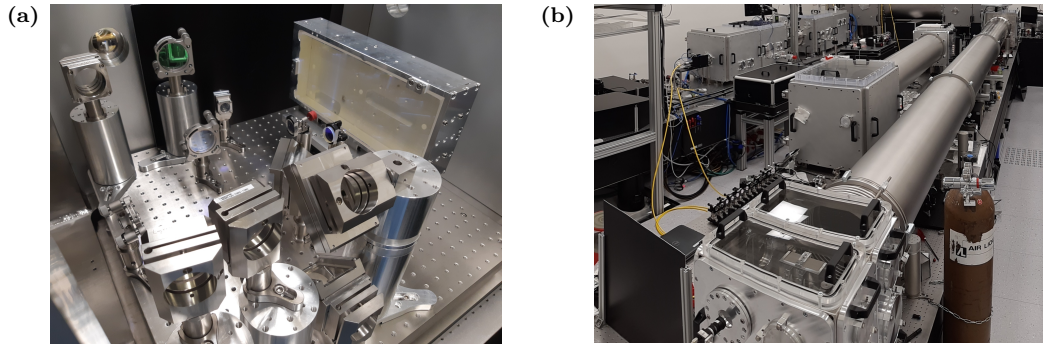


Figure 3.4: (a) One end mirror of the Herriott cell for an exemplary configuration together with its surrounding incoupling optics. (b) The vacuum chambers used for the Herriott cells. The results from the 3 m long variant (left) are presented in section 3.4, the 8 m long system (right) is later discussed in section 3.6.6.

3.4 Experimental Results

The output pulses from the amplifier discussed in chapter 2 seeded with the fiber laser frontend (see figure 2.27) are used as input for the previously introduced cell. The pulse duration during the following experiments is approximately 1.4 ps with a repetition rate of 5 kHz and the chamber is filled with 600 mbar of argon. Argon provides a sufficiently high nonlinear refractive index (at atmospheric pressure $n_{2,Ar} \approx 10 \times 10^{-20} \text{ cm}^2/\text{W}$ [119]), has a high ionization intensity on the order of $5 \times 10^{13} \text{ W}/\text{cm}^2$ [110], is cost-effective and shows no problematic rotational nonlinearity [62, p. 118] due to its monatomic nature. Up to 18.6 mJ of pulse energy can be coupled into the multipass cell before ionization is observed. Increasing the focal waist size is limited by the damage threshold of the end mirrors, as a larger waist directly leads to a smaller spot size on the mirror surface.

An exemplary experimental implementation of the introduced Herriott cell is depicted in figure 3.4 to convey an intuitive understanding of the size and design. Note that figure 3.4 shows a slightly different alignment than used to obtain the results presented in this section.

The nonlinearly broadened spectrum after the cell is shown in figure 3.5 and has a Fourier limit of 39 fs. Compared to the input pulse duration of approximately 1.4 ps, this is equivalent to a broadening factor of over 35. The output energy is 17.8 mJ and the throughput of the system is therefore approximately 95.7%. This is in good agreement with the expected linear losses determined by the number of passes and the reflectivity of the mirrors (i.e. $95.7\% \approx (99.9\%)^{45}$).

The total accumulated nonlinear phase shift is determined based on two methods. Assuming a dispersion free system, the input spectrum and the output spectrum are uniquely connected by a transformation defined by equation 3.36. A numerical optimization algorithm can find the phase of the input spectrum and the accumulated nonlinear phase that yields a simulated output spectrum with the best similarity to the measured output spectrum. This also provides an estimated input pulse shape as side product. This method is explained in more detail in appendix C. The second method relies on a retrieved input pulse shape, a well known propagation path and a known nonlinear refractive index n_2 . The total nonlinear phase is then calculated

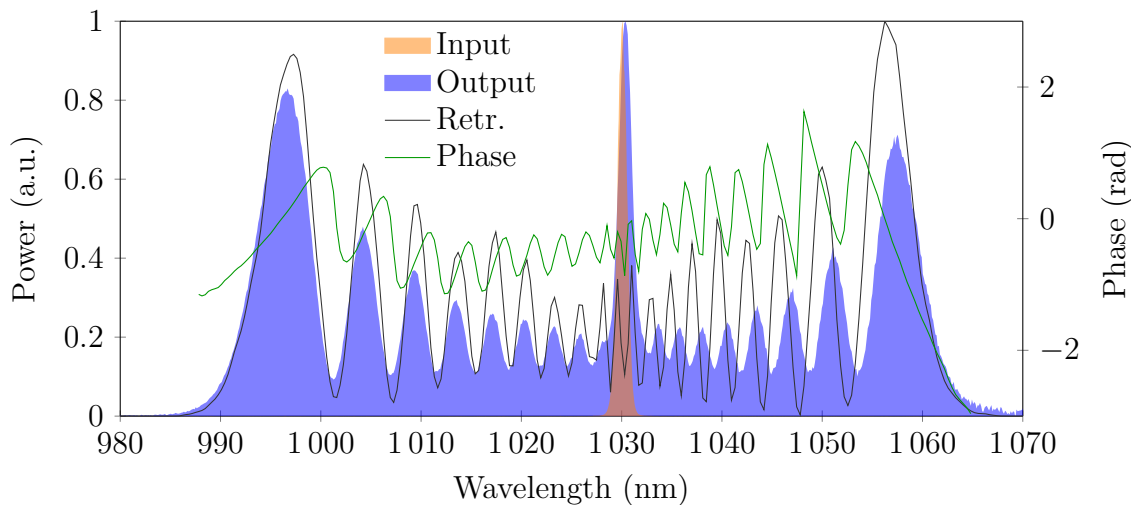


Figure 3.5: Measured input (orange) and output (blue) spectra after 45 focus transitions in 600 mbar of argon. Additionally depicted are the retrieved spectrum (black) and phase (green) from the SH-FROG measurement of the compressed pulse. The small wavelength offset of the central peak between input and output spectrum is attributed to the fact that the input spectrum was measured with a different spectrometer that provides a higher resolution.

based on equation 3.64. The first and the second method both yield a spatially averaged accumulated phase of

$$\Delta\phi \approx 59 \text{ rad.} \quad (3.69)$$

Since the first method is more independent of measured data and just relies on two measured spectra, it will be used for determining accumulated nonlinear phases in the next sections. The obtained nonlinear phase shift is in remarkable congruence with the Fourier limit scaling law (eq. 3.40), where using $\tau_{FL} = 39$ fs and $\tau_{FWHM} = 1.4$ ps yields an estimated phase shift of 59 rad.

The central peak visible in the broadened spectrum in figure 3.5 is attributed to low intensity input beam components that are not affected by the nonlinear processes like pre- and postpulses or some continuous wave background caused by amplified spontaneous emission in the amplifier chain. The shape of the spectrum closely resembles the expected shape based on the Fourier transformation of the self phase modulated pulse (see equation 3.36). This similarity indicates a virtually dispersion free propagation and an absence of more complex nonlinear effects that are not covered by equation 3.36. Also the condition for approximately dispersion free propagation (eq. 3.43) is fulfilled for the used parameters of a total length $L \approx 45 \times 3$ m, a nonlinear phase $\Delta\phi \approx 59$ rad and a dispersion length $L_D \approx 83$ km for 600 mbar of argon. This confirms the previously made assumptions of a virtually dispersion free system.

Since the nonlinear phase per pass of about $\Delta\phi_f = 1.3$ rad is still below the critical value (eq. 3.66), a higher nonlinear phase shift could be obtained simply by increasing the gas pressure. However the generation of new wavelengths around 950 nm at an argon pressure of 700 mbar indicated the onset of pulse breaking. The

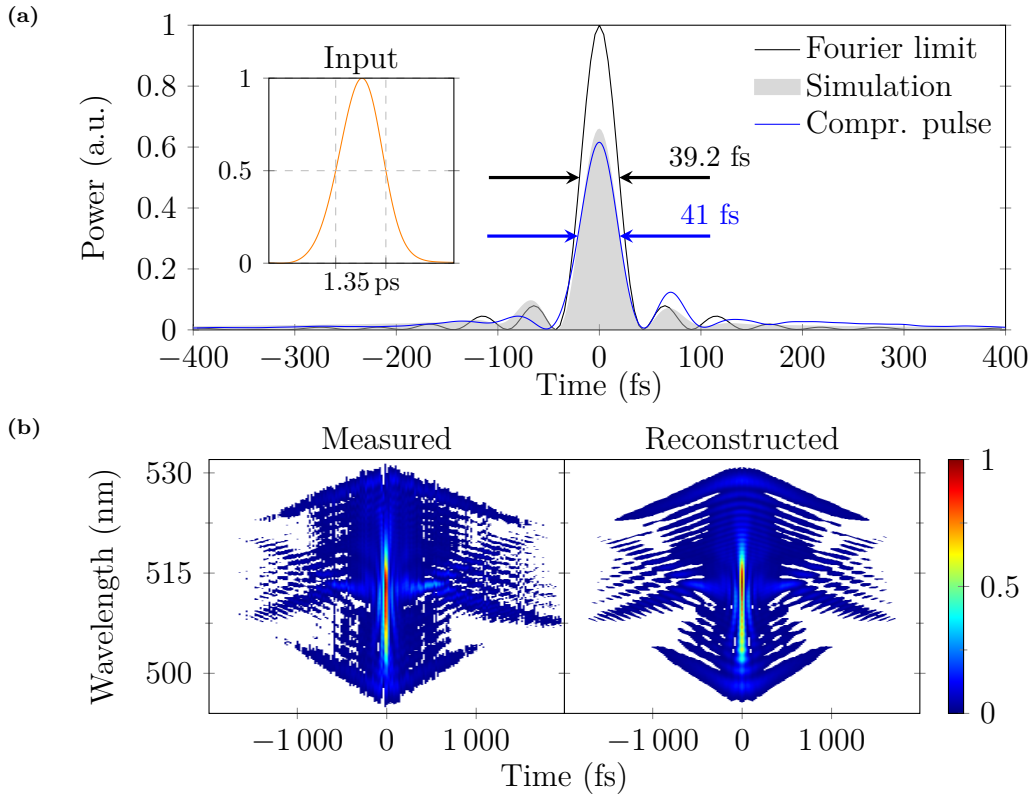


Figure 3.6: (a) Fourier-limited pulse calculated from the output spectrum shown in Fig. 2 (black), together with the retrieved compressed pulse (blue) and a simulation of the nonlinear compression (gray). The arrows mark the FWHM durations of the Fourier-limited pulse (black) and the compressed pulse (blue). The measured input pulse and its FWHM duration are shown in the inset. (b) Measured (left) and the retrieved (right) SH-FROG intensity for the compressed pulse in (a).

reason for this breaking despite the lack of dispersion or self-steepening is later investigated in section 3.5.2.

The output beam at 600 mbar of argon is attenuated using two uncoated fused silica wedges to a pulse energy of 20 μJ and sent through a chirped mirror compressor to test the compressibility. The attenuation avoids nonlinear contributions of air and damages of the chirped mirrors. The chirped mirror compressor consists of 17 mirrors with a total GDD of -9400 fs^2 and a total reflectivity of 98%. The pulse is then characterized by a SH-FROG and the temporal results are shown in figure 3.6. The SH-FROG error was 1.5% on a 512×512 grid. The retrieved spectrum and phase are shown in figure 3.5 featuring excellent agreement with the measured spectrum.

A FWHM pulse duration of 41 fs is obtained after compression with a peak power of 62% of the Fourier limited pulse ($\tau_{FL} = 39 \text{ fs}$). Compression closer to the Fourier limit is hindered by the phase ripples visible in figure 3.5 that are hardly removable by common compression techniques. These ripples are a consequence of SPM based nonlinear broadening. A simulated compressed pulse was obtained by propagating the retrieved input pulse (shown as inset in figure 3.6a) using equation 3.36 with a nonlinear phase shift of 59 rad and removing the GDD component of the Fourier

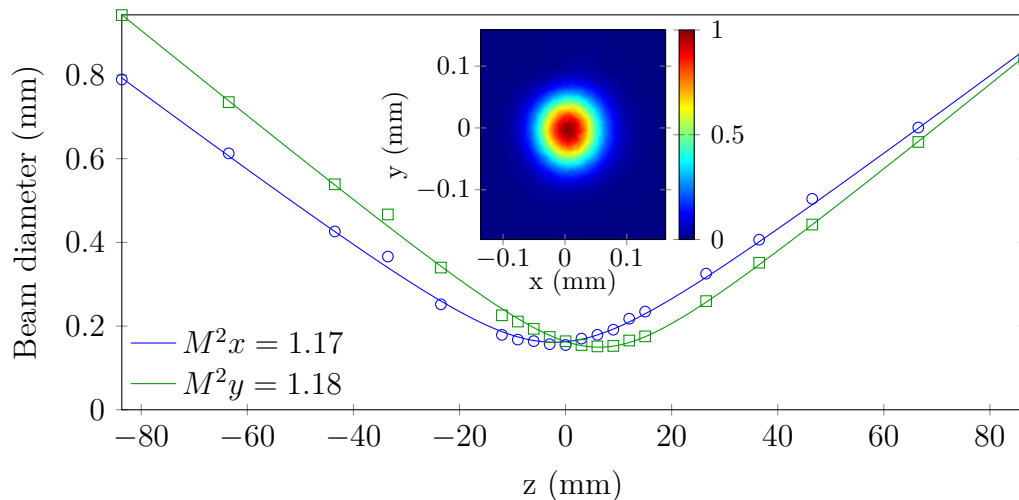


Figure 3.7: Beam quality factor M^2 of the spectrally broadened output beam. The inset shows the beam profile in the focus ($z = 0$).

domain phase term. The simulated compressed FWHM duration is 40 fs and the simulated peak intensity is 66 % of the Fourier limit, both in accordance with the measured values. The agreement between simulation and measurement also confirms that the problematic phase ripples originate from the self phase modulation and especially the mirror dispersion does not contribute significantly to the degradation of compression quality.

The multipass cell setup is expected to keep the beam profile spatially clean and preserve the propagating mode, hence the M^2 value of the broadened pulse is expected to be close to the input value. To verify this expectation the M^2 of the beam was determined using a commercial measurement device (*Ophir Spiricon M^2 -200 s*). A 1 : 4 mirror telescope in front of the measurement device was necessary to adapt the beam size to the specifications of the device. The M^2 of the input beam is 1.10×1.09 (x value \times y value, see figure 2.4). It slightly increases after propagation through the multipass cell in vacuum conditions to 1.15×1.11 . The increase is attributed to the imperfectness of curved optics, in combination with 45 mirror bounces. For the currently discussed working point at 600 mbar of argon the M^2 further increases to 1.17×1.18 . The measurement is shown in figure 3.7. This minor change of beam quality is attributed to some nonlinear effects that are not perfectly compensated for by the multipass setup. The slight astigmatism is likely caused by using the curved mirrors with an incident angle different from 0° . The behavior of astigmatic beams in a multipass cell is treated in more detail in section 3.6.1.

In addition to the mode preserving properties, the spatial distribution of frequencies is investigated using an imaging spectrometer. In an imaging spectrometer, a slit selects a central cut through the beam in vertical direction. A curved mirror system within the spectrometer images the slit plane onto a camera. A grating placed into the imaging system shifts the image position horizontally depending on the wavelength. By rotating the beam, the spatial distribution of wavelengths in x and y direction can be determined. A commercial device (*Acton Research*

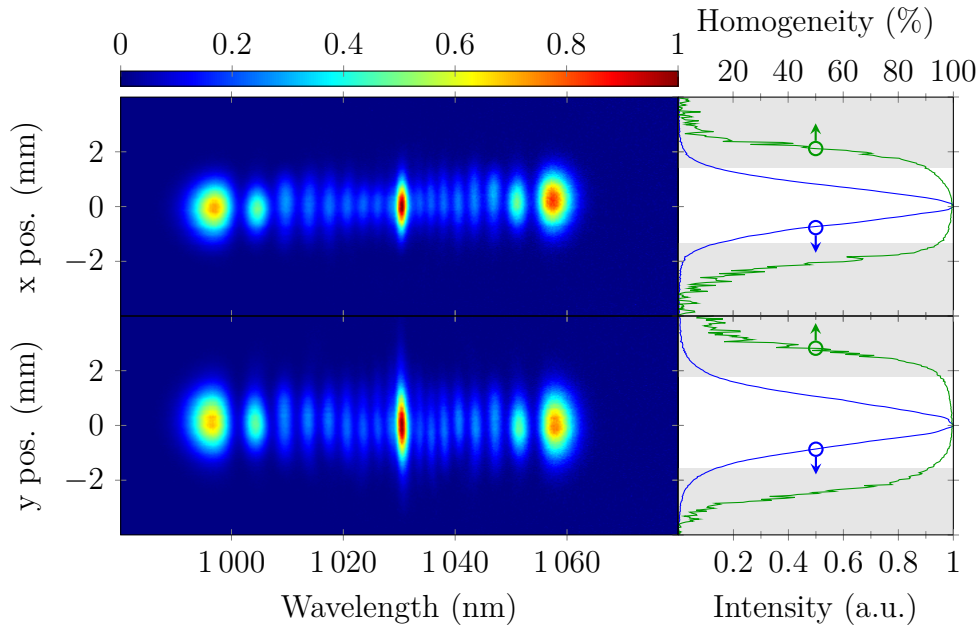


Figure 3.8: Spatial wavelength distribution for the x and y axis of the output beam. The blue curve on the right shows the normalized sum along the wavelength axis of the image on the left. The white area marks the positions where this normalized sum is bigger than $1/e^2$. The green curve shows the corresponding homogeneity value.

Corporation) is used for the following measurements. The wavelength axis of the camera image was calibrated by fitting the measured spectrum of the same beam to the vertical integral of the camera image. The measurement results are shown in figure 3.8. A figure of merit called homogeneity V is commonly used [115, 116, 120] to specify the spatial quality of the broadened beam. It is defined as a variant of a normalized cross correlation

$$V = \frac{[\int |A(\lambda)| |A_0(\lambda)| d\lambda]^2}{\int |A(\lambda)|^2 d\lambda \int |A_0(\lambda)|^2 d\lambda}, \quad (3.70)$$

where $|A(\lambda)|$ is the spectral amplitude, and $|A_0(\lambda)|$ is the reference amplitude at the peak intensity of the beam. The output spectrum features high homogeneity values over 90% within the $1/e^2$ diameter for both axes. The intensity-weighted averages of V over the beam are 96.7% for the x-axis and 97.3% for the y-axis. These values are in excellent agreement with the expected filtering capabilities of a multipass cell.

In conclusion the application of a multipass cell for high energy nonlinear broadening is demonstrated. To the best of the author's knowledge, the output energy of 17.8 mJ at a repetition rate of 5 kHz represented the highest output energy of a nonlinear broadening stage with preserved beam quality at the date of measurement. Higher energies are shown in later sections of this work. The achieved pulse duration of 41 fs is a promising first step towards the few-cycle regime.

Although the input energy of 18.6 mJ yields record breaking results, it is still significantly less than the 200 mJ available from the main thin-disk amplifier. Assuming perfect mode matching, the used input energy corresponds to a fluence of about 0.17 J/cm^2 on the end mirrors. The damage threshold of the used coating

was measured to be about 1 J/cm^2 (measurement was done in a dedicated setup in laboratory atmosphere) and consequentially the mirrors are supposed to support higher energies. However, experimentally damages were regularly observed close to 0.25 J/cm^2 if perfect mode matching is assumed. This difference of damage threshold is attributed to the following mechanisms: First of all perfect mode matching is hardly achievable and the beam size on the end mirrors typically oscillates. Thus spot sizes smaller than the eigenmode are regularly observed. Additionally Kerr lensing yields smaller eigenmodes and hence increases the fluence on the mirrors. The mirror coating is also used in a noble gas atmosphere with almost no water vapor present. This fact is assumed to lower the damage threshold of optics [89]. Finally the onset of ionization can alter the propagation due to the change of refractive index caused by the ionization [105]. If the ionization process does not absorb a significant portion of the pulse energy [121], the changed propagation can lead to a smaller spot size on the end mirrors with a fluence high enough to cause damages. In the current setup a target fluence of 0.17 J/cm^2 was determined to be robust against potential damages even considering all the effects mentioned above. Since the fluence on the mirrors and the intensity in the focus are both on the edge of what is considered safe, the energy sent through the setup is close to the theoretical maximum for this cell and pulse duration (see equation 3.63).

3.5 Limitations

To obtain a better understanding of the limiting factors and to reveal ways of scaling towards higher energies and shorter pulse durations, some features of multipass cell based broadening are discussed in more detail in the following sections. As the energy is mainly governed by the mirror damage and ionization threshold and the mirror damage threshold is difficult to optimize, a deeper investigation of gas ionization is performed. This is followed by an explanation why pulse durations shorter than approximately 40 fs could not be obtained in the presented system.

3.5.1 Ionization

The maximum energy in a multipass cell is limited by the ionization threshold and the damage threshold of the optics. Understanding the behavior of the ionization threshold in the proposed setup is hence an important aspect to investigate potential ways of energy scaling.

It is generally agreed upon that the ionization threshold depends on the pressure, the gas used and the pulse duration [122, 123]. Two regimes are typically distinguished to describe the breakdown intensity: the multiphoton ionization regime and the cascade ionization regime [123, p. 649]. In the multiphoton regime, the high intensity of a laser pulse triggers the simultaneous absorption of multiple photons. In this regime the ionization threshold scales approximately as

$$I_{th} \propto p^{-1/k}, \quad (3.71)$$

where k is the amount of laser photons needed to reach the ionization energy of the gas used [122]. For $\lambda = 1030 \text{ nm}$, $k \approx 21$ for helium and $k \approx 13$ for argon.

Experimentally slightly different values of k between 8 [124] and 10 [123, p. 634] were observed for argon. The multiphoton regime shows a weak pressure dependency and has been connected to low absorption [121].

The second regime is covered by cascade ionization. Free electrons are accelerated due to scattering processes triggered by the laser radiation field and eventually reach energies high enough to cause ionization. The numbers of free electron increases, they are again accelerated by the laser radiation and cause even more ionizations. This process is also called avalanche ionization. The ionization threshold in that case scales as

$$I_{th} \propto p^{-1/\alpha} \quad (3.72)$$

where α is a coefficient between zero and one. Assuming electron-ion recombination as dominating loss channel of the cascade process, α is estimated to be approximately $\alpha \approx -1/3$ [123, p. 649]. This regime shows a stronger pressure dependency and has been connected to high absorption [121].

For a pressure p and a pulse duration τ , multiphoton absorption is assumed to be dominant for $p\tau \leq 1 \times 10^{-7}$ torr s [122, 123]. For low pressures or short pulse durations, the probability of an electron triggering an avalanche is low and thus multiphoton ionization dominates [123, p. 645]. A study with a slightly different definition for the onset of breakdown observed a change from multiphoton to cascade behavior for a significantly different value of $p\tau \approx 3 \times 10^{-9}$ torr s in xenon [122].

As the cascade and multiphoton ionization regime show different features with different implications, an investigation was performed to determine in what regime the presented setup operates. To this end the pressure dependency of the breakdown was tracked in the multipass cell. Four configurations are compared: In configuration *A*, a beam diameter of 8 mm on the end mirrors was coupled into the chamber. The alignment was mismatched from the eigenmode on purpose to ensure a growing beam size over the first 20 bounces. Then the beam was coupled out before reaching a complete turn around the propagation ellipse. Configuration *B* is equal to configuration *A* with a mode matched beam. The eigenmode has a diameter of 8 mm on the end mirror and the beam is coupled out after 44 bounces. Configuration *C* is equal to the alignment used in section 3.3. These alignments provide measurements with different focus sizes and accumulated nonlinear phases and enable a more general conclusion. So far all configurations are used with argon. Helium was used in configuration *D*, that otherwise resembles the alignment of configuration *B*. The input energy is slowly increased (roughly 1 mJ steps) until some distortion of the output beam profile is visible. The lowest energy with visible distortions is defined as breakdown energy. The result of this measurement is shown in figure 3.9.

The measurement of helium follows the multiphoton dependency where the k value was previously predicted to be close to 21. In argon two regimes can be distinguished. For a pressure $p \leq 350$ mbar, the breakdown in argon is only weakly pressure dependent with a scaling law that is in accordance to the literature values of $k \approx 8$ [124]. For higher pressures the scaling changes to a stronger pressure dependency closer to $p^{-1/3}$ agreeing well with the value of $\alpha \approx -1/3$ expected for recombination dominated cascade ionization [123, p. 649]. The value of $p\tau$ where the regimes change is 3.7×10^{-10} torr s and hence differs significantly from the published

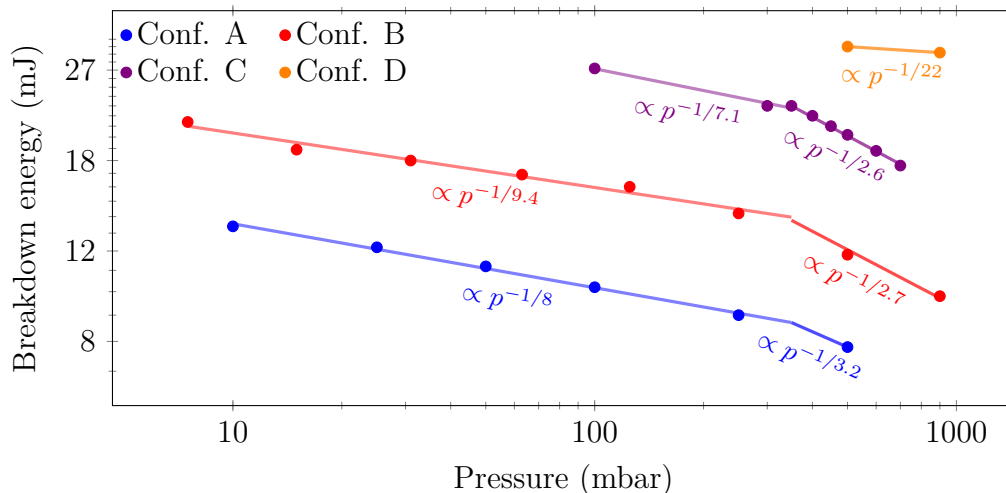


Figure 3.9: The pressure dependency of the observed breakdown energy for an input pulse duration of $\tau \approx 1.4$ ps and for different configurations *A* to *D* (see text) in a double logarithmic plot. Configuration *D* is based on helium, the other configurations use argon.

values of 1×10^{-7} torr s [123, p. 649] or 3×10^{-9} torr s [122]. A possible reason is the used definition of breakdown, that has been shown to alter the threshold value significantly [122]. No dependency on the laser repetition rate was observed as the breakdown energy did not change significantly when the repetition rate of the laser was changed to 1 kHz. Also a change of accumulated nonlinear phase and focus size did not change the scaling of the breakdown energy.

Besides the difference in pressure dependency, the impact of the ionization changed between the multiphoton and the cascade regime. For high argon pressures, a spontaneous sudden and intense drop of output energy to almost zero was observed as soon as the breakdown energy was reached. This is attributed to the expected higher losses during cascade ionization. In the multiphoton ionization regime, this drop was not observed. Instead the onset of ionization caused effects like stray light around the main beam, increased pointing and a lower throughput through the cell. Especially at higher energies mirror damages were observed that were attributed to the onset of multiphoton ionization due to their scaling with pressure and their appearance.

In fact all damages observed in this system occurred at pressures lower than 350 mbar. With the onset of multiphoton ionization, the beam can face serious distortions and develop hot spots or foci at unwanted positions. Without the strong energy absorbance of cascade ionization, this can lead to damages on the multipass optics. Although it is used in the multiphoton ionization regime, no damages have been observed in helium. This is attributed to the lower possible electron density of ionized helium that causes less wavefront distortions.

3.5.2 Wavebreaking

As already mentioned in section 3.4, spectral broadening in the proposed setup beyond a Fourier limit of 39 fs is limited by the generation of new wavelengths around 950 nm. These wavelengths cause an interference in time domain that is imprinted on the pulse phase and hinder the successful compression of the pulse. Broadening to even shorter Fourier limits is only possible if the reason for this wavebreaking is understood.

Operating points with argon pressures ranging from 350 mbar to 700 mbar, cell lengths of 3 m and 8 m, input pulse durations between 740 fs and 1.4 ps and two different end mirror coatings all with a total amount of passes of about 45 showed the generation of these frequencies after a spatially averaged nonlinear phase shift on the order of 50 rad to 60 rad. The generation of new wavelengths has also been observed in [125] for a spatially averaged nonlinear phase shift of about 50 rad accumulated over 44 passes in 4 bar of argon.

So far it was assumed that the nonlinear broadening within this setup is virtually dispersion free and no dispersion induced wavebreaking is possible. Since dispersive effects are expected to stretch the pulse duration during the propagation through the cell, the assumption of a dispersive free system can be validated by measuring the pulse duration after the cell using a SH-FROG. An argon pressure of 900 mbar with 44 passes (beam diameter on end mirror approximately 8 mm) is used to maximize dispersion effects. Since a pulse that is not fully compressed is difficult to retrieve by the SH-FROG algorithm, the output energy of the cell was reduced to 10 mJ yielding a slightly longer output Fourier limit of 58 fs that enables a successful pulse retrieval. The input pulse and the retrieved output pulse together with the measured and retrieved output spectrum are shown in figure 3.10a. The input pulse FWHM duration was measured to be 1.4 ps. The output pulse was measured with an FWHM of 1.3 ps. This measurement confirms the assumption of a virtually dispersion free system at least for this working point.

In a virtually dispersion free system, the measured broadening factor given by τ_{FWHM}/τ_{FL} and the *calculated* nonlinear phase shift $\Delta\phi$ based on equation 3.64 show a proportional behavior as given in equation 3.40. In a dispersive system, the broadening is expected to deviate from this proportional scaling and saturate while approaching higher values of $\Delta\phi$ as the actually experienced phase shift is less than the calculated phase shift due to the decreasing peak intensity during dispersive propagation. The setup described in section 3.3 is used with different argon pressures from 100 mbar to 700 mbar at the respective maximum possible input power before ionization breakdown to obtain a measurement of acquired nonlinear phase shift versus broadening factor. The result is shown in figure 3.10b. No saturation is observed for the used working points. In fact the measurement closely follows equation 3.40 as expected for virtually dispersion free systems.

The previous results lead to the conclusion that the generation of new wavelengths is not induced by dispersion. Also no indication of self-steepening (e.g. possibly induced by some higher order dispersion of the used optics [125]) has been observed. The generation of new wavelengths is hence attributed to attenuation effects. The strongest attenuator in this system is the limited bandwidth of the mirrors used.

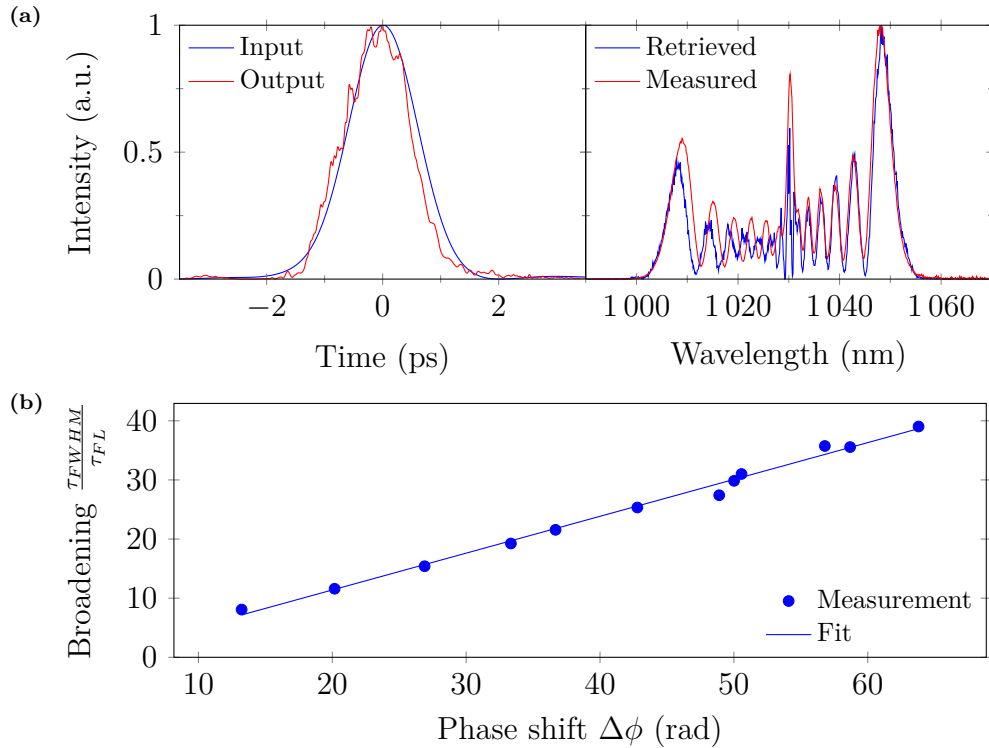


Figure 3.10: (a) The measured input and output pulse (left) together with the measured and retrieved output spectrum (right). The SH-FROG error of the retrieved output pulse is 1.35% with a gridsize of 1024×1024 . (b) The calculated nonlinear phase shift $\Delta\phi$ versus the measured broadening factor τ_{FWHM}/τ_{FL} with the input pulse duration τ_{FWHM} and the output Fourier limit τ_{FL} . The solid line is a linear fit with a proportionality factor of $\sim 0.62 \approx 1/\sqrt{e}$.

To show that this limited bandwidth can indeed trigger the breaking of an optical pulse even though the spectrum of this pulse is still fully supported by the mirror, a simple simulation is used. First an input pulse is retrieved that best connects the measured input spectrum to a reference output spectrum (shown in figure 3.11a, the retrieval method is introduced in appendix C). A nonlinear phase shift of 1.4 rad is added to this pulse corresponding to one transition through the focus. Subsequently the pulse is attenuated using the reflectivity curve of the mirrors as depicted in figure 3.11b. The addition of a phase shift and subsequent attenuation is repeated 45 times adding up to a total nonlinear phase shift of 63 rad. The resulting simulated output spectrum is then compared to the reference output spectrum measured under the same conditions: 45 passes of 17 mJ pulses in 700 mbar of argon resulting in a nonlinear phase shift of $\Delta\phi = 63$ rad. The simulated and measured spectrum are shown in figure 3.11b. A very similar buildup of wavelengths around 950 nm is observed in the simulation and measurement. Note that this simulation does not include any form of material or mirror dispersion.

A possible explanation for the observed buildup has already been given in section 3.1.3 as special case of four wave mixing. A buildup of wavelengths is observed since the recombination to the original center wavelength has been made impossible by the attenuation of the necessary symmetric wavelength. Changing the bandwidth of the coating in the previously introduced simulation has only a minor impact on this

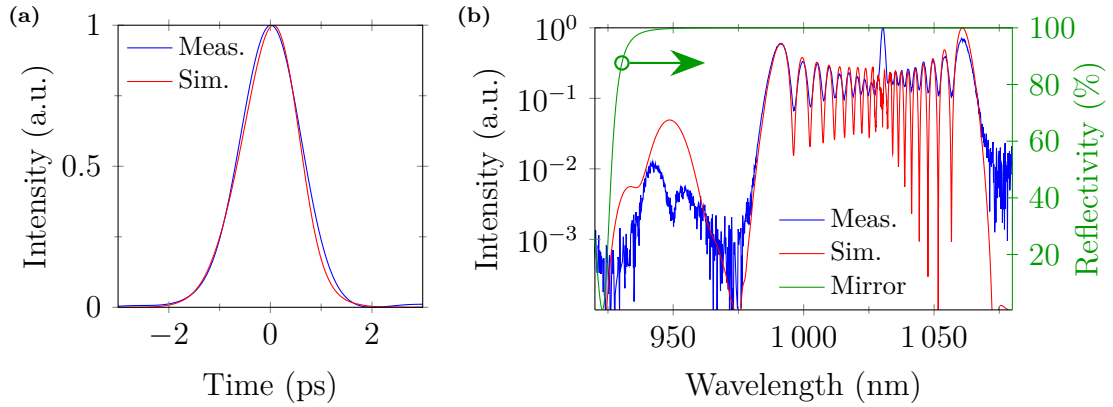


Figure 3.11: (a) The input pulse that best explains the observed broadening (simulated) compared to the actually retrieved input pulse (measured). (b) The reflectivity curve of the used mirror (green) and the measured (blue) and simulated (red) output spectrum, where the mirror reflectivity has been incorporated into the simulation.

effect, yet the simulation showed a reduced buildup if the nonlinear phase per pass is reduced. Thus the broadening factor can be possibly enhanced by distributing a nonlinear phase > 60 rad over more passes than 45. The current setup however does not support more than 50 passes. Thus an improved setup relies on bigger optics and more passes with potential disadvantages like lowered stability and stronger dispersion effects.

Even if the breakup of the pulse can be avoided, high damage threshold optics based on quarter wave stack coatings with Ta_2O_5 or HfO_2 as high index material only support a bandwidth of about 150 nm around a central wavelength of 1030 nm. It is later shown in section 3.6.6 that in a best case situation this would allow for a pulse duration of about 28 fs.

3.6 Energy Scaling

The results from the previous section revealed that a significant increase of the broadening factor is not feasible with the proposed setup and shorter pulses might be reached in a second nonlinear compression stage. Such a strict limitation has not been found for the input energy. If the coating of the end mirror is optimized for highest damage threshold, the input energy is only restricted by the ionization intensity of the gas used. Thus a straightforward way to increase the ionization intensity is to use a gas that is more difficult to ionize than argon, i.e. neon or helium. The nonlinear refractive indices for helium and neon are $n_2^{(He)} \approx 0.4 \times 10^{-20} \text{ cm}^2/\text{W}$ and $n_2^{(Ne)} \approx 0.9 \times 10^{-20} \text{ cm}^2/\text{W}$ [126], thus the nonlinearity is about 28 times (helium) or 11 times (neon) less than in argon while the estimated breakdown intensities in the multiphoton regime are about 3 times (helium) or 2.5 times (neon) higher than in argon [110]. The higher breakdown intensities can hence not compensate for the lower nonlinearity and significantly higher pressures are needed if helium or neon should be used in the proposed system. Due to its size and design, the pressure in the chamber is restricted to atmospheric pressure and neither the usage of helium

nor neon is expected to reach high broadening factors with this limitation. Thus in the following some methods are investigated that have the potential to avoid ionization even at higher energies with a focus on argon as nonlinear medium.

3.6.1 Astigmatic or Elliptic Beams

If the Gaussian input beam is exchanged for an elliptic or astigmatic beam, the waist diameter within the multipass cell becomes effectively larger. This is due to the fact that both axes of the beam have their focus at differing positions (astigmatic beam) or only the major axis experiences a strong focus while the minor axis cannot be focused tightly (elliptic beam).

Building a multipass cell with a proper eigenmode for an elliptic beam is challenging. Thus the prospects of this approach were investigated with the cell proposed in section 3.3. The results are assumed to hold for all variants of gas filled multipass cells.

It was noted that a slight astigmatism in an input beam is reduced after propagation through the cell. An exemplary propagation where this effect is especially pronounced is shown in figure 3.12a. The M^2 of the beam after 20 passes in the cell was measured in vacuum conditions (output energy 3.2 mJ) and with 500 mbar of argon (output energy 9.1 mJ). The beam diameter on the end mirrors was 8 mm. After a nonlinear shift of $\Delta\phi \approx 9$ is accumulated, the original astigmatism of the input beam seems to be gone. Note that mirror telescopes with large angle of incidents can obscure this effect as they reintroduce some astigmatism.

To investigate this cleaning mechanism further, an adaptive mirror was introduced in the beam path in front of the multipass cell. The adaptive mirror consists of a thin mirror in a custom mount. A screw on the back of the mount induces a cylindrical strain by pressing the mirror against two resting points. This strain is converted to a cylindrical bending of the mirror that creates a variable amount astigmatism. The astigmatism was changed such that the beam could propagate through the cell without any clipping (40 passes, 8 mm beam diameter on end mirror). The amount of introduced astigmatism was measured by focusing the input beam with a diameter of 16 mm using a $f = 1$ m lens and a focus distance between major and minor axis of 24 mm was observed. The cell was filled with 900 mbar of argon and the input power was gradually increased. The beam profile after the cell was attenuated by a fused silica wedge, decreased in size by a telescope and finally measured with a camera. The evolution of this highly astigmatic input beam is depicted in figure 3.12b. The shape of the beam profile saturated after 34 W input power. A notch filter was used after saturation was reached to remove the wavelengths around 1030 nm and only investigate the beamprofile of the newly generated wavelengths. The wavelengths that were created by the SPM effect show a virtually perfect Gaussian beam profile. Thus obviously some mechanism in the cell filters the astigmatism and the remaining high order aberrations can be exclusively attributed to remaining 1030 nm components.

The origin of this effect can be understood if the astigmatic input beam is decomposed into a fundamental mode and some higher order modes. The modes defined by equation 1.25 span the complete solution set of the paraxial Helmholtz

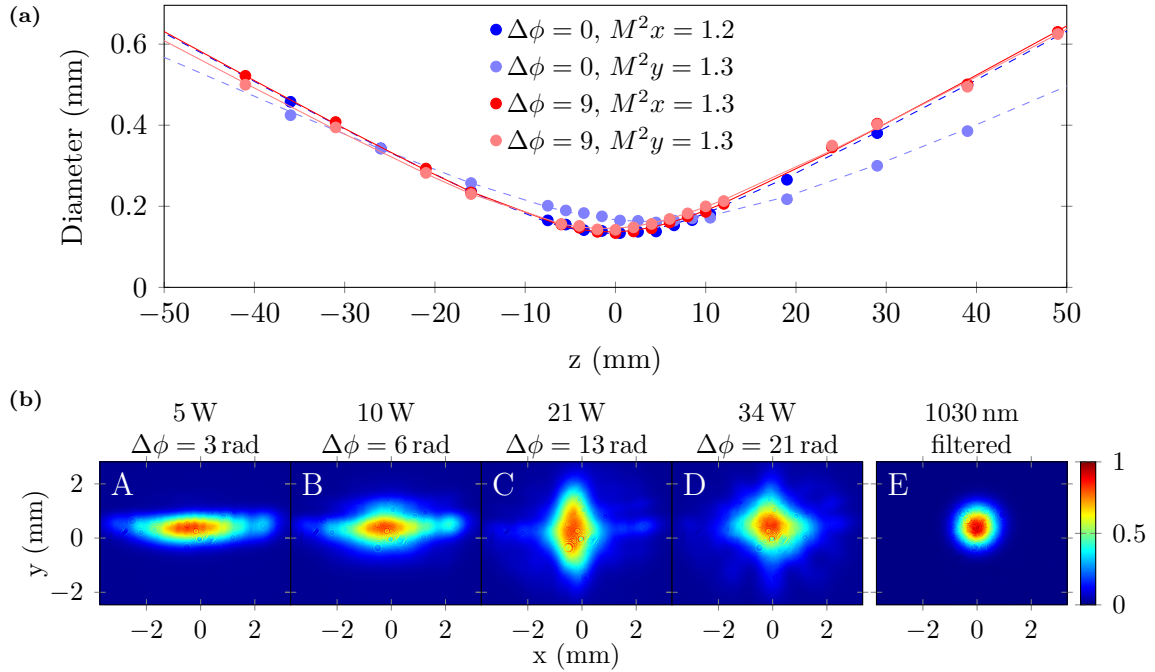


Figure 3.12: (a) The M^2 caustic after 20 passes in the multipass cell under vacuum conditions (blue) and for 500 mbar of argon (red). (b) The evolution of the output beam profile for a highly astigmatic input beam after 40 passes in 900 mbar of argon (A to D). Shown in plot E is the beam profile at 40 W if the input wavelength 1030 nm is filtered out.

equation. Hence every (coherent) paraxial beam can be decomposed into these modes. A simple example for an elliptical beam is the mode $E_{0,0} + 0.05E_{0,2}$. For an elliptical or astigmatic beam, the fundamental mode is often still the dominant mode. The Kerr lensing continuously couples some energy from the fundamental into the higher order modes, but the weak higher order modes still face the same dephasing mechanism that also ensures the mode preserving during self phase modulation (figure 3.2). Ultimately the energy is coupled back into the dominating fundamental mode and the output beam is cleaned.

Additionally to the mode dephasing, the Kerr effect also couples the major and minor axis of a beam. If for example the minor axis is at a focal position, a strong Kerr lens is induced for both the major and the minor axis due to the higher intensity. The major axis experiences an additional lensing effect and contracts. Thus the major axis caustic approximates the caustic of the minor axis. The mutual influence of major and minor axis is assumed to further enhance the evolution to a rotationally symmetric output mode.

While this process is useful to enhance the robustness of the output mode, it renders the usage of elliptical or astigmatic beams for energy throughput enhancement ineffective. The energy is eventually coupled back into the fundamental mode and the ionization would be triggered at comparable levels as for a Gaussian input beam.

3.6.2 Thin Plate Multipass Cells

Since ionization is the main challenge in energy scaling, using solid thin plates in a multipass cell may improve the energy throughput. The thin plates can be placed close to the end mirrors to avoid damages while the cell is operated in vacuum to avoid ionization in the focus. With each transition through a plate some nonlinear phase is accumulated. The buildup of unwanted modes is prevented if the fundamental mode and the higher order modes sufficiently dephase during the propagation between two passes. This is the same mechanism as introduced in figure 3.2 with the difference that the dephasing takes place over several passes instead of a single pass. The maximum nonlinear phase per pass is limited to values less than 0.1π rad [22] to avoid a catastrophic buildup of higher orders before the dephasing couples the energy back to the fundamental mode. Accumulating a significant amount of nonlinear phase shift hence calls for a large number of passes. As an example a thin plate multipass is expected to require about 200 passes to reach the previously demonstrated total nonlinear phase shift of ~ 60 rad. Also ensuring the dephasing is challenging for a resonator near the stability edge as needed in case of large beam diameters on the end mirror [22].

To test the performance of a thin plate approach in the multipass cell setup, two uncoated fused silica plates with a thickness of 1 mm and a diameter of 200 mm were placed in Brewster's angle into the setup. A configuration with the plates being close to the end mirrors and a configuration with the plates being close the focus was tested. The amount of passes is 45 and the eigenmode size is equal to the setup used in section 3.3. About 90 % of the input energy was measured at the output of this multipass cell configuration. The slightly higher losses compared to a gas filled chamber are attributed to the residual reflection from the surface of the uncoated fused silica substrates. The total dispersion caused by fused silica is about 1700 fs^2 [127] and hence comparable to the total dispersion in 1 bar of argon (1900 fs^2 [98]). Thus dispersion is assumed to be negligible.

The input power or equivalently the expected accumulated nonlinear phase is gradually increased and the broadening factor is measured. The result is shown in figure 3.13a. In a dispersionless case, the broadening factor is proportional to the calculated nonlinear phase (shown as solid line in figure 3.13a, compare to eq. 3.40 and figure 3.10b). This behavior is not observed for the thin plate multipass. Instead the broadening factor saturates at a value of about 8. Assuming a distortion free system and hence the validity of equation 3.40, this broadening factor can be reached over 45 passes with a phase shift per pass of 0.09π rad. Thus some mechanism stops the accumulation of nonlinear phase while approaching a nonlinear phase per pass of 0.09π rad.

The beam quality M^2 was measured using the same parameters as for the measurement of the broadening factor. Figure 3.13b shows the M^2 value of the output beam versus the accumulated nonlinear phase per pass. The phase shift per pass was obtained by finding the nonlinear phase that best explains the broadening from input to output spectrum (see appendix C for this method) and dividing this phase by 45. With this method the determined nonlinear phase is independent from a potential propagation distortion. Starting at a phase shift per pass of

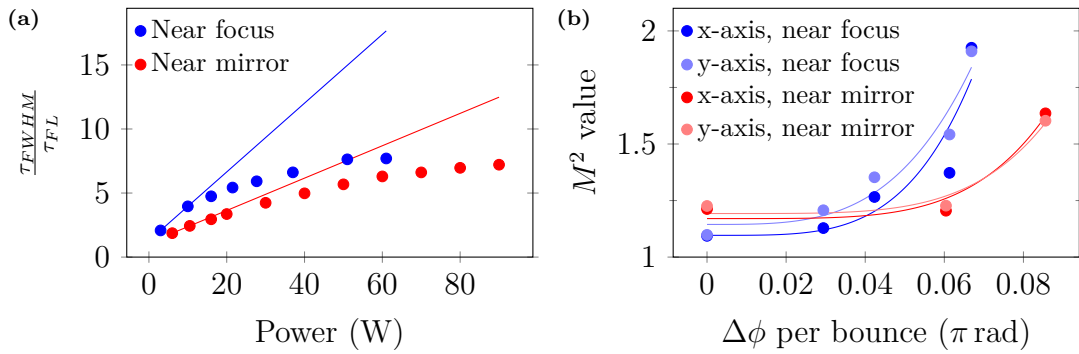


Figure 3.13: (a) The broadening factor of a thin plate multipass as ratio of input pulse duration τ_{FWHM} and output Fourier limit τ_{FL} versus the input power. The position of the thin plates was symmetric around the focus with a distance of 600 mm (blue) or 850 mm (red) from the focus. The solid lines show the expected linear evolution of the broadening factor (see eq. 3.40). (b) The measured M^2 value on x and y axis after propagation through the thin plate multipass for the configurations introduced in (a). The solids lines show a power function fit to the measurement points as guidance.

about 0.05π rad, the beam quality deteriorates quickly and significant higher order components are measured in the mode. With the approach towards a phase shift per pass of 0.09π rad the beam can be considered not to follow Gaussian propagation anymore. The saturation process observed in figure 3.13a is therefore attributed to the degradation of mode quality. The peak intensity of the beam decreased with the lower beam quality and hence the accumulation of nonlinear phase was stopped.

The configuration where the thin plates are close to the end mirrors shows a more robust behavior. This might be explained by the fact that the focal planes are imaged from one pass to another in a concentric resonator with a distance of $\sim 4f$ between the end mirrors. Thus distortions near the focus can build up more easily. The highest usable phase shift per bounce in the proposed setup is approximately 0.06π rad. According to [22] this value lowers even further if the cell is operated closer to its stability edge to reach bigger diameters on the end mirror.

A total nonlinear phase shift of ~ 60 rad for a broadening factor of about 35 hence requires a large amount of over 300 passes. Using 1 mm thick plates, a phase shift of 0.06π rad is experimentally reached with 10 mJ of input energy (1.4 ps pulse duration). Higher energies than 10 mJ require thinner plates that are difficult to manufacture with large diameters. This is in sharp contrast to the necessity of a larger diameter for a setup with 300 passes. Alternatively each pass can be equipped with its own thin plate. This would require each of the 300 mirror bounces to be separable and lead to an increased distance between the passes with even higher demands on space and optics.

In conclusion a thin plate based multipass cell that approximates the demonstrated performance of the gas filled cell puts significantly higher demands on the size of the setup and optics. While this approach is technically not feasible with the goal of a large broadening factor, it might be suitable for the nonlinear compression of shorter pulses with a smaller compression factor in mind. An example is the compression of the 40 fs pulse obtained in the presented cell towards a pulse duration on the order of 10 fs in a second multipass stage.

3.6.3 Pulse Stacking

The basic idea of pulse stacking is the division of a single input pulse into multiple weaker copies. Each of these copies is separately nonlinearly broadened and a higher total energy can be used since each pulse has a lower peak intensity. The division of the pulses can either happen by spatially dividing the pulses with beam splitters such that the nonlinear broadening is done on separate paths or in different setups [128]. Or alternatively by delaying a fraction of the pulse such that the broadening is performed at different points in time [129]. In both cases the pulses need to be coherently combined after propagation. This especially means that the accumulated phase of all pulses has to be exactly the same.

The case of spatial separation puts high demands on stability and reproducibility of the setup and often some active phase stabilization has to be implemented even if nonlinear effects are kept at a low level (e.g. in [47]). A stable implementation in a highly nonlinear system does not seem feasible [47].

A more promising approach for spectral broadening is the temporal separation of pulses [129]. The coherent combination is greatly simplified in this case since each pulse uses the same propagation path with a temporal distance of only a few picoseconds to nanoseconds – thus any distortion is imprinted on each pulse in a similar manner. To create a temporal separation, a highly birefringent material is used that causes a temporal delay between s and p polarization upon propagation.

A simple experiment in the presented system was performed to test this approach. Similar to the design proposed in [129], a highly birefringent calcite crystal with a size of $20 \times 20 \times 3 \text{ mm}^3$ is used to create a delay of about 1.6 ps. The nonlinear phase accumulated in this crystal is negligible for pulse energies up to 20 mJ and the delay introduced in this experiment is sufficient to separate the peaks of the generated two pulses. A complete separation of the pulses in time domain is not achieved. During the experiment it was noted that in the temporal regime where the shoulders of both pulses overlap, the polarization is in general elliptical. The third order nonlinearity introduces a change of polarization for input beams that are neither linearly nor circularly polarized [96, p. 220]. This effect is known as *nonlinear polarization rotation* and distorts the polarization of the overlapping pulses. A coherent combination of both pulses is severely hindered under this circumstance.

This process can be avoided by completely separating both pulses in time domain using delays on the order of 10 ps or more with calcite crystals longer than $\sim 20 \text{ mm}$. Keeping the unwanted nonlinear phase accumulated in the birefringent crystal constant then requires an about 2.5 times larger beam diameter or equivalently a crystal with a size of about $50 \times 50 \times 20 \text{ mm}^3$. Scaling the input energy to higher values than 20 mJ increases the unwanted nonlinear phase and hence an appropriate scaling of the crystal is necessary that soon reaches the limit of commercial availability. In fact no distributor was found even for a calcite crystal size of $50 \times 50 \times 20 \text{ mm}^3$ and similar restrictions apply for other crystal materials.

In addition to the problematic scaling of crystal size, the coherent combination turned out to be very sensitive to the broadened spectrum or equivalently the nonlinear phase of both pulses. The combination quality is insufficient if the accumulated nonlinear phase of both pulses is not nearly identical (e.g. because the

leading pulse is slightly stronger than the trailing pulse or due to energy fluctuations). Ensuring this identical phase is especially challenging in case of large broadening factors and thermal issues caused by high average powers. In conclusion pulse stacking is not considered to be a promising method in order to obtain higher throughput energies.

3.6.4 Circular Polarization

As previously mentioned only two polarization states are not changed by third order nonlinearities: Linear and circular polarization [96, p. 220]. The previous experiments were done with linear polarization as this is the preferred output polarization. However the breakdown intensity in gases can be increased if circular polarization is used. According to literature between 20 % and 50 % higher intensities can be used with circular polarization in hollow core fibers before ionization sets in [130–132]. At the same time the damage threshold of the optics is not expected to change significantly for a pulse duration of 1.4 ps [133].

The published results were reproduced in the multipass cell by placing a quarter wave plate ($\lambda/4$) with a thickness of 2 mm (aperture 38.1 mm) into the input beam (diameter 16 mm). In a first experiment the $\lambda/4$ waveplate was aligned to yield linear polarization and the power was increased until ionization was visible. Then the waveplate was rotated by 45° to obtain circular polarization and the experiment was repeated. With circular polarization gas breakdown could be observed for an input energy that was 39 % higher than for linear polarization.

A disadvantage of circular polarization is the effectively lowered nonlinear refractive index $n_2^{(circ)}$ compared to the index in case of linear polarization $n_2^{(lin)}$ [96, p. 221]

$$n_2^{(circ)} = \frac{2}{3}n_2^{(lin)}. \quad (3.73)$$

This is also confirmed by the narrower spectrum measured in the previously mentioned experiment in case of circular polarization. Hence the advantage in breakdown intensity is partially decreased by the necessity to increase the gas pressure by 50 % to compensate for the lower nonlinearity. Depending on the working point this pressure increase results in a breakdown intensity lowered by 5 % (multiphoton regime) or 13 % (cascade regime) for argon (see figure 3.9).

According to equation 3.63, the increase in actual maximum throughput energy scales with the squareroot of the breakdown energy increase, i.e. $E_{max} \propto \sqrt{E_{BD}}$. Incorporating the scaling induced by the required higher gas pressure, the total energy gain for circular polarization is approximately $\sqrt{1.39 * 0.87} \approx 1.1$ (cascade regime) or $\sqrt{1.39 * 0.95} \approx 1.15$ (multiphoton regime) compared to the linear case.

Not included in these numbers is the observed high nonlinearity in the L/4 waveplate for input powers beyond 110 W that is expected to cause higher losses and the losses of converting a broadband circularly polarized beam back to linear polarization.

In conclusion slightly higher energies are expected from using circular polarization. The benefit is however rather small compared to the added complexity and the usage of circular polarization is not considered to be reasonable in the discussed system.

3.6.5 Input Pulse Duration

The pulse duration used in the multipass is to a certain extent a variable that can be optimized. In the previous sections a pulse duration of 1.4 ps is used. An optimization of the amplifier system however also enables an input pulse duration down to 0.74 ps (see figure 2.30). Alternatively the input pulse can be stretched to a longer duration by tuning the compressor after the amplifier chain.

Thus in the following a theoretical investigation is done in order to estimate to what extent the pulse duration can be optimized to increase the energy after the cell. The Fourier limit of the output pulse is kept constant and the amount of passes is fixed to 45, which is close to the maximal feasible amount of about 50 in this setup. The following scaling laws are introduced

$$\frac{\tau_{FWHM}}{\tau_{FL}} \propto \Delta\phi \quad \text{eq. 3.40} \quad (3.74)$$

$$\Delta\phi \propto n_2 P_{max} \propto p \frac{E_{max}}{\tau_{FWHM}} \quad \text{eq. 3.64} \quad (3.75)$$

$$I_{BD} \propto \frac{E_{BD}}{\tau_{FWHM}} \propto (p \tau_{FWHM})^{-1/8} \quad \text{multiphoton, fig. 3.9 and [123]} \quad (3.76)$$

$$I_{BD} \propto \frac{E_{BD}}{\tau_{FWHM}} \propto (p \tau_{FWHM})^{-1/3} \quad \text{cascade, fig. 3.9 and [123]} \quad (3.77)$$

$$E_{LIDT} \propto \tau_{FWHM}^{0.3} \quad [134] \quad (3.78)$$

$$E_{max}^2 \approx E_{LIDT} E_{BD} \quad \text{eq. 3.63.} \quad (3.79)$$

Here I_{BD} is the breakdown intensity, E_{BD} is the energy at which gas breakdown occurs, p is the gas pressure, E_{LIDT} the energy at which a mirror damage occurs and E_{max} is the maximum possible input energy for the given parameters under the condition that the eigenmode is optimized. The scaling law for the breakdown intensity I_{BD} varies between the multiphoton absorption and cascade ionization regime and the pulse duration dependency is predicted [123, p. 648] to be similar to the pressure dependency.

Simplifying the scaling laws then finally yields

$$E_{max} \propto \tau_{FWHM}^{0.49} \quad \text{multiphoton regime} \quad (3.80)$$

$$E_{max} \propto \tau_{FWHM}^{0.18} \quad \text{cascade regime.} \quad (3.81)$$

Thus in both cases longer input pulses allow for higher input energies. While this relationship is especially pronounced in the multiphoton ionization regime, the dependency is significantly weaker within the cascade ionization regime.

Increasing the pulse duration to reach higher throughput energies is hence rather ineffective in the cascade ionization regime. Shorter input pulses require less nonlinear phase for the same output Fourier limit and show a less modulated spectrum leading to an increased compression quality. It is therefore favorable to use the shortest pulse that does not lead to significantly lower energies. In conclusion a good working point for the multipass cell is the transition between multiphoton and cascade ionization. For the proposed system this is at an argon pressure of about 350 mbar. This working point is reached with an input pulse duration of approximately 1 ps close to the actually used duration of 1.4 ps.

3.6.6 Cell Length

A parameter that has not been changed so far is the length d of the multipass cell. The total length of the setup is $d = 2R \cdot s$. Thus with a constant mode parameter s (i.e. a constant amount of passes), the cell length d and the radius of curvature of the end mirrors R are linearly connected. According to equations 3.58 and 3.59, the spot areas of the eigenmode scale linearly with R . This also means that the energies E_{LIDT} and E_{BD} required to reach a fluence close to mirror damage or gas breakdown also scale linearly with R . Using equation 3.63 this yields an expected scaling similar to

$$E_{max} \propto d \quad (3.82)$$

where d is the cell length.

To investigate this scaling a new multipass cell with a length of ~ 8 m is designed. The cell follows the design proposed in figure 3.3. The radius of curvature of the end mirrors is $R = 4$ m with a surface size of 300×130 mm². Also a new HfO_2 based coating with a damage threshold > 1.3 J/cm² is introduced for the end mirrors. Guiding and outcoupling optics are still based on the previously used coating design with a damage threshold of > 1 J/cm². Thus this improvement does not change the energy limitation, but decreases the risk of damaging the end mirrors. A concave mirror with 10 m RoC placed in an optical distance of about 1 m from the incoupling mirror matches the wavefront of the input beam to the eigenmode. The incoupling and outcoupling is done with plane mirrors (diameter 25 mm) placed directly in front of the end mirrors and a window thickness of 2 mm is used for the vacuum chamber. For the following experiments the mode diameter on the end mirrors was about 8.5 mm. The amount of passes was only slightly changed to 43 to enable better mode matching.

Two configurations are tested. In one case argon is used as nonlinear gas to provide maximum spectral broadening. In a second configuration argon is exchanged with 900 mbar of helium and the input pulse duration is significantly decreased. 900 mbar is the maximal pressure possible in the chamber used and allows for the maximum possible spectral broadening in helium with this system. At the same time the usage of helium should provide higher throughput energies. The shorter input pulse duration is also used in argon to evaluate the scaling of the shortest possible output Fourier limit below the 40 fs regime.

Argon Cell

During the commissioning of the new cell, the frontend of the amplifier was upgraded to a more powerful oscillator (*Menlo Systems YLMO*, also see section 2.9). The lower gain narrowing in the amplifier thanks to the higher oscillator energy slightly changed the pulse duration in the cell from 1.4 ps to about 1.25 ps (about 10% shorter). An argon pressure of at least 250 mbar was determined to be necessary to reach an output Fourier limit of $\tau_{FL} \approx 34.2$ fs that is comparable to the results from the previous shorter setup. With an argon pressure of 250 mbar, an energy of 40 mJ could be sent into the cell before damages were observed. Higher pressures caused a

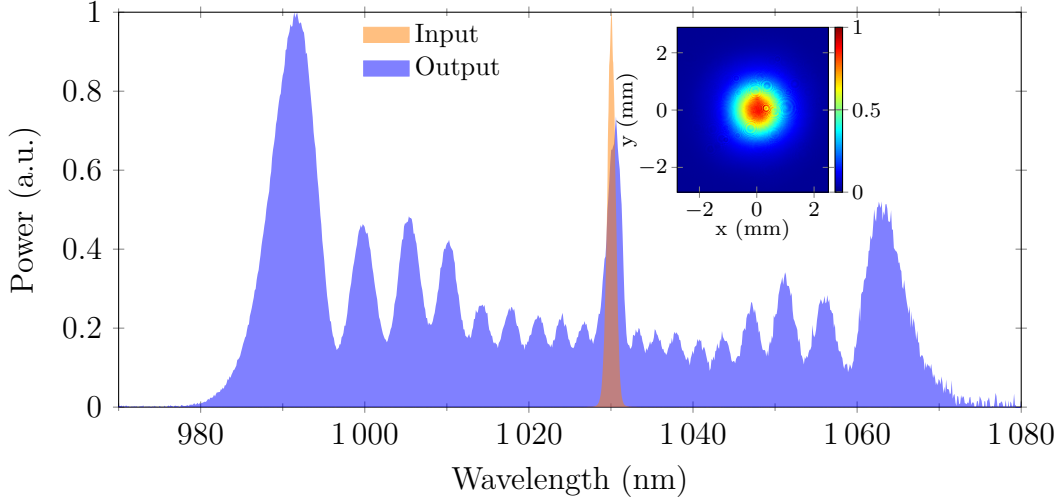


Figure 3.14: The spectrum and beam profile after a multipass cell with a length of ~ 8 m filled with 250 mbar of argon. 40 mJ of pulse energy is broadened over 43 passes from an input pulse duration of $\tau_{FWHM} \approx 1.25$ ps to an output Fourier limit of $\tau_{FWHM} \approx 34$ fs. The energy after the cell is about 39 mJ corresponding to a transmission of about 97.5%.

distorted spectrum similar to what is shown in figure 3.11b. The total accumulated nonlinear phase is retrieved by fitting the input and output spectrum (see appendix C) and is about $\Delta\phi \approx 63$. The corresponding measured spectrum and beamprofile is shown in figure 3.14. The output mode is still considered to be Gaussian and the spectral shape shows no signs of significant degradation. Thus scaling the cell length is a viable way to scale the nonlinear broadening to higher throughput energies.

The observed damages are attributed to the onset of ionization considering the low calculated fluence of just 0.14 J/cm^2 on the end mirrors at the point of damage. For comparison the same mirrors were used with a fluence of up to 0.5 J/cm^2 in a helium atmosphere. The damages were not in the center of the beam profile but distributed around it and the noise created by the damages did not follow the repetition rate of the laser. These observations also support gas ionization as reason for the damages. The ionization is presumably due to multiphoton absorption as indicated by the lack of significant absorption and the used pressure of just 250 mbar (see section 3.5.1).

If the scaling law for the multiphoton ionization regime from eq. 3.76 is combined with the linear length scaling (see eq. 3.82), the shorter pulse and lower pressure in combination with the longer cell is expected to increase the breakdown energy to at least

$$E_{BD}^{(8\text{m})} \approx \left(\frac{1.25 \text{ ps}}{1.4 \text{ ps}} \right)^{7/8} \left(\frac{250 \text{ mbar}}{350 \text{ mbar}} \right)^{-1/8} \frac{8 \text{ m}}{3 \text{ m}} E_{BD}^{(3\text{m})} \approx 58 \text{ mJ}. \quad (3.83)$$

Here $E_{BD}^{(8\text{m})}$ is the breakdown energy for the longer cell and $E_{BD}^{(3\text{m})} \approx 23 \text{ mJ}$ the multiphoton breakdown energy observed for the short cell at a pressure of 350 mbar (configuration C in figure 3.9). Damages that were attributed to ionization were however observed at input energies of about 40 mJ.

It is known from theory [123, p. 628] that the ionization threshold defined as the generation of a certain threshold electron density is independent of the focal volume in the multiphoton regime. Therefore changing the length or eigenmode of the setup should not alter the ionization threshold. Thus to explain the observed mismatch between predicted and observed ionization energy, some mechanism has to be found that causes a smaller waist size and consequentially a higher intensity than predicted. Possible candidates are nonlinear lenses (i.e. Kerr lenses or thermal lenses) or a bad mode matching.

The Kerr lensing in the longer cell is comparable to the lensing observed in the shorter cell due to the similar nonlinearity. If Kerr lensing has an impact on the breakdown energy, the effect is expected to be similar in the short and long cell and the system should still scale as expected. Also the scaling laws have been shown to hold for different Kerr lenses during the measurement in figure 3.9.

In total eight realignments of the input mode were done – partially also including a precompensation of the Kerr lens in the input window – to exclude a wrong mode matching as reason for the lowered ionization threshold. For all alignments severe distortions or damages that were attributed to ionization were observed for pulse energies between 30 mJ and 40 mJ. Hence a false mode matching as primary reason for the earlier breakdown seems unlikely.

Measurements with input powers up to 200 W in vacuum did reveal some mode variations that increased in magnitude over a timescale of 10 min. No spectral broadening was measured, so that these variations can be attributed with high certainty to thermal lenses in the setup. These thermal lenses might be a possible explanation for the creation of the threshold electron density at lower energies than expected. Further scaling should hence be possible if the power absorption in the used optics is reduced to a minimum by improving the coating quality.

Another possibility for the earlier breakdown is that the longer cell reacts more sensitive to the presence of electrons and the breakdown is reached at lower electron densities. It was proposed [135] that an ionized medium does not act back on a propagating beam as long as

$$n_e \ll \frac{7 \times 10^{13} / \text{m}}{w_0^2}, \quad (3.84)$$

where n_e is the electron density. Since the relationship between system length and waist size is $d \propto w_0^2$, a longer cell and equation 3.84 imply a reduced critical electron density $n_c \propto d^{-1}$. According to theory, the multiphoton breakdown intensity in argon scales as $I_{BD} \propto n_c^{1/8}$ [123, p. 628]. Expressing this scaling law using the system length d then yields $I_{BD} \propto d^{-1/8}$. Yet this scaling only accounts for a 10 % drop of breakdown intensity in the longer cell and can only partially explain the observed mismatch of breakdown energy. The thermal lens is hence assumed to be the main contribution leading to the lowered breakdown energies.

Helium Cell

The larger feasible energies in the longer cell enhance the spectral broadening in weakly nonlinear gases like helium. Helium provides a nonlinearity that is about

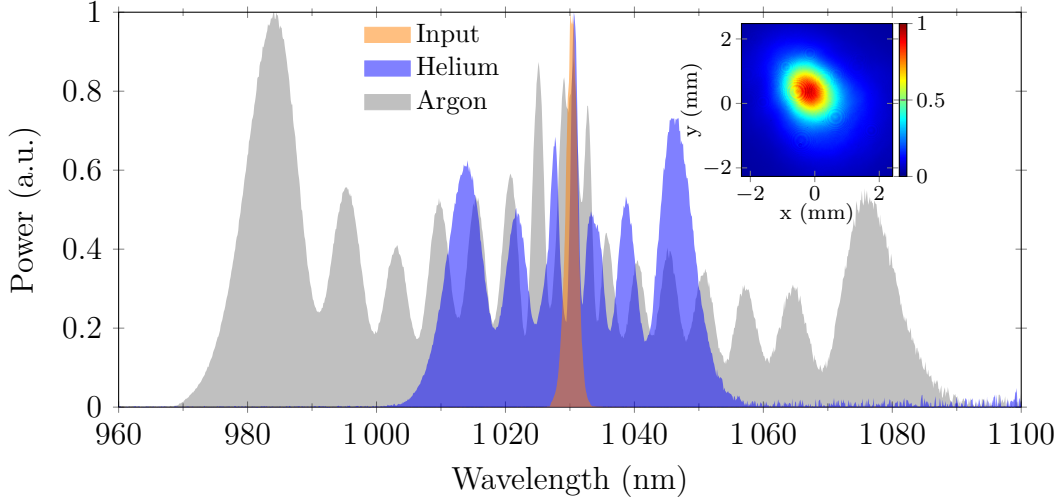


Figure 3.15: The spectrum (blue) and beam profile after a multipass cell with a length of ~ 8 m filled with 900 mbar of helium using an input pulse duration of 740 fs. 75 mJ of pulse energy is broadened over 43 passes to an output Fourier limit of $\tau_{FWHM} \approx 69$ fs. Also shown is the spectrum for 500 mbar of argon for the same pulse duration (grey). In argon 14 mJ were broadened to a Fourier limit of $\tau_{FWHM} \approx 28$ fs. The energy after the cell is about 72 mJ (helium) or 13.4 mJ (argon) corresponding to a transmission of about 96 %.

28 times weaker than in argon while the estimated breakdown intensities in the multiphoton regime are about 3 times higher (see introduction of section 3.6). Thus in the case of the longer cell helium might provide a sufficient broadening for some applications while maximizing the possible throughput energy. To further enhance the broadening in helium, the frontend of the amplifier chain was optimized to yield a shorter pulse duration of 0.74 ps (see figure 2.30).

Assuming a three times higher breakdown energy than in argon and using the multiphoton scaling laws from eq. 3.76 with $k = 21$ for helium [123, p. 634] instead of $k \approx 8$ for argon, the expected throughput energy before breakdown is

$$E_{BD}^{(helium)} \approx 3 \left(\frac{0.74 \text{ ps}}{1.25 \text{ ps}} \right)^{20/21} \left(\frac{900 \text{ mbar}}{250 \text{ mbar}} \right)^{-1/21} E_{BD}^{(argon)} \approx 69 \text{ mJ}. \quad (3.85)$$

Here $E_{BD}^{(argon)} \approx 40$ mJ is the previously measured breakdown energy of argon. These predictions are in good agreement with the measured maximum input energy of 75 mJ. The resulting spectrum and output beam profile are depicted in blue in figure 3.15. The broadening factor is about 11 with an output Fourier limit of $\tau_{FWHM} \approx 69$ fs. A nonlinear phase of $\Delta\phi \approx 20$ is retrieved by fitting, which is still in reasonable agreement with the scaling law from equation 3.40. The output beam profile is more distorted than in the case of argon. This is attributed to the stronger thermal lens and lower correcting nonlinearity. A strong nonlinearity can reduce beam distortions as has been shown in section 3.6.1. A reduction of coating absorption is assumed to yield beam profiles closer to a Gaussian shape

As expected even high pressures of helium yield significantly longer output Fourier limits and lower broadening factors than argon based systems. About 80 % more energy compared to the previously analyzed broadening in argon can be sent into

the setup before damages are observed on the outcoupling optics at a fluence of about 0.5 J/cm^2 . Ionization might play a role for the generation of these damages since ionization is predicted to take place at a similar energy. However the fluence is already close the measured damage fluence of 1 J/cm^2 of these optics. While the throughput energy is nearly doubled, the output Fourier limit is about two times longer than in the previous case of argon. Thus the peak intensity of the compressed pulse is expected to be comparable in both setups.

Still to the best of the authors knowledge the output pulse energies of 39 mJ in argon and 72 mJ in helium represent the highest output energies that were spectrally broadened over factor greater than 10 and output average powers of up to 360 W are reached. Output powers of over 500 W were already demonstrated in multipass cells [125] and the average power is not considered to be a limiting factor. A reduction of the observed thermal lenses should enable even higher energies up to 58 mJ in argon and 100 mJ in helium.

Scaling of Fourier Limit

In section 3.5.2 a wavebreaking mechanism was introduced that limits the total nonlinear phase to values around 60 rad. Reaching significantly shorter output Fourier limits is only possible by using a shorter input pulse (or significantly more passes). For the helium based broadening the input pulse was shortened by a factor of 0.6 from about 1.25 ps to 0.74 ps. To evaluate the expected decrease of the shortest possible output Fourier limit under this circumstance, the setup used for the helium experiment was filled with 500 mbar of argon. This provided a high nonlinearity with low energies around 14 mJ that do not pose a risk for ionization or damages.

A total accumulated nonlinear phase of $\Delta\phi \approx 49 \text{ rad}$ is retrieved for the measured output spectrum shown as grey curve in figure 3.15 and wavebreaking was observed for larger phases. Spectral components are present from 970 nm to 1092 nm and thus cover virtually the complete range of the optical mirror bandwidth in the system (950 nm to 1100 nm). The observed output Fourier limit is $\tau_{FWHM} \approx 28 \text{ fs}$. Thus the expected reduction of the shortest possible output Fourier limit for shorter input pulses can be confirmed, but the scaling is ultimately limited by the bandwidth of the optics used in the multipass cell.

A significant increase of the mirror bandwidth is only possible with lower damage threshold optics. A similar limitation to a Fourier limit of 30 fs has been observed for narrowband high damage threshold mirrors in a setup with an even shorter input pulse duration of 0.59 ps [125]. The obtained output Fourier limit of 28 fs is hence considered to be a lower limit (or close to the lower limit) of high energy multipass cells.

3.6.7 Higher Order Modes

While increasing the cell length is one possibility to further increase the throughput energy, it is limited by the available space and mechanical stability. Yet several possibilities to increase the throughput energy with a constant length discussed in the previous sections turned out to be either ineffective or technically not feasible.

So far the methods used the properties of a Gaussian beam or a change of the multipass design as free parameters to optimize the throughput energy. Input modes different from a Gaussian beam are subject of this section.

It has been noted in section 3.6.1 and figure 3.2 that the output beam of the multipass cell is close to the dominating input mode due to a dephasing of the different mode orders. Changing the dominant input mode from a Gaussian to a higher order mode is assumed to also change the preserved mode within the cell. A very beneficial group of higher order modes for this purpose are the helical *Laguerre-Gaussian* modes LG_{lm} [16, p. 98]

$$\mathbf{U}_{l,m}(r, \Phi, z) = \mathbf{E}_{0,0}(r, \Phi, z) \left(\frac{r}{w(z)} \right)^{|l|} \mathbb{L}_m^{|l|} \left[\frac{2r^2}{w^2(z)} \right] e^{-i(|l|+2m)\zeta+i\Phi}, \quad (3.86)$$

where $\mathbf{E}_{0,0}(r, \Phi, z)$ is the Gaussian beam, $w(z)$ the beam radius and ζ the Gouy phase as defined in equation 1.26 using the cylindrical coordinates $\{r, \Phi\}$ instead of cartesian coordinates $\{x, y\}$ and $\mathbb{L}_m^{|l|}$ is the generalized Laguerre polynomial. Note that the Gouy phase accumulation compared to a Gaussian beam is increased by the value $(|l| + 2m)\zeta$.

The high order modes have a waist size that is $\sqrt{M^2}$ times larger than their embedded Gaussian (equation 1.89). Thus the higher order eigenmodes are also $\sqrt{M^2}$ times larger than the Gaussian eigenmodes calculated in section 3.3. For Laguerre-Gaussian modes, the M^2 scales as [23]

$$M^2 = |l| + 2m + 1. \quad (3.87)$$

The so called *doughnut-modes* LG_{l0} , where $\mathbb{L}_0^{|l|} = 1$, have especially favorable properties. The intensity profile of these modes have a doughnut like shape with zero intensity in the center (at $r = 0$). Thus the point of highest intensity in case of a Gaussian beam has zero intensity for a doughnut-mode. This property is expected to render ionizations much more unlikely. The maximum peak intensity of a doughnut-mode compared to its embedded Gaussian scales as

$$\frac{\max(|\mathbf{U}_{l,0}|^2)}{\max(|\mathbf{U}_{0,0}|^2)} = \frac{(|l|/e)^{|l|}}{|l|!} \stackrel{l=1}{=} \frac{1}{e}. \quad (3.88)$$

Thus about $e \approx 2.7$ times more energy can be used for a $l = 1$ doughnut before the same peak intensity as for a Gaussian mode is reached. Besides the central hole in the intensity distribution, the main difference between a doughnut-mode and a Gaussian mode is the vortex phase component $l\Phi$.

The intensity pattern of a doughnut mode and a Gaussian beam are similar enough that a mode conversion can be done with good efficiency simply by adding a vortex phase component $l\Phi$ to a Gaussian beam. After some propagation the mode then develops a typical doughnut like pattern. The vortex phase component can be added with vortex phase plates. Vortex phase plates are (for example) fused silica plates with a thickness of a few millimeters, where one surface has a staircase like structure. Hence the thickness of the plate varies with the angular position Φ . This also imprints a retardation, i.e. a phase shift, that depends on Φ . By tailoring

the slope of the staircase, an arbitrary retardation following a $l\Phi$ function can be introduced. These plates are commercially available with large diameters, have a high damage threshold and do not introduce a significant nonlinearity due to their small thickness.

Thus the following method to use doughnut modes for higher throughput energies is proposed: the Gaussian input beam is scaled in diameter by a factor of $M = \sqrt{|l| + 1}$. Then a dominant energy fraction is coupled into a doughnut mode by placing a vortex phase plate with the order l into the beam path. The beam is coupled into the multipass cell and nonlinearly broadened. The preserved mode of the output beam still has a vortex phase component, that is converted to a plane phase by placing a second vortex phase plate in a reversed alignment and with the same order l after the multipass. Thanks to the plane wavefront, the beam should still be focusable to high intensities.

The feasibility of this approach is tested with a nonlinear 4D simulation [136] for a mode with order $l = 1$. The XY-T grid of the simulation that covers the pulse in space (XY) and time (T) has a size of $128 \times 128 \times 256$ points equal to a space of $10 \text{ mm} \times 10 \text{ mm} \times 5 \text{ ps}$. An eigenmode parameter of $s = 0.8$ is used to avoid a focus size that is too small for the grid resolution. A nonlinear refractive index of $5 \times 10^{-20} \text{ W/cm}^2$ is used corresponding to about 500 mbar of argon. Self-steepening and dispersion is neglected. A cell with an end mirror radius of curvature of 1.5 m is assumed (i.e. the cell is about 2.4 m long) and the beam is propagated over 45 bounces. The input FWHM pulse duration is 1.4 ps and the input beam is perfectly mode matched to the eigenmode. A pulse energy of 52 mJ needs to be coupled into into the cell to obtain a similar broadening as for a Gaussian beam with 20 mJ. This corresponds well to the calculated factor of 2.6 between the spatially averaged accumulated nonlinear phase of a Gaussian beam and a $l = 1$ doughnut mode.

Figure 3.16 shows the simulated collimated beamprofiles and corresponding phases for the input, output and focus of this cell. The input intensity profile (profile A) is a Gaussian beam and the conversion to a higher order mode with $l = 1$ is simply done by adding a staircase like phase that corresponds to the angle Φ of the coordinate. The phase is quantized with 16 steps as commonly done for the manufacturing of fused silica vortex plates. After propagation in the cell the staircase phase changed to a continuous vortex (profile B in figure 3.16). The beam intensity represents a clean doughnut shape as expected. The phase is then compensated by a second reversed vortex plate and focused with a lens using a focal length of 2 m. The focus is shown as profile C in figure 3.16 and features a plane wavefront with a nearly Gaussian shape. The simulated Fourier limit of this beam is 33 fs and the intensity weighted homogeneity of the spectrum over the whole profile is 99.5 % (see eq. 3.70). 76.4 % of the pulse energy is within the $1/e^2$ diameter of the focus, which is about 12 % less than in the case of a Gaussian beam, where 86.4 % of the energy is within the $1/e^2$ diameter. This drop of central energy is negligible compared to the theoretical maximal throughput increase by a factor of 2.7.

The simulation was repeated with an elliptic input mode to test the robustness against input mode variations. Even with a major to minor axis ratio of 0.5, a rotational symmetric output mode is obtained and the features of the output beam remain similar to the results calculated for a circular input.

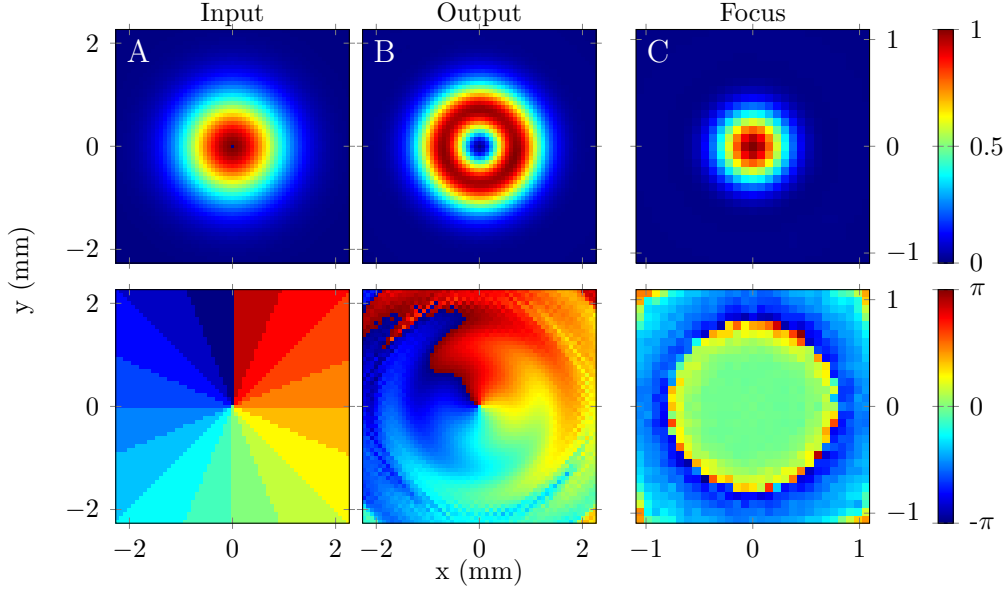


Figure 3.16: The mode converted input mode A , the calculated output mode B and the resulting focus of the phase compensated output C for the setup described in the text. The top row shows the intensity, the bottom row the corresponding phase or wavefront at the peak intensity of the pulse. 2.6 times more energy than for a fundamental beam is used for the mode converted input while maintaining a similar peak intensity.

A second test with a higher order input mode ($l = 2$) revealed significant distortions attributed to accidental phase matching with other higher order modes. The energy within the $1/e^2$ diameter of the focus dropped to only 42%. Including the potential energy gain by the further reduced peak intensity (eq. 3.88) yields a total energy drop in the central focus of 25% when the mode order is increased from $l = 1$ to $l = 2$.

This distortion is attributed to the following difference between a first order and second order doughnut mode: for a first order mode $l = 1$, no other combination $\{l, m\}$ (except for the reversed vortex $l = -1$) exists that accumulates the same Gouy phase. The buildup of the mode $l = -1$ is suppressed as the resulting mode consisting of $+1$ and -1 components would violate the rotational intensity symmetry expected from Kerr induced distortions. In contrast, for modes with $|l| > 1$ (or $m \neq 0$), several higher order modes with rotational symmetry are in phase and can build up simultaneously leading to a possible degradation of the mode quality. As example for $l = 2$ the modes $\mathbf{U}_{\pm 2,0}$ and $\mathbf{U}_{0,1}$ are phase matched. Higher mode orders with $l > 1$ are hence not considered to be useful for energy scaling.

In conclusion higher order modes are a promising tool to further extend the throughput energies. An energy scaling factor of up to 2.7 is expected from simulation with only minor losses in focus quality for a first order doughnut mode with $l = 1$. Using orders with $l > 1$ suffers from accidental phase matching with other higher order modes and is not expected to facilitate further energy scaling.

3.7 Conclusion

Nonlinear broadening in gas filled multipass cells constitutes a promising method to directly compress highly energetic picosecond scale pulses to a duration of tens of femtoseconds.

Gas filled multipass cells have a simple design consisting of just two curved mirrors in a vacuum chamber that can be filled with different noble gases. High broadening factors over 35 are achieved for picosecond pulses with a pulse energy of 18 mJ featuring excellent spatial properties and compressibility down to 41 fs. Also the broadening is in virtually perfect agreement with theory and well understood.

Except for potential absorption in dielectric coatings that is largely avoidable in high quality optics, no limitation for the average power is found and average powers up to 375 W are successfully broadened. Thus this technology is expected to be suitable for high average powers even exceeding the kilowatt range while providing a high throughput over 95 %. This property is a clear advantage over systems based on OPA chains that suffer from a low infrared pump to signal efficiency on the order of 10 % and average power limitations due to thermal constraints.

The throughput energy is solely limited by the breakdown of the gas as well as the mirror damage threshold. A thorough investigation of potential energy scaling methods revealed two possibilities to achieve higher energies without changing the gas or coating technology. The multipass cell can be increased in length with an expected linear scaling of throughput energy, or a first order Laguerre-Gaussian mode LG_{10} (also known as doughnut mode) can be used as propagating beam to obtain an up to 2.7 times higher throughput energy.

In an experimental realization of a longer multipass cell with a length of 8 m an output energy of 39 mJ is obtained in argon and 72 mJ in helium most likely limited by the onset of thermal lensing due to highly absorptive mirror coatings. No detailed investigation of spatial homogeneity or compressibility was performed in this experiment as the main goal was the scaling of throughput energy. However, the broadening mechanism has already been demonstrated to yield excellent results in this regard. To the best of the authors knowledge, the energies of this experiment are the highest energies nonlinearly broadened in a multi-kilohertz system and the highest energies spectrally broadened with a factor greater than 10.

By additionally using a first order Laguerre-Gaussian mode LG_{10} , throughput energies over 100 mJ are feasible in setups that do not exceed the length of a typical laboratory. In a best case the output Fourier limit (and hence the potentially reachable output pulse duration) was shown to reach values as short as ~ 28 fs.

A compressed pulse duration shorter than ~ 28 fs depends on a shorter input pulse duration and a different coating technology for the used optics with a more broadband reflection bandwidth at the cost of a lowered damage threshold. A thin plate based multipass broadening is proposed as a subsequent second stage to avoid ionization issues and hence allow for potentially high energies even if broadband optics are used. Under the given conditions, thin plate based broadening is limited to low broadening factors (on the order of 3 to 4). The potentially short input pulse duration of this second stage of around 28 fs can then be further reduced to a duration of ~ 10 fs approaching the few-cycle regime.

Summary and Outlook

A laser system that combines high repetition rates, high energies and potentially low pulse durations in a unique way was developed and presented throughout this thesis. A record breaking amplifier system delivers pulse energies up to 200 mJ with a repetition rate of 5 kHz and a pulse duration of about 1 ps. One of the first experimental implementations of a promising high power pulse compression method was shown to nonlinearly compress the picosecond scale output pulses of the amplifier system towards tens of femtoseconds. Using a gas filled multipass cell pulse energies up to 40 mJ (in argon) or 75 mJ (in helium) were successfully spectrally broadened with broadening factors between 11 (helium) and 37 (argon). These energies are the highest energies spectrally broadened at multi-kilohertz repetition rate and the highest energies spectrally broadened with a factor higher than 10. The broadening in multipass cells was shown to provide compressible and spatially homogeneous pulses and pulse durations down to 28 fs are potentially reachable. The unprecedented results are considered to be a first step towards even stronger next generation femtosecond laser systems.

The development of a highly stable kilowatt amplifier system was founded on detailed mechanical and novel theoretical considerations, state of the art Yb:YAG thin-disk technology and a thorough investigation of thermal properties.

Since the thermal load of the presented amplifier system is significant, a proper understanding of the amplifier resonator and its sensitivity regarding thermal lenses and thermal drifts was essential to provide a stable output. The accumulated Gouy phase within a resonator roundtrip was identified to be a key variable. It determines the resonator robustness and length, the propagation of non-eigenmodes, off-axis propagation and the buildup of higher order modes. To obtain a robust resonator with a high beam quality in ring resonators, a Gouy phase of 0.55π was found to be ideal. This finding allowed to design an optimized generalized caustic that was approximated with commercially available optics. The presented formalism based on the accumulated Gouy phase also allowed for the direct measurement of the resonator stability parameter.

A numeric model was introduced that can calculate the dynamic behavior of a multi-kilohertz thin-disk amplifier system. This highly dynamic behavior is one of the fundamental differences between a (sub-)kilohertz and a multi-kilohertz system due to the lifetime of Yb:YAG of about 1 ms. Thanks to the numeric model an operating point was found that maximized the distortion robustness of the amplifier system. Input energies of about 1 mJ were determined to be essential and hence the usage of a preamplification stage was suggested. Additional thermal and mechanical optimization of the laser setup lead to excellent thermal stability and reproducibility with thermalization times of about 1 h.

The numeric model also revealed a disagreement between expected and obtained output energy. This disagreement motivated the analysis of thermally induced

wavefront distortion effects on the output power and a significant drop of output energy could be attributed to these wavefront distortions. Methods to reduce this energy drop were evaluated and the usage of a 969 nm pump and Gaussian-like pump spots on the gain medium were shown to yield significant improvements. Further improvements of wavefront distortions, e.g. the compensation via adaptive optics, seem feasible but their implementation often pose an additional alignment constraint in the amplifier and lead to a potentially higher mechanical sensitivity. Also they were not considered to be necessary to reach the targeted output energy. Nevertheless the potential of wavefront compensation for higher output energies was demonstrated to be considerable throughout this thesis.

The amplifier system can be flexibly combined with different frontends. In a space optimized variant, a fiber laser oscillator combined with a fiber Bragg stretcher was successfully applied to the amplifier system reducing the frontend footprint to only 8 % of its original size. The output pulse duration could be optimized by using a Yb:CALGO based preamplifier system and an output pulse duration of only 740 fs was obtained.

A further reduction of pulse duration required the implementation of a nonlinear compression stage. Pulses with a duration of a few tens of femtosecond and pulse energies approaching 100 mJ with a multi-kilohertz repetition rate have not been demonstrated before. Thus this stage necessitated a novel compression scheme that is suited for high energies and high average powers without sacrificing the energy throughput. Especially schemes with a low throughput like for example optical parametric amplification (OPA) systems would require a considerable amount of input energy close to the joule level to obtain an output energy of several tens of millijoule significantly increasing the complexity of the amplifier chain.

As alternative a gas-filled multipass cell based on a simple two-mirror resonator was implemented as novel compression scheme and optimized for high energies. Record breaking pulse energies of 40 mJ (and more) could be nonlinearly broadened in these cells with an energy throughput of up to 97 % and broadening factors up to 37. This scheme is capable of supporting high average powers (up to 375 W were used in the presented setup but no fundamental limit was found) and an output pulse duration of 41 fs could be demonstrated with a high spatial homogeneity of about 97 %. For this amplifier chain pulse durations down to 28 fs were shown to be feasible. Possible limitations regarding the shortest output pulse duration were discussed and a further reduction of pulse duration was reasoned to require a second nonlinear compression stage.

The input energy of gas-filled multipass cells is limited by the mirror damage threshold and the ionization threshold of the used gas. Several possibilities to avoid gas ionization or mirror damages were investigated and finally two possibilities for further energy scaling were determined: a simple scaling of the multipass in length and the usage of a first order Laguerre-Gaussian mode LG_{10} . While the first method was successfully implemented, the latter is subject of a future implementation and promises an energy scaling up to a factor of 2.7.

Based on the results of this work a high energy thin-disk amplifier combined with an argon-filled multipass cell with a length of 8 m and a first order Laguerre-Gaussian mode conversion facilitates the generation of multi-kilohertz pulses with

an energy beyond 100 mJ and pulse durations down to 28 fs. Even further nonlinear compression in a second thin plate based multipass has the potential to decrease the pulse duration to the few-cycle regime.

In a thin plate multipass a broadening factor of about 4 was determined to be feasible over 45 bounces. With an input pulse energy of 100 mJ and an input pulse duration of 30 fs this already suggests pulse durations below 10 fs with expected output pulse energies of more than 90 mJ equivalent to several terawatt of peak power. Assuming fused silica as thin plate material, the plates are required to have a thickness of a few tens of micrometer if they are located close to the end mirrors. This thickness is on the same scale as the thickness of the used mirror coating and hence a custom mirror coating with a thick fused silica layer as first layer can act as nonlinear material. Alternatively less bounces and thicker plates are feasible at the cost of a stronger degradation of the beam quality. For a plate thickness of about half a millimeter even four to five bounces are theoretically sufficient to obtain a broadening factor of 4. After compression this stage then provides few-cycle pulses with an energy close to 100 mJ and a five kilohertz repetition rate. As there are no strict average power limitations, even higher repetition rates are feasible. Higher energies are just limited by the available laboratory space and can be obtained by elongating the first multipass cell.

Two different systems with parameters similar to the presented system are the *SYLOS* laser system of the *ELI-ALPS* facility (53 mJ with sub-9 fs or 35 mJ with 6.3 fs [137]) and the *Allegra kilohertz femtosecond laser system* at *ELI-Beamlines* (20 mJ with 14.2 fs [138]). These systems are intended to be used (amongst others) for attosecond pulse and X-ray generation and are based on a chain of optical parametric amplification (OPA) stages. With OPA high contrast pulses and carrier envelope phase stable few-cycle pulses were already demonstrated. However, both mentioned systems run at a multiple times lower repetition rate of 1 kHz with a much lower average power than the system presented in this thesis.

To drive such OPA chains energetic kilohertz pump lasers are necessary. In fact the thin-disk amplifier introduced in this thesis is also an ideal pump source for OPA systems and can be used to increase their repetition rate to the multi-kilohertz regime. Average power scaling in OPA systems is however challenging and the presented direct broadening in multipass cells with its high throughput and thermal robustness features more promising prospects in this regard.

The repetition rate scalability of multipass cell broadening can for example be utilized in a laser wakefield accelerator based on a pulse burst instead of a single driving pulse. A burst of ultrashort pulses with a spacing equal to the plasma period and a repetition rate of several kilohertz can efficiently accelerate electrons and subsequently X-ray sources with a high mean photon flux become feasible [139]. Thanks to the burst operation, the driving laser requires relatively low peak intensities but high average powers – a parameter set that is ideally suited to be generated with the presented multipass cells.

In conclusion the presented laser system provides a unique combination of high intensity and high repetition rate and opens up a new field of applications. A laser based X-ray source driven by such a laser system applied to medical imaging applications has the potential to provide unprecedented resolutions at low doses.

Weak or time-varying effects that originate for example from nonlinear extreme ultraviolet or X-ray processes can be effectively analyzed with a high repetition rate intense laser system and a deeper understanding of fundamental physical processes is rendered possible. The developed technology has a vast amount of use cases and can also be applied for driving OPA systems (e.g. for the generation of energetic attosecond pulses) or to generate ultrashort pulse bursts with high average power to efficiently drive electron accelerators.

Appendix A

Preamplifier

A preamplifier is used in the system to provide a wider range of input powers for the high energy amplifier. The output energies are in the millijoule range. Thus the constraints with respect to average power and damage thresholds are greatly reduced and the amplifier can be optimized with a larger degree of freedom.

A main difference to the main amplifier is the usage of a linear resonator. The following sections derive the robustness parameters for linear resonators similar to section 1.3.6. An optimized resonator is proposed and implemented as preamplifier.

A.1 Robustness of a Linear Resonator

In contrast to a ring resonator, in a linear resonator the beam is guided twice through any optical system involved in the resonator before it reaches its initial position again. To this end two end mirrors reflect the beam as depicted in figure A.1. This fact changes some of the conclusions derived in section 1.3.6.

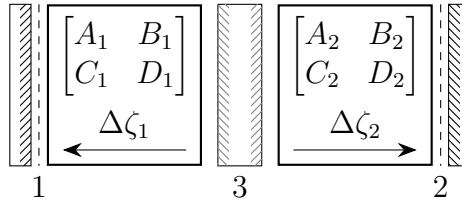


Figure A.1: A schematic of a linear resonator. The resonator has two end mirrors labeled 1 and 2, some optical element under investigation named 3 and a laser mode that oscillates between both end mirrors. The ABCD matrices describe the propagation starting from the central optical element 3 towards one of the end mirrors 1 or 2 as indicated by the arrows. The accumulated Gouy phase in each segment is $\Delta\zeta_1$ and respectively $\Delta\zeta_2$. Also the ABCD matrices are chosen such that the beam is collimated ($R \rightarrow \infty$) at the positions 1, 2 and 3 without loss of generality.

A.1.1 Mechanical Robustness

Similar to the ring resonator case, an arbitrary distortion $\{s, \sigma\}$ is introduced into the system. Thus the propagation from position 1 to position 2 (see figure A.1) is described by

$$\begin{bmatrix} x_2 \\ \theta_2 \end{bmatrix} = \begin{bmatrix} A & B \\ C & D \end{bmatrix} \begin{bmatrix} x_1 \\ \theta_1 \end{bmatrix} + \begin{bmatrix} s \\ \sigma \end{bmatrix} \quad (\text{A.1})$$

where the ABCD matrix describes the propagation from end mirror 1 to end mirror 2. The beam is then reflected and propagates back to mirror 1 following the equation [140]

$$\begin{bmatrix} x_1 \\ \theta_1 \end{bmatrix} = \begin{bmatrix} D & B \\ C & A \end{bmatrix} \left(\begin{bmatrix} x_2 \\ \theta_2 \end{bmatrix} + \begin{bmatrix} -s \\ \sigma \end{bmatrix} \right). \quad (\text{A.2})$$

This is due to the reciprocal property of optical systems: Feeding the reversed system with an input equal to the reflected distortion vector $\{s, -\sigma\}$ has to yield an output of zero. The system can be solved for the eigenmode position at mirror 1 by plugging in $\{x_2, \theta_2\}$ and solving the system for $\{x_1, \theta_1\}$ [140]. The result is simplified using eq. 1.35 to 1.38 together with the properties of a linear resonator: $w_{in} = w_1$, $w_{out} = w_2$, $R_{in,out} \rightarrow \infty$ and $\Delta\zeta = \Delta\zeta_{eig}/2$ (propagation from 1 to 2 corresponds to a half roundtrip)

$$\begin{bmatrix} x_1 \\ \theta_1 \end{bmatrix} = \begin{bmatrix} 1 \\ 0 \end{bmatrix} \frac{\pi w_1 w_2}{\lambda \sin(\Delta\zeta_{eig}/2)} \sigma. \quad (\text{A.3})$$

The fact that the eigenmode at the collimated position 1 is only subject to translation is a property similar to a ring resonator. These translations are minimized for small spot sizes on the end mirrors and an accumulated Gouy phase close to $\Delta\zeta_{eig} \approx \pi$. This corresponds to the mechanical stability condition for the ring resonator.

A.1.2 Spot Size Robustness

The main source of spot size distortions are focal length shifts of resonator elements. Thus to determine the point of maximum robustness, such a shift is simulated by an ABCD matrix \mathbf{M}_f with dioptric power $1/f$. This distortion is placed at the position under investigation 3. Without loss of generality, it is further assumed that $|B_1 D_1| > |B_2 D_2|$ (the opposite case is obtained by simply flipping the following results such that position 1 becomes position 2 and vice versa). The eigenmode equation can be solved for this distorted system to determine the spot size $w_3^4(f)$. The point of maximum robustness is then found by solving an equivalent to the equation $dw_3/df^{-1}|_{1/f=0} \stackrel{!}{=} 0$ yielding the robustness criterion [140]

$$u = \frac{1}{2B_1 D_1} - \frac{1}{2B_2 D_2} \quad (\text{A.4})$$

$$v = -\frac{1}{2B_1 D_1} - \frac{1}{2B_2 D_2} \quad (\text{A.5})$$

$$\eta = \frac{1}{f} - \frac{1}{2} \left(\frac{A_1}{B_1} + \frac{C_1}{D_1} + \frac{A_2}{B_2} + \frac{C_2}{D_2} \right) \quad (\text{A.6})$$

$$\eta^2|_{1/f=0} = uv \quad (\text{robustness criterion}) \quad (\text{A.7})$$

where $uv > 0$ since we assumed $|B_1 D_1| > |B_2 D_2|$. Furthermore the matrices $A_1 B_1 C_1 D_1$ and $A_2 B_2 C_2 D_2$ are calculated based on eq. 1.35 to 1.38. $\Delta\zeta_1$ and $\Delta\zeta_2$ are the Gouy phases accumulated in the first and second part of the resonator. With these values, the robustness criterion is solved for $\Delta\zeta_1$ and yields

$$\Delta\zeta_1 = \Delta\zeta_{1,robust} = \frac{\pi}{4} + k_1 \frac{\pi}{2} \quad k_1 \in \mathbb{Z}. \quad (\text{A.8})$$

This means that maximum robustness is achieved if a Gouy phase shift of $\Delta\zeta_{1,robust}$ is accumulated in the first resonator part.

The second Gouy phase $\Delta\zeta_2$ defines the maximum and minimum possible dioptric power of the distortion that still fulfills the resonator condition 1.42. To determine these thresholds, the property that η has to be in the range $\pm u < \eta < \pm v$ or $\pm v < \eta < \pm u$ [140] is used. η has a constant sign and u and v have an equal sign (due to $uv > 0$). These inequalities are simplified for the focal length f using the previously calculated values for the matrices $A_1B_1C_1D_1$ and $A_2B_2C_2D_2$, where $\Delta\zeta_1$ is set to $\Delta\zeta_{1,robust}$. An effective focal shift f_{eff} is introduced and the resonator is then stable for dioptric powers f_{eff}^{-1} over a range of

$$\frac{1}{f_{eff}} = \frac{\pi w_3^2}{\lambda} \frac{1}{f} \quad (\text{A.9})$$

$$-1 - \tan \Delta\zeta_2 < f_{eff}^{-1} < 1 - \tan \Delta\zeta_2 \quad \text{for} \quad -\frac{\pi}{4} \leq \Delta\zeta_2 + k_2\pi \leq \frac{\pi}{4} \quad (\text{Zone I}) \quad (\text{A.10})$$

$$-1 + \cot \Delta\zeta_2 < f_{eff}^{-1} < 1 + \cot \Delta\zeta_2 \quad \text{for} \quad \frac{\pi}{4} \leq \Delta\zeta_2 + k_2\pi \leq \frac{3\pi}{4} \quad (\text{Zone II}) \quad (\text{A.11})$$

where $k_2 \in \mathbb{Z}$. The constraints for $\Delta\zeta_2$ ensure that the undistorted resonator $f_{eff}^{-1} = 0$ is part of the range.

For $\Delta\zeta_2 = (\pi/4 \text{ or } 3\pi/4) + k_2\pi$, the stability zones join and the total stability range doubles its width

$$-2 < f_{eff}^{-1} < 2. \quad (\text{A.12})$$

This width corresponds the stability range of the ring resonator. However, in contrast to the ring resonator, at $\Delta\zeta_1 = \Delta\zeta_2 = \pi/4$ (or $3\pi/4$) the total roundtrip Gouy phase $\Delta\zeta_{eig} = 2(\Delta\zeta_1 + \Delta\zeta_2)$ becomes π (or 3π). This means that the point of maximum mechanical stability and the point of maximum spot size robustness coincide making operation close to this point favorable.

A.1.3 Temporal Robustness

The temporal robustness criterion discussed in [21] and already introduced for ring resonators can be adapted to linear resonators as well. To this end, the accumulated Gouy phase in the first section is again set to $\Delta\zeta_1 = \Delta\zeta_{1,robust}$. The optical element under investigation at position 3 is tilted by an angle $\sigma_3/2$ causing an eigenmode shift x_3 of [21]¹

$$x_3 = -\sigma_3 \frac{D_1 D_2}{D_1 C_2 + D_2 C_1}. \quad (\text{A.13})$$

Using eq. 1.35 to 1.38, this can be converted to an expression based on accumulated Gouy phases

$$x_3 = \sigma_3 \frac{\pi w_3^2}{2\lambda} \left((-1)^{k_1} + \cot \frac{\Delta\zeta_{Eig}}{2} \right). \quad (\text{A.14})$$

¹the notation is adapted to match the previously introduced linear resonator scheme. I.e. $A_1B_1C_1D_1 = D_L B_L C_L A_L$ and $A_2B_2C_2D_2 = A_R B_R C_R D_R$

Here $\Delta\zeta_{Eig} = 2(\Delta\zeta_1 + \Delta\zeta_2)$ is the roundtrip Gouy phase. The temporal robustness criterion $G = V_{LB}x_3/\sigma_3 < 1$ [21] is consequentially expressed as

$$\cot \frac{\Delta\zeta_{Eig}}{2} < \frac{2\lambda}{\pi w_3^2 V_{LB}} - (-1)^{k_1}. \quad (\text{A.15})$$

Limiting the analysis to one period $k_1 2\pi \leq \Delta\zeta_{Eig} \leq (k_1 + 1)2\pi$ and positive focal strengths $V_{LB} > 0$, the following conclusions can be drawn to ensure temporal robustness

$$\Delta\zeta_1 = \frac{\pi}{4} \quad (k_1 = 0) \quad \rightarrow \quad \frac{3\pi}{2} \leq \Delta\zeta_{Eig} \leq 2\pi \quad (\text{A.16})$$

$$\Delta\zeta_1 = \frac{3\pi}{4} \quad (k_1 = 1) \quad \rightarrow \quad \frac{5\pi}{2} \leq \Delta\zeta_{Eig} \leq 4\pi. \quad (\text{A.17})$$

These limits fulfill the more strict inequation $\cot(\Delta\zeta_{Eig}/2) \leq -(-1)^{k_1}$. In other cases large values of $\Delta\zeta_{Eig}$ help to increase the range of focal strengths V_{LB} that are still stable. However only for $\Delta\zeta_1 = \Delta\zeta_2 = 3\pi/4$, mechanical, focal length and temporal robustness for all V_{LB} is achieved simultaneously. A setup with such a property would however require multiple foci or very long resonator lengths. While the former is undesirable for high energy lasers, the latter induces additional mechanical instabilities.

A.1.4 Conclusion

An optimized design for a linear resonator consists of a first resonator part with an accumulated Gouy phase of $\Delta\zeta_1 = \pi/4$. This ensures a short propagation duration (implying a large mechanical stability) and maximum spot size robustness. The second part of the resonator is optimized based on the available length with the robustness parameters (lower values are better)

$$\text{Mechanical Robustness} \propto \left| \csc \frac{\Delta\zeta_{Eig}}{2} \right| \quad (\text{eq. A.3}) \quad (\text{A.18})$$

$$\text{Temporal Robustness} \propto \cot \frac{\Delta\zeta_{Eig}}{2} \quad (\text{eq. A.15}). \quad (\text{A.19})$$

Consequentially roundtrip Gouy phases $\Delta\zeta_{Eig} = 2(\Delta\zeta_1 + \Delta\zeta_2)$ close to π (or equivalently $\Delta\zeta_2 \approx \pi/4$) yield highly robust resonators.

The buildup of wavefront distortions as discussed in section 1.3.3 is reduced if the accumulated Gouy phase $\Delta\zeta_{Eig}$ is outside the buildup regions shown in figure 1.6 [22, p. 7]. Thus in general $\Delta\zeta_{Eig}$ should not be exactly π but slightly larger or smaller.

The length (eq. 1.49) of the resonator is also modified due to the folded nature of linear resonators and becomes

$$L = \frac{\Delta\zeta_{Eig}}{2} \frac{\bar{A}_{spot}}{\lambda}. \quad (\text{A.20})$$

Hence large Gouy phases are reached with smaller setups compared to ring resonators.

A.2 Design for a Millijoule Thin-Disk Resonator

The preamplifier used in this work is a linear thin-disk regenerative amplifier. Its schematic layout is shown in figure 2.24 and its optimized resonator caustic in figure 2.25. For the optimization, the results from the previous section were implemented. The thin-disk of this resonator is assumed to increase its radius of curvature from 2 m to 2.05 m when pumped with up to 150 W with a wavelength of 940 nm and a pump spot size of 3 mm. For the optimization, a radius of curvature of 2 m is assumed. The linear resonator is build as merged zone linear resonator. This means the accumulated Gouy phases left and right of the disk are symmetric with a value of $\Delta\zeta_1 = \Delta\zeta_2 = \pi/4$. This ensures maximal mechanical and mode size robustness with a large stability zone while keeping the beam diameters reasonably large. This also implies a loose focus on both sides of the disk. During operation, the curvature of the disk flattens slightly and the resonator shifts towards an operation point with a smaller accumulated Gouy phase $< \pi$ thus preventing potential build-ups of wavefront aberrations. The mode size on the disk is chosen rather large to optimize the beam quality at the cost of lower efficiency. The mode with a diameter of 2.7 mm covers 90% of the pump spot. The resonator needs a length of at least 4 m to provide a roundtrip time long enough for the Pockels cell to switch correctly (more than 25 ns). The Pockels cell is placed close to one end mirror to maximize the duration the Pockels cell has to switch. With these parameters, a ideal resonator shape can be defined. A numeric optimization algorithm approximates the ideal resonator shape shown in grey in figure 2.25 with the goal of a maximized beam diameter in the Pockels cell. Since every curved optic is a potential source of error (in terms of positioning and focal length), their amount is minimized. A reasonable fit to the ideal resonator shape is possible with three curved optics. Only solutions with curved mirror distances that can be realized on a footprint of 0.45×0.75 m are selected.

Appendix B

Numeric Thin-Disk Amplification Model

Pump and emission mechanics of thin-disk lasers are often discussed based on the assumption of a fully pumped system. An Yb:YAG system needs about 1 ms (i.e. about one radiation lifetime) to reach this fully pumped state. For a 5 kHz system, a pulse is amplified every 200 μ s and hence the population inversion is depleted before the disks reach their fully pumped state. A model of such an amplification system therefore requires time dependent solutions and is implemented numerically due to its complexity.

After the determination of the average disk temperature T_{avg} using the model introduced in section 2.6.1, the temperature dependent values for the cross sections $\sigma_{\{a,e\}\{P,L\}}$ can be extracted from [45] and used in the following numeric model.

The amplification process is separated into two sections: a pump phase where no amplification of a laser pulse takes place and an emission phase that models the typically short duration in which a pulse is amplified. To this end the quasi-three-level gain material Yb:YAG is modeled as effective two level system (section 1.6): The upper level population density is N_2 , the lower level density N_1 and the total dopant density N_0 is

$$N_0 = N_1 + N_2 = c_{Yb}N_+ \quad (\text{B.1})$$

with the cation density N_+ (for Yb:YAG $N_+ = 1.38 \times 10^{22}/\text{cm}^3$ [53]) and the doping concentration c_{Yb} .

B.1 Pump Phase

During the pump phase, a pump laser is absorbed and excites atoms to a higher energy level. This process is counteracted by spontaneous emission that depletes the upper laser level. Both processes can be combined to yield the upper level population density N_2 over time.

B.1.1 Excitation

The pump laser enters the pump head and is folded onto the disk M_p times (e.g. $M_p = 24$) like depicted in figure 2.7. Accordingly for a disk thickness of H , the pump laser propagates through a total effective thickness of $L = 2M_pH$. The photon flux of the pump laser $\Phi_P(z)$ is defined in eq. 1.114, where z describes a position in the dimension perpendicular to the disk surface. The amount of absorbed photons

per second in the disk equals the input photon flux $\Phi_P(0)$ minus the output photon flux $\Phi_P(L)$ times the pump area A . As such the average photon absorption rate per unit volume in a disk of thickness H and pump area A is

$$\dot{N}_{2E} = \frac{[\Phi_P(0) - \Phi_P(L)] A}{HA} = \frac{\Phi_P(0)}{H} [1 - \exp(-L\alpha)]. \quad (\text{B.2})$$

Obviously the density of absorbed photons per timestep equals the density of excited electrons per timestep \dot{N}_{2E} .

B.1.2 Depletion

While the pumping populates the upper laser level, fluorescence mainly caused by amplified spontaneous emission (ASE) causes a depopulation. The origin of ASE is discussed in section 1.6.3, but an analytic expression requires some approximations for the gain medium. Speiser [32] reduced the complexity of the disk geometry by deriving a worst case model for τ_{ASE} assuming a single line emission at 1030 nm, where the amplification of the spontaneous emission reaches a maximum. The result of this model is the following effective lifetime

$$\begin{aligned} \tau_{ASE} &= \frac{\tau}{\exp(2Hg) + 2Hg \operatorname{Ei}(2Hg\xi) - 2Hg \operatorname{Ei}(2Hg)} & (\text{B.3}) \\ g &= N_2\sigma_{eL} - N_1\sigma_{aL} & \text{1030 nm gain coefficient} \\ \xi &= \frac{\sqrt{w_{Pump}^2 + H^2}}{H} & \text{Geometry Parameter} \\ w_{Pump} &= \sqrt{\frac{A}{\pi}} & \text{Pump Radius} \\ \operatorname{Ei}(x) &= \int_{-\infty}^x \frac{\exp(t)}{t} dt & \text{Exponential integral.} \end{aligned}$$

The depletion rate under the influence of ASE is therefore modeled as

$$\dot{N}_{2D} = \frac{N_2}{\tau_{ASE}}. \quad (\text{B.4})$$

B.1.3 Upper Level Population

The overall change of the population density N_2 can now be written as sum of upper level excitation and depletion

$$\dot{N}_2 = \dot{N}_{2E} + \dot{N}_{2D}. \quad (\text{B.5})$$

This differential equation is only solvable numerically due to the various occurrences of N_2 . A simple reformulation yields

$$t = \int_0^t dt = \int_0^t \frac{dt}{dN_2} dN_2 = \int_{N_2(0)}^{N_2(t)} \frac{1}{\dot{N}_2} dN_2 = \int_0^{N_2(t)} \frac{1}{\dot{N}_2} dN_2 - \int_0^{N_2(0)} \frac{1}{\dot{N}_2} dN_2. \quad (\text{B.6})$$

This equation gives the time necessary to pump from a starting population $N_2(0)$ to a target population $N_2(t)$. Obviously the target population has to be smaller than

the steady state population $N_2(\infty)$ that is reached after an infinitely long pump duration. The steady state is found by demanding a constant upper level population (i.e. $\dot{N}_2 = 0$) and numerically solving

$$N_2(\infty) = \text{root} \left(\dot{N}_2(N_2) \right), \quad (\text{B.7})$$

where $r = \text{root}(f(x))$ gives a value r such that $f(r) = 0$. Unfortunately solving eq. B.6 for $N_2(t)$ with a given time t is computationally expensive. A more efficient solution is to generate a look-up table with value pairs $\{\mathcal{N}_2, \text{T}(\mathcal{N}_2)\}$ for $\mathcal{N}_2 \in [0, N_2(\infty)]$

$$\text{T}(\mathcal{N}_2) = \int_0^{\mathcal{N}_2} \frac{1}{\dot{N}_2} dN_2. \quad (\text{B.8})$$

$\text{T}(\mathcal{N}_2)$ is the time needed to reach an upper level population \mathcal{N}_2 starting from an empty upper level. With this look-up table, the upper state population $N_2(t)$ that can be reached from a given start population $N_2(0)$ within a given time t is efficiently determined by looking up $\text{T}(N_2(0))$, then calculating

$$\text{T}(N_2(t)) = \text{T}(N_2(0)) + t \quad (\text{B.9})$$

and finding the $N_2(t)$ in the look-up table that belongs to the duration $\text{T}(N_2(t))$. Simple linear interpolation yields sufficiently accurate results if a value is not found in the look-up table. With these methods the calculation of a time dependent upper level population $N_2(t)$ for an arbitrary start population $N_2(0)$ is possible.

B.2 Emission Phase

During the emission phase, a seed beam with fluence $J(0)$ bounces over the thin-disk with an effective propagation length through the material of $2H$ thereby amplifying the fluence to the value $J(2H)$ and decreasing the upper level population to a value $N_2(t + dt)$. This repeats several times to provide sufficient gain (e.g. by using a multipass structure over the disk).

B.2.1 Gain

The amplification of a seed photon flux Φ_L that propagates through the disk happens nearly instantaneous within a timespan dt , thus the slow pumping dynamics can be neglected. The pulse fluence J can be calculated by the expression $J = E_L \int \Phi_L dt$ (eq. 1.115) and further treatment is based on the input fluence $J(0)$ and the amplified output fluence $J(2H)$ according to the generalized equation for signal amplification 1.117. Amplification depletes the upper level and the change of the population density equals the amount of emitted photons per unit volume

$$\Delta N_{2L} = \frac{J(0) - J(2H)}{HE_L}. \quad (\text{B.10})$$

In conclusion the upper level change introduced by amplification is

$$N_2(t + dt) = N_2(t) + \Delta N_{2L}. \quad (\text{B.11})$$

B.2.2 Multipass

A complete multipass roundtrip consists of e.g. two disks that amplify the signal and some lossy guiding optics to enable the next bounce over these disks. Each disk i is assigned an own population density $N_{2,k,i}(t)$ as variable of state for the roundtrip k . Assuming a seed pulse with fluence J_{in} enters the multipass, it will suffer some losses $1 - \mathcal{T}_1$ to the first disk yielding

$$J_{k=1,i=1}(0) = \mathcal{T}_1 J_{in} \quad (\text{B.12})$$

as input fluence for the first disk $i = 1$ at the first roundtrip $k = 1$. The disk amplifies this fluence according to equation 1.117 to $J_{k=1,i=1}(2H)$ with the updated state variable

$$N_{2,k=1,i=1}(dt) = N_{2,k=1,i=1}(0) + \frac{J_{k=1,i=1}(0) - J_{k=1,i=1}(2H)}{HE_L}. \quad (\text{B.13})$$

A second loss channel \mathcal{T}_2 between the first disk and the second disk follows and the input fluence for the second disk is

$$J_{k=1,i=2}(0) = \mathcal{T}_2 J_{k=1,i=1}(2H). \quad (\text{B.14})$$

This fluence is amplified to $J_{k=1,i=2}(2H)$ and the state variable of the second disk is updated as

$$N_{2,k=1,i=2}(dt) = N_{2,k=1,i=2}(0) + \frac{J_{k=1,i=2}(0) - J_{k=1,i=2}(2H)}{HE_L}. \quad (\text{B.15})$$

This process can be repeated for an arbitrary number of disks. The pulse is then guided back to the first disk with the transmission $\mathcal{T}_3 \mathcal{T}_1$ and the second roundtrip $k = 2$ begins

$$J_{k=2,i=1}(0) = \mathcal{T}_3 \mathcal{T}_1 J_{k=1,i=2}(2H). \quad (\text{B.16})$$

At this point a more precise but also computationally more expensive model could implement the pumping of the upper level $N_2(\Delta t_R)$ between two bounces of the disk by implementing a look-up according to equation B.9

$$N_{2,k=2,i=1}(0) = N_{2,k=1,i=1}(\Delta t_R + dt) = N_2(\Delta t_R)|_{N_2(0)=N_{2,k=1,i=1}(dt)}, \quad (\text{B.17})$$

where Δt_R is in this case the roundtrip time between two bounces on the order of some tens of nanoseconds. However for kilohertz repetition rates, the pumping between two pulses on the order of several tens to hundreds of microseconds clearly dominates over the total pumping during the emission phase of up to a few microseconds. Neglecting the pump during the emission phase significantly enhances the overall speed of the numeric model and therefore $\Delta t_R \approx 0$ is assumed

$$N_{2,k=2,i=1}(0) \approx N_{2,k=1,i=1}(dt). \quad (\text{B.18})$$

The second roundtrip can be calculated by restarting from equation B.13 with $k = 2$. The output fluence and upper level population of the multipass system after N roundtrips is then

$$J_{out} = \frac{J_{k=N+1,i=1}(0)}{\mathcal{T}_1} \quad (\text{B.19})$$

$$N_{2,k=N,i}^{out} = N_{2,k=N+1,i}(0). \quad (\text{B.20})$$

The main losses typically appear in the section after the incoupling \mathcal{T}_1 . Thus $\mathcal{T}_2 = \mathcal{T}_3 = 1$ can be assumed in good approximation.

B.3 Equilibrium Population

For a reproducible amplification, the depopulation of the upper laser level during the emission phase has to equal the population of the upper laser level during the pump phase

$$N_{2,k=1,i}(0) - N_{2,k=N,i}^{out} \stackrel{!}{=} N_2(\Delta t_P)|_{N_2(0)=N_{2,k=N,i}^{out}} - N_{2,k=N,i}^{out} \quad (\text{B.21})$$

Where $\Delta t_P = f_{rep}^{-1}$ is the duration between two pulses (which is equal to the inverse of the repetition rate f_{rep}). This can be simplified to

$$Pump(x) = N_2(\Delta t_P)|_{N_2(0)=x} \quad (\text{B.22})$$

$$Emission(x) = N_{2,k=N,i}^{out}|_{N_{2,k=1,i}(0)=x} \quad (\text{B.23})$$

$$PumpEm(x) = Pump(Emission(x)) \quad (\text{B.24})$$

$$N_{2,k=1,i}(0) \stackrel{!}{=} PumpEm(N_{2,k=1,i}(0)) \quad (\text{B.25})$$

with the pump function $Pump(x)$ defined by the look-up according to equation B.9 and the emission function $Emission(x)$ defined by equation B.20. This equation is fulfilled if the upper level population at the beginning of amplification is

$$N_{2,k=1,i}(0) = N_2^{Eq} = \text{root}(PumpEm(N_2) - N_2). \quad (\text{B.26})$$

Or in other words the equilibrium upper level population N_2^{Eq} marks the fixed point of the function $PumpEm(N_2)$. After numerically solving equation B.26, the final output fluence can be calculated by following the procedure of section B.2.2.

B.4 Dynamics

The equilibrium population N_2^{Eq} is reached by a fixed point iteration physically done by the amplifier. If the upper level population is higher than the equilibrium population, the gain of the amplifier is too high, the depopulation too strong and hence the next pulse is confronted with an upper level population that is lower than equilibrium. Thus the gain is too low and the increase of population is stronger than the small depopulation. This eventually leads to an upper level population being higher than equilibrium and the circle restarts. Ideally this iteration converges to the stable operating point where the upper level population equals the equilibrium. Mathematically, this fixed point iteration equals the repeated solution of the equation

$$N_2^{(j+1)} = PumpEm(N_2^{(j)}) \quad (\text{B.27})$$

until $N_2^{(j+1)} \approx N_2^{(j)}$, where j marks the j th iteration. In a general case (e.g. with multiple disks $i = 1, 2, \dots$), this fixed point iteration is multidimensional and the

first order Taylor approximation around N_2^{Eq} of equation B.27 is

$$\mathcal{J}_{Eq} = \mathcal{J}(PumpEm(N_2))|_{N_2=N_2^{Eq}} \quad (\text{B.28})$$

$$N_2^{(j+1)} \approx N_2^{Eq} + \mathcal{J}_{Eq}[N_2^{(j)} - N_2^{Eq}] \quad (\text{B.29})$$

$$N_2^{(j+1)} - N_2^{Eq} \approx \mathcal{J}_{Eq}[N_2^{(j)} - N_2^{Eq}]. \quad (\text{B.30})$$

\mathcal{J}_{Eq} is the Jacobi matrix of $PumpEm(N_2)$ at the position N_2^{Eq} . Hence the new difference to the equilibrium population is the difference from the previous step times the Jacobian. The difference after j steps (i.e. after j pulses) is therefore

$$N_2^{(j)} - N_2^{Eq} \approx \mathcal{J}_{Eq}^j [N_2^{(j=0)} - N_2^{Eq}], \quad (\text{B.31})$$

where \mathcal{J}_{Eq}^j is the j th power of the Jacobian \mathcal{J}_{Eq} . This only converges to a difference of zero if \mathcal{J}_{Eq}^j is a zero matrix with eigenvalues being zero for $j \rightarrow \infty$. Since \mathcal{J}_{Eq} is a square matrix with eigenvalues λ_i , the eigenvalues of \mathcal{J}_{Eq}^j are λ_i^j . Thus to reach convergence (i.e. $\lambda^{j \rightarrow \infty} = 0$), all eigenvalues of the Jacobian \mathcal{J}_{Eq} must fulfill ¹

$$|\lambda_i| < 1. \quad (\text{B.34})$$

For a single disk system ($i = 1$), the Jacobian equals its eigenvalue $\mathcal{J}_{Eq} = \lambda_1$ and the difference from equation B.31 is reduced to $\exp(-\ln[|\lambda_1|^{-1}]j)$ of its initial value after j pulses. Convergence is therefore reached after approximately

$$j_{conv} \approx \ln[|\lambda_1|^{-1}]^{-1} \quad (\text{B.35})$$

pulses. The larger the the eigenvalues $|\lambda_i|$, the longer it takes to reach the equilibrium point and the more sensitive the system reacts to distortions of working parameters like input energy, pump intensity and so forth. If the absolute value of any eigenvalue is bigger than one, no equilibrium is reached and the amplifier will amplify each pulse with a varying gain [34]. If the eigenvalues are close to zero, the new equilibrium point is reached almost immediately after working parameters have been changed and negligible gain variations are observed.

If the pumping time is longer than the lifetime τ , the upper level population after pumping is constant

$$PumpEm(N_2) \approx N_2(\infty) \quad (\text{B.36})$$

and the Jacobian \mathcal{J}_{Eq} is always a zero matrix. Hence for repetition rates lower than the inverse lifetime $f_{rep} < \tau^{-1}$ (for $\tau \approx 1$ ms this yields $f_{rep} < 1$ kHz), gain variations from pulse to pulse are in general not observable [34].

¹Some algorithms (e.g. *MATLAB*'s *fsolve*) that can be used to solve $x_{Eq} = \text{root}(f(x))$ (see B.26) calculate the Jacobian $\mathcal{J}_{sol} = \mathcal{J}(f(x))|_{x=x_{Eq}}$ as side product. The Jacobian \mathcal{J}_{sol} calculated during the solution of equation B.25 is easily converted to the Jacobian necessary for the stability analysis by noting that (I is a unity matrix)

$$\mathcal{J}_{sol} = \mathcal{J}(PumpEm(N_2) - N_2)|_{N_2=N_2^{Eq}} \quad (\text{B.32})$$

$$\mathcal{J}_{Eq} = \mathcal{J}(N_2 + PumpEm(N_2) - N_2)|_{N_2=N_2^{Eq}} = I + \mathcal{J}_{sol}. \quad (\text{B.33})$$

Appendix C

Nonlinear Phase Retrieval

For third order nonlinear processes, the accumulated nonlinear phase of a propagating pulse is an important measure that enables immediate conclusions about the strength of the nonlinearity. The nonlinear phase is typically calculated by using a literature value for the nonlinear refractive index n_2 of the medium, measuring (or estimating) the pulse energy, the pulse shape and the beam profile of the propagating pulse, deducing a peak intensity I_{max} from these measurements and using these values in equation 3.35 to obtain the accumulated nonlinear phase.

This calculation method is severely distorted if any of the measured properties does not stay constant during the propagation through the medium. This is especially problematic for the beam profile as it naturally changes during propagation. As long as the profile follows a simple Gaussian beam propagation, its change can be estimated and equation 3.35 can be modified accordingly to incorporate these changes. More complex changes however require a complex propagation model to correctly calculate the accumulated nonlinear phase despite varying beam parameters during the propagation. Also this approach of calculating the nonlinear phase relies on the correct measurement of several beam parameters and even a single measurement error automatically yields a wrong result for the nonlinear phase.

These issues can be solved for third order nonlinear systems that are dominated by self phase modulation and show negligible self-steepening or dispersion. In that case a simple measurement of the input $|\mathcal{A}_{In}(\omega)|$ and output spectrum $|\mathcal{A}_{SPM}(\omega)|$ is enough to retrieve a value for the accumulated nonlinear phase. A similar idea has been published in [141].

In a first step both spectra have to be normed to the same energy, i.e. they have to fulfill

$$\int_{-\infty}^{\infty} |\mathcal{A}_{In}(\omega)|^2 d\omega = \int_{-\infty}^{\infty} |\mathcal{A}_{SPM}(\omega)|^2 d\omega. \quad (\text{C.1})$$

Then the known connection between the input and output spectrum is used to determine unknown system variables.

The input amplitude spectrum $|\mathcal{A}_{In}(\omega)|$ and the input pulse $A(t)$ are related by

$$A(t) = \mathcal{F} [|\mathcal{A}_{In}(\omega)| \exp(i\varphi(\omega))], \quad (\text{C.2})$$

where $\mathcal{F}[\cdot]$ describes the Fourier transform. The input phase $\varphi(\omega)$ is unknown but commonly written as Taylor series

$$\varphi(\omega) = \varphi(0) + \frac{\partial\varphi(\omega)}{\partial\omega} \omega + \frac{\partial^2\varphi(\omega)}{\partial\omega^2} \frac{\omega^2}{2} + \frac{\partial^3\varphi(\omega)}{\partial\omega^3} \frac{\omega^3}{6} + \dots. \quad (\text{C.3})$$

The constant (zero order) and first order phase term do not change the shape of the pulse $A(t)$ and can be neglected. The remaining terms with an order greater than one are referred to as higher order in the following. The second order and third order derivatives of the phase φ are also known as *group delay dispersion (GDD)* and *third order dispersion (TOD)* and are often sufficient to describe the phase of an input pulse, but more accurate results are obtained if more orders are included in the calculation of $\varphi(\omega)$. For $N - 2$ higher order dispersions where N is the amount of measurement points in the input and output spectra, a complete description of the phase is obtained.

With this expression of $A(t)$ and the relation $I(t)/I_{max} = |A(t)|^2/|A_{max}|^2$ (where I_{max} and $|A_{max}|^2$ are the peak values of $I(t)$ and $|A(t)|^2$), the output amplitude spectrum $|\mathcal{A}_{SPM}(\omega)|$ is calculated as Fourier transform of equation 3.36

$$|\mathcal{A}_{SPM}(\omega)| = \left| \mathcal{F} \left[A(t) \exp \left(-i\Delta\phi \frac{|A(t)|^2}{|A_{max}|^2} \right) \right] \right|. \quad (\text{C.4})$$

Even if a complete set of $N - 2$ dispersion orders is used in the description of $A(t)$, the amount of unknowns in this equation is only $N - 1$ (dispersion orders plus nonlinear phase $\Delta\phi$). At the same time N equations exist as $|\mathcal{A}_{SPM}(\omega)|$ consists of N measurement points. Thus the system is potentially overdetermined.

In most cases two dispersion orders (GDD and TOD) are sufficient for the description of $A(t)$. This case is hence treated in more detail for the sake of simplicity. The right hand side of equation C.4 can then be written as function of nonlinear phase $\Delta\phi$, GDD and TOD

$$|\tilde{\mathcal{A}}_{SPM}^{(\Delta\phi, GDD, TOD)}(\omega)| = \left| \mathcal{F} \left[A^{(GDD, TOD)}(t) \exp \left(-i\Delta\phi \frac{|A^{(GDD, TOD)}(t)|^2}{|A_{max}^{(GDD, TOD)}|^2} \right) \right] \right|. \quad (\text{C.5})$$

A simple numeric minimization then yields a result for the nonlinear phase

$$[\Delta\phi, GDD, TOD] = \arg \min_{\Delta\phi, GDD, TOD} \sum_{\omega} \left[|\mathcal{A}_{SPM}(\omega)| - |\tilde{\mathcal{A}}_{SPM}^{(\Delta\phi, GDD, TOD)}(\omega)| \right]^2. \quad (\text{C.6})$$

The success of this minimization is visually easily confirmed by comparing the retrieved spectrum $|\tilde{\mathcal{A}}_{SPM}^{(\Delta\phi, GDD, TOD)}(\omega)|$ to the measured spectrum $|\mathcal{A}_{SPM}(\omega)|$. Note that this method also provides an estimate for the GDD and TOD of the input pulse and hence allows for the calculation of an input pulse shape $A(t)$.

Even more dispersion orders can be added to the minimization process but a retrieval of more orders than 6 turned out to be challenging as most minimization algorithms slow down with more orders and tend to converge to a local minimum that does not represent a good fit between measured and retrieved spectrum.

Appendix D

Data Archiving

The experimental data is saved on the data archive server of the Laboratory for Attosecond Physics at the Max Planck Institute of Quantum Optics and can be found in the following directory

/afs/ipp-garching.mpg.de/mpq/lap/publication_archive/Theses/2020/

The folder *Calculations* lists analytical calculations derived within the scope of this thesis. Mentioned measurements without a corresponding figure are listed in the folder *RawDataMentioned*. Any data connected to figures is listed in the folder *Images*. Every folder contains a *ReadMe.txt* file with explanations and instructions about the data in the corresponding folder.

Bibliography

- [1] T. H. Maiman. “Stimulated optical radiation in ruby”. In: *Nature* 187.4736 (Aug. 1960), pp. 493–494.
- [2] A. E. Siegman. *Lasers*. University Science Books, 1986.
- [3] F. Krausz and M. Ivanov. “Attosecond physics”. In: *Rev. Mod. Phys.* 81 (1 Feb. 2009), pp. 163–234.
- [4] I. Pupeza, M. Huber, M. Trubetskov, W. Schweinberger, S. A. Hussain, C. Hofer, K. Fritsch, M. Poetzlberger, L. Vamos, E. Fill, T. Amotchkina, K. V. Kepesidis, A. Apolonski, N. Karpowicz, V. Pervak, O. Pronin, F. Fleischmann, A. Azzeer, M. Zigman, and F. Krausz. “Field-resolved infrared spectroscopy of biological systems”. In: *Nature* 577.7788 (2020), pp. 52–59.
- [5] J. W. Yoon, C. Jeon, J. Shin, S. K. Lee, H. W. Lee, I. W. Choi, H. T. Kim, J. H. Sung, and C. H. Nam. “Achieving the laser intensity of 5.5 W/cm^2 with a wavefront-corrected multi-PW laser”. In: *Opt. Express* 27.15 (July 2019), pp. 20412–20420.
- [6] R. Behling and F. Grüner. “Diagnostic X-ray sources—present and future”. In: *Nuclear Instruments and Methods in Physics Research Section A: Accelerators, Spectrometers, Detectors and Associated Equipment* 878 (2018). Radiation Imaging Techniques and Applications, pp. 50–57.
- [7] J. Schreiber, P. R. Bolton, and K. Parodi. “Invited Review Article: “Hands-on” laser-driven ion acceleration: A primer for laser-driven source development and potential applications”. In: *Review of Scientific Instruments* 87.7 (2016), p. 071101.
- [8] H. Fattahi, H. G. Barros, M. Gorjan, T. Nubbemeyer, B. Alsaif, C. Y. Teisset, M. Schultze, S. Prinz, M. Haefner, M. Ueffing, A. Alismail, L. Vámos, A. Schwarz, O. Pronin, J. Brons, X. T. Geng, G. Arisholm, M. Ciappina, V. S. Yakovlev, D.-E. Kim, A. M. Azzeer, N. Karpowicz, D. Sutter, Z. Major, T. Metzger, and F. Krausz. “Third-generation femtosecond technology”. In: *Optica* 1.1 (July 2014), pp. 45–63.
- [9] G. Sansone, L. Poletto, and M. Nisoli. “High-energy attosecond light sources”. In: *Nature Photonics* 5.11 (Sept. 2011), pp. 655–663.
- [10] C. J. Saraceno, D. Sutter, T. Metzger, and M. A. Ahmed. “The amazing progress of high-power ultrafast thin-disk lasers”. In: *Journal of the European Optical Society-Rapid Publications* 15.1 (June 2019).
- [11] B. E. Schmidt, A. Hage, T. Mans, F. Légaré, and H. J. Wörner. “Highly stable, 54mJ Yb-InnoSlab laser platform at 0.5kW average power”. In: *Opt. Express* 25.15 (Dec. 2017), pp. 17549–17555.

- [12] H. Stark, J. Buldt, M. Müller, A. Klenke, A. Tünnermann, and J. Limpert. “23 mJ high-power fiber CPA system using electro-optically controlled divided-pulse amplification”. In: *Opt. Lett.* 44.22 (Nov. 2019), pp. 5529–5532.
- [13] A. Giesen, H. Hügel, A. Voss, K. Wittig, U. Brauch, and H. Opower. “Scalable concept for diode-pumped high-power solid-state lasers”. In: *Applied Physics B* 58.5 (May 1994), pp. 365–372.
- [14] R. Budriūnas, T. Stanislauskas, J. Adamonis, A. Aleknavičius, G. Veitas, D. Gadonas, S. Balickas, A. Michailovas, and A. Varanavičius. “53 W average power CEP-stabilized OPCPA system delivering 5.5 TW few cycle pulses at 1 kHz repetition rate”. In: *Opt. Express* 25.5 (Mar. 2017), pp. 5797–5806.
- [15] M. K. R. Windeler, K. Mecseki, A. Miahnahri, J. S. Robinson, J. M. Fraser, A. R. Fry, and F. Tavella. “100 W high-repetition-rate near-infrared optical parametric chirped pulse amplifier”. In: *Opt. Lett.* 44.17 (Sept. 2019), pp. 4287–4290.
- [16] B. Saleh and M. Teich. *Fundamentals of Photonics*. Wiley Series in Pure and Applied Optics. Wiley, 2007.
- [17] M. F. Erden and H. M. Ozaktas. “Accumulated Gouy phase shift in Gaussian beam propagation through first-order optical systems”. In: *J. Opt. Soc. Am. A* 14.9 (Sept. 1997), pp. 2190–2194.
- [18] K. Arai. *On the accumulated round-trip Gouy phase shift for a general optical cavity*. Tech. rep. LIGO-T1300189–v1. LIGO Scientific Collaboration, Mar. 2013, p. 10.
- [19] R. Paschotta. “Beam quality deterioration of lasers caused by intracavity beam distortions”. In: *Opt. Express* 14.13 (June 2006), pp. 6069–6074.
- [20] S. D. Silvestri, P. Laporta, and V. Magni. “Rod thermal lensing effects in solid-state laser ring resonators”. In: *Optics Communications* 65.5 (1988), pp. 373–376.
- [21] K. Schuhmann, K. Kirch, F. Nez, R. Pohl, and A. Antognini. “Thin-disk laser scaling limit due to thermal lens induced misalignment instability”. In: *Appl. Opt.* 55.32 (Nov. 2016), pp. 9022–9032.
- [22] P. Russbuedt, J. Weitenberg, A. Vernaleken, T. Sartorius, and J. Schulte. “Method and arrangement for spectral broadening of laser pulses for non-linear pulse compression”. Patent US 9847615B2 (US). Dec. 2017.
- [23] A. E. Siegman. “New developments in laser resonators”. In: *Optical Resonators*. Vol. 1224. International Society for Optics and Photonics. 1990, pp. 2–14.
- [24] *Lasers and laser-related equipment — Test methods for laser beam widths, divergence angles and beam propagation ratios*. Standard. Geneva, CH: International Organization for Standardization, Jan. 2005.
- [25] *M2-200s User Guide*. Ophir Spiricon Europe GmbH. 2018.
- [26] A. E. Siegman. “How to (Maybe) Measure Laser Beam Quality”. In: *DPSS (Diode Pumped Solid State) Lasers: Applications and Issues*. Optical Society of America, 1998, MQ1.

- [27] S. Piehler, T. Dietrich, P. Wittmüss, O. Sawodny, M. A. Ahmed, and T. Graf. “Deformable mirrors for intra-cavity use in high-power thin-disk lasers”. In: *Opt. Express* 25.4 (Feb. 2017), pp. 4254–4267.
- [28] D. Strickland and G. Mourou. “Compression of amplified chirped optical pulses”. In: *Optics Communications* 55.6 (1985), pp. 447–449.
- [29] D. E. McCumber. “Einstein Relations Connecting Broadband Emission and Absorption Spectra”. In: *Phys. Rev.* 136 (4A Nov. 1964), A954–A957.
- [30] W. H. Lowdermilk and J. E. Murray. “The multipass amplifier: Theory and numerical analysis”. In: *Journal of Applied Physics* 51.5 (1980), pp. 2436–2444.
- [31] C. C. Ranaud, H. L. Offerhaus, J. A. Alvarez-Chavez, C. J. Nilsson, W. A. Clarkson, P. W. Turner, D. J. Richardson, and A. B. Grudinin. “Characteristics of Q-switched cladding-pumped ytterbium-doped fiber lasers with different high-energy fiber designs”. In: *IEEE Journal of Quantum Electronics* 37.2 (Feb. 2001), pp. 199–206.
- [32] J. Speiser. “Scaling of thin-disk lasers—influence of amplified spontaneous emission”. In: *J. Opt. Soc. Am. B* 26.1 (Jan. 2009), pp. 26–35.
- [33] J. Dörring, A. Killi, U. Morgner, A. Lang, M. Lederer, and D. Kopf. “Period doubling and deterministic chaos in continuously pumped regenerative amplifiers”. In: *Opt. Express* 12.8 (Apr. 2004), pp. 1759–1768.
- [34] M. Grishin, V. Gulbinas, and A. Michailovas. “Dynamics of high repetition rate regenerative amplifiers”. In: *Opt. Express* 15.15 (July 2007), pp. 9434–9443.
- [35] M. Eichhorn and M. Pollnau. “Spectroscopic Foundations of Lasers: Spontaneous Emission Into a Resonator Mode”. In: *IEEE Journal of Selected Topics in Quantum Electronics* 21.1 (Jan. 2015), pp. 486–501.
- [36] L. E. Hargrove, R. L. Fork, and M. A. Pollack. “Locking of He-Ne Laser modes induced by synchronous intracavity modulation”. In: *Applied Physics Letters* 5.1 (1964), pp. 4–5.
- [37] J. Brons, V. Pervak, E. Fedulova, D. Bauer, D. Sutter, V. Kalashnikov, A. Apolonskiy, O. Pronin, and F. Krausz. “Energy scaling of Kerr-lens mode-locked thin-disk oscillators”. In: *Opt. Lett.* 39.22 (Nov. 2014), pp. 6442–6445.
- [38] C. Y. Teisset, M. Schultze, R. Bessing, M. Häfner, S. Prinz, D. Sutter, and T. Metzger. “300 W Picosecond Thin-Disk Regenerative Amplifier at 10 kHz Repetition Rate”. In: *Advanced Solid-State Lasers Congress Postdeadline*. Optical Society of America, 2013, JTh5A.1.
- [39] O. Pronin, J. Brons, C. Grasse, V. Pervak, G. Boehm, M.-C. Amann, V. L. Kalashnikov, A. Apolonski, and F. Krausz. “High-power 200 fs Kerr-lens mode-locked Yb:YAG thin-disk oscillator”. In: *Opt. Lett.* 36.24 (Dec. 2011), pp. 4746–4748.

- [40] O. E. Martinez, J. P. Gordon, and R. L. Fork. “Negative group-velocity dispersion using refraction”. In: *J. Opt. Soc. Am. A* 1.10 (Oct. 1984), pp. 1003–1006.
- [41] E. Treacy. “Optical pulse compression with diffraction gratings”. In: *IEEE Journal of Quantum Electronics* 5.9 (Sept. 1969), pp. 454–458.
- [42] A. A. Jalali, J. Rybarsyk, and E. Rogers. “Thermal lensing analysis of TGG and its effect on beam quality”. In: *Opt. Express* 21.11 (June 2013), pp. 13741–13747.
- [43] R. Trebino, K. W. DeLong, D. N. Fittinghoff, J. N. Sweetser, M. A. Krumbügel, B. A. Richman, and D. J. Kane. “Measuring ultrashort laser pulses in the time-frequency domain using frequency-resolved optical gating”. In: *Review of Scientific Instruments* 68.9 (1997), pp. 3277–3295.
- [44] G. Imeshev, I. Hartl, and M. E. Fermann. “Chirped pulse amplification with a nonlinearly chirped fiber Bragg grating matched to the Treacy compressor”. In: *Opt. Lett.* 29.7 (Apr. 2004), pp. 679–681.
- [45] J. Koerner, C. Vorholt, H. Liebetrau, M. Kahle, D. Kloepfel, R. Seifert, J. Hein, and M. C. Kaluza. “Measurement of temperature-dependent absorption and emission spectra of Yb:YAG, Yb:LuAG, and Yb:CaF₂ between 20°C and 200°C and predictions on their influence on laser performance”. In: *J. Opt. Soc. Am. B* 29.9 (Sept. 2012), pp. 2493–2502.
- [46] G. Huber, C. Kränkel, and K. Petermann. “Solid-state lasers: status and future [Invited]”. In: *J. Opt. Soc. Am. B* 27.11 (Nov. 2010), B93–B105.
- [47] M. Müller, A. Klenke, A. Steinkopff, H. Stark, A. Tünnermann, and J. Limpert. “3.5 kW coherently combined ultrafast fiber laser”. In: *Opt. Lett.* 43.24 (Dec. 2018), pp. 6037–6040.
- [48] P. Russbuedt, D. Hoffmann, M. Höfer, J. Löhring, J. Luttmann, A. Meissner, J. Weitenberg, M. Traub, T. Sartorius, D. Esser, R. Wester, P. Loosen, and R. Poprawe. “Innoslab Amplifiers”. In: *IEEE Journal of Selected Topics in Quantum Electronics* 21.1 (Jan. 2015), pp. 447–463.
- [49] P. Russbuedt, T. Mans, G. Rotarius, J. Weitenberg, H. Hoffmann, and R. Poprawe. “400 W Yb:YAG Innoslab fs-amplifier”. In: *Opt. Express* 17.15 (July 2009), pp. 12230–12245.
- [50] P. Rußbüldt, J. Weitenberg, T. Sartorius, G. Rotarius, H. D. Hoffmann, and R. Poprawe. “Ytterbium Innoslab amplifiers - The high average power approach of ultrafast lasers”. In: *AIP Conference Proceedings* 1462.1 (2012), pp. 120–123.
- [51] C. J. Saraceno, D. Sutter, T. Metzger, and M. A. Ahmed. “The amazing progress of high-power ultrafast thin-disk lasers”. In: *Journal of the European Optical Society-Rapid Publications* 15.1 (June 2019).

- [52] T. Gottwald, V. Kuhn, S.-S. Schad, C. Stolzenburg, and A. Killi. “Recent developments in high power thin disk lasers at TRUMPF Laser”. In: *Technologies for Optical Countermeasures X; and High-Power Lasers 2013: Technology and Systems*. Proc. SPIE 8898 (2013). Ed. by D. H. Titterton, M. A. Richardson, R. J. Grasso, H. Ackermann, and W. L. Bohn. Dresden, Germany, 2013, 88980P1–88980P7.
- [53] T. Südmeyer, C. Kränkel, C. R. E. Baer, O. H. Heckl, C. J. Saraceno, M. Golling, R. Peters, K. Petermann, G. Huber, and U. Keller. “High-power ultrafast thin disk laser oscillators and their potential for sub-100-femtosecond pulse generation”. In: *Applied Physics B* 97.2 (Sept. 2009), pp. 281–295.
- [54] P. Crump, G. Erbert, H. Wenzel, C. Frevert, C. M. Schultz, K. Hasler, R. Staske, B. Sumpf, A. Maaßdorf, F. Bugge, S. Knigge, and G. Tränkle. “Efficient High-Power Laser Diodes”. In: *IEEE Journal of Selected Topics in Quantum Electronics* 19.4 (July 2013), pp. 1501211–1501211.
- [55] *Laser Crystals*. ALPHALAS GmbH. 2019.
- [56] V. Lupei. “Efficiency enhancement and power scaling of Nd lasers”. In: *Optical Materials* 24.1 (2003). Proceedings of the Fifth French-Israeli Workshop on Optical Properties of Inorganic Materials, pp. 353–368.
- [57] R. Peters, C. Kränkel, S. T. Fredrich-Thornton, K. Beil, K. Petermann, G. Huber, O. H. Heckl, C. R. E. Baer, C. J. Saraceno, T. Südmeyer, and U. Keller. “Thermal analysis and efficient high power continuous-wave and mode-locked thin disk laser operation of Yb-doped sesquioxides”. In: *Applied Physics B* 102.3 (Feb. 2011), pp. 509–514.
- [58] K. Beil, S. T. Fredrich-Thornton, F. Tellkamp, R. Peters, C. Kränkel, K. Petermann, and G. Huber. “Thermal and laser properties of Yb:LuAG for kW thin disk lasers”. In: *Opt. Express* 18.20 (Feb. 2010), pp. 20712–20722.
- [59] *Laser Materials Lu₃Al₅O₁₂*. Scientific Material Corp. 2010.
- [60] *Nd:YAG*. Crylink Inc. 2019.
- [61] S. Breitkopf, T. Eidam, A. Klenke, L. von Grafenstein, H. Carstens, S. Holzberger, E. Fill, T. Schreiber, F. Krausz, A. Tünnermann, I. Pupeza, and J. Limpert. “A concept for multiterawatt fibre lasers based on coherent pulse stacking in passive cavities”. In: *Light: Science & Applications* 3 (Oct. 2014), e211.
- [62] M. Ueffing. “Direct amplification of femtosecond pulses”. PhD thesis. Mar. 2018.
- [63] M. Roth, M. Tseitlin, and N. Angert. “Oxide crystals for electro-optic Q-switching of lasers”. In: *Glass Physics and Chemistry* 31.1 (Jan. 2005), pp. 86–95.
- [64] *Beta-Barium Borate*. CASTECH Inc. 2017.

- [65] N. F. Andreev, A. A. Babin, V. S. Davydov, A. Z. Matveev, S. G. Garanin, Y. V. Dolgopolov, S. M. Kulikov, S. A. Sukharev, and S. V. Tyutin. “Wide-aperture plasma-electrode pockels cell”. In: *Plasma Physics Reports* 37.13 (Dec. 2011), pp. 1219–1224.
- [66] *Crystals*. Eksma Optics. 2016.
- [67] A. Gutsol, A. Fridman, and Y. Cho. “Non-Thermal Atmospheric Pressure Plasma”. In: *Advances in Heat Transfer* 40 (Jan. 2007), pp. 1–142.
- [68] B. C. Stuart, M. D. Feit, A. M. Rubenchik, B. W. Shore, and M. D. Perry. “Laser-Induced Damage in Dielectrics with Nanosecond to Subpicosecond Pulses”. In: *Phys. Rev. Lett.* 74 (12 Mar. 1995), pp. 2248–2251.
- [69] W. Koechner. “Absorbed Pump Power, Thermal Profile and Stresses in a cw Pumped Nd:YAG Crystal”. In: *Appl. Opt.* 9.6 (June 1970), pp. 1429–1434.
- [70] J. Rothhardt, S. Hädrich, J. Delagnes, E. Cormier, and J. Limpert. “High Average Power Near-Infrared Few-Cycle Lasers”. In: *Laser & Photonics Reviews* 11.4 (2017), p. 1700043.
- [71] J. Rothhardt, S. Demmler, S. Hädrich, T. Peschel, J. Limpert, and A. Tünnermann. “Thermal effects in high average power optical parametric amplifiers”. In: *Opt. Lett.* 38.5 (Mar. 2013), pp. 763–765.
- [72] R. Riedel, J. Rothhardt, K. Beil, B. Gronloh, A. Klenke, H. Höppner, M. Schulz, U. Teubner, C. Kränkel, J. Limpert, A. Tünnermann, M. Prandolini, and F. Tavella. “Thermal properties of borate crystals for high power optical parametric chirped-pulse amplification”. In: *Opt. Express* 22.15 (July 2014), pp. 17607–17619.
- [73] K. Contag. “Modellierung und numerische Auslegung des Yb:YAG-Scheibenlasers”. PhD thesis. 2002.
- [74] S. Piehler, B. Weichelt, A. Voss, M. A. Ahmed, and T. Graf. “Power scaling of fundamental-mode thin-disk lasers using intracavity deformable mirrors”. In: *Opt. Lett.* 37.24 (Dec. 2012), pp. 5033–5035.
- [75] H. Fattahi, A. Schwarz, X. T. Geng, S. Keiber, D. E. Kim, F. Krausz, and N. Karpowicz. “Decoupling chaotic amplification and nonlinear phase in high-energy thin-disk amplifiers for stable OPCPA pumping”. In: *Opt. Express* 22.25 (Dec. 2014), pp. 31440–31447.
- [76] B. C. Stuart, M. D. Feit, S. Herman, A. M. Rubenchik, B. W. Shore, and M. D. Perry. “Nanosecond-to-femtosecond laser-induced breakdown in dielectrics”. In: *Phys. Rev. B* 53 (4 Jan. 1996), pp. 1749–1761.
- [77] R. Lange. “Design and Characterization of a Yb:YAG Thin-Disk Multipass Amplifier for 20 mJ, Sub-Picosecond Laser Pulses”. MA thesis. Dec. 2015.
- [78] I. Astrauskas, E. Kaksis, T. Flöry, G. Andriukaitis, A. Pugžlys, A. Baltuška, J. Ruppe, S. Chen, A. Galvanauskas, and T. Balčiūnas. “High-energy pulse stacking via regenerative pulse-burst amplification”. In: *Opt. Lett.* 42.11 (June 2017), pp. 2201–2204.

- [79] T. Y. Fan. “Heat generation in Nd:YAG and Yb:YAG”. In: *IEEE Journal of Quantum Electronics* 29.6 (June 1993), pp. 1457–1459.
- [80] N. Barnes and B. Walsh. “Quantum efficiency measurements of Nd:YAG, Yb:YAG, and Tm:YAG”. In: *Advanced Solid State Lasers* 68 (Feb. 2002), pp. 284–287.
- [81] C. Stewen, K. Contag, M. Larionov, A. Giesen, and H. Hugel. “A 1-kW CW thin disc laser”. In: *IEEE Journal of Selected Topics in Quantum Electronics* 6.4 (July 2000), pp. 650–657.
- [82] D. Blázquez-Sánchez, B. Weichelt, A. Austerschulte, A. Voss, T. Graf, A. Killi, H.-C. Eckstein, M. Stumpf, A. L. Matthes, and U. D. Zeitner. “Improving the brightness of a multi-kilowatt single thin-disk laser by an aspherical phase front correction”. In: *Opt. Lett.* 36.6 (Mar. 2011), pp. 799–801.
- [83] T. Dietrich, S. Piehler, C. Röcker, M. Rumpel, M. A. Ahmed, and T. Graf. “Passive compensation of the misalignment instability caused by air convection in thin-disk lasers”. In: *Opt. Lett.* 42.17 (Sept. 2017), pp. 3263–3266.
- [84] A. Diebold, F. Saltarelli, I. J. Graumann, C. J. Saraceno, C. R. Phillips, and U. Keller. “Gas-lens effect in kW-class thin-disk lasers”. In: *Opt. Express* 26.10 (May 2018), pp. 12648–12659.
- [85] R. G. Eldridge. “Water Vapor Absorption of Visible and Near Infrared Radiation”. In: *Appl. Opt.* 6.4 (Apr. 1967), pp. 709–713.
- [86] J. C. Owens. “Optical Refractive Index of Air: Dependence on Pressure, Temperature and Composition”. In: *Appl. Opt.* 6.1 (Jan. 1967), pp. 51–59.
- [87] M. E. Innocenzi, H. T. Yura, C. L. Fincher, and R. A. Fields. “Thermal modeling of continuous-wave end-pumped solid-state lasers”. In: *Applied Physics Letters* 56.19 (1990), pp. 1831–1833.
- [88] R. Penndorf. “Tables of the Refractive Index for Standard Air and the Rayleigh Scattering Coefficient for the Spectral Region between 0.2 and 20.0 μ and Their Application to Atmospheric Optics”. In: *J. Opt. Soc. Am.* 47.2 (Feb. 1957), pp. 176–182.
- [89] D. N. Nguyen, L. A. Emmert, P. Schwoebel, D. Patel, C. S. Menoni, M. Shinn, and W. Rudolph. “Femtosecond pulse damage thresholds of dielectric coatings in vacuum”. In: *Opt. Express* 19.6 (Mar. 2011), pp. 5690–5697.
- [90] T. Pleyer. “Design of a Dielectric Chirped Mirror Compressor for a CPA free Sub-Picosecond Multi-mJ Multi-kHz Yb:YAG Amplifier”. MA thesis. Apr. 2015.
- [91] R. Goldstein. “Pockels Cell Primer”. In: *Laser Focus Magazine* (Feb. 1968).
- [92] *WinCamD User Manual*. DataRay Inc. 2019.
- [93] G. Cheriaux, P. Rousseau, F. Salin, J. P. Chambaret, B. Walker, and L. F. Dimauro. “Aberration-free stretcher design for ultrashort-pulse amplification”. In: *Opt. Lett.* 21.6 (Mar. 1996), pp. 414–416.
- [94] *Yb:CALGO*. Crylink Inc. 2019.

- [95] S. Ricaud, A. Jaffres, P. Loiseau, B. Viana, B. Weichelt, M. Abdou-Ahmed, A. Voss, T. Graf, D. Rytz, M. Delaigue, E. Mottay, P. Georges, and F. Druon. “Yb:CaGdAlO₄ thin-disk laser”. In: *Opt. Lett.* 36.21 (Nov. 2011), pp. 4134–4136.
- [96] R. W. Boyd. *Nonlinear Optics*. Elsevier, 2008.
- [97] G. Agrawal. *Nonlinear Fiber Optics*. Elsevier, 2013.
- [98] E. R. Peck and D. J. Fisher. “Dispersion of Argon”. In: *J. Opt. Soc. Am.* 54.11 (Nov. 1964), pp. 1362–1364.
- [99] D. Anderson, M. Desaix, M. Lisak, and M. L. Quiroga-Teixeiro. “Wave breaking in nonlinear-optical fibers”. In: *J. Opt. Soc. Am. B* 9.8 (Aug. 1992), pp. 1358–1361.
- [100] N. Milosevic, G. Tempea, and T. Brabec. “Optical pulse compression: bulk media versus hollow waveguides”. In: *Opt. Lett.* 25.9 (May 2000), pp. 672–674.
- [101] F. Batysta, R. Antipenkov, J. Novák, J. T. Green, J. A. Naylon, J. Horáček, M. Horáček, Z. Hubka, R. Boge, T. Mazanec, B. Himmel, P. Bakule, and B. Rus. “Broadband OPCPA system with 11 mJ output at 1 kHz, compressible to 12 fs”. In: *Opt. Express* 24.16 (Aug. 2016), pp. 17843–17848.
- [102] S. Prinz, M. Schnitzenbaumer, D. Potamianos, M. Schultze, S. Stark, M. Häfner, C. Y. Teisset, C. Wandt, K. Michel, R. Kienberger, B. Bernhardt, and T. Metzger. “Thin-disk pumped optical parametric chirped pulse amplifier delivering CEP-stable multi-mJ few-cycle pulses at 6 kHz”. In: *Opt. Express* 26.2 (Jan. 2018), pp. 1108–1124.
- [103] K. Mecseki, M. K. R. Windeler, A. Miahnahri, J. S. Robinson, J. M. Fraser, A. R. Fry, and F. Tavella. “High average power 88 W OPCPA system for high-repetition-rate experiments at the LCLS x-ray free-electron laser”. In: *Opt. Lett.* 44.5 (Mar. 2019), pp. 1257–1260.
- [104] L. Gallmann, T. Pfeifer, P. Nagel, M. Abel, D. Neumark, and S. Leone. “Comparison of the filamentation and the hollow-core fiber characteristics for pulse compression into the few-cycle regime”. In: *Applied Physics B* 86 (Mar. 2007), pp. 561–566.
- [105] C. Brée, A. Demircan, S. Skupin, L. Bergé, and G. Steinmeyer. “Plasma Induced Pulse Breaking in Filamentary Self-Compression”. In: *Laser Physics* 20 (Apr. 2010), p. 1107.
- [106] C. Hauri, W. Kornelis, F. Helbing, A. Heinrich, A. Couairon, A. Mysyrowicz, J. Biegert, and U. Keller. “Generation of intense, carrier-envelope phase-locked few-cycle laser pulses through filamentation”. In: *Applied Physics B* 79 (Oct. 2004), pp. 673–677.
- [107] A. Zaïr, A. Guandalini, F. Schapper, M. Holler, J. Biegert, L. Gallmann, A. Couairon, M. Franco, A. Mysyrowicz, and U. Keller. “Spatio-temporal characterization of few-cycle pulses obtained by filamentation”. In: *Opt. Express* 15.9 (Apr. 2007), pp. 5394–5405.

- [108] M. Nisoli, S. Stagira, S. D. Silvestri, O. Svelto, S. Sartania, Z. Cheng, M. Lenzner, C. Spielmann, and F. Krausz. “A novel-high energy pulse compression system: generation of multigigawatt sub-5-fs pulses”. In: *Applied Physics B: Lasers and Optics* 65.2 (Aug. 1997), pp. 189–196.
- [109] S. Bohman, A. Suda, T. Kanai, S. Yamaguchi, and K. Midorikawa. “Generation of 5.0fs, 5.0mj pulses at 1kHz using hollow-fiber pulse compression”. In: *Opt. Lett.* 35.11 (June 2010), pp. 1887–1889.
- [110] C. Vozzi, M. Nisoli, G. Sansone, S. Stagira, and S. De Silvestri. “Optimal spectral broadening in hollow-fiber compressor systems”. In: *Applied Physics B* 80.3 (2005), pp. 285–289.
- [111] M. Nisoli, S. Stagira, S. De Silvestri, O. Svelto, S. Sartania, Z. Cheng, G. Tempea, C. Spielmann, and F. Krausz. “Toward a terawatt-scale sub-10-fs laser technology”. In: *IEEE Journal of selected topics in quantum electronics* 4.2 (1998), pp. 414–420.
- [112] E. A. J. Marcatili and R. A. Schmeltzer. “Hollow Metallic and Dielectric Waveguides for Long Distance Optical Transmission and Lasers”. In: *Bell System Technical Journal* 43.4 (1964), pp. 1783–1809.
- [113] S. Hädrich, J. Rothhardt, S. Demmler, M. Tschernajew, A. Hoffmann, M. Krebs, A. Liem, O. de Vries, M. Plötner, S. Fabian, T. Schreiber, J. Limpert, and A. Tünnermann. “Scalability of components for kW-level average power few-cycle lasers”. In: *Appl. Opt.* 55.7 (Mar. 2016), pp. 1636–1640.
- [114] M. Hanna, X. Délen, L. Lavenu, F. Guichard, Y. Zaouter, F. Druon, and P. Georges. “Nonlinear temporal compression in multipass cells: theory”. In: *J. Opt. Soc. Am. B* 34.7 (July 2017), pp. 1340–1347.
- [115] M. Ueffing, S. Reiger, M. Kaumanns, V. Pervak, M. Trubetskov, T. Nubbe-meyer, and F. Krausz. “Nonlinear pulse compression in a gas-filled multipass cell”. In: *Opt. Lett.* 43.9 (May 2018), pp. 2070–2073.
- [116] L. Lavenu, M. Natile, F. Guichard, Y. Zaouter, X. Delen, M. Hanna, E. Mottay, and P. Georges. “Nonlinear pulse compression based on a gas-filled multipass cell”. In: *Opt. Lett.* 43.10 (May 2018), pp. 2252–2255.
- [117] J. Schulte, T. Sartorius, J. Weitenberg, A. Vernaleken, and P. Russbuedt. “Nonlinear pulse compression in a multi-pass cell”. In: *Opt. Lett.* 41.19 (Oct. 2016), pp. 4511–4514.
- [118] D. R. Herriott and H. J. Schulte. “Folded Optical Delay Lines”. In: *Appl. Opt.* 4.8 (Aug. 1965), pp. 883–889.
- [119] S. Zahedpour, J. K. Wahlstrand, and H. M. Milchberg. “Measurement of the nonlinear refractive index of air constituents at mid-infrared wavelengths”. In: *Opt. Lett.* 40.24 (Dec. 2015), pp. 5794–5797.
- [120] J. Weitenberg, A. Vernaleken, J. Schulte, A. Ozawa, T. Sartorius, V. Pervak, H.-D. Hoffmann, T. Udem, P. Russböldt, and T. W. Hänsch. “Multi-pass-cell-based nonlinear pulse compression to 115 fs at 7.5 μ J pulse energy and 300 W average power”. In: *Opt. Express* 25.17 (Aug. 2017), pp. 20502–20510.

- [121] C. V. Bindhu, S. S. Harilal, M. S. Tillack, F. Najmabadi, and A. C. Gaeris. “Laser propagation and energy absorption by an argon spark”. In: *Journal of Applied Physics* 94.12 (2003), pp. 7402–7407.
- [122] R. K. Avery. “Interpretation of picosecond laser-induced breakdown in argon and xenon”. In: *Journal of Physics D: Applied Physics* 17.8 (Aug. 1984), pp. 1657–1663.
- [123] C. G. Morgan. “Laser-induced breakdown of gases”. In: *Reports on Progress in Physics* 38.5 (May 1975), pp. 621–665.
- [124] C. L. M. Ireland and C. G. Morgan. “Gas breakdown by a short laser pulse”. In: *Journal of Physics D: Applied Physics* 6.6 (Apr. 1973), pp. 720–729.
- [125] P. Russbuedt, J. Weitenberg, J. Schulte, R. Meyer, C. Meinhardt, H. D. Hoffmann, and R. Poprawe. “Scalable 30 fs laser source with 530 W average power”. In: *Opt. Lett.* 44.21 (Nov. 2019), pp. 5222–5225.
- [126] C. Bree, A. Demircan, and G. Steinmeyer. “Method for computing the nonlinear refractive index via Keldysh theory”. In: *IEEE Journal of Quantum Electronics* 46.4 (2010), pp. 433–437.
- [127] I. H. Malitson. “Interspecimen Comparison of the Refractive Index of Fused Silica*,†”. In: *J. Opt. Soc. Am.* 55.10 (Oct. 1965), pp. 1205–1209.
- [128] T. Y. Fan. “Laser beam combining for high-power, high-radiance sources”. In: *IEEE Journal of selected topics in Quantum Electronics* 11.3 (2005), pp. 567–577.
- [129] H. Jacqmin, A. Jullien, B. Mercier, M. Hanna, F. Druon, D. Papadopoulos, and R. Lopez-Martens. “Passive coherent combining of CEP-stable few-cycle pulses from a temporally divided hollow fiber compressor”. In: *Opt. Lett.* 40.5 (Mar. 2015), pp. 709–712.
- [130] S. Ghimire, B. Shan, C.-Y. Wang, and Z. Chang. “High-energy 6.2-fs pulses for attosecond pulse generation”. In: *Laser Physics* 15 (June 2005), pp. 838–842.
- [131] X. Chen, A. Jullien, A. Malvache, L. Canova, A. Borot, A. Trisorio, C. G. Durfee, and R. Lopez-Martens. “Generation of 4.3 fs, 1 mJ laser pulses via compression of circularly polarized pulses in a gas-filled hollow-core fiber”. In: *Opt. Lett.* 34.10 (May 2009), pp. 1588–1590.
- [132] F. Böhle, M. Kretschmar, A. Jullien, M. Kovacs, M. Miranda, R. Romero, H. Crespo, U. Morgner, P. Simon, R. Lopez-Martens, and T. Nagy. “Compression of CEP-stable multi-mJ laser pulses down to 4 fs in long hollow fibers”. In: *Laser Physics Letters* 11.9 (June 2014), p. 095401.
- [133] W. Rudolph, L. Emmert, Z. Sun, D. Patel, and C. Menoni. “Laser damage in dielectric films: What we know and what we don’t”. In: *Laser-Induced Damage in Optical Materials: 2013*. Ed. by G. J. Exarhos, V. E. Gruzdev, J. A. Menapace, D. Ristau, and M. Soileau. Vol. 8885. International Society for Optics and Photonics. SPIE, 2013, pp. 143–152.

-
- [134] M. Mero, J. Liu, W. Rudolph, D. Ristau, and K. Starke. “Scaling laws of femtosecond laser pulse induced breakdown in oxide films”. In: *Phys. Rev. B* 71 (11 Mar. 2005), p. 115109.
- [135] A. Borovskii and A. Galkin. “Propagation of an intense ultrashort laser pulse under conditions of multiple nonlinear ionization”. In: *Journal of Experimental and Theoretical Physics* 81.2 (1995), pp. 230–234.
- [136] T. M. Kardaś. *Hussar software. Matlab framework*. Faculty of Physics University of Warsaw. July 2018. URL: <http://ufs.edu.pl>. License: Creative Commons 4.0 BY-NC-SA.
- [137] T. Stanislauskas, I. Balčiūnas, R. Budriūnas, G. Veitas, D. Gadonas, J. Adamonis, A. Michailovas, Á. Börzsönyi, S. Tóth, J. Csontos, and K. Osvay. “Chirped pulse parametric amplifier producing 5-TW, 2.1-cycle, CEPstable pulses at 1 kHz repetition rate”. In: *2019 Conference on Lasers and Electro-Optics Europe and European Quantum Electronics Conference*. Optical Society of America, 2019, cg_p_16.
- [138] R. Antipenkov, F. Batysta, R. Boge, E. Erdman, M. Greco, J. T. Green, B. Himmel, M. Horáček, Z. Hubka, L. Indra, K. Majer, T. Mazanec, P. Mazurek, J. Naylor, J. Novák, Václav Šobr, A. Špaček, P. Strkula, M. Torun, B. Tykalewicz, P. Bakule, and B. Rus. “The construction of Allegra kilohertz femtosecond laser system at ELI-Beamlines”. In: *Short-pulse High-energy Lasers and Ultrafast Optical Technologies*. Ed. by P. Bakule and C. L. Haefner. Vol. 11034. International Society for Optics and Photonics. SPIE, 2019, pp. 58–63.
- [139] S. M. Hooker, R. Bartolini, S. P. D. Mangles, A. Tünnermann, L. Corner, J. Limpert, A. Seryi, and R. Walczak. “Multi-pulse laser wakefield acceleration: a new route to efficient, high-repetition-rate plasma accelerators and high flux radiation sources”. In: *Journal of Physics B: Atomic, Molecular and Optical Physics* 47.23 (Nov. 2014), p. 234003.
- [140] V. Magni. “Multielement stable resonators containing a variable lens”. In: *J. Opt. Soc. Am. A* 4.10 (Oct. 1987), pp. 1962–1969.
- [141] B. Prade, J. Schins, E. Nibbering, M. Franco, and A. Mysyrowicz. “A simple method for the determination of the intensity and phase of ultrashort optical pulses”. In: *Optics Communications* 113.1 (1994), pp. 79–84.

List of Publications

Peer Reviewed Journal Articles

- Thomas Nubbemeyer, Martin Kaumanns, Moritz Ueffing, Martin Gorjan, Ayman Alismail, Hanieh Fattahi, Jonathan Brons, Oleg Pronin, Helena G. Barros, Zsuzsanna Major, Thomas Metzger, Dirk Sutter, and Ferenc Krausz, "1 kW, 200 mJ picosecond thin-disk laser system," *Opt. Lett.* 42, 1381-1384 (2017)

I designed the resonator and performed the measurements. Also I had a major contribution in the development process as well as the mechanical setup and system design.

- Moritz Ueffing, Simon Reiger, Martin Kaumanns, Vladimir Pervak, Michael Trubetskov, Thomas Nubbemeyer, and Ferenc Krausz, "Nonlinear pulse compression in a gas-filled multipass cell," *Opt. Lett.* 43, 2070-2073 (2018)

I performed a preliminary proof of concept experiment and investigated the underlying theory.

- Martin Kaumanns, Vladimir Pervak, Dmitrii Kormin, Vyacheslav Leshchenko, Alexander Kessel, Moritz Ueffing, Yu Chen, and Thomas Nubbemeyer, "Multipass spectral broadening of 18 mJ pulses compressible from 1.3 ps to 41 fs," *Opt. Lett.* 43, 5877-5880 (2018)

I did the theoretical and mechanical design as well as the implementation and performed the experiments.

Selected Conference Talks

- M. Kaumanns, T. Nubbemeyer, M. Ueffing, M. Gorjan, H. G. Barros, Z. Major, T. Metzger, D. Sutter, and F. Krausz, "Highly Stable 5 kHz 200 mJ Ultrafast Thin-Disk Laser," in 2017 European Conference on Lasers and Electro-Optics and European Quantum Electronics Conference, (Optical Society of America, 2017), paper CA_7_4.
- M. Kaumanns, V. Pervak, D. Kormin, V. Leshchenko, A. Kessel, Y. Chen, and T. Nubbemeyer, "Multipass spectral broadening with tens of millijoule pulse energy," in 2019 Conference on Lasers and Electro-Optics Europe and European Quantum Electronics Conference, OSA Technical Digest (Optical Society of America, 2019), paper cd_9_2.

Acknowledgements

First of all I wish to extend a huge thank you to Ferenc Krausz. Without the possibilities, the amazing supply of research equipment and knowledge in his group this thesis would not have been possible. Also I thank him for his continuous support and valuable advice and I especially want to thank him for making my dissertation in the field of physics possible.

I also want to thank my project coordinators Helena Barros, Zsuzsanna Major and Thomas Nubbemeyer. They never stopped to shield the experiments from organizational problems. I cannot thank Thomas Nubbemeyer enough for his support in the laboratory, his efforts in providing good contracts, his professional project coordination and for showing me how to align a laser beam through two pinholes.

I thank Vyacheslav Leshchenko and Alexander Kessel for their help with the multipass experiments. Their thin-plate and pulse stacking experiments provided important results that contributed to this thesis. Their help in creating the longer multipass chamber saved more time than I can imagine. I also want to thank the whole PFS team for providing so many components and for sharing the laboratory with us. Also thanks to Dmitrii Kormin for the interesting discussions, being a great office mate, for his help in keeping the laser system alive and for his support in alignment, design, ordering, calculation and so much more.

Thanks to Lenard Vamos for going with me through the difficult first year, teaching me the basics of laboratory work and always letting me try my own ideas.

The discussion with Jonathan Brons and Kilian Fritsch were always fruitful and helped me to understand the world of laser resonators and multipass cells much better. The mutual and open sharing of experimental results between their development and the development presented in this thesis helped to quickly solve issues before they even showed up. I also want to thank Jonathan Brons for his laboratory alarm that helped me to remember the time and Kilian Fritsch for the organization of several gaming events and of course for organizing my crane license. A special thanks goes to Jonathan Brons for the development and (rarely needed) maintenance of the KLM oscillator. I also want to thank Oleg Pronin for his helpful remarks and relaxing nature. And of course I do respect him.

A special thanks is appropriate for the industrial partners TRUMPF GmbH + Co. KG and TRUMPF Scientific Lasers GmbH + Co. KG. Their knowledge and products are the cornerstone of the presented amplifier system.

Thanks to Martin Gorjan for sharing my name and starting the work on the amplifier system. Not having to start on an empty table and not having to deal with the beginner's mistakes was so much more rewarding.

A lot of aspects of this work would not have been possible without the unique possibility of in-house coating design by Vladimir Pervak and Michael Trubetskov. I thank their whole group for their efforts to provide every coating I asked for. I

especially want to thank Yu Chen for actually having to go through the work of coating the optics I used.

I also want to thank Hanieh Fattahi for her motivational nature and her great impulses. As is tradition I hereby refer to her as the best colleague ever.

Thanks to Nick Karpowicz for answering any question and keeping the IMPRS-APS network alive. I also want to thank the current IMPRS-APS coordinators (and influential persons) Kerstin Schmidt-Buchmann, Monika Wild, Matthias Kling, Vladislav Yakovlev and Kafai Mak.

At this point I want to mention the continuous efforts of Kafai Mak and his group to create events and get-togethers. Some major breakthroughs were obtained by simply talking about it with some drinks.

Thanks to my previously not mentioned co-workers and lab-members especially Gaia Barbiero, Ayman Alismail, Haochuang Wang, Moritz Ueffing, Simon Reiger, Mathias Krüger and Andreas Münzer. Organizing a laboratory is difficult but the atmosphere was always familial and we always managed to organize the equipment, share it properly and solve experimental problems together.

I want to thank our technical staff for their help in drawing and developing components and helping me to learn how a proper drawing has to look like. Especially the seemingly ubiquitous presence of Florian Saran for every small problem you encounter (or simply to give you nice easter and christmas gifts) is without example. I also want to express my gratitude towards Klaus Wirgler for designing my vacuum chambers and converting my mount design to an actually usable drawing. I also thank the LMU mechanical workshop for their fast and problem-oriented work and for not always asking for a drawing.

And finally thanks to the administration of the LMU. Especially the administration in Garching helped me wherever they could and never declined a request. In particular I want to thank Klaus Franke, Martin Groß and Hans-Friedrich Wirth.